

DESIGN AND CHARACTERIZATION OF
INNOVATIVE MATERIALS AND STRUCTURAL SYSTEMS FOR
RESILIENT CONCRETE STRUCTURES

A Dissertation
by
Muhammad Mohsen Sherif

Presented To
The School of Engineering and Applied Science of
The University of Virginia

in partial fulfillment of the requirements for the degree of

DOCTOR OF PHILOSOPHY

May 2018

Major Subject: Civil Engineering

DESIGN AND CHARACTERIZATION OF
INNOVATIVE MATERIALS AND STRUCTURAL SYSTEMS FOR
RESILIENT CONCRETE STRUCTURES

A Dissertation
by
Muhammad Mohsen Sherif

Presented To
The School of Engineering and Applied Science of
The University of Virginia

in partial fulfillment of the requirements for the degree of

DOCTOR OF PHILOSOPHY

Approved by:

Chair of Advisory Committee
Committee Members

Devin K. Harris
Osman E. Ozbulut (Advisor)
Jose Gomez
Steven B. Chase
Baoxing Xu

May 2018

Major Subject: Civil Engineering

Dedication

To my lovely parents
Mohsen Sherif, and Hala ElKordi
&
my lovely young sister
Mai Sherif

For their endless kindness, forgiveness, gaudiness, support and inspiration
without whom my humble work would have not seen
light and none of my achievements would have been possible

To my extended family
Grandparents, Aunts, Uncle and Cousins

For their countless support and their believing in me

Abstract

Design and Characterization of Innovative Materials and
Structural Systems for Resilient Concrete Structures (May 2018)

Muhammad M. Sherif
B.Sc. United Arab Emirates University
M.S. Carnegie Mellon University

Advisor: Dr. Osman E. Ozbulut
Assistant Professor, Department of Civil & Environmental Engineering
University of Virginia

Concrete is the most widely used material for the design of civil structures. However, traditional cementitious materials are brittle and susceptible to cracking and have no functional properties. One approach to enhance longevity and structural performance of concrete structures is the use of high performance materials and structural systems that are durable and safe. Smart materials have received significant interest for civil engineering applications in recent years and are being increasingly explored for achieving high performance, adaptive, and resilient structural systems. A particularly appealing and interesting class of smart materials is shape memory alloys (SMAs). SMAs are a class of metallic alloys that possess several unique characteristics. As a result of their unique solid-to-solid phase transformations, SMAs can produce very high actuation strain, stress, and work output. In addition, SMAs have excellent self-centering ability, good energy dissipation capacity, high corrosion resistance, and long service life. The use of SMAs in concrete structures can enable more resilient designs.

This research explores the design and characterization of SMA-based innovative materials and structural systems to enhance the resiliency of concrete structures. First, the tensile and functional fatigue response of large-diameter SMA cables that offer large force capacities, superior mechanical properties, and lower cost were evaluated. An optical digital image correlation measurement system and an infrared thermal imaging camera were employed to obtain the full-

field strain and temperature fields. A vibration control device that employs the studied SMA cables as re-centering elements was fabricated and tested. Second, the development of advanced cementitious composites by exploiting intrinsic smart properties of SMA fibers in a cementitious composite matrix was explored. SMA-fiber reinforced composite specimens with varying fiber volume fractions were prepared and tested under cyclic flexural loading. Test results were analyzed in terms of flexural strength capacity, mid-span deflection, crack width, and re-centering and crack recovery ratios. Finally, the feasibility of activating SMA tendons using heat of hydration of grout in order to develop self-post-tensioned concrete elements was explored. Results obtained from experimental test indicate that the materials and structural systems investigated in this research can provide good self-recovery and energy dissipation abilities and can potentially improve resilience of concrete structures.

Keywords: Shape memory alloys, SMA cables, Superelastic, Shape memory effect, Fiber reinforced, Cementitious composites, Self-stressing, Post-tensioning, Self-post-tensioning, Acoustic emissions, Heat of hydration, Functional fatigue

Acknowledgement

I would like to express my sincere appreciation and deep gratitude to **Prof. Osman E. Ozbulut** for providing me with the opportunity to work under his supervision on this dissertation as well as other related projects that have broadened my knowledge and expertise. He has always been there whenever needed. His continuous guidance, support, and encouragement were the prime enablers for the successful completion of this dissertation. His teaching and mentoring skills are remarkable and have positively impacted my progress in my study and research. He represents an outstanding model of a university professor and a true scientist. He taught me the fine art of research. I have been privileged and honored to be among his students and work under his supervision during the course of study at the University of Virginia.

I would like to thank **Prof. Devin K. Harris** for serving on my supervisory committee and for his continuous support and feedback on various research topics. Specifically, his guidance and technical support related to Digital Image Correlation Systems were extremely useful and facilitated the successful completion of the experimental tests.

I would like to share my admiration of the teaching and mentoring skills of **Prof. Jose Gomez**. His wealth of knowledge and practical experience have inspired me to solidify my fundamentals in engineering theory and to pursue the research of interdisciplinary fields. It has been my privilege to serve with him as a co-instructor for an advanced course, which contributed to the advancement of my teaching skills.

I would also like to thank **Prof. Steven B. Chase** for serving on my committee and for his valuable input during my research path. His knowledge and expertise on the use of Non-Destructive Evaluation Techniques in evaluating structural components were very useful and supported the successful completion of related experimental work.

I would like to deeply express my appreciation to **Prof. Baoxing Xu** for his continuous support and service on my committee. He provided the needed guidance throughout my academic career at the University of Virginia.

Special thanks are due to the technical staff at University of Virginia and Virginia Transportation Research Council for their assistance and guidance in this research. My appreciation and thanks are specifically directed to **Mr. William Ordell**, **Mr. Keegan Gumbs**, **Dr. Andrei Ramniceanu**, **Mr. Michael Burton** and **Mr. Kenneth Herrick**.

I am very thankful to the Department of Civil and Environmental Engineering, College of Engineering and the University of Virginia for hosting me during my Ph.D. study and for providing the opportunity to serve as a co-instructor and a teaching assistant. Their support to conduct my research and present my work at several international conferences is highly appreciated.

I would like to also express my appreciation to all the staff, mentors and professors at University of Virginia, Carnegie Mellon University and United Arab Emirates University, for their endless support and remarkable research experiences which contributed to the development of my skills. My learning and research experiences in each of the three universities contributed to, and positively impacted my, knowledge and academic life. Living in United Arab Emirates (a very well-developed and diversified country implementing the highest standards in all engineering fields) for more than a decade, has exposed me to the best engineering and ethical practices.

Furthermore, I would like to sincerely thank my friends and colleagues for their continuous support during my graduate study journey. Specifically;

- **Sherif M. Daghsh** for his support and encouragement during the doctoral degree. I am really glad that destiny has united us to pursue our academic careers together at University of Virginia.
- **Mohamed Alipour** for his time, effort and endless discussions about our research and possible approaches to solve problems.
- **Mohamed Amine & Mark Saliba**, for their help, moral support and company during and after their presence as graduate students at University of Virginia.
- **Salman Usmani & Abdou K. Ndong**, for their motivational speeches and patience. They have positively impacted my life and thoughts.
- **Lauren Bolton, Evelina Khakimova, Victoria Tsamis, and John Civitillo**, I greatly appreciate their help and presence in social and academic events. We shared exceptional memories that will always be in my mind. They remain as sisters and brothers and I hope that our paths will intersect again in the near future.
- **Prathamesh S. Desai** for his continuous support, encouragement, help and believing in my capabilities during my time both at Carnegie Mellon University and University of Virginia.

- **Navid Kazem** & **Amin Anvari** for inspiring me to pursue perfection and seek new knowledge.
- I would also like to thank all my fellow graduate and undergraduate students during my undergraduate and graduate education, who have contributed, in one way or the other, towards the success of my research and academic achievements.

Finally and most importantly, I would like to extend my appreciation to my family's generous love and support during my lifetime. Without the strong support of each member of my family, none of my achievements would have been possible.

Nomenclature

BRBs	<u>B</u> uckling- <u>R</u> estrained <u>B</u> races
CFRP	<u>C</u> arbon <u>F</u> iber <u>R</u> einforced <u>P</u> olymer
CNTs	<u>C</u> arbon <u>N</u> ano- <u>T</u> ubes
DICs	<u>D</u> igital <u>I</u> mage <u>C</u> orrelation <u>S</u> ystems
DSC	<u>D</u> ifferential <u>S</u> canning <u>C</u> alorimetry
ECC	<u>E</u> ngineered <u>C</u> ementitious <u>C</u> omposites
EVD	<u>E</u> quivalent <u>V</u> iscous <u>D</u> ampers
FHWA	<u>F</u> ederal <u>H</u> ighway <u>A</u> dmistration
FRC	<u>F</u> iber <u>R</u> einforced <u>C</u> oncrete
FRP	<u>F</u> iber <u>R</u> einforced <u>P</u> olymer
GFRP	<u>G</u> lass <u>F</u> iber <u>R</u> einforced <u>P</u> olymer
HSC	<u>H</u> igh <u>S</u> trength <u>C</u> oncrete
LVDT	<u>L</u> inear <u>V</u> ariable <u>D</u> ifferential <u>T</u> ransformer
MSMAs	<u>M</u> agnetic <u>S</u> hape <u>M</u> agnetic <u>A</u> lloys
NDE	<u>N</u> on- <u>D</u> estructive <u>E</u> valuation
NSM	<u>N</u> ear <u>S</u> urface <u>M</u> ounting
PE	<u>P</u> oly- <u>E</u> thylene
PO	<u>P</u> oly- <u>O</u> lefin
PP	<u>P</u> oly- <u>P</u> ropylene
PVA	<u>P</u> oly- <u>V</u> inyl <u>A</u> lcohol
SFRC	<u>S</u> teel <u>F</u> iber <u>R</u> einforced <u>C</u> oncrete
SIM	<u>S</u> tress- <u>I</u> nduced <u>M</u> artensite
SMAAs	<u>S</u> hape <u>M</u> emory <u>A</u> lloys
SME	<u>S</u> hape <u>M</u> emory <u>E</u> ffect
SPT	<u>S</u> elf- <u>P</u> ost- <u>T</u> ensioned
SVD	<u>S</u> uperelastic <u>V</u> iscous <u>D</u> amper
UHPFRC	<u>U</u> ltra <u>H</u> igh <u>P</u> erformance <u>F</u> iber <u>R</u> einforced <u>C</u> oncrete

Symbols

A_s	Austenite Start Temperature
A_f	Austenite Finish Temperature
A_s^*	A_s of Free Ends for Recovery after pre-strain/pre-stress
A_f^*	A_f of Free Ends for Recovery after pre-strain/pre-stress
A_s^{**}	A_s of Constrained Ends for Recovery after pre-strain/pre-stress
A_f^{**}	A_f of Constrained Ends for Recovery after pre-strain/pre-stress
b	Width of Mortar Flexural Specimen
d	Depth of Mortar Flexural Specimen
d_b	Nominal Bar Diameter for Pullout
d_{max}	Maximum Displacement for Each Tensile Cycle
d_{min}	Minimum/Residual Displacement for Each Tensile Cycle
D_{max}	Maximum Displacement for Each Flexural Cycle
$D_{residual}$	Residual Displacement for Each Flexural Cycle
E_D	Energy Dissipation per Cycle
ε	Strain
ε_{rec}^{full}	Recovered Strain Post-Thermal Activation
ε_{res}	Residual Strain Pre-Thermal Activation
ε_{perm}	Permanent Strain Post-Thermal Activation
f'_c	Compressive Strength
F_{max}	Maximum Tensile Force for Each Cycle
F_{min}	Minimum Tensile Force for Each Cycle
K_s	Secant Stiffness
L	Span of Flexural Specimen
l_b	Embedment Length of the Bar during Pullout
M_s	Martensite Start Temperature
M_f	Martensite Finish Temperature
P	Applied Flexural Load
R	Re-Centering Ratio for Flexural Specimens
T	Temperature
T_b	Tensile Force of a Bar during Pullout
σ_r	Modulus of Rupture
τ	Shear Force per Unit Surface Area of the Bar during Pullout
ΔT_R	Differential Temperature ($A_f - A_s$)
ΔT_R^*	Differential Temperature ($A_f^* - A_s^*$)
ΔT_R^{**}	Differential Temperature ($A_f^{**} - A_s^{**}$)
ζ_{eq}	Equivalent Viscous Damping Coefficient

Table of Contents

Dedication.....	i
Abstract.....	ii
Acknowledgement.....	iv
Nomenclature.....	vii
Symbols.....	viii
Table of Contents.....	ix
List of Tables.....	xii
List of Figures.....	xiii
1 Introduction.....	1
1.1 Background and Motivation.....	1
1.2 Research Goals and Objectives.....	6
1.3 Organization of this Dissertation.....	7
2 Literature Review.....	8
2.1 Shape Memory Alloys (SMAs).....	8
2.1.1 Discovery and Composition of SMAs.....	10
2.1.2 Applications of SMAs in Structural Engineering.....	12
2.1.2.1 Steel Beam-Column Connections.....	12
2.1.2.2 Vibration Control Devices.....	13
2.1.2.3 Reinforced Concrete Beams and Columns.....	15
2.1.2.4 Rehabilitation of Reinforced Concrete.....	17
2.2 Cementitious Composites.....	19
2.2.1 Reinforced Concrete.....	19
2.2.2 Fiber Reinforced Concrete.....	20
2.2.3 Fiber Reinforced Mortar.....	22
2.2.4 Fiber Reinforced Engineered Cementitious Composites.....	23
2.2.4.1 ECC Composition.....	25
2.2.4.2 Self-Healing ECC.....	26
2.2.4.3 Hybrid Fiber Reinforced ECC.....	27
2.2.5 SMA Fiber Reinforced Cementitious Composites.....	28
2.3 Pre-stressed Concrete.....	32
2.4 Summary.....	34
3 Characterization of Superelastic SMA Cables.....	35
3.1 Overview.....	35

3.2	Materials	36
3.3	Experimental Test Setup	36
3.4	General Characterization	40
3.5	Strain Dependency	44
3.6	Strain Rate Dependency	45
3.7	Functional Fatigue	46
3.7.1	Stress-Strain Response	46
3.7.2	Maximum Tensile Stress	53
3.7.3	Residual Strain	55
3.7.4	Energy Dissipation	57
3.8	SEM analysis	60
3.9	Thermal Response	62
3.10	Electrical Resistivity	68
3.11	Fabrication of a SMA Cable-based Control Device	71
3.12	Summary	75
4	Fiber Reinforced Cementitious Composites	78
4.1	Overview	78
4.2	SMA Fiber Reinforced Mortar	78
4.2.1	Material and Specimen Preparation	78
4.2.2	Test Plan and Setup	80
4.2.3	Force-Displacement Curves	83
4.2.4	Re-Centering Capabilities	86
4.2.5	Crack Recovery	88
4.2.6	Energy Dissipation Capacity	90
4.2.7	Acoustic Emissions Analysis	91
4.3	Hybrid Fiber Reinforced Concrete	98
4.3.1	Material and Specimen Preparation	98
4.3.2	Test Plan and Setup	99
4.3.3	Force-Displacement Curves	101
4.3.4	Re-Centering	102
4.3.5	Crack Recovery	103
4.3.6	Energy Dissipation Capacity	105
4.3.7	Acoustic Emissions Analysis	106
4.4	Summary	112

5	Self-Post-Tensioning of Concrete Members Using SMAs.....	114
5.1	Overview.....	114
5.2	Proposed Self-Post-Tensioning Mechanism.....	114
5.3	Materials Characterization.....	117
5.4	Pre-Straining and Strain-Recovery.....	121
5.5	Assessment of Pre-Straining and Pre-Stressing.....	123
5.6	Heat of hydration of grout.....	126
5.7	SMA-Grout Bond Behavior.....	128
5.8	Feasibility of SPT.....	130
5.9	Summary.....	135
6	Summary, Conclusions and Recommendations.....	137
6.1	Summary.....	137
6.2	Conclusions and Recommendations.....	139
7	References.....	143

List of Tables

Table 2-1. Compositions of shape memory alloys and its transformation range ⁸⁷⁻⁸⁹	11
Table 2-2. Typical Physical Properties of fibers used in ECC.....	25
Table 3-1. Summary of the testing procedure for phase 1 and 2 of characterization for superelastic SMA cables.....	39
Table 3-2. Coefficients and statistical parameters of the fitted model for maximum stress	54
Table 3-3. Coefficients and R-square of the fitted model for energy dissipation and equivalent viscous damping for the second cable.....	57
Table 4-1. Mortar mix design	79
Table 4-2. Chemical composition of NiTi strands in atomic percentage.....	79
Table 4-3. Concrete Mixture Design	99
Table 5-1. Mechanical properties for the NiTiNb alloys	120
Table 5-2. Summary of grout temperature test results.....	127
Table 5-3. Characteristic metrics for pre-strain deformation of NiTiNb alloy sheet material	131

List of Figures

Figure 1-1. Typical stress-strain (temperature) response of SMA with phase transformation stages (a) shape memory effect; (b) superelastic effect	2
Figure 1-2. Superelastic SMA applications in concrete members	3
Figure 2-1. Phase transformations with respect to change in temperature, and the change in transformation temperature with applied stress	8
Figure 2-2. Typical stress, strain and temperature interactions of shape memory effect and superelastic SMAs	10
Figure 2-3. (a) Typical beam-column connection using SE-SMA ring-springs; and (b) typical hysteresis of a beam-column connection with SE-SMA ring-springs under cyclic drifts of 5% ⁹³	13
Figure 2-4. (a) Schematic drawing and (b) final assembly of proposed damper by Alipour et al. ⁹⁶	14
Figure 2-5. (a) Schematic drawing of the damper in a chevron brace configuration ⁹⁷ ; and (b) 3D rendering of a damper with NiTiHfPd springs ⁹⁸	15
Figure 2-6. (a) SMA-bars at critical sections coupled with conventional reinforcement; and (b) force-displacement curve of steel (B3-SR) and SMA (B6-NR) reinforced concrete sections ³⁶	16
Figure 2-7. (a) Cross-sectional area for the strengthened reinforced concrete beams using Iron-based SMAs; and (b) Infrared image of the SMA strips post activation ⁶⁸	18
Figure 2-8. Numerical response of the retrofitted shear wall with (a) SMA link elements; and (b) Steel link elements ¹⁰⁵	19
Figure 2-9. (a) Illustrated the typical stress-strain curves of concrete, FRC and ECC ¹³ ; and (b) displays the micro-cracking behavior of ECC ²²⁴	24
Figure 2-10. (a) Fiber Pull-out Specimen dimensions and test-setup ³⁰⁸ ; and (b) SME-SMA fiber reinforced mortar beam specimens for flexural testing ³¹¹	29
Figure 2-11. (a) Schematic drawing of the SMA reinforced ECC; and (b) The flexural behavior under cyclic loading ⁵³	31
Figure 2-12. (a) Experimental test-setup; and (b) numerical and experimental force displacement curves for the column with SMA wire jackets ³²³	34
Figure 3-1. (a) Schematic drawing of the cross-section and longitudinal section of the first cable; and (b) Cross-section of the second cable	36
Figure 3-2. (a) Test setup for the first cable with laser extensometer, DIC and infrared camera; and (b) Test setup for the second cable with laser extensometer, DIC, infrared camera and DMM	37
Figure 3-3. Stress-strain curves for 1 st cable for target strains of 2 to 9% at 0.05Hz	40
Figure 3-4. Stress-strain curve of 1 st cable at 5.4% strain with corresponding DIC axial strain field maps	41
Figure 3-5. Stress-strain curves for second cable: (a) three cycles at a strain of 5%; and (b) response at 3% to 10% strain	42
Figure 3-6. Stress-strain curves for superelastic SMA (a) strands and (b) 2 nd cable subjected to a target strains for 3%, 4%, 5%, 6%, and 7% strains	43
Figure 3-7. (a) Stress-strain response of the 2 nd cycle of the second cable when subjected to 7% target strain and strain contours at maximum tensile stress; and residual strains corresponding to the 2 nd cycle of the cable subjected to (b) 3; (c) 4; (d) 5; (e) 6; and (f) 7% target strains	44
Figure 3-8. Dissipated energy, equivalent viscous damping, and secant stiffness of 1 st cable as a function of strain amplitude	45
Figure 3-9. (a) stress-strain curves of the first cable tested under various loading frequencies; and (b) Dissipated energy, equivalent viscous damping; and secant stiffness of the first cable as a function of loading frequency	46
Figure 3-10. (a) 3D plot of stress-strain curves of the first cable subjected to 100 cycles for every 10 th cycle; stress-strain curves of first cable for (b) 1 st to 10 th cycle; (c) 41 st to 50 th cycle, and (d) evolution of residual strain as a function of number of cycles	47
Figure 3-11. Second cable stress-strain response at 3% strain for 2500 loading cycles	48
Figure 3-12. Second cable stress-strain response at 4% strain for 5000 loading cycles	49
Figure 3-13. Second cable stress-strain response at 5% strain for 5000 loading cycles	50
Figure 3-14. Second cable stress-strain response at 6% strain for 2500 loading cycles	51
Figure 3-15. Second cable stress-strain response at 7% strain for 5000 loading cycles	52
Figure 3-16. Evolution of maximum tensile stress versus cycle number during cyclic tests for 2 nd cable at different strain amplitude: (a) cycles 1 to 2500; and (b) cycles 2500 to 5000	55

Figure 3-17. Evolution of residual strain versus cycle number during cyclic tests for the 2 nd cable at different amplitudes: (a) cycles 1 to 2500; and (b) cycles 2500 to 5000.....	56
Figure 3-18. Evolution of (a) dissipated energy; and (b) equivalent viscous damping ratio during cyclic tests at different strain amplitudes up to cycle 2500.....	58
Figure 3-19. Surface plots illustrating the variation of (a) dissipated energy; and (b) equivalent viscous damping ratio with number of loading cycle and loading strain amplitude for the second cable.....	58
Figure 3-20. Evolution of (a) dissipated energy; and (b) equivalent viscous damping ratio during cyclic tests at different strain amplitudes between cycles 2500 and 5000 for the second cable.....	59
Figure 3-21. SEM images for the second cable: (a) inner core and first outer layer zoomed at 30X; (b) topographic imaging of the first wire zoomed at 255X; (c) secondary imaging of the first wire zoomed at 255X; (d) ductile fracture region of first wire zoomed at 2500X; (e) topographic imaging of the second wire zoomed at 300X; (f) fatigue region of the second wire zoomed at 700X; (g) secondary imaging of fatigue region zoomed at 5000X; (h) topographic imaging of the third wire zoomed at 300X; and (i) crack initiation due to an inclusion for the third wire zoomed at 5000X.....	61
Figure 3-22. Typical temperature variation for the first cable subjected to a cyclic loading at a strain amplitude 5.4%	62
Figure 3-23. Maximum temperature profile of the first cable as a function of strain amplitude	63
Figure 3-24. Variation of temperature morphology along the length of the first cable at (a) 0.05Hz; (b) 0.1Hz; and (c) 0.5Hz cyclic loading.....	64
Figure 3-25. Temperature variations of the second cable for the 1 st cycle with the corresponding full-field temperature profile for strain amplitudes of (a) 3%, (b) 4%, (c) 5%, (d) 6% and 7% strains.....	66
Figure 3-26. Correlation of (a) applied strain, and (b) maximum tensile stress response with the temperature change for the second SMA cable.....	67
Figure 3-27. (a) Temperature evolution during the cycling loading of the second cable specimen with a 3% target strain, and (b) change in temperature with the number of cycles	68
Figure 3-28. (a) Normalized change in resistance of both strand and the 2 nd cable subjected to 6% target strain, (b) Scatter plot of change in resistance with the applied strain, (c) stress-strain curve of the strain subjected to 6% target strain, and (d) stress-resistance curve of the strand subjected to 6% target strain.....	70
Figure 3-29. Force-displacement curves of the sub-components (a) SMA, and (b) elastomer compound, and (c) the hybrid behavior (superelastic viscous damper) ⁵⁷	71
Figure 3-30. (a) 3D rendering of SVD, and (b) schematic drawing at its un-deformed and deformed positions ⁵⁷	72
Figure 3-31. (a) Side view of the elastomer with steel plates, and (b) top view section of the elastomer with the bolt holes location of the steel plates	73
Figure 3-32. Schematic drawing for (a) top steel plates, (b) middle steel plates with delrin rods, and (c) the complete assembly of the superelastic viscous damper.....	74
Figure 3-33. (a) Test setup of the superelastic viscous damper including low-, high-speed cameras and thermal camera FLIR A615, and (b) Test results for displacement amplitudes of ± 12.7 mm, ± 25.4 mm, and ± 50.8 mm at a loading frequency of 0.1Hz	75
Figure 4-1. Cross-sectional and longitudinal view of SMA fibers	79
Figure 4-2. Stress-strain curve of SMA strand: (a) Monotonic response until failure; and (b) Hysteresis loop for 6% strain	80
Figure 4-3. (a) Mortar cyclic displacement protocol; and (b) test setup for mortar testing	81
Figure 4-4. A typical AE signal for (a) tensile mode (mode I) and shear mode (mode II).....	82
Figure 4-5. Identification of failure mode using acoustic emission parameters	83
Figure 4-6. Cyclic force-displacement curves for mortar specimens	85
Figure 4-7. Average strength of mortar specimens (a) peak strength; and (b) residual strength	85
Figure 4-8. Mid-span displacement history and recovery ratio for mortar specimens.....	87
Figure 4-9. Force-displacement curves for the last two cycles for (a) M-SMA-3; and (b) M-SMA-4.....	88
Figure 4-10. Full-field strain measurement of SMA fiber reinforced mortar with 2D-DIC (a) at the first cracking; (b) at the peak load; (c) at the peak load of the 13 th cycle; and (d) at the end of the cyclic loading protocol.....	89
Figure 4-11. Crack width history and crack recovery ratio for mortar specimens.....	90
Figure 4-12. (a) Energy dissipation per individual cycle; and (b) cumulative energy dissipation after each cycle for SMA fiber-reinforced mortar specimens	91
Figure 4-13. Average frequency distribution of acoustic events for different mortar specimens: (a) individual loading cycles, and (b) complete loading protocol	92

Figure 4-14. Acoustic emissions durations for (a) control specimen, and (b) fiber reinforced mortar specimen with 1.0% SMA fibers	93
Figure 4-15. Cumulative energy evolution for (a) control specimen, and (b) fiber reinforced mortar specimen with 1.0% SMA fibers	94
Figure 4-16. Changes in cumulative energy and crack width for (a) specimen with 1.0% of 30 mm SMA fibers for cycles 5 to 13, and (b) specimens with 0.3% of 20 mm, 0.3% of 30 mm and 0.5% of 30 mm long SMA fibers for the last three cycles	95
Figure 4-17. Moving average of hits and average frequency as well as crack width history for (a) control specimen, and (b) fiber reinforced mortar specimen with 1.0% SMA fibers	96
Figure 4-18. Moving average of average frequencies during unloading for (a) control specimen, and (b) alongside with crack width history for fiber reinforced mortar specimen with 1.0% SMA fibers	97
Figure 4-19. (a) Concrete cyclic displacement procedure; (b) speckle pattern on the fiber reinforced concrete; and (c) test setup for concrete testing	100
Figure 4-20. Cyclic force-displacement curves for fiber reinforced concrete specimens.....	101
Figure 4-21. Fiber-reinforced concrete peak and residual flexural strength.....	102
Figure 4-22. Mid-span displacement history and recovery ratio for fiber reinforced mortar specimens.....	103
Figure 4-23. Full-field strain measurement of fiber reinforced concrete with 2D-DIC (a) at the first cracking load; (b) at the peak load; (c) at the peak load of the 8 th cycle; and (d) at the end of the loading protocol	104
Figure 4-24. Crack width history and crack recovery ratio for mortar specimens.....	105
Figure 4-25. Energy dissipation per cycle for each SMA fiber-reinforced concrete specimens.....	106
Figure 4-26. Cumulative energy evolution for (a) C-Control, and (b) C-Hybrid-2	107
Figure 4-27. Cumulative energy as a function of crack width.....	108
Figure 4-28. Increase in cumulative energy and crack width for C-Hybrid-2	109
Figure 4-29. Average frequency distribution of acoustic events for different concrete specimens: (a) individual loading cycles, and (b) complete loading protocol	110
Figure 4-30. Average frequency as a function of rise amplitude during the last capture three cycles during: (a) loading, and (b) unloading.....	111
Figure 5-1. Self-post-tensioning process	115
Figure 5-2. Phase transformation temperatures of SME SMAs.....	117
Figure 5-3. SEM images showing (a) the microstructure in a cast Ni _{47.3} Ti _{44.1} Nb _{8.6} (%) alloy; (b) the micro-constituents in a cast Ni _{47.3} Ti _{44.1} Nb _{8.6} (%) alloy; (c) the microstructures of the Ni _{47.7} Ti _{43.5} Nb _{8.8} (%) alloy sheet; and (d) the microstructure of Ni _{44.6} Ti _{42.8} Nb _{12.6} (%) alloy rod.....	119
Figure 5-4. Tensile stress-strain response of the NiTiNb Alloy	121
Figure 5-5. (a) Stress-strain curves for pre-straining of sheet and rod; and (b) the subsequent strain-temperature ($\epsilon - T$) response during shape memory recovery for sheet and rod materials.....	123
Figure 5-6. Tensile stress-strain curves for the sheet pulled to increasing pre-strain levels at room temperature	124
Figure 5-7. Stress-temperature response during constrained heating and cooling of specimens that have been pre-strained to (a) 5.4%; (b) 10.1%; and (c) 12.2%. The double arrows indicate heating, and the single arrows indicate cooling.....	125
Figure 5-8. Temperature measured in different commercially available grouts during curing for: (a) Grout I; (b) Grout II; (c) Grout III; (d) Grout IV	127
Figure 5-9. (a) Pull-out test specimen and (b) test setup	129
Figure 5-10. Bond stress-slip relationship for SMA bars for specimen 1 at (a) loaded end and (b) loaded end; and for specimen 2 at (c) loaded end and (d) free end	130
Figure 5-11. Variation of (a) ΔTR * and (b) recovery ratio with pre-strain level for free recovery experiments	132
Figure 5-12. Variation of (a) ΔTR ** and (b) recovery stress with pre-strain level for constrained recovery experiments.....	133
Figure 5-13. (a) Strain recovered per unit temperature increase as a function of pre-strain level, and (b) recovery stress per unit temperature increase as a function of pre-strain level.....	134

1 Introduction

1.1 Background and Motivation

Concrete is the most widely used material for the design of civil structures. However, traditional cementitious materials are brittle and susceptible to cracking and have no functional properties. Numerous factors cause damage to concrete structures over their service life [1-3]. Rebar corrosion is a leading cause of deterioration [4-6]. In addition, seismic events may cause significant damage and failure [7-9]. Furthermore, as extreme weather events such as hurricanes, tropical storms, and prolonged intense temperatures occur more frequently, they are expected to considerably impact the health of concrete infrastructure [10-13]. Also, it should be noted that the National Academy of Engineering has identified the restoration and improvement of the national infrastructure to be one, out of 14 grand challenges, of the 21st century [14]. One approach to enhance longevity and structural performance of concrete structures is the use of high performance materials and structural systems that are durable and safe.

Shape Memory Alloys (SMAs) are an appealing and interesting class of smart materials that can remember their original shape upon being deformed. SMAs have been used in different engineering fields such as biomedical [15-17] (artificial plasma [18], dentinal tubes [19], and vascular stents [20]) and mechanical and aerospace [21] (automotive and control devices [22]). The shape recovery ability is attributed to reversible phase transformations between different solid phases of the material. SMAs can be classified into two groups: shape memory effect SMAs and superelastic SMAs; with both groups having the ability to recover their original shape after exhibiting inelastic deformations. For the shape memory effect SMAs, the shape recovery occurs due to thermal activation (Figure 1-1a); while for the superelastic SMAs shape recovery is mechanically (stress) induced. Superelastic SMAs can reach up to 6-8% of elastic strains under stress induced phase transformations (Figure 1-1b). On the other hand, shape memory effect SMAs can recover 6% of inelastic strain under thermal activation phase transformations.

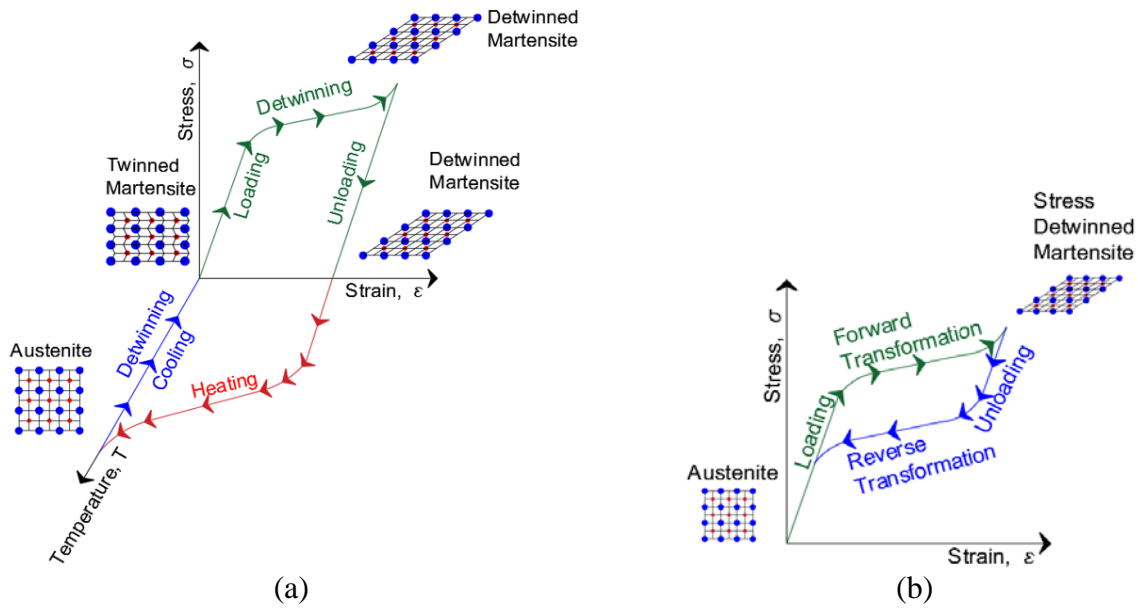


Figure 1-1. Typical stress-strain (temperature) response of SMA with phase transformation stages (a) shape memory effect; (b) superelastic effect

Due to their excellent re-centering and good energy absorbing capabilities in passive nature, superelastic SMAs have received great interest for applications in concrete structures (Figure 1-2). Several researchers studied the use of superelastic SMA bars as longitudinal reinforcement in the critical region of reinforced concrete beams and columns to reduce and recover residual deformations of these structural members [23-33]. SMA bars were placed at the plastic hinge region and connected to conventional steel bars with mechanical coupler. Both experimental and numerical studies revealed that SMA reinforced concrete members demonstrate superior response in limiting residual displacements and crack widths as compared to those reinforced with conventional deformed steel bars [34-38]. Research activities have confirmed the beneficial use of SMAs in concrete structures. In addition, bars have recently been implemented in the plastic hinge region of a newly constructed bridge structure [39, 40]. SMAs have also been used in reinforcing structural elements to provide seismic resiliency [41, 42]. Other researchers have investigated the possible use of SMAs to reduce the vibrations in structural cables subjected to wind loading [43, 44]. Nevertheless, the fabrication of SMA rebars is extremely difficult and the threading of large diameter SMA rebars reduces the strength of the bars significantly [31, 45]. The fracture of SMA bars at the coupling locations has been observed during experimental testing [36, 46-48]. In addition, a more recent study has showed that coupling the SMA bars with carbon steel bars

increased the corrosion of steel significantly as compared to that in steel-only rebars due to galvanic corrosion [49].

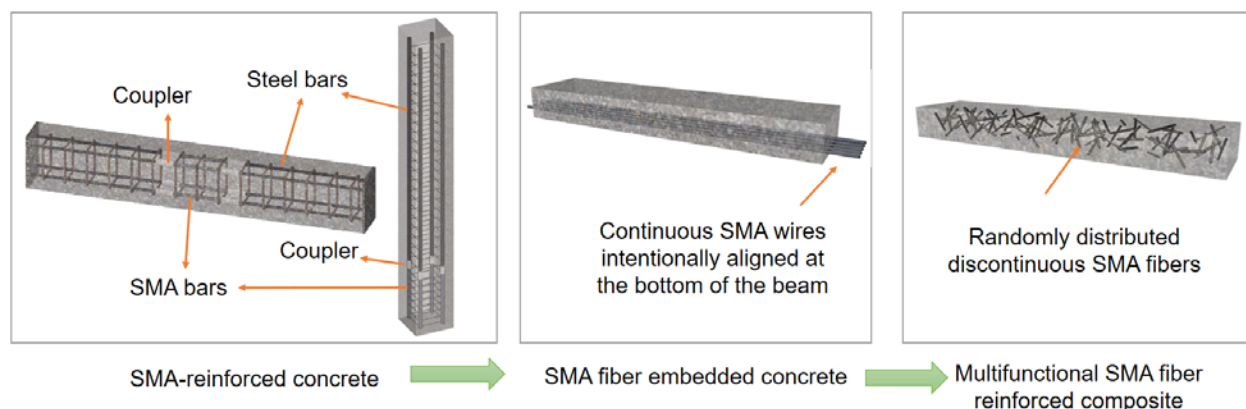


Figure 1-2. Superelastic SMA applications in concrete members

A few researchers considered the use of superelastic SMA fibers in cementitious composites. Kim et al. [50] performed pullout tests on NiTi and NiTiNb SMA fibers embedded in a mortar matrix to observe their bond strength and slip properties. It was elaborated that cold-drawn and end-deformed SMA fibers possess higher pullout resistance. Shajil et al. [51, 52] conducted three-point bending tests on cement mortar beam specimens reinforced with steel and NiTi SMA fibers to assess self-centering mechanism of the SMA fiber reinforced beams. The results of the test indicated that the beams with NiTi SMA fibers have considerably superior self-centering behavior as compared to the beams with steel fibers. Li et al. [53] investigated the performance of a composite material system that integrates continuous superelastic NiTi SMA fibers into Engineered Cementitious Composites (ECC). ECC exhibits high tensile ductility and micro-cracking behavior, while the SMA fibers used in the composite material provided self-recovery capabilities. A small-scale beam specimen with six pre-strained SMA fibers placed in a conduit at the bottom of the specimen was tested under cyclic flexural loading. It was observed that the SMA reinforced specimen significantly recovered the mid-span deflection during unloading and demonstrated crack recovery. In the studies discussed above, the continuous superelastic SMA fibers were intentionally placed at the tension side of the beam, where flexural cracks form, to study re-centering and crack-closing capabilities of SMAs. Further research is needed to study the effectiveness of discontinuous, randomly distributed SMA fibers in cementitious composites. Moreover, while improving mechanical properties and providing re-centering capabilities, the

addition of SMA fibers can also render functional properties such as strain-sensing and damage-sensing into cementitious composites.

In addition, there have been extensive research efforts on the use of SMAs in damping systems over the last decade to enable more resilient designs [54]. Dieng et al. [55] suggested the use of thin NiTi superelastic SMA wires to reduce the amplitudes of vibrations in structural cables. They conducted several experimental and numerical tests to investigate the effectiveness of a SMA damping device. Parulekar et al. [56] conducted several shake table tests and performed a number of analytical simulations for a scaled six-story steel structure fitted with a SMA damper in a V-bracing configuration. Silwal et al. [57] numerically investigated the performance of a Superelastic Viscous Damper (SVD) which combined SMA cables and viscoelastic dampers to provide high re-centering and damping energy dissipation. Soul et al. [58] investigated the use of a tension-compression device fitted with superelastic NiTi wires for self-centering and damping capabilities. Qiu et al. [59] conducted shake table tests as well as numerical simulations of self-centering steel equipped with a SMA brace to replace Buckling-Restrained Braces (BRBs). They used superelastic SMA wires that were always subjected to tensile loading. Nespoli et al. [60] proposed a numerical model to investigate complex passive dampers incorporating multiple NiTi superelastic wires to assess the damping capacity at various strain amplitudes. Speicher et al. [61] used a bundle of NiTi superelastic SMA wires in an articulated quadrilateral bracing system to investigate its effectiveness in reducing the inter-story drift of a nine story structure.

Despite these numerical and experimental efforts, the widespread use of SMA-based control devices in civil structures has been hindered by several factors such as the need for larger capacity SMAs and high material cost. Since the SMA wires are more readily available and have lower cost, many researchers considered the use of small diameter SMA wires, which led to laboratory-scale investigations. For actual structural engineering applications, large size structural elements are usually needed. SMA cables are relatively new structural elements that possess many advantages of the traditional wire cables while offering additional unique properties such as superelasticity. Cables formed of SMAs, which offer higher force capacities, superior mechanical properties, and lower cost, may expedite the implementation of SMA-based dampers in real-world structural applications. However, the extensive characterization of large-diameter SMA cables is missing from the current body of literature.

To improve the performance of concrete structures, the use of shape memory effect SMAs, which require heating to recover their deformations, in concrete members has also been explored. Active confinement of concrete columns with prestrained SMA spirals [42, 62-67] and near-surface-mounted strengthening of concrete beams with SMA strips or bars [68, 69] are among these efforts. In addition, the potential use of thermally-induced SMAs to prestress concrete has been investigated by several researchers [70-73]. The use of SMA tendons in prestressed concrete elements can increase the overall sustainability of structures by minimizing the susceptibility of prestressing tendons to corrosion and by enabling the adjustment of prestressing force during their service life. However, in all of the available studies on the use of SMA elements for prestressing, the SMA elements were triggered by an electrical source. This research will explore the development of Self-Post-Tensioned (SPT) concrete members by activating SMAs using the heat that is released during grout hydration.

1.2 Research Goals and Objectives

The main objective of this Ph.D. study is to explore the characterization, design and implementation of shape memory alloys in civil engineering applications for achieving a new generation of resilient and sustainable concrete infrastructure. This research thoroughly evaluates inclusion of shape memory alloys in various forms in concrete structures. First, the behavior of cement-matrix composites that contains short distributed SMA fibers is systematically evaluated to achieve improved structural performance and/or non-structural functionalities. Next, the tensile response of superelastic cables, that are relatively low-cost form of SMAs compared to large diameter bars, is fully characterized. The SMA cables are then used in the development of a passive control device that can effectively mitigate seismic response of concrete frame buildings. Furthermore, the feasibility of pre-stressing concrete members using shape memory effect SMAs is investigated. The research plan includes the following milestones and objectives:

Milestone 1: Characterization of Superelastic SMA Cables and their Implementation into a Vibration Control Device

- *Objective 1.1:* Thermomechanical and Electrical Characterization of Superelastic SMAs Cables and Strands
- *Objective 1.2:* Investigation on Low-cycle Fatigue Properties of SMA Cables
- *Objective 1.3:* Fabrication and Testing of an SMA Cable-based Passive Control Device

Milestone 2: Development and Characterization of Superelastic SMA Fiber Reinforced Cementitious Composites

- *Objective 2.1:* Development and Characterization of Randomly Distributed SMA Fiber Reinforced Mortar
- *Objective 2.2:* Development and Characterization of Hybrid SMA and Steel Fiber Reinforced Concrete

Milestone 3: Feasibility of Self-Post-Tensioning of Concrete Members using Shape Memory Effect SMA Bars

- *Objective 3.1:* Characterization of a Tailored Shape Memory Effect SMA bars
- *Objective 3.2:* Assessment of the Heat of Hydration of Commercially Available Grout to Thermally Activate the SME SMA Bars

The results obtained from these investigations provide a better understanding of the potential applications of SMA-based material and structural systems in the design, construction, and rehabilitation of various concrete infrastructure systems and reveal the limitations.

1.3 Organization of this Dissertation

This dissertation consists of six sections that are organized as follows:

Section 1 includes a brief description of the innovative technologies and methodologies to mitigate the drawbacks of concrete structures. The motivation of the conducted research work and its scope are presented.

Section 2 provides a concise summary of the development and mechanical response of shape memory alloys and its applications in concrete and steel structures. Also, a comprehensive review of fiber reinforced cementitious composites and the latest research in the field of SMA fiber reinforced cementitious composites are presented. Furthermore, the application of shape memory effect SMAs for pre- and post-stressing concrete members is discussed.

Section 3 investigates the mechanical response of superelastic cables and strands subjected to various strain amplitudes and rates under tensile loading protocols. The stress-strain response and the degradation of various properties of the superelastic SMAs under fatigue loading are examined. Moreover, the thermal and electrical response are investigated and SEM images of the fracture of a superelastic SMA cable due to fatigue loading are presented. At the end of this section, the manufacturing, testing and preliminary results of a superelastic viscous damper are discussed.

Section 4 presents the use of randomly distributed superelastic SMA fibers in mortar and concrete beams to resist flexural loads. The enhancement of various properties such as, flexural strength, residual deformations, and crack recovery are investigated.

Section 5 discusses the technique of the proposed self-post-tensioning of concrete members using shape memory effect SMAs and its limitations.

Section 6 presents a summary of the dissertation work and its conclusions along with its recommendations for the use of innovative materials in concrete structures for increasing the resiliency and sustainability of such structures.

2 Literature Review

2.1 Shape Memory Alloys (SMAs)

SMAs are classified as a group of smart materials due to their ability to recover large deformations that are several orders of magnitudes higher compared to traditional metal alloys. This deformation recovery is based on a reversible solid phase transformation between austenite (parent crystalline) and martensite (product crystalline) phases. The phase transformations can be stress induced (superelastic/pseudo-elastic effect) or thermally induced (shape memory effect). In general, SMA phase transformations are characterized mainly by transformation temperatures that define the start and finish of the two phases. Figure 2-1 illustrates an example of the phase transformations with respect to temperature changes. M_s and M_f define the start and finish of the transformation from austenite to martensite, respectively. While, A_s and A_f define the start and finish of the transformation from martensite to austenite. The phase transformation temperatures are depended on the chemical composition of the SMAs and the applied stress level. The inner plot in Figure 2-1 illustrates the change of the characteristic transformation temperatures when a stress is applied.

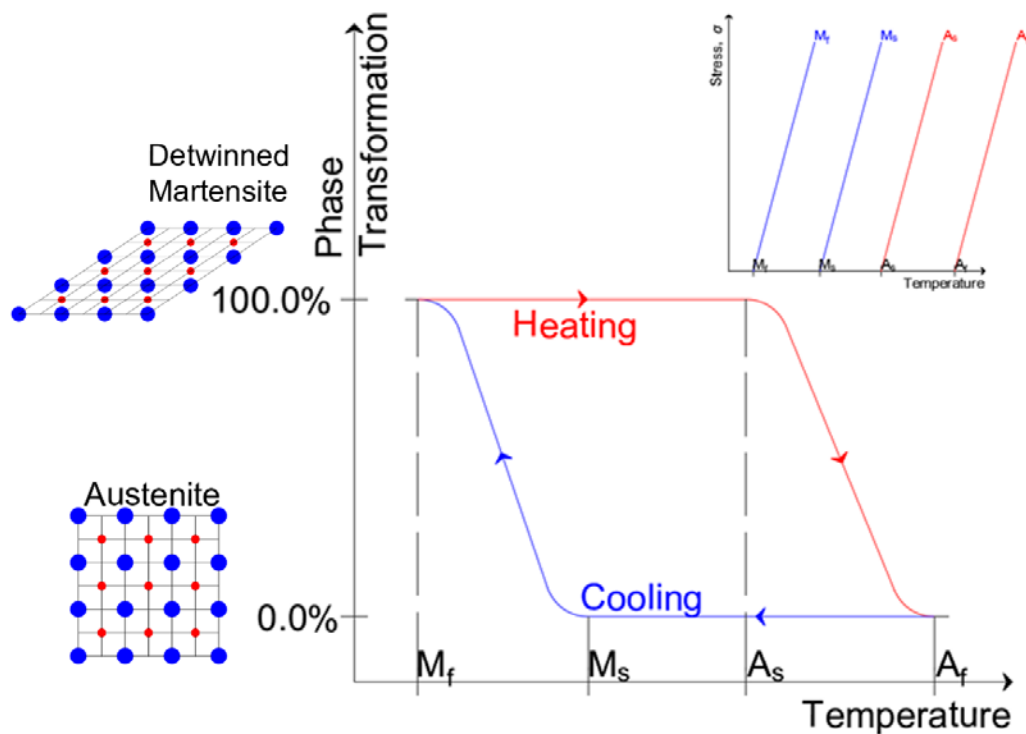


Figure 2-1. Phase transformations with respect to change in temperature, and the change in transformation temperature with applied stress

Shape Memory Effect (SME) occurs when the SMA temperature is lower than the martensite finish temperature (M_f) and the material is in a twinned martensite phase. Under the applied deformations, the molecular bonds are de-twinned, and the molecular structure in that state is defined as de-twinned martensite. Once the material is relieved from the applied stress, the molecular structure remains de-twinned martensite and exhibits inelastic deformations/strains. If the material is thermally activated beyond the austenite finish temperature (A_f), the micro-structure will completely transform to austenite phase and recover the inelastic deformations/strains to reach the original shape. If the material cools down to a temperature below M_f , it will completely transform to twinned-martensite. Superelasticity (pseudo-elasticity) is the recovery of large inelastic strains using the stress-induced phase transformation. For a superelastic behavior to occur the temperature of the SMA has to be higher than the austenite finish (A_f) temperature, where the material is in the austenite phase. The phase transformation occurs from austenite to martensite and vice-versa due to loading and unloading of the SMA. The phase transformation allows the recovery of strains up to 8.0% to 10.0% depending on the metallic composition [74, 75]. Figure 2-2 illustrates the typical interactions of the stress, strain and temperature of shape memory effect and superelastic SMAs. Due to the superior properties of the SMAs which include excellent self-centering ability, energy dissipation capacity and high corrosion resistance and fatigue life [76], SMAs have been used in many engineering applications ranging from biomedical [77] to mechanical engineering [78].

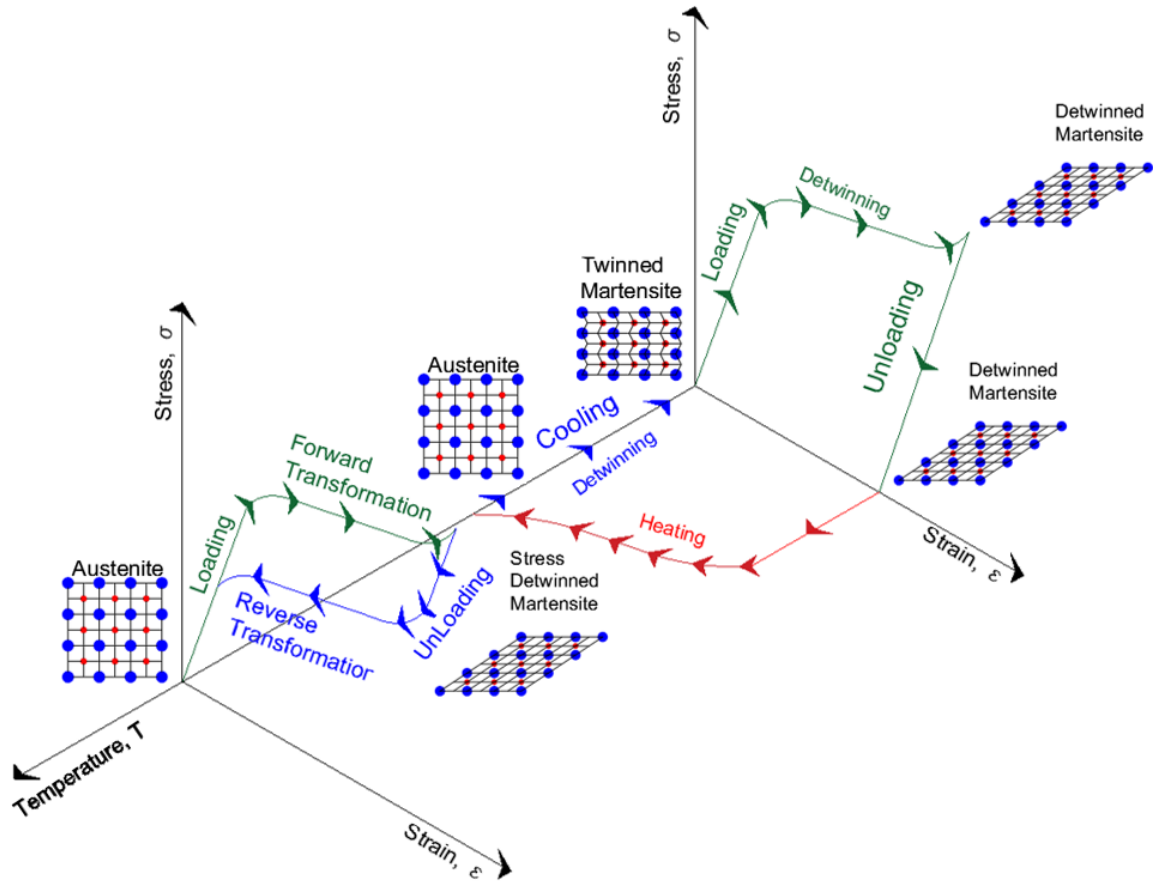


Figure 2-2. Typical stress, strain and temperature interactions of shape memory effect and superelastic SMAs

2.1.1 Discovery and Composition of SMAs

The phase transformations of SMAs were first observed in 1932 by Ölander et al. while studying the resistivity changes of cadmium-gold (Cd-Au) [79]. In 1938, Greninger et al. observed similar phase transformations while investigating the thermal fluctuations of brass (Cu-Zn) [80]. In 1951, Chang et al. further investigated the phase changes and interactions between stress, strain and temperature of gold-cadmium, and were the first to define “shape memory effect” [81]. Shape memory alloys gained a lot of interest during the 1960 with the introduction of nickel-titanium (NiTi) alloys known by NiTiNOL by Buehler et al. in the 1963 [82]. During the investigation of the resistance of NiTiNOL to cyclic fatigue, it was observed that the wires recovered their original shape upon heating. In general, the ratios of the composition of SMAs can influence the shape memory characteristics such as recovery strains and material zero-stress temperatures (M_s , M_f , A_s , A_f). Typical NiTi composition ranges from 49 to 57% and 38 to 50% for Ni and Ti, respectively, in order to achieve the shape memory characteristics [83]. Although NiTiNOL has excellent

characteristics, it is difficult to process and has high production cost, due to the presence of titanium [17]. Other alternatives of SMA compositions including copper and iron based SMAs, such as copper-zinc-aluminum (CuZnAl), copper-aluminum-nickel (CuAlNi), and iron-manganese-silicon (FeMnSi) were investigated by a number of researchers.

Copper based SMAs are cost effective, the stress-strain response is independent to strain rate and have a larger operating temperature range [84]. However, when compared to NiTi, they have lower strain recovery and transformation stresses. Omori et al. introduced iron based SMAs with superelastic behavior of 6% at room temperature [85]. These investigations led to further discoveries of new properties in SMAs such as magnetic shape memory alloys (ferromagnetic materials) [86]. Table 2-1 displays a comparison between the various compositions of SMAs in the temperature transformation range [87-89].

Table 2-1. Compositions of shape memory alloys and its transformation range⁸⁷⁻⁸⁹

Alloy	Composition	Transformation Range (°C)
Ag-Cd	Cd: 44.0 to 49.0%	-190 to -50
Au-Cd	Cd: 46.5 to 50.0%	30 to 100
Cu-Al-Ni	Al: 14.0 to 41.5%	-140 to 100
	Ni: 3.0 to 4.5%	
Cu-Au-Zn	Au: 23.0 to 28.0%	-190 to 40
	Zn: 45.0 to 47.0%	
Cu-Sn	Sn: 15.0%	-120 to 30
Cu-Zn	Zn: 38.5 to 41.5%	-180 to -10
Cu-Zn-Al	Al: 3.0 to 8.0%	0 to 150
	Zn: 22.0 to 28.0%	
In-Ti	Ti: 18.0 to 23.0%	60 to 100
Ni-Al	Al: 36.0 to 38.0%	-180 to 100
Ni-Ti	Ni: 49.0 to 51.0%	-50 to 110
Fe-Pd	Pd: 30%	-100
Fe-Pt	Pt: 25%	-130
Fe-Mn-Si	Mn: 32.0%	-200 to 150
	Si: 6.0%	
Mn-Cu	Cu: 5.0 to 35.0%	-250 to 180

2.1.2 Applications of SMAs in Structural Engineering

Superelastic SMAs have been explored by a number of researchers in the civil engineering community for various applications such as beam-column connections [23-26], damping devices [90] and reinforcement bars [27-30]. Sections 2.1.2.1 to 2.1.2.4 present a brief summary of the use of SMAs in civil engineering.

2.1.2.1 Steel Beam-Column Connections

Leon et al. experimentally investigated the use of SME SMA tendons in beam-column connections and provided a comparison with conventional steel connections [91]. The connection experienced cyclic loading to 8.0% drift. The results indicated that SME tendons can sustain repeated large deformations (4.0% drift) without strength degradation. The SME tendons were thermally activated to recover any residual deformations. The activated SME tendons were subjected to a second series of cyclic loading. A similar hysteresis to that of the 1st cyclic loading was observed. Speicher et al. compared the use of SME and superelastic tendons at connections in a moment-resisting frame, which was subjected to 5.0% drift [32]. SME connections remained elastic up to 0.75%, after which the tendons yielded. Post cyclic protocol, the tendons were heat treated using a heat gun. The tendons recovered 75% of the residual deformations. In the case of superelastic tendons, the tendons were pre-strained to 0.5% strain in order to enhance the re-centering capabilities. Up to 0.75% drift, the connection was reentering to the zero position but with a minimal energy dissipation. Wang et al. conducted further investigations on connections subjected to cyclic loads, using pre-stressed superelastic SMA bars as bolts to attach beams to columns [92]. Eight full-specimens were experimentally tested to investigate various parameters such as the pre-stressing force, SMA bars, and layout of the bolts. The proposed connections exhibited good self-centering behavior up to 2% drift and were ductile up to 4% drift. Wang et al. investigated an innovative methodology for achieving self-centering connections for steel structures using superelastic SMA ring springs placed at bolted connections [93]. The study included characterizing the SMA ring springs. Experimental and numerical cyclic testing on beam-column connections were conducted. Figure 2-3a illustrates a typical superelastic SMA spring connection for steel beam-column. The newly proposed system prevented the main steel members from inelastic deformed, which would result in minimizing post-hazard repairs. The connection experienced a maximum of 0.45% in residual drift corresponding to a recovery ratio of 91.0% when a 5% of drift is applied. A SMA ring failed when a 4.0% drift was applied to the connection,

which might be attributed to material defects due to the manufacturing process. Figure 2-3b displays the typical behavior of the ring spring system experiencing a cyclic drift up to 5.0%. Oudah et al. investigated various mechanical anchorage systems for SMA bars in reinforced concrete at beam-column connections under compression and tension loadings [94]. Two types of failure occurred due to the screws of the anchorage systems and fracture or slippage of the screws by tearing out. A flipped anchorage system resulted in a stiffer post-cracking response and is expected to develop high strains in SMA bars.

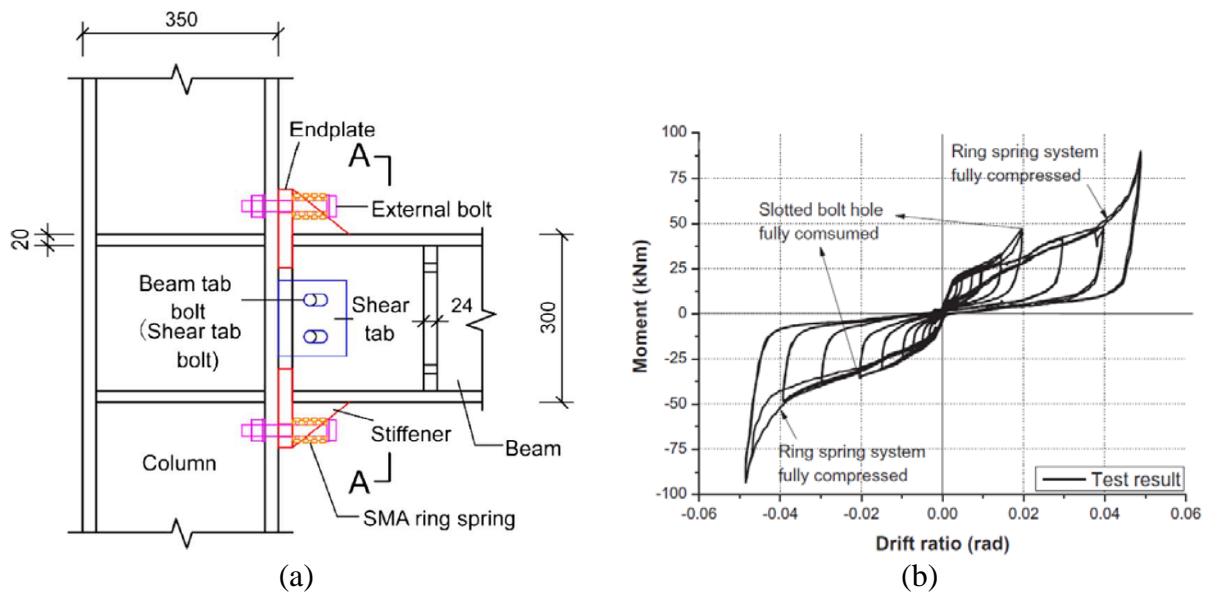


Figure 2-3. (a) Typical beam-column connection using SE-SMA ring-springs; and (b) typical hysteresis of a beam-column connection with SE-SMA ring-springs under cyclic drifts of 5%⁹³

2.1.2.2 Vibration Control Devices

Over the past decade, a number of researchers explored the use of SMAs in bracing systems, passive controls and adaptive-passive control. McCormick et al. investigated the use of superelastic SMA wires and bars as bracing elements to control the vibrations of a structure when subjected to a hazard load [95]. The study included characterization of wires and bars to determine the damping and re-centering capabilities. The characterization tests illustrated that wires and bars had similar equivalent viscous damping (EVD) up to 3% strains. Beyond 3% strain, the wires had a higher EVD under both quasi-static and dynamic loadings, however, they had higher residual strains up to 1% under dynamic loading for 6% strains. A small shake table test was conducted to illustrate the feasibility of using SMA cross-bracing system and compared it to an unbraced frame. The SMA braced-system experienced a maximum roof lateral displacement of 65.1 mm while the

unbraced system experienced a lateral displacement of 90.3 mm. The SMA-braced system did not experience residual displacements. Alipour et al. designed and analyzed a self-centering damper under tension and compression employing superelastic SMA wires that undergo tension in both cases [96]. To evaluate the performance of the damper, the damper was loaded in tension to 4.8 mm and then in compression to 4.8 mm under a strain rate of 2.5×10^{-4} /s. The EVD of the damper was 11.6% and had a dissipated energy of 13.7% kN m/m³. Figure 2-4a and b illustrate a schematic drawing of the proposed damper by Alipour et al. and the final assembly, respectively.

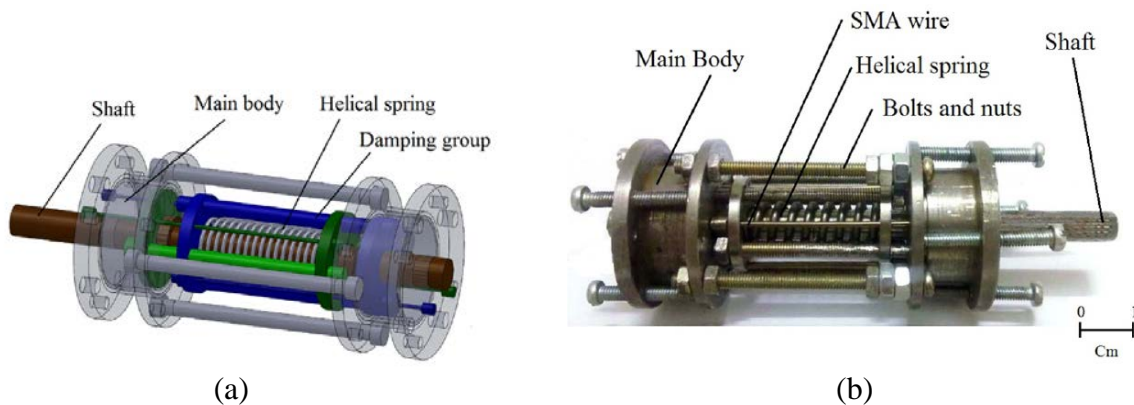


Figure 2-4. (a) Schematic drawing and (b) final assembly of proposed damper by Alipour et al.⁹⁶

Asgarian et al. numerically investigated a self-centering hybrid damper, with superelastic SMA wires [97]. The damper had a steel pipe placed vertically as a link element, while the superelastic SMA wires were placed in transversely to support for energy dissipation and re-centering components. The hybrid device was placed as a chevron brace. The numerical simulation displayed a reduction in the permanent displacement, peak inter-story drifts and accelerations. Figure 2-5a displays a schematic drawing of the proposed damper using chevron brace. Saedi et al. proposed the use of a newly developed NiTi alloy, NiTiHfPd as springs in a damper device [98]. The NiTiHfPd possess superior properties when compared to NiTi due to its higher strength and damping capacity, as well as its hysteresis stability under cyclic loading. In addition, it has a large operating temperature. Characterization tests were conducted to understand the behavior of the developed material under compression at various strain levels ranging between 2% to 6% and at different temperatures ranging between -30 to 50°C. Figure 2-5b displays a 3D rendering of the proposed damper with NiTiHfPd SMAs. Magnetic Shape Magnetic Alloys (MSMAs) are a special class of smart materials, which have a great potential for active vibration control applications due

to their fast response when compared to regular SME SMAs. Minorowicz et al. investigated the use of MSMA as an actuator and the position of the actuator was controlled by applying a magnetic flux [99]. A sine wave was applied to control the position of the actuator from 0 to $500\mu\text{m}$. The error of the applied command and the actuator position of $20\mu\text{m}$ correspond to a maximum error of 4%.

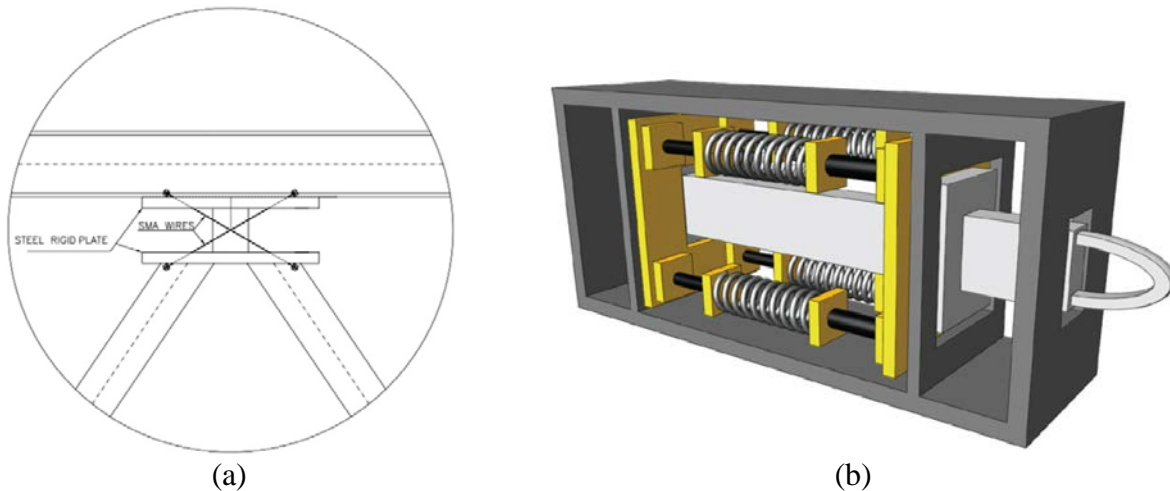


Figure 2-5. (a) Schematic drawing of the damper in a chevron brace configuration⁹⁷; and (b) 3D rendering of a damper with NiTiHfPd springs⁹⁸

2.1.2.3 Reinforced Concrete Beams and Columns

A number of researchers in the civil engineering community examined the use of superelastic SMAs as reinforcement in concrete structures to increase their ductility, energy dissipation and re-centering capabilities. Kuang et al. investigated the reinforcement of concrete beams using superelastic SMA wires [100]. Furthermore, they embedded hollow tubes filled with adhesives to achieve self-repairing. The experimental results indicated that SMA reinforcement has enhanced ductility and crack-closing capabilities after applying large deformations; due to the release of adhesive from the broken-open tubes into the existing cracks. The adhesive sealed the cracks, and when the beam was re-loaded, new cracks were formed. Abdulridha et al. investigated the use of superelastic SMA bars at the critical sections coupled with conventional steel reinforcement [36]. Figure 2-6a illustrates SMA bars coupled with conventional steel reinforced bars. The beams experienced monotonic and cyclic loading schemes. The study revealed that large scale concrete beams with superelastic SMA reinforcement performed similar to small-scale specimens. The use of superelastic SMA bars limited the residual displacements and crack width while enhancing the

yield and ultimate loads. However, the energy-dissipation of the SMA-reinforced specimens was half of that of conventional steel reinforced specimens, due to the consecutive yielding of steel reinforcement which limits the re-centering capabilities of the section. Figure 2-6b displays the load-displacement for the conventional steel reinforced concrete (B3-SR) and SMA-reinforced concrete (B6-NR).

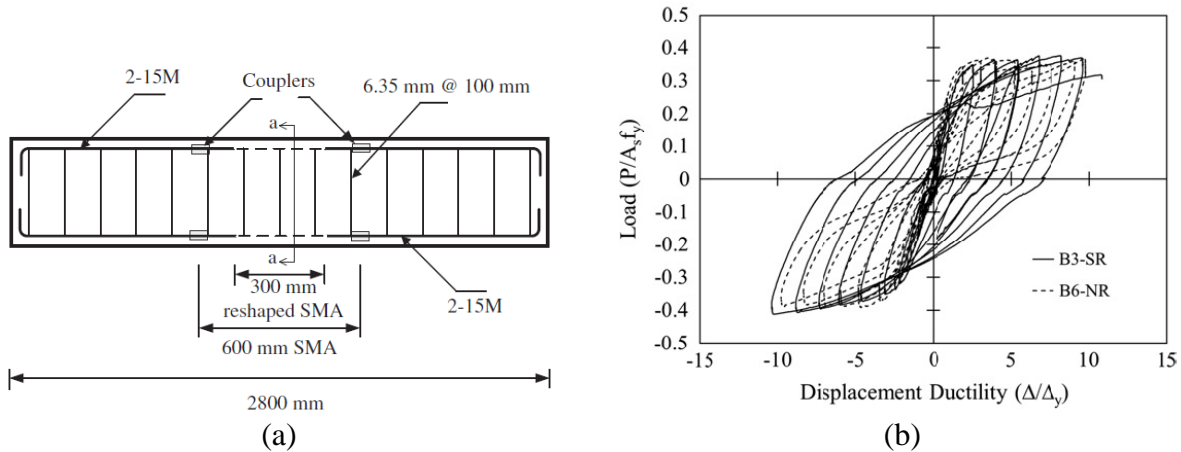


Figure 2-6. (a) SMA-bars at critical sections coupled with conventional reinforcement; and (b) force-displacement curve of steel (B3-SR) and SMA (B6-NR) reinforced concrete sections³⁶

Li et al. investigated the use of SE-SMA wires to reinforce concrete and ECC to enhance the mechanical properties under cyclic-flexural loading [53]. They suggested the use of ECC to solve the displacement incompatibility between concrete and SMAs. Li et al. observed distributed micro-cracks with a width of $40 \mu m$. In each cyclic loading level, the number of cracks increased while maintaining a small crack width, which allowed the SMA-ECC to withstand very large deformations and recover mid-point displacements and cracks. Billah et al. suggested the use of superelastic SMA reinforced bars at plastic hinges for columns and stainless steel or Fiber Reinforced Polymer (FRP) bars as main reinforcement to mitigate corrosion of steel [101]. The seismic performance of the hybrid concrete columns was investigated. Hybrid columns included: SMA and Stainless Steel (SMA bars are in plastic hinge), SMA-FRP (SMA bars are in plastic hinge) and Stainless Steel-FRP (Stainless Steel bars are in plastic hinge). The results indicated that the residual displacements for the SMA bars in the plastic hinge were less than 87% of the residual displacements of the stainless steel.

Shrestha et al. investigated the use of SMA reinforced ECC column to mitigate hazard loads and compared it to post-tensioned column with an elastomer pad at the bottom of the column and to a post-tensioned column with confined concrete [102]. A three-dimensional assembly of beam and column elements was used to evaluate the resilience of the columns. The numerical model was validated by conducting experimental testing on a 33m quarter-scale model of a four-span bridge and the scaled model was excited using a shake table. The numerical simulation revealed the peak drifts, residual drifts and base shears in terms of the structural response and peak values. The results indicated that the presence of superelastic SMA in combination with ECC displayed a remarkably superior response with minimal damages and excellent re-centering capabilities. Billah et al. suggested a performance based seismic design for superelastic SMA reinforced concrete bridge piers [103]. The study developed a performance based damage states for five different types of SMAs in terms of maximum and residual drifts. The prediction of the residual displacement of the SMA reinforced concrete piers was based on the maximum and residual drifts as well as the superelastic strain of the SMAs. The analytical model was verified with experimental observations.

2.1.2.4 Rehabilitation of Reinforced Concrete

In recent years, SMAs have been examined for the strengthening, repairing and rehabilitation of concrete structures. Shin et al. investigated the retrofitting of reinforced concrete columns with SME-SMA wire jackets to resist seismic loads [104]. Four columns were prepared, of which one represented the control specimen without any retrofitting technique. The second column was retrofitted using Glass Fiber Reinforced Polymer (GFRP), the third column was retrofitted using SMA wires, and the fourth column had a hybrid strengthening using SMA wires and GFRP. The SME-SMAs were thermally activated to a temperature of 150°C using an electric current. The results revealed that applying active confinement using SMA spirals significantly enhanced the ability of columns to dissipate energy as compared to the passive confinement applied by the GFRP. Shahverdi et al. investigated the use of low cost iron-based SME-SMAs for strengthening reinforced concrete beams by Near Surface Mounting (NSM) [68]. Six beams were prepared. The first beam represented a control specimen with regular reinforcement. Beam 2 was strengthened using two SMA strips that are not activated, while beams 3, 4 and 6 were strengthened using two SMA strips that were activated. Beam 5 was strengthened using one Carbon Fiber Reinforced Polymer (CFRP) strip. A power supply was used to activate the SMA strands with a high current density of 9 Amperes/mm. The cracking load of the specimens with activated SMAs was higher

than 80% of that of the specimens which were not activated. The pre-stressing of SMAs offered many advantages including reduced crack widths, deflections and stresses in the internal steel. The activation of the SMAs applied a recovery stress of 200 MPa, the bond behavior of the ribbed Iron-SMA with the cement-based mortar was good and judged to be sufficient for strengthening applications. Figure 2-7a and b illustrate the cross-sectional area of the beam strengthened with iron based SMAs and an infrared image displaying the maximum captured temperature after thermal activation, respectively.

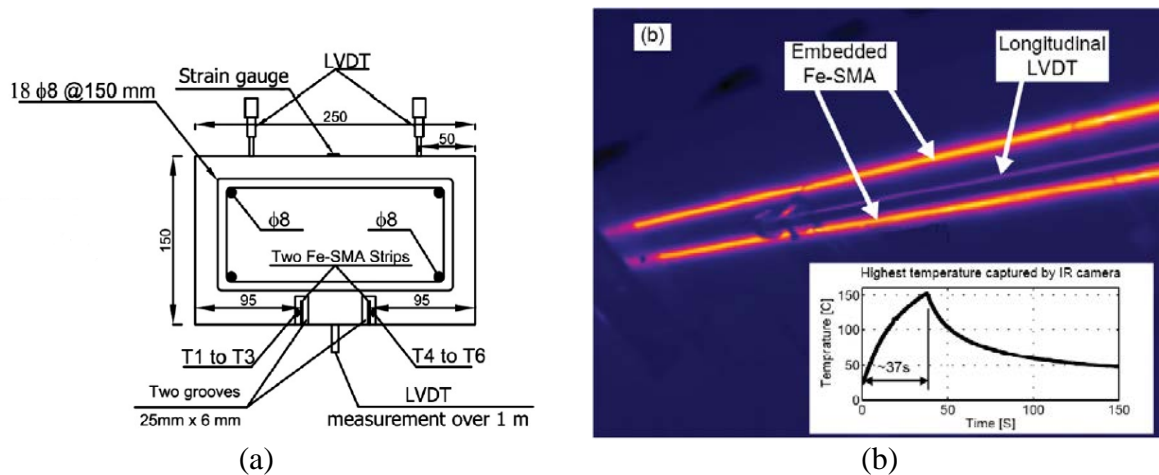


Figure 2-7. (a) Cross-sectional area for the strengthened reinforced concrete beams using Iron-based SMAs; and (b) Infrared image of the SMA strips post activation⁶⁸

Cortés-Puentes et al. investigated the retrofitting of concrete shear walls with superelastic SMA bracings [105]. The braces were made of SMAs and reinforcing steel links connected to the corners using steel plates. The braces were optimized to ensure that SMA links will transform from austenite to de-twinned martensite and have a maximum 6% strains under seismic loadings. The braces will resist tensile loads only. Two bracing systems of SMA and Steel link elements were fabricated. The bracing elements of SMA and Steel link were each tested to capture the typical response of the bracing system. To further evaluate the effectiveness of the SMA bracing system a numerical model was implemented. The numerical solution was verified using a small-scale testing model. The designed steel braces dissipated energy up to a cycle before the targeted elongation, while for the SMA braces the dissipated energy was higher at the targeted elongations and beyond. As stated before, due to the excellent strain response of SMAs, the SMA bracing system was able to experience an excellent re-centering of the shear structure. However, for the steel bracing system, and due to the yielding of the steel elements, it experienced extensive

permanent deformations. The numerical models illustrated an increase in the lateral strength of the SMA bracing system. The steel bracing system had an increase in the strength. Figure 2-8a and b illustrate the numerical response of the SMA and steel retrofitted shear wall.

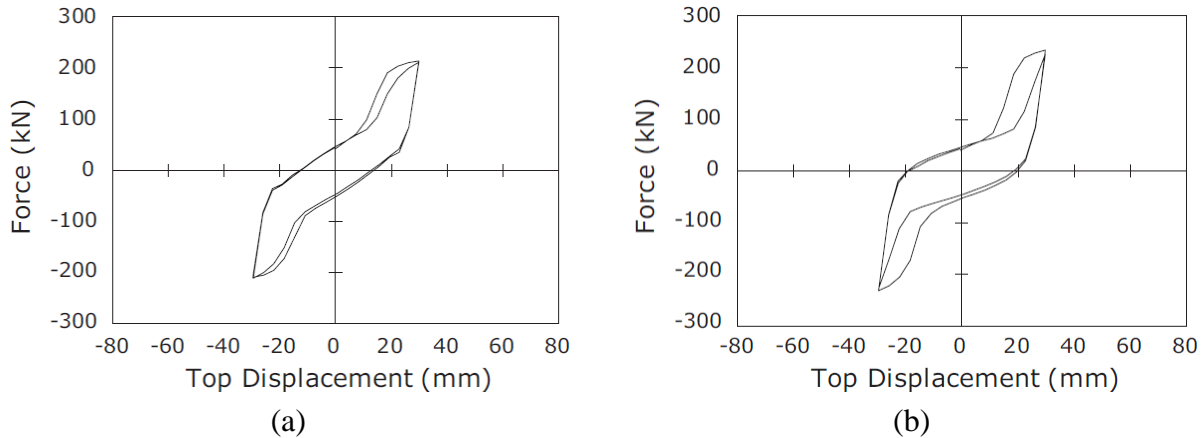


Figure 2-8. Numerical response of the retrofitted shear wall with (a) SMA link elements; and (b) Steel link elements¹⁰⁵

2.2 Cementitious Composites

2.2.1 Reinforced Concrete

Conventional concrete is a widely used construction material in the civil engineering community, due to its low cost and high compressive strength of about 35 MPa (5,000psi) at 28 days [106]. The use of chemical and mineral admixtures that reduce water content has led to compressive strength that can reach up to 70 MPa (10,000 psi). The newly developed material is known as High Strength Concrete (HSC) [107]. However, concrete experiences cracks when subjected to flexural loads due to its relatively low tensile strength [108]; On the other hand, HSC is costly and time consuming due to its dependence on the ambient temperature, cement chemistry and fineness of aggregate [109]. To overcome the low tensile strength of concrete, steel reinforcement bars are used to design reinforced concrete. Although, reinforced concrete can resist flexural loads, it has problems related to its durability due to cracking of concrete during its service life. Cracks occur due to mechanical factors (early-age shrinkage, impact loading, fatigue and hazard loads) and environmental factors (freeze-thaw cycles) [110, 111]. Cracks allow aggressive substances, such as, chloride ions, carbon dioxide and moisture, to reach the reinforcing steel and accelerates the cracking process [112].

Structures that are exposed to harsh environmental factors such as, offshore structures including, among others, floating bridges and sea tanks are usually built using pre-stressed concrete as it demonstrates a superior corrosion resistance compared to other conventional structural materials when exposed to the marine environment [113]. During construction of pre-stressed concrete, it is difficult to control crack initiation and propagation due to shrinkage and changes in temperature [114]. Furthermore, the expected lifetime of such structures are limited to 50 years due to the chloride damage from aquatic settings [115, 116].

Concrete structures have significant challenges due to the deformation incompatibility between concrete and steel reinforcement. Structures are subjected to hazard loads that are dynamic in nature such as earthquake and wind. They resist such loading mechanisms by yielding of steel reinforcement at plastic hinges [117]. Under severe dynamic loading, the steel reinforcement yields and cracking and crushing of concrete are exhibited. This causes severe damage and large permanent deformations that might require urgent and costly repairs [53]. In the USA, it is estimated that the cost of reconstruction of deteriorated RC structures is around \$200 billion [118]. While the annual cost of maintaining existing bridges is around \$5.2 billion [119]. The US Federal Highway Administration (FHWA) estimated that bridges require an investment of \$20.5 billion annually due to the corrosion of steel. Repairs are usually applied using conventional materials which are more prone to cracking and usually fail [120].

In recent years, many researchers have investigated resilient and sustainable structures incorporating corrosion resistant structural members that can mitigate dynamic loads and limit post-event residual damages through ductility and energy dissipation [53]. These structures lead to functional transportation networks and structural systems that are necessary in the aftermath of a major disaster [53]. This would result in a reduction of direct and indirect losses and secures the lives of civilians [117].

2.2.2 Fiber Reinforced Concrete

Fiber Reinforced Concrete (FRC) is a composite material that possesses large energy-dissipation capacity that is suitable for structures subjected to severe loads such as blast, impacts and earthquakes [121]. FRC is widely used in civil infrastructures including airports, highways, industrial floors, bridge decks, elevated slabs, overlays, tunnel linings and precast elements [122-124]. Using FRC is beneficial for structures and increases their durability through reduction in the crack width and permeability [125]. The addition of fibers to concrete prevents the creation and

propagation of cracks by the fiber bridging mechanism which can increase the toughness and impact resistance [126]. FRC can mitigate deteriorations due to shrinkage and early age cracking [127]. It also improves the freezing resistance, due to the increase of harmless pores that can relieve the freezing pressure [128-130]. Although the production cost of FRC is high, it has high mechanical properties and it is environmentally friendly, thus proving to be more sustainable than traditional concrete [131, 132]. Moreover, a potential cost saving is the reduction in using steel reinforced bars [133].

Steel Fiber Reinforced Concrete [SFRC] has been widely investigated in the literature under compressive, tensile and flexural loading due to the relatively high strength and resistance to crack growth [134, 135]. Hakeem et al. investigated SFRC under compression and found that it can reach a compressive strength of 163MPa and an elastic modulus of 57GPa [136]. Zhang et al. reported that steel fibers enhance ductility and impact resistance of concrete [137]. Hussein et al. illustrated that SFRC possesses enhanced flexural and shear capacity [138]. Lee et al. investigated the structural behavior of RC beams with steel fibers under dynamic loading. The results indicated an enhancement in static, impact and blast resistance in terms of higher energy absorption capacity and lower maximum and residual displacements [134]. Karadelis et al. subjected SFRC to flexural loads and concluded that the efficiency of SFRC is higher than traditional concrete [139]. Yoo et al. used steel fibers with high strength concrete (Ultra-High Performance Fiber Reinforced Concrete - UHPFRC) to decrease residual displacement, enhance residual capacity and prevent local failures at contact surfaces [140]. Dagenais et al. investigated the retrofitting of RC bridge piers using UHPFRC. The strengthening of the columns enhanced its ductility. The failure occurred at the reinforcing bars of the footing at a very large displacement under seismic loadings [141]. It was also reported that the addition of steel fibers beyond a critical fiber volume ratio does not significantly increase the structural capacity [142, 143]. In fact, increasing the steel fiber content may lead to a loss of ductility as well as a reduction in the workability and an increase in the structural weight [144-146]. In order to encounter these issues, some researchers investigated the use of basalt and Poly-Propylene (PP) fibers. Colombo et al. suggested the use of basalt FRC due to its low cost, good compatibility with the concrete matrix, superior mechanical property, strong corrosion resistance and environment friendly in its production [147]. Zhao et al. assessed the behavior of basalt FRC under flexural loading, the results indicated that basalt fibers enhance the resistance to elastic and plastic deformations [148]. Moreover, the use of PP-FRC can improve

the durability of concrete by increasing ductility and energy absorption when subjected to impact loads and external vibrations [149].

To further enhance the properties of FRC, hybrid synthetic fiber reinforced concrete, composing of micro and macro fibers, has been investigated in lightweight concrete to enhance the resistance of the composite to micro and macro-cracks [150]. Short fibers enhance the fracture toughness of the cementitious matrix in tension, while the long fibers are important to arrest and delay the macro-crack growth [151, 152]. Kwon et al. introduced the hybrid-FRC and the results indicated that the hybrid performance exceeds the sum of individual fiber performances [153, 154]. The most common hybrid-FRC is composed using steel and PP fibers which have proved to be effective in improving the strength, ductility and resistance to impact loads [155-158].

2.2.3 Fiber Reinforced Mortar

FRC has superior properties when compared to conventional concrete as it limits the crack growth. Most of the special structures such as dams and breakwaters, suffer from erosions due to the water tides [159]. In the case of SFRC, fibers are either pulled out or sheared depending on the orientation of the steel fibers [160]. The seepage of harmful solutions, which leads to corrosion of steel fibers or reinforcement, is not eliminated. The use of CFRP and GFRP reinforcement bars to mitigate the issues raised by the corrosion of steel has been investigated by a number of researchers. Mohamed et al. investigated the use of CFRP bars and spirals in a circular beam under a four-point bending to resist shear loading [161]. Ali et al. have used GFRP in reinforced concrete columns subjected to seismic performance [162]. The results of the two studies indicated an enhancement in ductility. Nevertheless, the concern of cracking in concrete members was not fully addressed by the proposed measures [163].

On the other hand, mortar is used to bind two structural elements such as bricks and connections such as beams to columns [164]. Other techniques have been used to repair/strengthen concrete structures to overcome deteriorations including, but not limited to, NSM and bonding glass/carbon FRP [165-170]. Although these techniques have proven to be successful in extending the lifetime of a structure, wrapping members with FRP laminates is a tedious and time consuming task and can be deployed for certain accessible sections. Moreover, FRP can be easily deboned when subjected to fatigue loading. Nevertheless, mortar is an effective material for repairing concrete members. However, due to its brittle nature and low tensile strength, cracks develop overtime [171].

To mitigate these issues, polymeric (polyethylene, polyvinylchloride, polypropylene, polyvinyl-alcohol), inorganic (steel, glass and carbon) and natural fibers (bamboo and hemp) in reinforcement of mortar are used [172]. The use of various types of fibers at different fiber volume ratios to increase the workability, setting time, fluidity and mechanical properties such as impact resistance and flexural strength, was investigated [173-177]. The bridging action of fibers improves the durability and resistant to abrasion and freezing-thawing action [178-181]. Fibers are used to enhance the bond strength between old cementitious members and the fiber reinforced mortar layer, to achieve a successful repair [182-185]. The enhanced properties depend on the amount of fibers, the modulus of elasticity of fibers, fiber aspect ratio, fiber orientation and aggregate size.

Natural fibers, such as coconut husk [186-187] and bamboo [188], were found to be successful for applications of lightweight composites. Fantilli et al. investigated the use of wool as an organic fiber reinforced mortar which was subjected to flexural loads. The results indicated an enhancement in the flexural strength and ductility [172]. The addition of natural fibers is promising but their applications are still limited when compared to industrial fibers. Due to the alteration of properties of the natural fibers when exposed to alkaline environment [189-192]. Polymeric fibers can control crack openings and distribute the stresses over multiple cracks, however they have low-modulus [193, 194]. Hybrid fiber reinforcement, such as the combination of steel and nylon fibers, could provide a high modulus of elasticity and control cracking [195-201].

2.2.4 Fiber Reinforced Engineered Cementitious Composites

In 1998, Li et al. developed ECC and illustrated high resistance to tensile loading [202]. ECC exhibit superior properties when compared to fiber reinforced mortar and concrete, including high tensile strength and ultimate strain capability with significant tensile strain hardening capacity [203-205]. These properties led to the use of ECC in structural components including beams, columns, walls, and connections under monotonic and cyclic loading [206-209]. ECC are considered as an eco-friendly cementitious composites as they reduce the use of raw materials such as stone aggregates and water [210]; In addition, the traditional cement (clinker) is substituted with pozzolanic mineral admixtures such as fly ash and silica fume [211].

Kim et al. investigated the flexural response of fiber reinforced cementitious composites subjected to biaxial flexural loading. The results indicated that the equivalent flexural strength and the normalized energy absorption capacity under biaxial condition are higher than uniaxial

conditions [212]. Kosa et al. increased the ultimate displacement and the maximum strength by 60% and 10%, respectively, by using high performance fiber reinforced cementitious composites for bridge piers at plastic hinge regions [213]. Dehghani et al. investigated the use of ECC to enhance lateral strength and to maintain the integrity of the walls [214].

ECC can be used in rehabilitation of dams and retaining walls [215]. Zheang et al. explored the benefits of using a layer of ECC to strengthen the shear behavior of RC beams [216]. Huo et al. used layers of ECC to improve the yield strength and the crack dispersion capacity of RC beams subjected to flexural loading [217]. The tensile strain-hardening was achieved by adding a relatively low volume fraction, typically 2% of short randomly distributed fibers [218]. The mechanical response of ECC depends on the fibers volume, aspect ratio, fiber strength, and matrix bonding interface [203, 219]. The strain-hardening behavior is associated with multiple tight cracking in the brittle matrix [220]. The multiple tight cracks exhibit $100\mu\text{m}$ in crack width when deformed to high tensile strain during saturated multiple cracking [221]. The generation of distributed multiple cracks is achieved by the bridging stresses of fibers, that can be tailored by micromechanical modeling [222, 223]. Figure 2-9a illustrates the typical stress-strain curve for concrete, FRC and ECC [13]. Figure 2-9b displays the micro-cracking behavior of ECC [224].

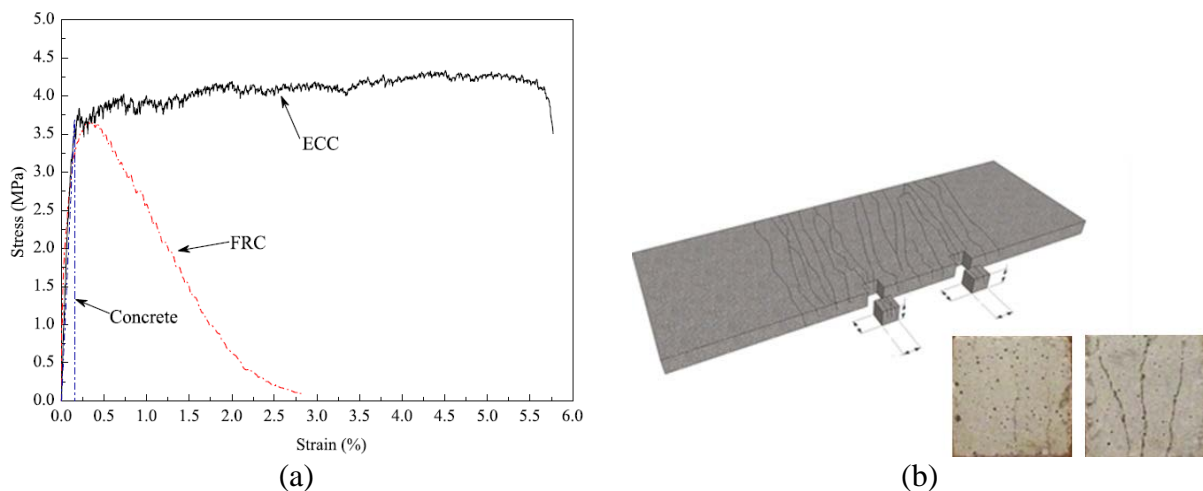


Figure 2-9. (a) Illustrated the typical stress-strain curves of concrete, FRC and ECC¹³; and (b) displays the micro-cracking behavior of ECC²²⁴

ECC possess high fracture energy [225-228], energy dissipation and impact shutter resistance due to their mixture proportions. Such properties are necessary for protective and defensive structures [229]. Cho et al. embedded steel reinforcement in ECC at plastic hinge regions and subjected them to cyclic loading, which resulted in elimination of concrete crushing and spalling [230]. Kang et al. experimentally investigated the effectiveness of ECC on mitigating the progressive collapse of structures subjected to hazard loads [231]. The results indicated that ECC limit cracks width and are more compatible to steel reinforcement. ECC can be used in corrosion-resistant structures, due to its low permeability in both cracked and un-cracked sections [232]. A small crack width would reduce the ingress of aggressive substances reaching the steel reinforcement, and prevent delamination and concrete cover spelling [233].

2.2.4.1 ECC Composition

M45 is a standard ECC mixture that utilizes CEM I Portland cement, low calcium fly ash, fine silica sand, PVA fibers, water and superplasticizer. Fly ash, a by-product of fire power stations, was reported to be effective in improving both the short- and long-term mechanical properties of ECC [234, 235]. ECC have been focused on mono-fiber systems using steel, basalt, PE and PVA fibers [236-240]. Table 2-2 presents a list of typical physical properties of steel and synthetic fibers in cementitious composites [241].

Table 2-2. Typical Physical Properties of fibers used in ECC

Fiber Type	Diameter (μm)	Tensile Strength (MPa)	Density (g/cm^3)	Elastic Modulus (GPa)	Length (mm)
Basalt	12	1,773	2.65	89	12
PVA	40	1,202	1.3	41	12
PE	12	2,757	0.97	110	12

The advancement in industrial technologies related to the development of synthetic fibers provided a variety of properties and geometries. Asbestos cement was successful in prefabricated elements and was extensively used, but it has been banned in many countries for health reasons [242]. Steel fiber reinforced ECC was first introduced in the 1960s by Romualdi et al., providing a strain hardening behavior and an increase in the ultimate strength [243]. However, there is a risk of corrosion when the composite is exposed to saline or acidic environment; which can lead to deterioration in the strength and toughness [244]. Another aspect, is the difficulty in preparing

steel fiber composites with a fiber volume ratio greater than 2.0% [245]. Also, researchers investigated the effect of adding Carbon Nano-Tubes (CNTs) into cementitious matrix [246-249]. The addition of CNTs provided a better ductility, an increase of the fracture energy, and durability that led to a reduction in the reinforcement [250]. Nevertheless, CNTs are limited due to their high production cost [251], and also due to the use of acid functionalization for enhancing adhesion, and hence increasing the toxicity of CNTs [252].

Another viable option is the use of basalt fibers as they do not corrode and have a high tensile strength. The theoretical fiber bridging stresses illustrated a high cracking strength than conventional ECC, but they show a softening behavior after cracking, which can be attributed to the low slip-hardening and high strength reduction of the composite [241]. Nylon fibers, such as Poly-Ethylene (PE), Poly-Vinyl Alcohol (PVA), and Poly-Olefin (PO), have been investigated and are advantageous due to their low production costs. PVA fibers exhibit higher mechanical properties such as tensile strength, and Young's modulus than PP and PO fibers [253]. PVAs are hydrophilic fibers which enhance the fiber wettability and improve the fiber dispersion [254]. During dehydration, PVA fibers are capable of creating molecular bond with the cementitious matrix [255]. The optimal PVA fiber volume ratio is 2.0%, but to achieve a high ultimate tensile strain, a fiber volume ratio ranging from 4.0% and 5.0% is suggested [254]. Said et al. investigated the use of ECC for slabs to enhance flexural strength. The results revealed displayed that the composite did not attain the desired ductility due to rupture of PVA fibers [256].

2.2.4.2 *Self-Healing ECC*

Self-healing can be achieved by including hollow fibers [257-267], chemical encapsulations [268-271], bacterial-based biological self-healing [272-275], expensive agents and mineral admixtures [276-278], shape memory alloys [279-282] and self-controlled tight micro-cracking [283-289]. Self-healing can assist in repairing members with access restriction, especially in the case of large infrastructures [221]. The self-healing mechanism is initiated without external intervention due to the tight cracks and high amounts of cementitious material in the mixing proportions [221, 290]. This could lead to a reduction of the deterioration rate and repair frequencies and would minimize the cost and extend the service life of structures [291].

Li et al. performed mechanical and permeability tests on ECC to investigate the effects of multiple cracking on self-healing. They concluded that a maximum crack of $50\mu\text{m}$ would result in a complete recovery, and partial recovery can be achieved to a crack size of $150\mu\text{m}$ [292]. Other

researchers have reported that crack width ranging from 5 to 300 μm could be sealed completely [293-297]. Self-healing has been associated with the ongoing hydration of cementitious matrix [298], however, this is only valid for young specimens. The formation of calcium carbonate is the likelihood of repairing cracks at later ages [299]. It results from the reaction of calcium ions, water and carbon dioxide, that depends on the several parameters such as, temperature, concentration of reactants and pH value [300]. Alyousif et al. investigated the effects of self-healing on the different transport properties of micro-cracked ECC with different maturity levels and incorporated three different mineral admixtures [301]. Said et al. investigated the effect of replacing cement by fly ash on the self-healing behavior of ECC. Experimental results demonstrated that all mixtures exhibited self-healing with slight differences [302]. Yildirim et al. investigated the cracks and gas permeability to assess the self-healing of ECC [303]. All of the previous research indicated the feasibility of achieving self-healing by controlling the crack sizes, which led to the investigation of hybrid fiber reinforced ECC using micro-mechanical modelling.

2.2.4.3 Hybrid Fiber Reinforced ECC

Hybrid fiber reinforced ECC involves the use of multiple types of fibers in a cementitious matrix to achieve better performance than that of the mono-fiber reinforcement ECC [304]. Maalej et al. achieved high strength and strain capacity ECC by combining high-modulus steel fibers and relatively low modulus PE fibers [226]. Zhang et al. examined the effect of using various types and length of fibers on the impact resistance of cementitious composites [305]. Li et al. recommended the use of hybrid fiber reinforcement of 0.5% steel and 1.5% PVA fibers for resisting dynamic loads [203]. Mono-fiber ECCs containing high modulus fibers, such as steel and carbon will exhibit a different behavior than ECCs with relatively low modulus fibers like nylon fibers (PP, PE and PVA). High modulus fibers increase the bulk strength and toughness, however they decrease ductility and strain hardening behavior. Low modulus fibers displayed an improved ductility and a reduction in crack width [229]. Strain capacity is important for energy absorption, reduction of fragmentation and velocities of fragments, and residual strength. Shaikh et al. investigated the corrosion durability of reinforcing steel in three series of pre-cracked beams of ordinary mortar, PE fiber reinforced and hybrid fiber reinforced ECC (Steel and PE fibers). The results indicate that hybrid fiber reinforced specimens' exhibit better performance [112]. In order to achieve the high strength and strain hardening behavior as well as ductility, a micro-mechanical model has to be applied to assess the optimal hybrid configuration.

2.2.5 SMA Fiber Reinforced Cementitious Composites

The use of new materials, such as FRP and non-corrosive stainless-steel, as reinforcement bars for concrete members have generally been successful. However they do not provide re-centering capabilities that are essential for hazard mitigation. On the other hand, steel fiber reinforced mortar does not provide a reduction in crack size once deformed permanently [306]. To overcome these issues, a number of researchers investigated the use of innovative and smart materials as fiber reinforcement in cementitious composites. In 1998, Maji et al. introduced the use of SME-SMA strands with a diameter of 2.5 mm as longitudinal reinforcement for concrete beams [307]. The strands were activated using electrical heating, which resulted in a pre-stressing force. Strands may require a lot of electrical power to activate the shape memory effect, therefore, it would be better to use SME-SMA fibers.

It is essential to achieve a strong interfacial bond strength between the fibers and cementitious matrix. Kim et al. conducted pull-out tests of NiTi SMA fibers from three different cementitious mortar mixtures [308]. The fibers had a diameter of 1 mm and an embedded length of 15 mm. Results indicated that heat treatment of the SMA fibers enhances the bond strength. Also, Choi et al. investigated the bond strength of SME-SMA fibers and illustrated that cold-drawn dog-bone fibers have higher bond strength than strain cold-drawn and heat treated NiTi fibers [309]. Figure 2-10a illustrates the pull-out test setup and specimen dimensions.

Moser et al. conducted experimental tests on the pre-tensioning of fiber reinforced concrete using SME-SMA fibers at the bottom of the beams with a non-traditional star shaped geometry. The specimens were subjected to cyclic temperature changes ranging from 24 to 160°C. The results indicated that the pre-stressing forces would eliminate the cracks due to shrinkage, however, higher pre-stressing forces are required to resist bending and tensile loads [310]. Choi et al. investigated the effectiveness of closing cracks using SME-SMA NiTi fibers in mortar beams that are layered at the bottom of a beam. After cracking, the fibers were thermally activated using a flame torch. Upon thermal activation of fibers, the specimens recovered residual displacements up to 0.72 to 1.75 recovery ratio [311]. Figure 2-10b displays schematic drawings for the fiber reinforced beam specimens. Furthermore, Choi et al. compared the use of NiTiNb to NiTi SME-SMA fibers, as NiTiNb can provide higher post-tensioning stresses after thermal activation [312]. After cracking of the beams, the fibers were thermally activated using the flame torch and a flexural load was applied to the repaired specimens. The repaired sections exhibited an increase of flexural strength

in the order of 1.4 and 1.75 for NiTi and NiTiNb fibers, respectively. The failure of the repaired specimens occurred due to a crack that is at a deviated location from the repaired crack.

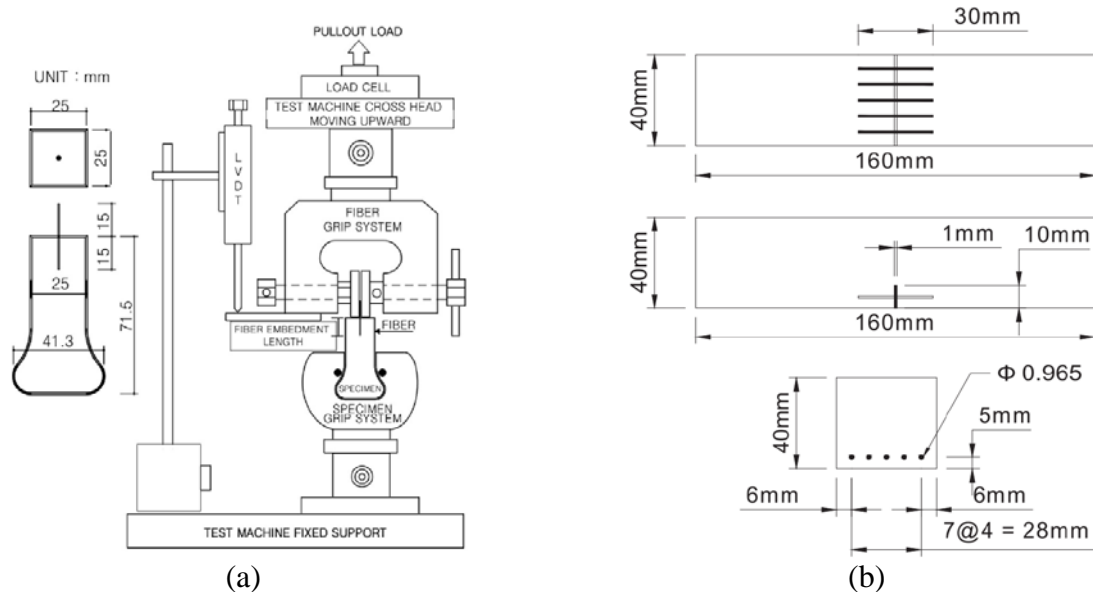


Figure 2-10. (a) Fiber Pull-out Specimen dimensions and test-setup³⁰⁸; and (b) SME-SMA fiber reinforced mortar beam specimens for flexural testing³¹¹

Kim et al. explored the use of SME-SMA as randomly distributed fiber reinforced mortar with a fiber volume ratio of 1.5% [313]. The experiments included the tensile testing of NiTi and NiTiNb dog-bone fibers in mortar coupons before and after thermal activation. The thermal activation was achieved by using a heat gun. In general, specimens with NiTiNb fibers had a slightly higher elastic modulus and tensile strength. Post thermal activation specimens had a higher elastic modulus. For the tensile strength, after the pre-stressing effect, specimens exhibited a lower tensile strength. This can be attributed to the generation of radial cracks near the SMA fibers due to the increase of fiber's diameter after heat treatment. The NiTi fibers displayed a higher pre-stressing force than NiTiNb fibers after heat treatment.

Ali et al. investigated the tensile strength and impact resistance of randomly distributed hybrid-fiber (PVA and SME-SMAs) reinforced engineered cementitious composites [314]. The specimens had 2.0% PVA and SME-SMA fibers with fiber volume ratios of 0.0%, 0.5%, 1.0%, and 1.5%. The testing procedure of the tensile strength did not include heat treatment. The tensile strength and strain capacity were enhanced by 80% and 150%, respectively, with the increase of SME-SMA fibers up to 1.0%. Specimens with a SME-SMA fibers of 1.5% had a lower tensile

strength and strain capacity due to the tendency of clustering of the fibers. The experimental procedure was extended to investigate the resistance of the composite pre- and post-heat treatment to impact loading using a weight drop. The results revealed an enhancement in the fracture energy due to the increase of SME-SMA fibers. Post-thermal activation, the impact resistance of the heat-treated specimens with SMA fibers have increased. However, specimens with 2.0% PVA fibers only exhibited a decrease in the impact resistance post heat treatment due to the degradation of the PVA fibers. A statistical spatial point pattern analysis was conducted to investigate the randomness of fibers in ECC.

Ali et al. extended the testing matrix with the same mixture matrix to investigate the composite behavior under compression and flexural loading at various curing ages of 3, 28 and 90 days [315]. The compressive strength of the specimens were similar, indicating that the inclusion of fibers do not affect the compressive strength. However, the elastic modulus and passion's ratio had a slight decrease. The tensile strength of the composite was investigated using splitting tensile. The results revealed an increase in tensile strength up to the inclusion of 3.0% of fibers (2.0% PVA and 1.0% SME-SMA). The tensile strength of the specimen with 3.5% fibers (2.0% PVA and 1.5% SME-SMA) had a lower tensile strength than that of 3.0% of fibers which might be attributed to the fiber clustering which was proved in the previous study by tensile coupons [314, 315].

In the instance of flexural strength, the increase of the fiber volume ratio enhanced the flexural strength, modulus of rupture and ductility at various ages. The flexural strength experienced a slight decrease with the aging time and the ductility was less than half at 90 days when compared to that measured at 3 days. This was attributed to the increase of the hydration products of the cementitious matrix which may have increased the interfacial bond between the fibers and the matrix. The cracked specimens were heat treated to achieve self-healing and then retested under flexural loading and compared to un-treated specimens. The treated specimens with SME-SMA fibers experienced a post-stressing force and exhibited a higher flexural strength as compared to the un-treated specimens. A strain recovery ranging from 22% to 40% was achieved.

It is obvious that SMA fibers represent an ideal reinforcement for acquiring ductile and self-centering in cementitious composites. However, SME-SMAs require thermal activation by using flame torch or electrically, which would be a challenging task for large structures. Therefore, superelastic/Pseudo-Elastic SMAs can be used as reinforcement fibers to provide instantaneous recovery of deformations and cracks and high energy-dissipation that is essential for hazard

mitigation. Li et al. investigated the use of SMA wires as a reinforcement for ECC flexural specimens with a cross-sectional area of 50.8 mm by 25.4 mm and a span length of 508 mm [53]. The SMA wires were set to a 1.8% of volume ratio. The flexural specimens were subjected to 10 flexural cyclic loads and the mid-point displacement was recorded using Linear Variable Differential Transformer (LVDT). Digital Image Correlation Systems (DICs) was used to monitor the full-field displacement and strains. As noted before, superelastic SMA exhibit elastic behavior up to 6.0% strains through phase transformations which is compatible to ECC that exhibits a high tensile ductility through micro-cracking. The SMA-ECC experienced a significant mid-point displacement and crack recovery. Figure 2-11a and b illustrate a schematic drawing of the SE-SMA reinforced ECC and the flexural response of the SMA-ECC, respectively.

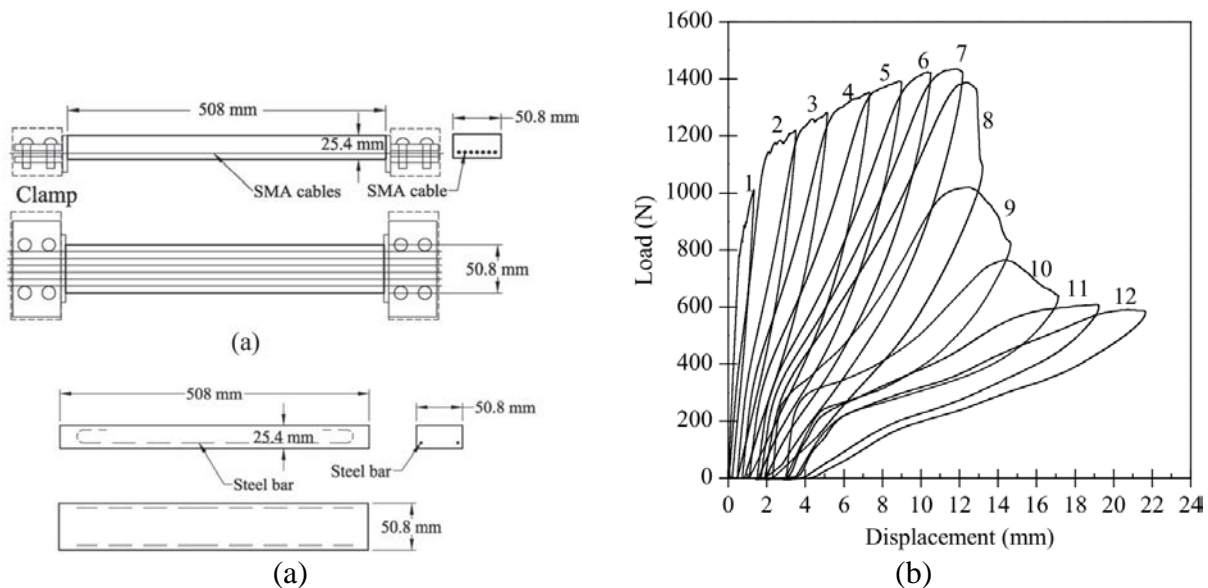


Figure 2-11. (a) Schematic drawing of the SMA reinforced ECC; and (b) The flexural behavior under cyclic loading⁵³

Relevant to fiber reinforced experiments, Shajil et al. conducted pull-out tests on superelastic SMA NiTi fibers with hooked ends and investigated the performance of layered SE-SMA fiber-reinforced mortar [51]. The fiber reinforced mortar specimens were subjected to three cyclic flexural loading. The results indicated that SE-SMA fibers provide a re-centering capability when compared to steel fibers. Shajil et al. extended the experimental investigation to assess the effect of fiber volume ratios on the flexural behavior of the specimens [52]. The fiber volume ratios ranged from 0.12% to 1.00% of superelastic SMA fibers placed at the bottom of the beams. The

results indicated self-centering factors of 0.4 and 0.45 for specimens with 0.5% and 1.0% fiber reinforced mortar, respectively. Furthermore, the 1.0% fiber reinforced specimen exhibited a strain hardening behavior. The experimental procedure was extended to compare between 0.5% of fiber volume ratio of steel fibers and superelastic SMA fibers for a beam-column connections. The results indicated that SE-SMA fiber reinforced mortar has a better toughness and enhanced the ductility and energy dissipation capabilities.

2.3 Pre-stressed Concrete

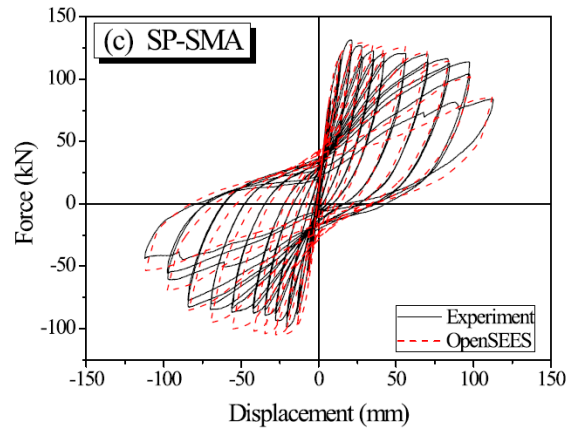
Pre-stressing of concrete is an effective technique to overcome possible issues of concrete when subjected to tensile loads. The mechanism includes applying a compressive load in a perpendicular direction to the applied load. This leads to the application of a compressive load over the full section if the pre-stressing force is at the center of the cross-section. In reinforced concrete beams, the pre-stressing force is usually applied near to the tension face. The amount of pre-stressing force is dependent on the applied load to ensure that the section will be un-cracked under service limits. To apply the pre-stressing force there are two techniques; pre-tensioning and post-tensioning. In pre-tensioning the steel tendons are placed in position and tensioned before casting of concrete. The tendons are released once concrete hardens. In post-tensioning the tendons are placed in ducts, concrete is then casted and left to harden. After hardening of concrete, the tendons are tensioned using hydraulic jacks to a pre-determined strain level. The ducts are then filled with grout to ensure the transfer of strains from steel tendons to the surrounding concrete and vice-versa and to protect the tendons from corrosion [316]. However, corrosion for the stressed steel tendons resulting in failure of several tendons was reported [317]. The corrosion of steel could be attributed to poor sealing by the galvanized grout [318]. Furthermore, there are losses in the pre-stressing forces due to relaxation of the steel tendons and fatigue loading [319]. Hurlbaeus et al. presented guidelines for inspecting post-tensioned of concrete using Non-Destructive Evaluation (NDE) methods [320]. In general, assessing the durability of the pre-stressed tendons is complex and time consuming that requires extensive knowledge of NDE.

More recently, several researchers investigated the use of SME-SMAs to pre-stress concrete members. This can eliminate the use of hydraulic jacks and make possible to increase pre-stressing forces during the service life of the structure [321]. Li et al. investigated the use of SME-SMA bundles to construct two smart concrete beams [322]. The cross-section of the beams was 99 mm by 85 mm with an approximate span of 20 m. The beams were reinforced with regular pre-stressing

strands that were connected in the middle portion of the beam with SMA bundles. The SMAs in each beam were thermally activated by applying an electrical current. The SMAs were activated several times at different current levels to analyze the pre-stressing force and the SME mechanism. The experimental results indicated that a camber of 0.44 mm was generated at the middle section post activation of the SMA bundles. Also, the beams were capable of resisting overloads around 3kN. However, the environmental temperatures affected the displacement at the mid-span due to the transformation temperatures of the NiTi-SMA. Choi et al. investigated the use of NiTiNb SME-SMA wires to confine concrete cylinders [67]. The thermal activation of the SMA was established by using an electronic oven set to 70°C to simulate the heat of hydration of concrete during the setting phase. The study proved that SME-SMAs can provide active confinement in concrete cylinders and increase the peak strength. However, the austenite finish A_f temperature for the material was at 84°C, therefore a complete transformation to the austenite phase, which is responsible for achieving the maximum pre-stressing force, did not take place. Choi et al. developed seismic fragility curves of reinforced concrete columns retrofitted using active confinement of SME-SMA wire jackets [323]. Numerical modelling using OpenSEES was developed and validated using a series of experimental testing. The static experimental tests revealed that reinforced concrete columns with SMA wire jackets had a displacement ductility larger by a factor of 2.3 and 1.06 for the lap-spliced and continuous reinforcement columns, respectively. The numerical models revealed that the columns with SMA wire jackets had a yield and collapse limit of 0.162g and 0.567g, respectively. The collapse limit of the SMA wire jackets was higher than that of the continuously reinforced column by a factor of 1.33, however, the yielding limit was similar to that of the continuously reinforced column. Figure 2-12a and b display the experimental test setup and the experimental and numerical force-displacement response for the column with SMA wire jackets, respectively.



(a)



(b)

Figure 2-12. (a) Experimental test-setup; and (b) numerical and experimental force displacement curves for the column with SMA wire jackets³²³

2.4 Summary

This section provided a review of literature on the characteristics and applications of shape memory alloys in civil engineering. The unique behavior and characteristics of shape memory alloys were discussed. Then, a brief history on the discovery and various compositions of shape memory alloys was presented. Also, the applications of shape memory alloys in various civil engineering applications such as beam-column connection, vibration control devices and as reinforcement in concrete beams was reviewed. Moreover, the potential use of shape memory alloys to rehabilitate reinforced concrete structural members was examined.

Next, the limitations of conventional concrete materials and the need for innovative materials for concrete structures was discussed. A review on the development of fiber reinforced cementitious composite to obtain advanced properties such as limiting crack propagation and self-healing characteristics was provided. Also, several attempts where SMA fibers were used in cementitious composites for re-centering and crack recovery were discussed. Finally, the earlier studies on the use shape memory effect SMAs in pre-stressing was reviewed.

3 Characterization of Superelastic SMA Cables

(Most of the discussions presented in this section were published in the following conference and journal papers [324-326])

3.1 Overview

In this section, the results from a set of experiments that were conducted to characterize the tensile properties of superelastic SMA cables were discussed. First, the performance of large-diameter nickel-titanium (NiTi) SMA cables for their potential use in civil engineering was explored. The SMA cable had a diameter of 8 mm, and was composed of 7 strands with each strand consisting of 7 wires with a diameter of 0.885 mm. Uniaxial tensile tests were conducted at various loading rates and strain amplitudes to characterize the superelastic properties of the SMA cable. An optical digital image correlation (DIC) measurement system and an infrared thermal imaging camera were employed to obtain the full-field strain and temperature fields. Cyclic tests were performed to evaluate low-cycle fatigue characteristics of the SMA cable.

Second, the functional fatigue characteristics of a complex configuration of a NiTi SMA cable with an outer diameter of 5.5 mm was investigated. The cable was composed of multiple strands arranged as one inner core and two outer layers. The tensile behavior of the NiTi SMA cable was analyzed by conducting uniaxial tensile tests up to 10% strain. The fatigue characteristics were investigated under strain amplitudes ranging from 3% to 7% and a minimum of 2500 loading cycles. The evolution of maximum tensile stress, residual strains, energy dissipation, and equivalent viscous damping under a number of loading cycles were analyzed. The fracture surface of a specimen subjected to 5000 loading cycles and 7% strain were discussed. The optical digital image correlation measurement system, infrared thermal imaging camera, and a digital multimeter were employed to obtain the full-field strain and temperature fields as well as the change in electrical resistance.

Finally, the fabrication and experimental testing of an SMA cable-based vibration control device were discussed. Results from cyclic loading tests were presented to assess the force-displacement response and damping properties of such a device.

3.2 Materials

Two configurations of NiTi SMA cables obtained from Fort Wayne Metals Research Products Corporation, were examined. The first SMA cable consisted of a helix configuration that composed of 7 strands with each strand having 7 wires. Each wire had a diameter of 0.885 mm, while the outer diameter of the cable was 8 mm. The total cross-sectional area of the cable was computed as the sum of the individual cross-sectional areas of the wires and was equal to 30.14 mm². Figure 3-1a displays a schematic drawing of the cross-section and a longitudinal section of the first cable. The second cable consisted of 163 individual wires with an overall outer diameter of 5.5 mm. The cable had a non-conventional multi-layered construction with an inner core and two outer layers. The inner core strand consisted of a central straight wire with six outer wires wrapped in a right-handed layout (i.e., 1×7 configuration). The first outer layer consisted of six strands each has a 1×7 configuration and wrapped in a right-handed layout around the core strand. The second outer layer composed of six strands with a 1×19 configuration wrapped in a left-handed layout. The core and first outer layer strands were made out of NiTi wires with a diameter of 0.279 mm, while the second outer layer strands were made out of wires with a diameter 0.300 mm. Figure 3-1b illustrates the cross-section of the second cable.

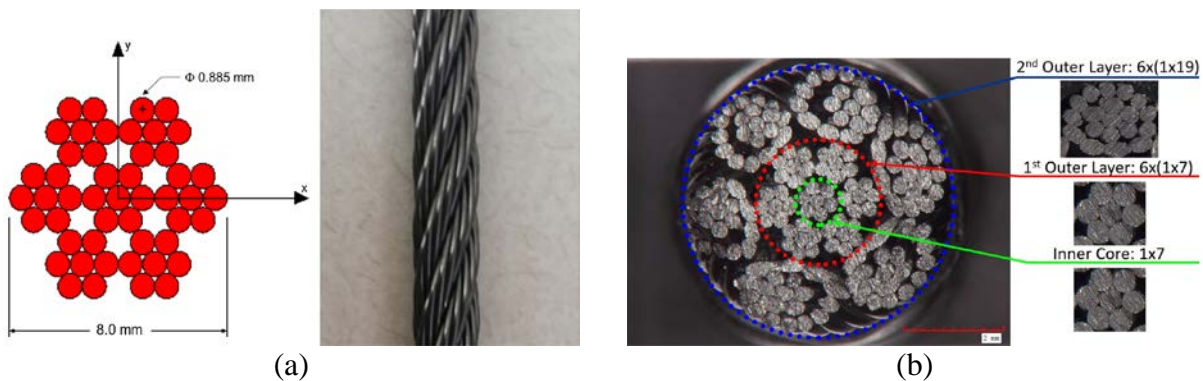


Figure 3-1. (a) Schematic drawing of the cross-section and longitudinal section of the first cable; and (b) Cross-section of the second cable

3.3 Experimental Test Setup

All tensile tests were conducted using a MTS 810 servo-hydraulic system with mechanical grips and a capacity of 100kN. The displacement and force data was recorded using an MTS data acquisition system. The recorded force values were divided by the cross-sectional area of the cables to obtain the equivalent stress. The strains were monitored and measured using a laser

extensometer (MTS LX1500). In addition, the DIC system, which was provided by Correlated Solution, was employed to obtain the full-field displacements and strains. DIC is a real-time, full-field and non-contact optical measurement system that utilizes a series of sequential images captured during loading to track and correlate patterns within a subset space, which can in turn be used to describe deformation. The DIC can be used to obtain three-dimensional or two-dimensional deformations based on the number of optical cameras used during the tests and their placement angles (i.e. single camera for 2D; stereo-paired cameras for 3D). The DIC measurements depend mainly on the quality of the speckle pattern [327]. The surface pattern should be non-periodic, isotropic, and of high contrast to guarantee accurate measurements of the DIC system with the lowest possible noise. This can be achieved by applying black dots on a white background painted on the specimen surface. Therefore, a speckle surface pattern was applied to one side of the specimen. A single camera with 12 mm lens was used for 2D-DIC as there was no significant out-of-plane movement. The camera resolution was 2448 x 2048 pixels with a CCD sensor that has a format of 2/3in. The maximum frame rate for the camera is 15 frames per second. Finally, the variation of temperature in the cables was captured during the testing program. The temperature fields across the entire specimen length were measured, using an infrared FLIR A615 camera. For the second cable the change in electrical resistivity using a two-probe system was captured by digital multi-meters (DMM). Figure 3-2a displays the test setup for the first cable with laser extensometer, DIC system, and an infrared camera. Figure 3-2b illustrates the test setup for the second cable with laser extensometer, DIC system, DMM, and an infrared camera.

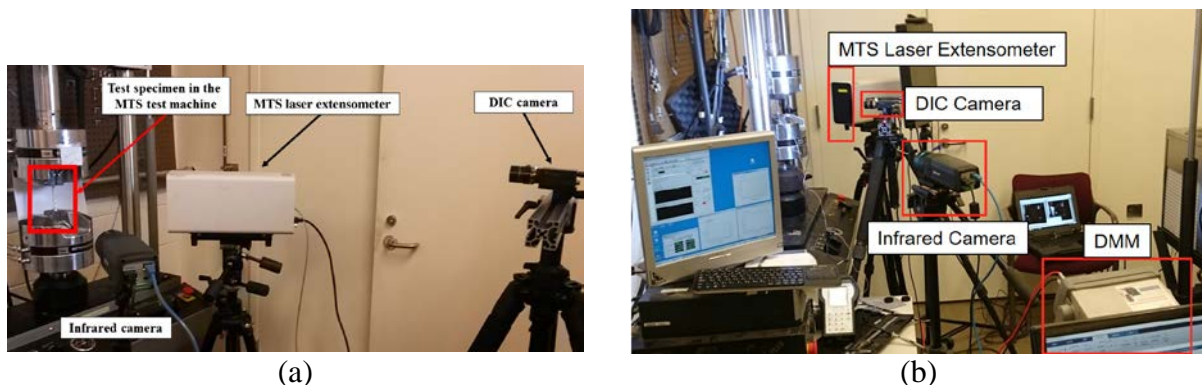


Figure 3-2. (a) Test setup for the first cable with laser extensometer, DIC and infrared camera; and (b) Test setup for the second cable with laser extensometer, DIC, infrared camera and DMM

The testing procedure was carried out onto two different phases. Phase 1 was devoted to the experimental testing related to the first cable to investigate the general tensile behavior of the superelastic SMA cables. Phase 2 focused on the fatigue behavior of the second cable and investigating its feasibility to be used in vibration control application. In both phases, a gauge length of 75 mm was used. In phase 1, a training test procedure, consisting of 20 load cycles to obtain 5% strain at 0.01 Hz, was applied on all specimens, before formal tests. Afterwards, a thorough experimental testing program was implemented. All tests, were displacement controlled in loading and force-controlled in unloading to avoid applying any compression force on the cable during unloading. To investigate the mechanical response of the cable under different strain amplitudes, the first specimen was cycled at target strain amplitudes of 2–9% at a loading frequency of 0.05Hz. All the tests lasted for 3 cycles. Data sampling rate for the MTS data acquisition, extensometer, and DIC system was 10Hz.

The test matrix was then extended to include the behavior of the cable under higher frequency cyclic loads. The tensile loads were applied to a second specimen to obtain approximately 6% strain at loading frequencies of 0.05, 0.1, 0.5, 1.0, and 2.0 Hz. Because of the limited capability of the DIC system at higher test frequencies, the tests' data were recorded using the MTS data acquisition system and the extensometer only, with a data sampling rate of 200 Hz.

To study the behavior of the cable under low-cycle fatigue loads a third specimen was used. The specimen was subjected to cyclic loads in a force-controlled procedure for 100 cycles between stresses of 560MPa (corresponds to a target strain amplitude of 6%) and near-zero stress at a frequency of 0.05Hz. The MTS data acquisition system, the laser extensometer, and the DIC system were used to record the data with a sampling rate of 10Hz.

In phase 2, prior to the fatigue testing of the cable, a training test procedure including 20 loading cycles at 4% strain with a strain rate of $5 \times 10^{-3} \text{ s}^{-1}$, was conducted. To investigate the tensile response of the cable, the specimen was subjected to target strain amplitudes of 3% to 10% for three cycles. Then, the superelastic fatigue tests were conducted at target strain amplitudes of 3%, 4%, 5%, 6%, and 7%. During fatigue tests, a minimum of 2500 cycles were performed. All tests were conducted in displacement control. The measured strain amplitudes were somewhat different but close to the target strain amplitudes. The tests were conducted at the room temperature of $27 \pm 1 \text{ }^\circ\text{C}$ and at a strain rate of $5 \times 10^{-3} \text{ s}^{-1}$, which corresponds to loading frequencies ranging from 0.083Hz for 3% strain amplitude and 0.025Hz for 10% strain amplitudes.

In order to further assess the effect of multi-layering of the strands on the mechanical properties of the cable, a similar strand with the same material properties was investigated. The strand had a configuration similar to that of the inner core (1×7), with wires having an outer diameter of 0.117 mm, and a total cross-sectional outer diameter of 0.350 mm. The loading protocol involved the characterization of the behavior of the strand at various strain amplitudes ranging from 3% to 7% subjected to three loading cycles. A laser extensometer and a DMM were used to monitor the gauge length strain and electrical resistivity, respectively. The full-field strains, and displacement and thermal profile were not identified as the strand diameter was relatively small and, hence could not be captured by the DIC cameras and the thermal changes were nominal. Table 3-1 lists a summary of the testing procedure for the two phases.

Table 3-1. Summary of the testing procedure for phase 1 and 2 of characterization for superelastic SMA cables

Phase	Cable	Specimen Number	Test Type	Frequency (Hz)	Target Strains (%)	Cycles
1	1	1	Strain Effect	0.05	2 to 9	3
		2	Frequency Effect	0.05 to 2.0	6	3
		3	Low-Cycle Fatigue	0.05	6	100
2	2	1	Strain Effect	0.036 to 0.025	3 to 10	3
		2	Fatigue	0.0830	3	2500
		3	Fatigue	0.0625	4	5000
		4	Fatigue	0.0500	5	5000
		5	Fatigue	0.0417	6	2500
		6	Fatigue	0.0357	7	5000
	3	1	Strain Effect	0.036 to 0.025	3 to 7	3

3.4 General Characterization

Figure 3-3 presents stress-strain curves for experimental tests at measured strain amplitudes varying from 1.6 to 7.7% which correspond to the target strains of 2 to 9% for phase 1 using the first cable. It can be observed that the material exhibited the well-known flag-shaped cycles (common behavior of SMAs). The cable recovered almost all of its deformations upon unloading, when it was loaded up to 6.4% strain. In contrast, recorded residual strains at higher strain amplitudes were approximately 0.2% only. This small amount of residual strain can also be attributable to the friction between the wires in the cable. It is shown that the strength of the cable decreased at those strain amplitudes, possibly because of the failure of individual wires at the gripping region.

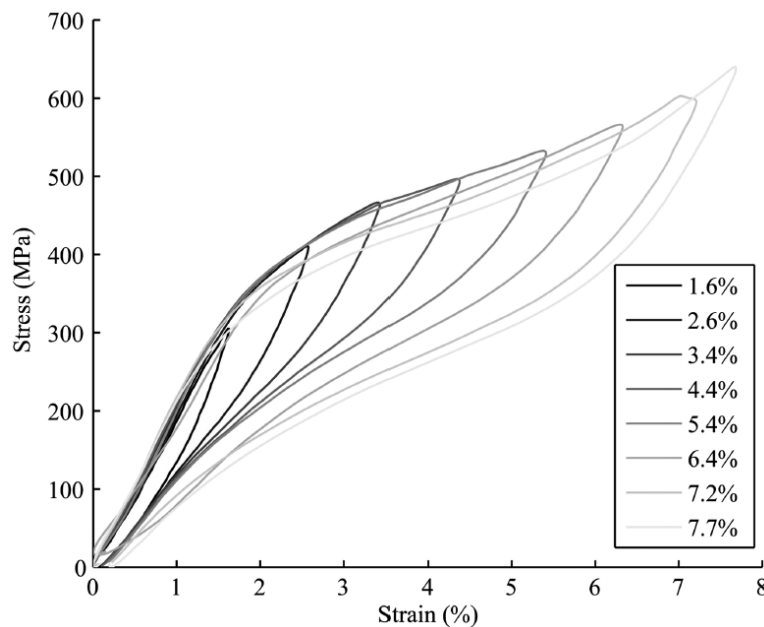


Figure 3-3. Stress-strain curves for 1st cable for target strains of 2 to 9% at 0.05Hz

Figure 3-4 illustrates the stress-strain curve of the 1st cable with the strain-field maps obtained at different loading levels using DIC. The strain rate was equal to $0.005\% \text{ s}^{-1}$ during the loading phase, and the maximum global strain was 5.4%. The specimen was unloaded back to zero stress with a stress rate of -0.50 MPa s^{-1} . The global strain can be correlated to the strain field maps at different levels of loading. However, the higher strains at the gripping regions can be observed from the strain field maps. The increase in local strain along the gauge length was mostly uniform, which indicates that the growth of martensitic phase proceeds homogeneously at this loading rate.

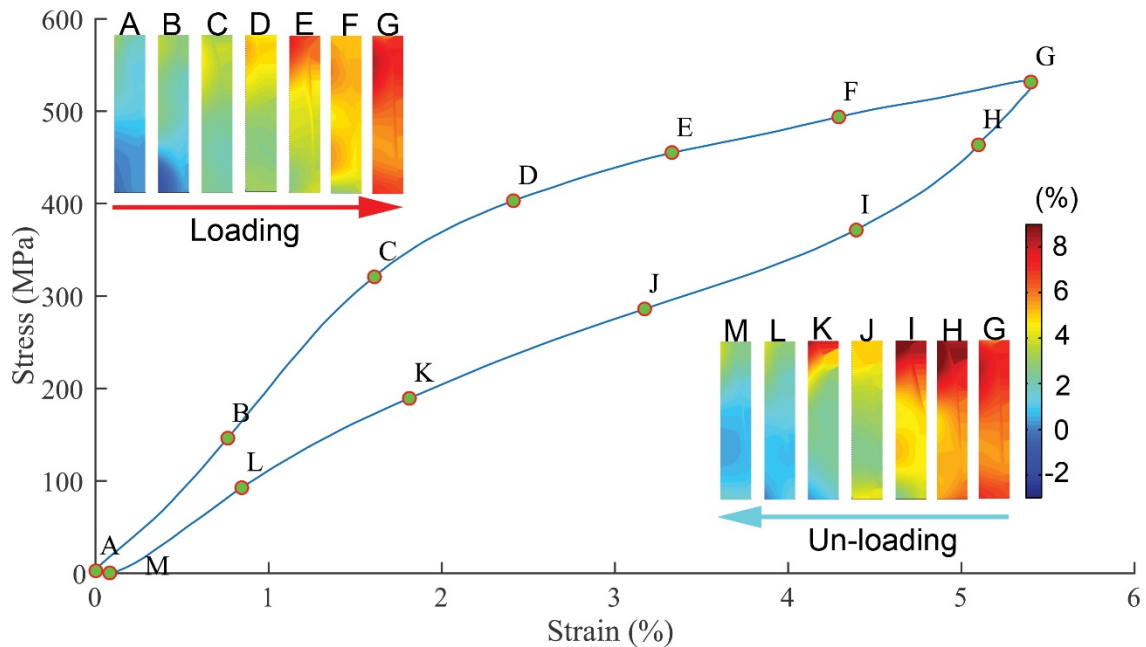


Figure 3-4. Stress-strain curve of 1st cable at 5.4% strain with corresponding DIC axial strain field maps

Results from the tensile testing of the 2nd cable are shown in Figure 3-5. Figure 3-5a shows the stress-strain curves for three cycles for a specimen subjected to 5% strain. Since the cycles were stable, only the second cycle of the loading cycles at different strain amplitudes is presented in Figure 3-5b. It can be observed that the stress-strain curve of the cable exhibited a high positive stress-strain slope over the transformation range. This indicates a non-uniform transformation initiation in the individual wires of the cable. Nominal permanent deformations for cycles at loading strains of 3% to 7% were observed. The residual strains for cycles at loading strains of 8%, 9%, and 10% were 0.20%, 0.52%, and 0.76%, respectively. A decrease at forward transformation stress level and transformation plateau was observed at 7% strain. A similar decrease in the stress levels was visible for cycles with 10% strain.

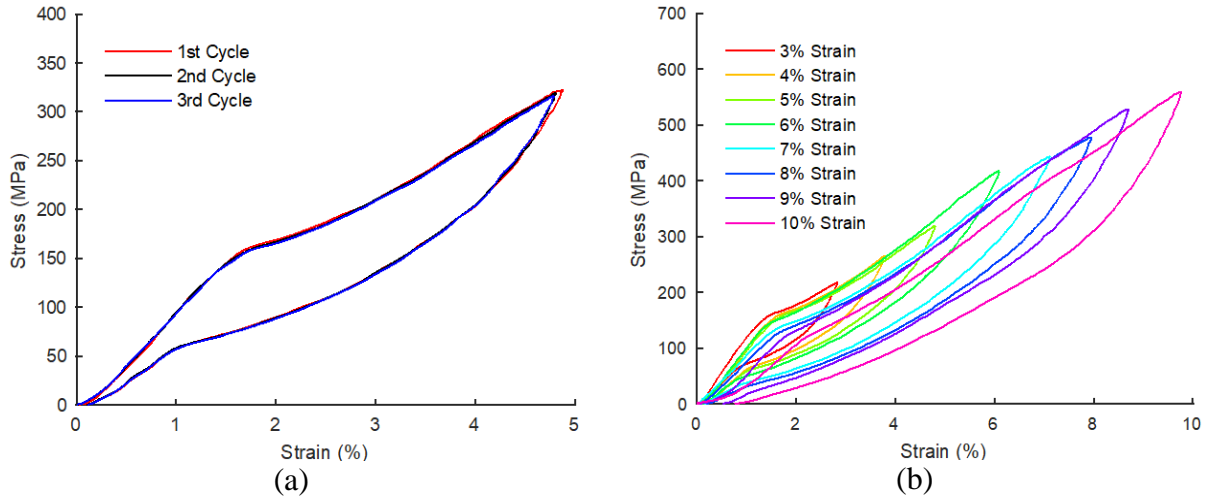


Figure 3-5. Stress-strain curves for second cable: (a) three cycles at a strain of 5%; and (b) response at 3% to 10% strain

Results from the tensile testing of the NiTi SMA strand and the second cable are presented in Figure 3-6a and b, respectively. The stress-strain curves of the cable illustrate a lower elastic modulus, transformation, and peak stresses when compared to the strand configuration. The cable exhibited a high positive stress-strain slope over the transformation range, while the strand had a zero stress-strain slope. The low transformation stresses and high positive stress-strain indicate a non-uniform transformation initiation in the individual wires of the cable. Reedlunn et al. reported a similar behavior of cables with multi-layered strands [327]. This might be attributed to the fact that multi-layering increases the length of wires at the outer-layers relative to the inner core. This leads to a non-uniform strain distribution at the outer surface and the cross-sectional level (i.e. the inner core will experience higher strains/stress compared to the outer-layers). The strand configuration recovered the full strains, however, the cable minimal residual strains were observed up to 0.2% strains. Even though the cable experienced low stresses at high strains, the force levels were higher due to the number of wires used. The use of the cable provides a better flexibility in the construction process as they do not require tedious arrangements or advance tools.

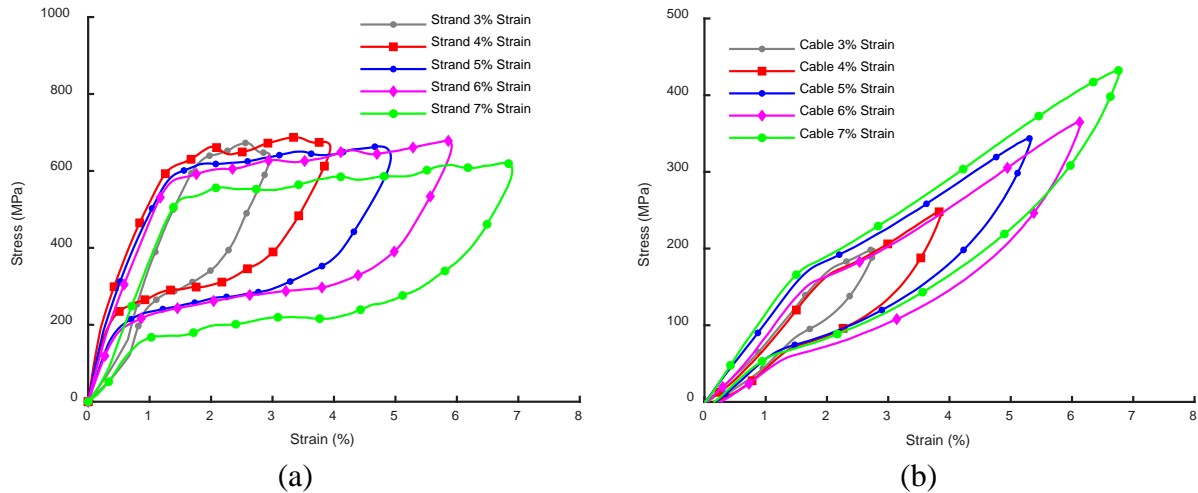


Figure 3-6. Stress-strain curves for superelastic SMA (a) strands and (b) 2nd cable subjected to a target strains for 3%, 4%, 5%, 6%, and 7% strains

Figure 3-7a illustrates the stress-strain curves with strain contours captured at specific stages by DIC for the 2nd cycle of the second cable subjected to a 7% target strain. The colors in the DIC-strain contours represent the local strain distribution using a linear color-coded spectrum ranging from a -1 to 7% strain. The strain contours display a visible band that is known as Lüders band, which usually propagates to the loading grip [328]. The strain distribution is divided into three regions, the first region is located near the fixed end, where the strains are constant at a minimal level usually not exceeding 3% for the maximum loading strain. The second region is located near the moving head with a homogenous tensile strain that is similar to the applied target strain. The third region is located between the first and second regions. The third region “transitional region” consists of a linear varying strain. In general, for SMA rods the transitional regions are constant across the cross-section, while for the SMA cable, the bands are angled similar to the wrapping angle. Figure 3-7b to e represent the strain contours at the 5th and 9th stage corresponding to the maximum tensile stress and the residual strains for strains amplitudes of 3%, 4%, 5%, 6%, and 7%, respectively. The contours illustrate the propagation of strains for the various target strains at the maximum tensile stress. The strain contours at the unloading stage display the localized residual strains.

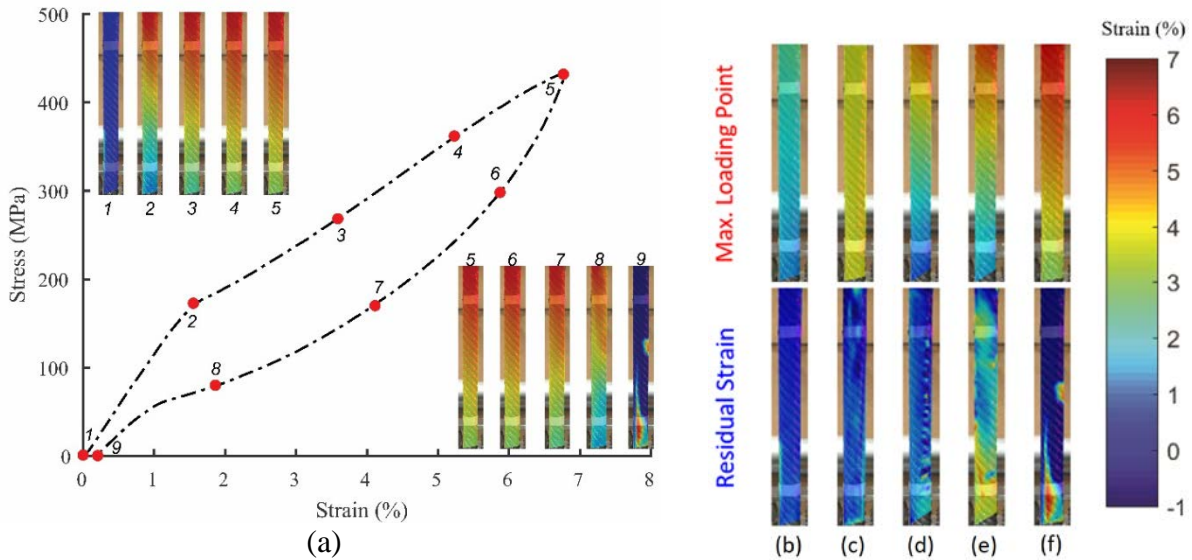


Figure 3-7. (a) Stress-strain response of the 2nd cycle of the second cable when subjected to 7% target strain and strain contours at maximum tensile stress; and residual strains corresponding to the 2nd cycle of the cable subjected to (b) 3; (c) 4; (d) 5; (e) 6; and (f) 7% target strains

3.5 Strain Dependency

To enable the evaluation of the test results in a quantitative way, the energy dissipated per cycle (E_D), the equivalent viscous damping (ζ_{eq}), and the secant stiffness (K_s) are calculated. The dissipated energy is calculated by computing the area between the loading and unloading force-displacement curves. The equivalent viscous damping and secant stiffness are defined as:

$$\zeta_{eq} = \frac{\Delta W}{4\pi W} \quad (1)$$

$$K_s = \frac{F_{max} - F_{min}}{d_{max} - d_{min}} \quad (2)$$

where ΔW = energy dissipated per cycle (hysteresis area); W = maximum strain energy for the same cycle calculated as the energy absorbed in a linear system that has the same maximum displacement and force; and F_{max} and F_{min} = maximum and minimum forces attained for the maximum and minimum cyclic displacements, d_{max} and d_{min} . Figure 3-8 provides the variation of the dissipated energy, equivalent viscous damping, and secant stiffness with the strain amplitude for the 1st cable tested at 0.05Hz. It is shown that the energy dissipated by the cable increases rapidly with the increasing strain amplitude up to 7.2% strain. On the other hand, the energy dissipated at 7.7%, increased only slightly. The equivalent viscous damping first increases, and then gradually tends to its stable value but exhibits a slight decrease at the 7.7% strain. This can be attributed to failure of some wires inside the cable at this strain level.

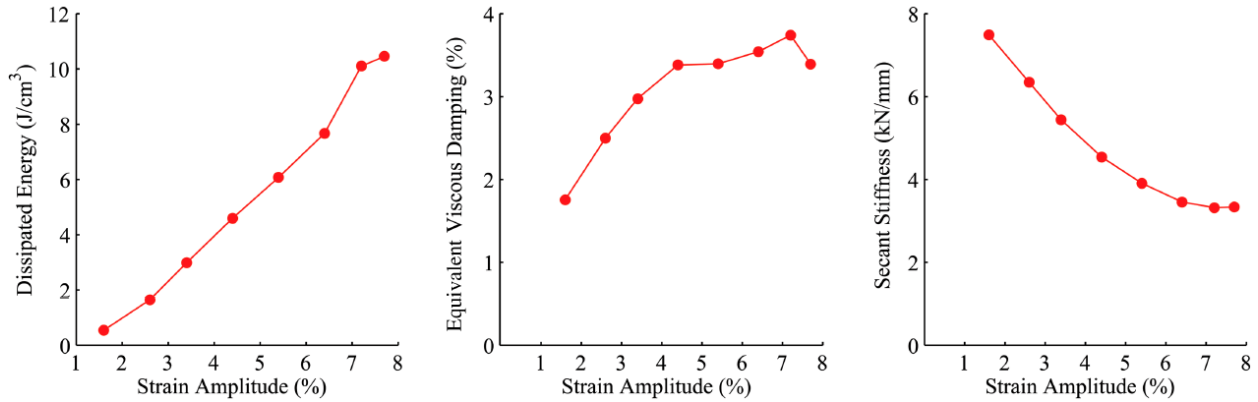


Figure 3-8. Dissipated energy, equivalent viscous damping, and secant stiffness of 1st cable as a function of strain amplitude

3.6 Strain Rate Dependency

In order to explore strain rate effects on the mechanical response of 1st cable, the tensile tests were conducted at a target strain of 6% for loading frequencies of 0.05, 0.1, 0.5, 1.0, and 2.0Hz. Figure 3-9a shows the hysteresis loop at each loading frequency. It can be observed that the forward transformation stresses are approximately equal for all frequencies, while the reverse transformation stresses increase at higher test frequencies. Figure 3-9b illustrates the variation of the dissipated energy, equivalent viscous damping, and secant stiffness with loading frequency. It is shown that the damping ratio reduces by approximately 13% in the range of 0.05–2 Hz. This can be attributed to the decrease of the dissipated energy as a result of the increased reverse transformation stresses at higher test frequencies. There is also a notable increase in the secant stiffness with the increase in the loading frequency, especially when the loading frequency exceeds 0.5Hz.

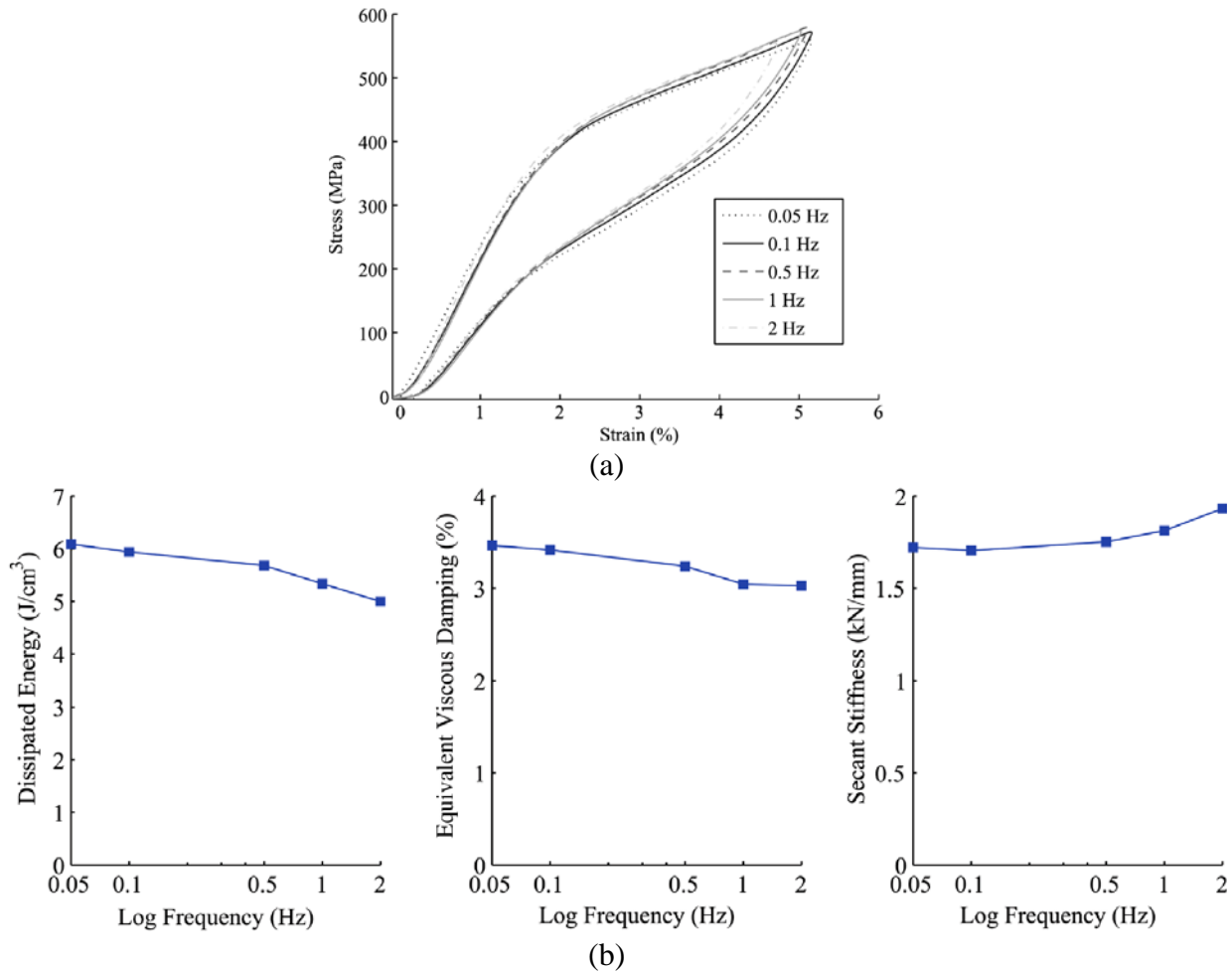


Figure 3-9. (a) stress-strain curves of the first cable tested under various loading frequencies; and (b) Dissipated energy, equivalent viscous damping; and secant stiffness of the first cable as a function of loading frequency

3.7 Functional Fatigue

3.7.1 Stress-Strain Response

Knowledge of material behavior under repeated loading conditions is essential for civil engineering applications of SMAs. Figure 3-10a shows the evolution of stress-strain curves for 100 cycles to a maximum strain of approximately 6% of the first cable. It is shown that the response of the first cable specimen, up to 100 cycles, represents the typical flag-shaped hysteresis. However, the stress levels for both the forward and reverse transformation decrease with increasing the number of loading cycles. The decrease in transformation stress is more pronounced during forward transformation as compared to reverse transformation. Therefore, the area of the hysteresis loop becomes smaller with the progression of cycles. Nevertheless, the change in hysteresis loop is more significant in the early cycles and the hysteresis loop tends to stabilize as

the number of cycles increases. This is shown more clearly in Figure 3-10b and c, which show the stress-strain curves for the first ten cycles and cycles 41–50, respectively. Because of the accumulated residual strains, the hysteresis loops of SMA cable shift to the right with the increase of the number of cycles in Figure 3-10a. The evolution of residual strain versus number of cycles is given in Figure 3-10d. The maximum residual strain of the SMA cable subjected to 100 loading-unloading cycles is approximately 1.1%. It can be observed that the increment of the residual strain progressively reduces during cyclical loading. This might be attributed to the accumulation of the permanent localized deformations in the early cycles and their disappearance in the later cycles.

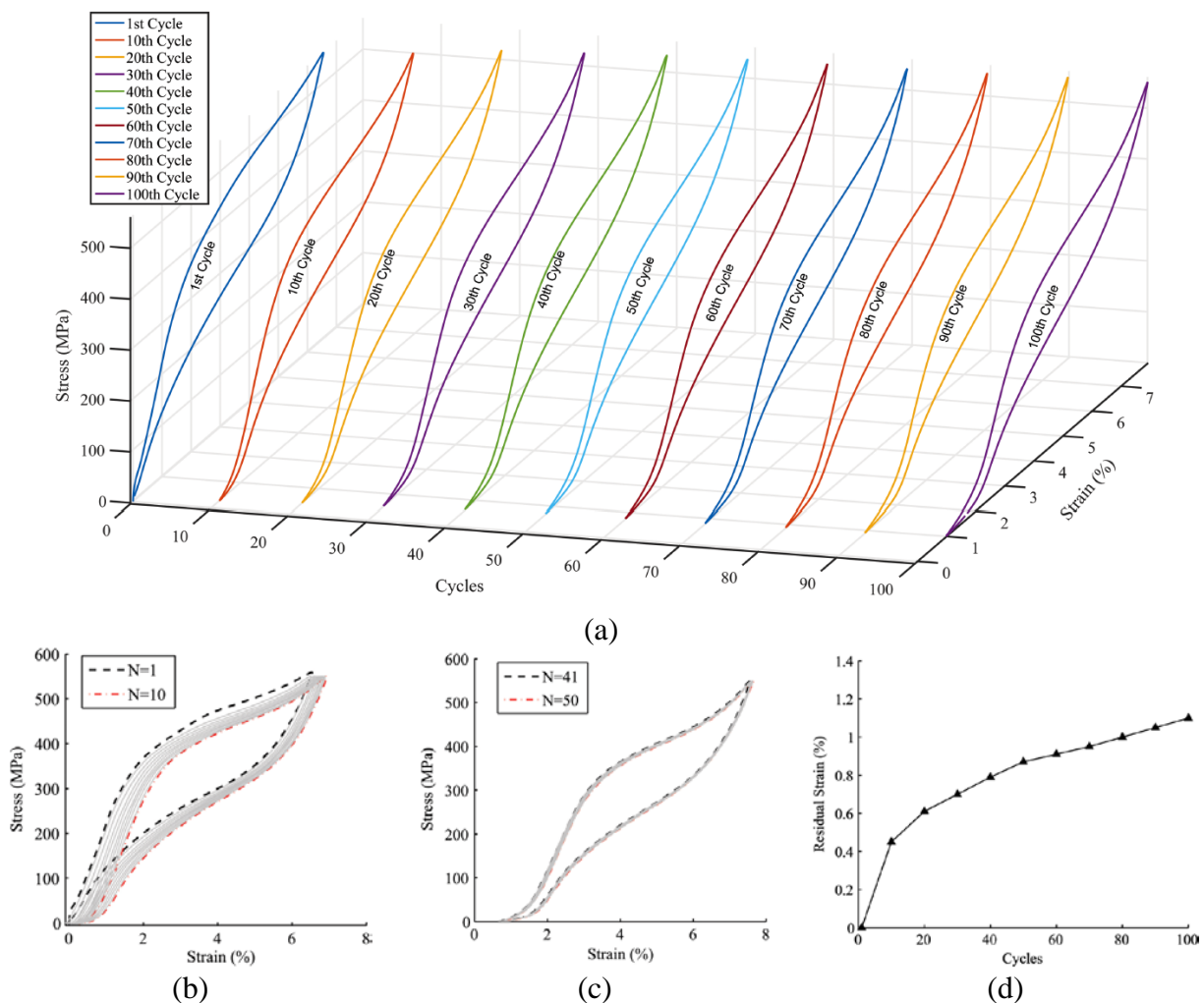


Figure 3-10. (a) 3D plot of stress-strain curves of the first cable subjected to 100 cycles for every 10th cycle; stress-strain curves of first cable for (b) 1st to 10th cycle; (c) 41st to 50th cycle, and (d) evolution of residual strain as a function of number of cycles

The hysteretic response of 2nd cable subjected to cyclic loading at different strain amplitudes is presented. For fatigue testing at each strain amplitude, stress-strain curves were plotted at the 1st, 5th, 10th, 50th, and 100th cycles for the first 100 cycles. For the following cycles, the stress-strain curves of every 250th cycle were presented. Figure 3-11 illustrates the cyclic response of the 2nd cable subjected to 3% strain. It can be seen that both the forward and reverse transformation stress levels decreased with the increase of the number of loading cycles. However, the rate of decrease in reverse transformation stresses was smaller than that of forward transformation. Therefore, the area of hysteresis loop decreased. The response was stable at higher loading cycles, especially after the first 500th cycles.

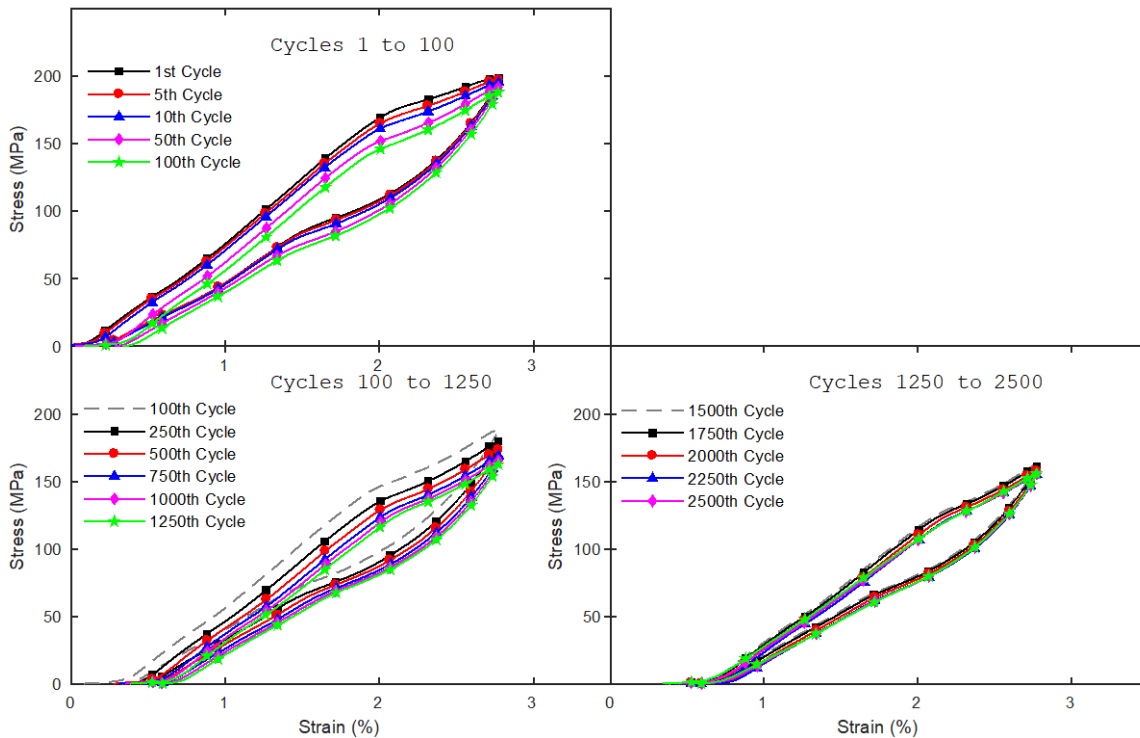


Figure 3-11. Second cable stress-strain response at 3% strain for 2500 loading cycles

The stress-strain curves for the second cable subjected to 4% strain are shown in Figure 3-12. The decrease in the transformation stresses was more pronounced in the first 50 cycles. Between the 100th cycle and 2250th cycle, there was no significant change in the hysteretic response. After the 2500th cycle, the transformation stresses were not visible and the flag-shaped response vanished. The decrease in stress levels was obvious until the 3500th cycle; after which the stress-strain curves were stable up to the 5000th cycle.

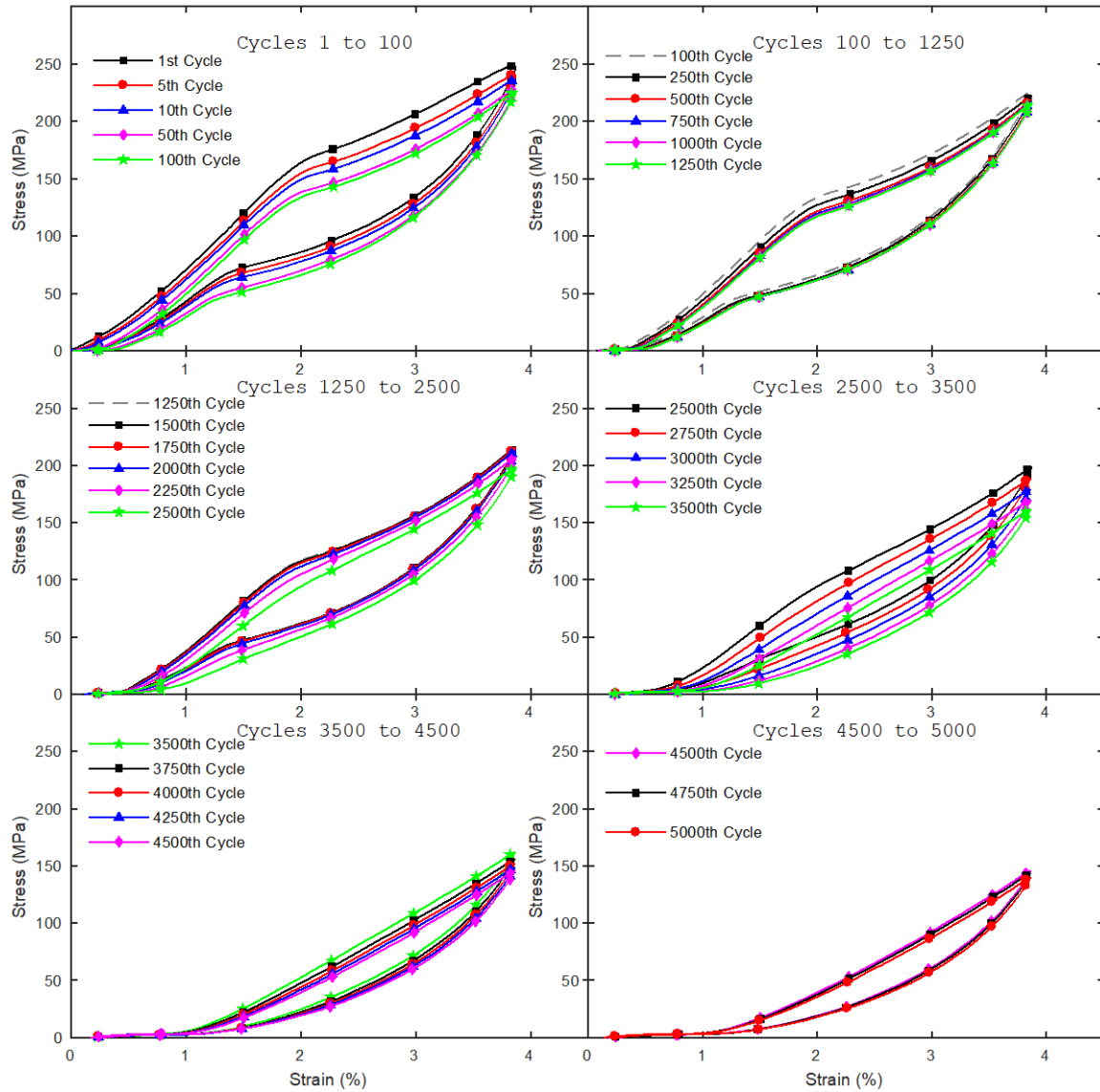


Figure 3-12. Second cable stress-strain response at 4% strain for 5000 loading cycles

Figure 3-13 illustrates the hysteresis loops of the second cable with a strain of 5%. The results of the first 100 cycles were similar to those observed for the specimen tested at 4%. After the 100th cycle, a relatively stable behavior was observed up to the 1750th cycle as opposed to the stable behavior observed until 2250th cycle for the tests at 4% strain. After the 1750th cycle, the degradation in the hysteresis continued and the stress levels decreased until the 5000th cycle.

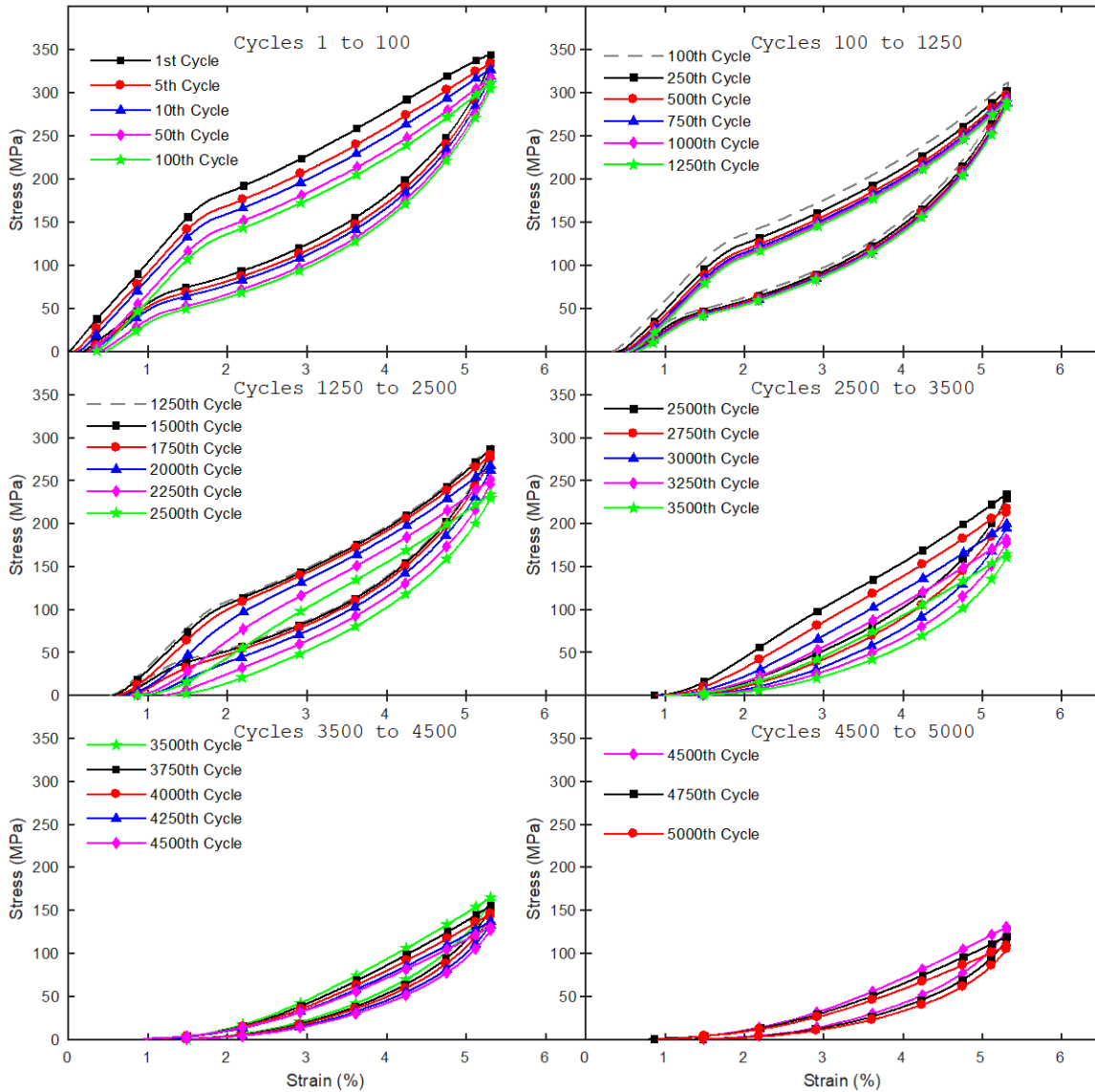


Figure 3-13. Second cable stress-strain response at 5% strain for 5000 loading cycles

The stress-strain curves of the second cable subjected to a strain of 6% for 2500 loading cycles are presented in Figure 3-14. It is deduced that the decrease in the forward transformation stresses was more rapid as compared to the response at lower strain amplitudes. Hysteresis loops considerably narrowed in the first 100 cycles. The stress-strain curves were stable after 250th cycle, with an almost complete stable response between the 1000th cycle and 2000th cycle. The forward transformation stress level decreased again at the loading cycles of 2250 and especially at the 2500th cycle.

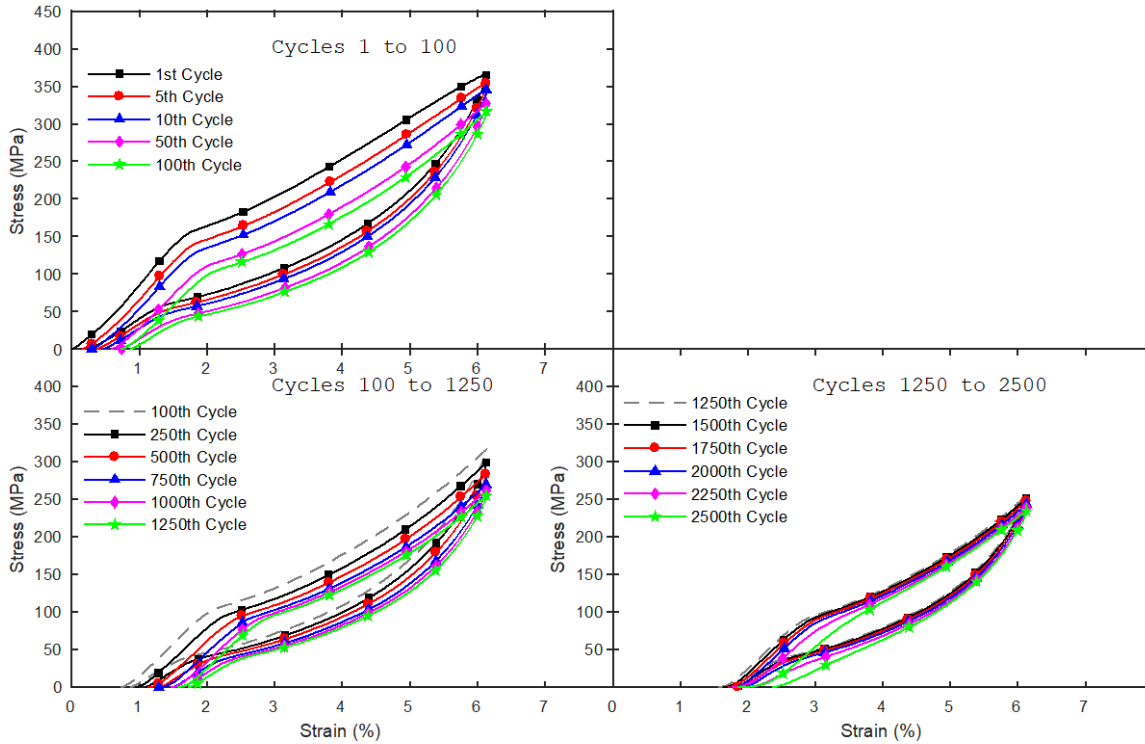


Figure 3-14. Second cable stress-strain response at 6% strain for 2500 loading cycles

The evolution of the stress-strain response of the SMA cable subjected to a 7% strain is shown in Figure 3-15 for 5000 loading-unloading cycles. For this strain amplitude, the degradation in hysteretic response continued with the increase of the number of loading cycle without any stable response range. The flag-shaped hysteresis can be observed only up to the 1250th cycle. After the 3500th cycle, a rapid decrease in the tensile stress was observed with almost a complete loss of load carrying capacity after 4000th cycles.

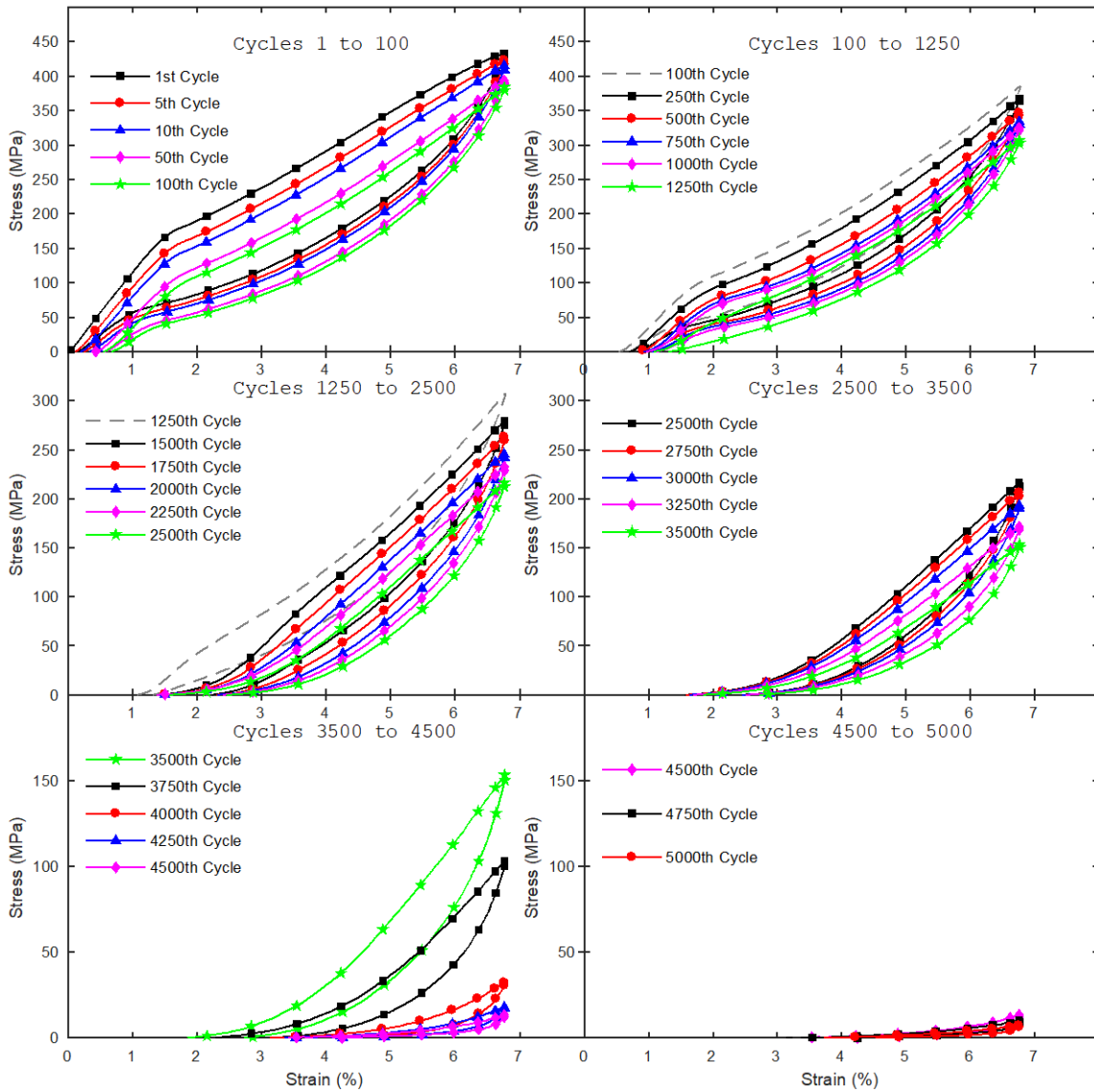


Figure 3-15. Second cable stress-strain response at 7% strain for 5000 loading cycles

3.7.2 Maximum Tensile Stress

The variation in maximum tensile stress of the second cable during fatigue testing at different strain amplitudes for 2500 loading cycles is presented in Figure 3-16a. As expected, the cable reached higher tensile strengths with the increase of the strain amplitude in the initial cycles. For all strain amplitudes, the maximum tensile stress experienced a relatively high drop in the first 100 cycles. The variation in the maximum stress after the initial 100 cycles exhibited different characteristics depending on the strain amplitude. At loading strains of 3% and 4%, there was a very slow degradation in the tensile stress and almost a stable maximum tensile stress was observed up to 2500 cycles. Cycles with 5% strain also exhibited a stable tensile stress, but only up to the 1500th cycle; after which a continuous reduction in the maximum tensile stress was noted. At a loading strain of 6%, the decrease in the maximum tensile stress continued during the first 1000 cycles and then a stable tensile stress was observed. The maximum tensile stress was observed at loading strain of 6% and then dropped below the one observed at a loading strain of 5% at about the 300th cycle; indicating a higher degradation rate in the tensile stress for a 6% loading strain. When the cable was cycled at 7% strain, an approximately linear degradation in tensile stress was observed after the first 100 cycles. However, around the 1300th loading cycle, a small drop in tensile stress was noted, which might be attributed to a rupture of a single wire. In addition, around the same loading cycle, the maximum stress became lower than that of the 5% strain loading cycles. A fitted model in the form of the following equation is developed to describe the variation in the maximum tensile stress with the number of loading cycles at each strain amplitude:

$$\sigma_{Max} = a \times N_{Cycles}^b \quad (3)$$

The coefficients a and b of equation (3) are given in Table 3-2 together with the R-square (R²) and root mean squared errors (RMSE) of the models. As can be noted from Figure 3-16a, the fitted models can adequately predict the actual data except 5% and 7% loading amplitude, where the models exhibit an RMSE of 12.42 and 27.50 MPa, respectively.

Table 3-2. Coefficients and statistical parameters of the fitted model for maximum stress

Strain (%)	<i>a</i>	<i>b</i>	R^2	<i>RMSE (MPa)</i>
3	240.5	-0.0565	0.928	2.755
4	235.4	-0.0246	0.726	3.069
5	399	-0.0498	0.596	12.42
6	450.5	-0.0799	0.945	5.538
7	671.9	-0.119	0.706	27.5

Figure 3-16b illustrates the evolution curves of the maximum tensile stress for loading cycles between 2500 and 5000 for SMA cables cycled at loading strains of 4%, 5%, and 7%. It can be seen that all specimens experienced a continued degradation in the maximum tensile stress after the 2500th cycle. The reduction rate of tensile stress was the least at 4% loading strain. At the end of the 5000th cycle, the specimen tested at 4% strain reached a maximum of 125 MPa tensile stress, which is about 52% of the maximum stress observed in the first cycle. At a loading strain of 5%, a linear decrease in the tensile strength was observed for all cycles between 2500 and 5000. The maximum tensile stress at the end of the 5000th loading cycle was 110 MPa, indicating a 69% reduction when compared to the initial tensile stress of 350 MPa. For the specimen tested at 7% strain, the rate of decrease in the tensile stress was similar to that of the specimen cycled at 6% strain for the cycles between 2500 and 3650. After which, a sudden and significant drop in the maximum tensile stress was detected up to 4200th cycle. This was due to the fracture of wires in the inner core and the first outer layer of the cable. At the end of the 4200th cycle, the wires of the outer layer of the cable were the only component that did not fracture.

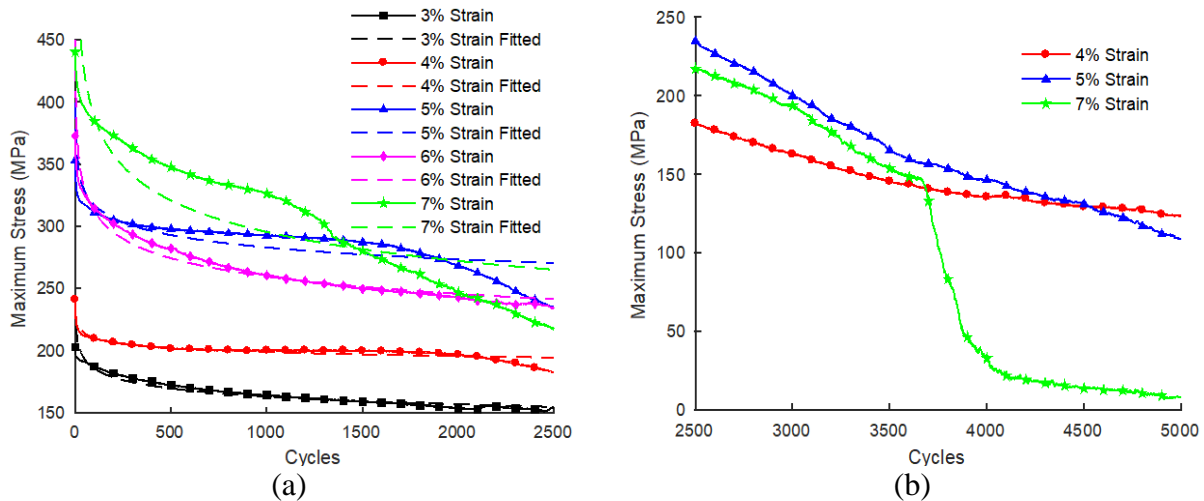


Figure 3-16. Evolution of maximum tensile stress versus cycle number during cyclic tests for 2nd cable at different strain amplitude: (a) cycles 1 to 2500; and (b) cycles 2500 to 5000

3.7.3 Residual Strain

Figure 3-17a illustrates the evolution of the residual strain for the 2500 loading and unloading cycles under loading strains of 3% to 7%. During the first 100 cycles of cyclic tension at different strain amplitudes, the maximum residual strain was in the range of 0.2% to 0.4%. At 3% loading strain, the rate of the residual strain accumulation was very slow, and the peak residual strain at cycle 2500 was 0.89%. The stable values of residual strains were also observed for cyclic tension under 4% and 5% strain amplitudes. The accumulation of residual strain started at cycle 2000 for a loading strain of 4% and at cycle 1674 for loading strain of 5%. The peak residual strains were 1.16% and 1.43% for loading strains of 4% and 5%, respectively, at the end of the 2500th cycle. In addition, it was observed that the residual strains for 5% strain loading was slightly lower than that of the 4% strain loading during the first 1750 cycles. A gradual increase in the residual strain was observed for the specimens cycled under 6% and 7% strain amplitudes up to 2500th cycle. However, at a strain loading of 7%, an abrupt increase in residual strains was observed at around 1300th cycle. This might be attributed to the failure of some wires within the cable since there was also a decrease in the maximum tensile strain as shown in Figure 3-16a. During the first 1350 cycles, a lower residual strain was encountered in the specimen tested at 7% strain as compared to that cycled at 6%. The residual strains reached 2.63% and 3.01% at the 2500th cycle for the specimens tested at 6% and 7% strain amplitudes, respectively.

The variations in residual strains between cycles 2500 and 5000 for the specimens with loading strains of 4%, 5% and 7% are illustrated in Figure 3-17b. The specimens cycled under 4% and 5% strains possessed about the same residual strains after 3500 loading cycles and exhibited almost stable residual strains until the end of the 5000th cycle with peak residual strains of 1.90% and 2.20%, respectively. The specimen subjected to cyclic loading under 7% strain showed a slow rate of increase in residual strain from 3.00% at cycle 2500 to 3.30% at cycle 3650. After cycle 3650, there was a rapid increase in the residual strain due to the failure of the inner core as well as the first outer layer. The residual strains reached 5.70% at cycle 4700 and 6.2% by the end of the 5000th cycle.

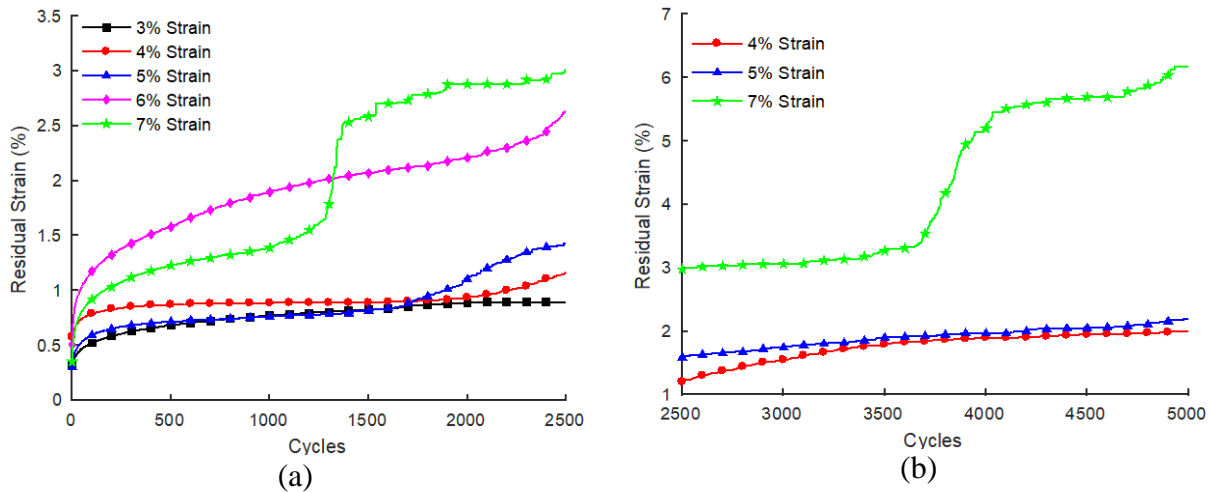


Figure 3-17. Evolution of residual strain versus cycle number during cyclic tests for the 2nd cable at different amplitudes: (a) cycles 1 to 2500; and (b) cycles 2500 to 5000

3.7.4 Energy Dissipation

Figure 3-18 shows the evolution of the dissipated energy (E_D) and the equivalent viscous damping ratio (ζ_{eq}) as a function of loading cycle up to 2500 cycles for different values of maximum strain. A rapid decrease in both the dissipated energy and the equivalent viscous damping ratio occurred during the first 50 cycles for all loading strain amplitudes. This decrease continued after cycle 50, especially for cases with higher strain amplitudes, however, the dissipated energy and ζ_{eq} reached stable values with the progression of loading cycles. At loading strains of 3%, 4%, and 5%, the stabilized values of dissipated energy were around 42%, 48% and, 30% of the values of the first cycle. The corresponding equivalent viscous damping ratios at the same strain amplitudes were 54%, 59%, and 51% for the first loading cycle, respectively. The dissipated energy was mostly constant between cycles 1300 and 2500 for loading strain of 6% and between cycles 600 and 1300 for loading strain of 7%, but then slightly decreased until cycle 2500. To relate the variation in the dissipated energy and equivalent viscous damping to the number of loading cycle, non-linear regression models are developed based on the following equation:

$$y = a \times x^b + c \quad (4)$$

The coefficients of the models for each loading amplitude are given in Table 3-3. To assess the goodness-of-fit of each model, the R-square for each model is also given. The fitted models for the dissipated energy and equivalent viscous damping are illustrated in Figure 3-18a and b, respectively. The largest model error is observed at 5% loading amplitude for the dissipated energy and at 7% loading amplitude for the equivalent viscous damping. However, the developed models follow the data almost exactly at all other strain amplitudes.

Table 3-3. Coefficients and R-square of the fitted model for energy dissipation and equivalent viscous damping for the second cable

Strain (%)	a_{DE}	b_{DE}	c_{DE}	R_{DE}^2	a_{EVD}	b_{EVD}	c_{EVD}	R_{EVD}^2
3	1024	-0.0711	-363.3	0.987	2.949	-0.103	-0.0019	0.963
4	1353	-0.0757	-96.19	0.987	2.948	-0.0821	0.491	0.988
5	1806	-0.0105	-15500	0.933	2.677	-0.178	1.351	0.981
6	3382	-0.209	301	0.997	2.938	-0.331	1.483	0.982
7	6146	-0.106	-1680	0.969	3.678	-0.356	1.111	0.870

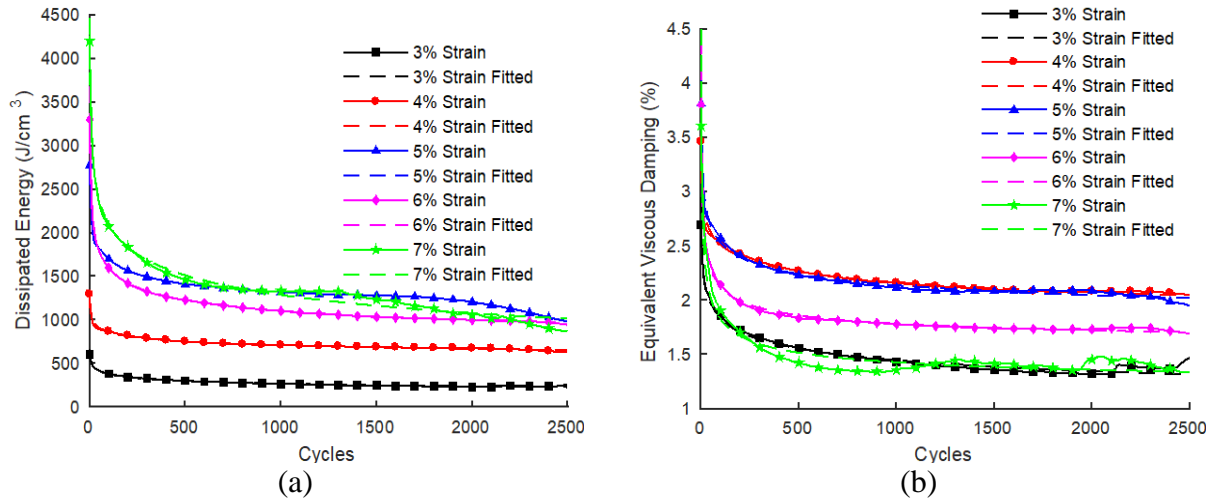


Figure 3-18. Evolution of (a) dissipated energy; and (b) equivalent viscous damping ratio during cyclic tests at different strain amplitudes up to cycle 2500

To better visualize the effect of cyclic loading at various strain amplitudes on energy parameters, surface plots are illustrated in Figure 3-19. It can be seen that for the earlier stage of the loading cycles, the dissipated energy rapidly increased with the increase of strain amplitude, while the ζ_{eq} exhibited an initial increase and then approached a constant value. However, at the later stage of the loading cycles, both the dissipated energy and ζ_{eq} attained their peak value at about 5% loading strain.

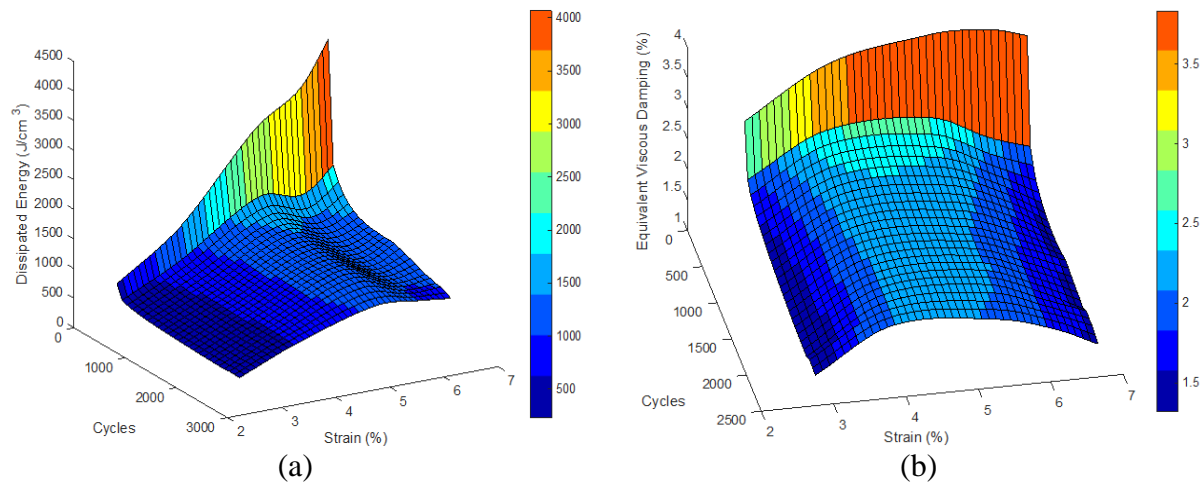


Figure 3-19. Surface plots illustrating the variation of (a) dissipated energy; and (b) equivalent viscous damping ratio with number of loading cycle and loading strain amplitude for the second cable

The variations in energy parameters with number of loading cycles for specimens tested under 4%, 5%, and 7% strain amplitudes for cycles between 2500 and 5000 are shown in Figure 3-20. All specimens displayed a continuous reduction in the dissipated energy after the 2500th cycle. The rate of the reduction was the least for the loading strain of 4% and was almost the same for loading strains of 5% and 7%. A sudden decrease in the energy dissipation at around the 3650th cycle for 7% loading strain was noted due to the failure of most of the individual wires of the cable as discussed earlier. On the other hand, the ζ_{eq} showed a linear decrease between cycles 2500 and 3650 for 7% loading strain. This is due to a higher decrease observed in the maximum tensile stress, i.e. in the maximum elastic energy, at that loading strain amplitude. For 4% loading strain, the ζ_{eq} gradually decreased and reached 1.4% at cycle 5000. The ζ_{eq} initially decreased for 5% loading strain and remained stable at a value of about 1.5% between cycles 3200 and 4100, and then increased up to 2% by the end of the 5000th cycle.

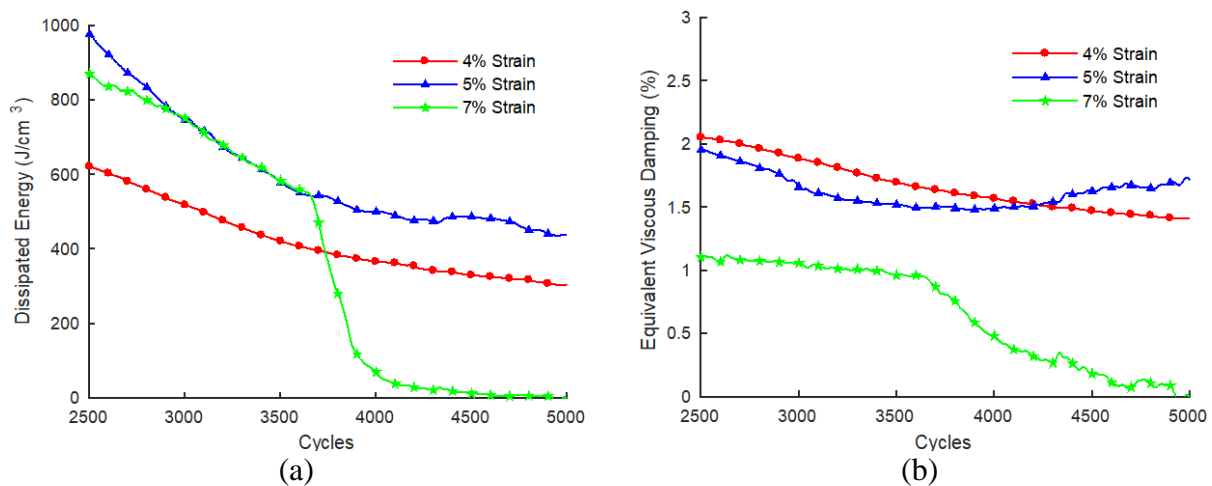


Figure 3-20. Evolution of (a) dissipated energy; and (b) equivalent viscous damping ratio during cyclic tests at different strain amplitudes between cycles 2500 and 5000 for the second cable

3.8 SEM analysis

The fracture surfaces of the second cable tested under 7% strain were characterized through SEM imaging. Figure 3-21a illustrates an SEM micrograph of the inner core and first outer layer zoomed at 30X. Figure 3-21b and c show the topographic and secondary images for a single wire zoomed at 255X. In Figure 3-21c, an indentation at the longitudinal surface, which is marked in the image as local surface stress, was observed. The main reason for this type of surface indentations is the twisting effect since each wire rubs the surfaces as the cable elongates. The images also clearly distinguish the fatigue and fracture surfaces that are characterized with different morphologies. It is noted that the fatigue region with striations of shear lines is small as compared to the fracture region characterized with a dimpled morphology as shown in Figure 3-21d.

Figure 3-21e illustrates a topographic imaging of another single wire zoomed at 300X. Similar to the previous images, the three regions, fatigue, ductile fracture, and local surface stress are visible. However, the fatigue region has an inclined surface; indicating that the material had a crack growth at an angled position. Moreover, the fracture region possesses a relatively flat surface. This indicates that a change in the angle of crack growth occurred at the same time of the fracture occurrence. Figure 3-21f and g display a secondary imaging of the wire zoomed at 700X and 5000X. The fatigue bands, which are of an average width of $0.30\mu\text{m}$, are clearly identified in Figure 3-21g. Figure 3-21h illustrates a secondary imaging of a third wire zoomed at 30X, with a size indicator for the fatigue region. Figure 3-21i represents a zoomed image of the crack initiation region for this wire. It is noticeable that the fatigue region initiated from an inclusion.

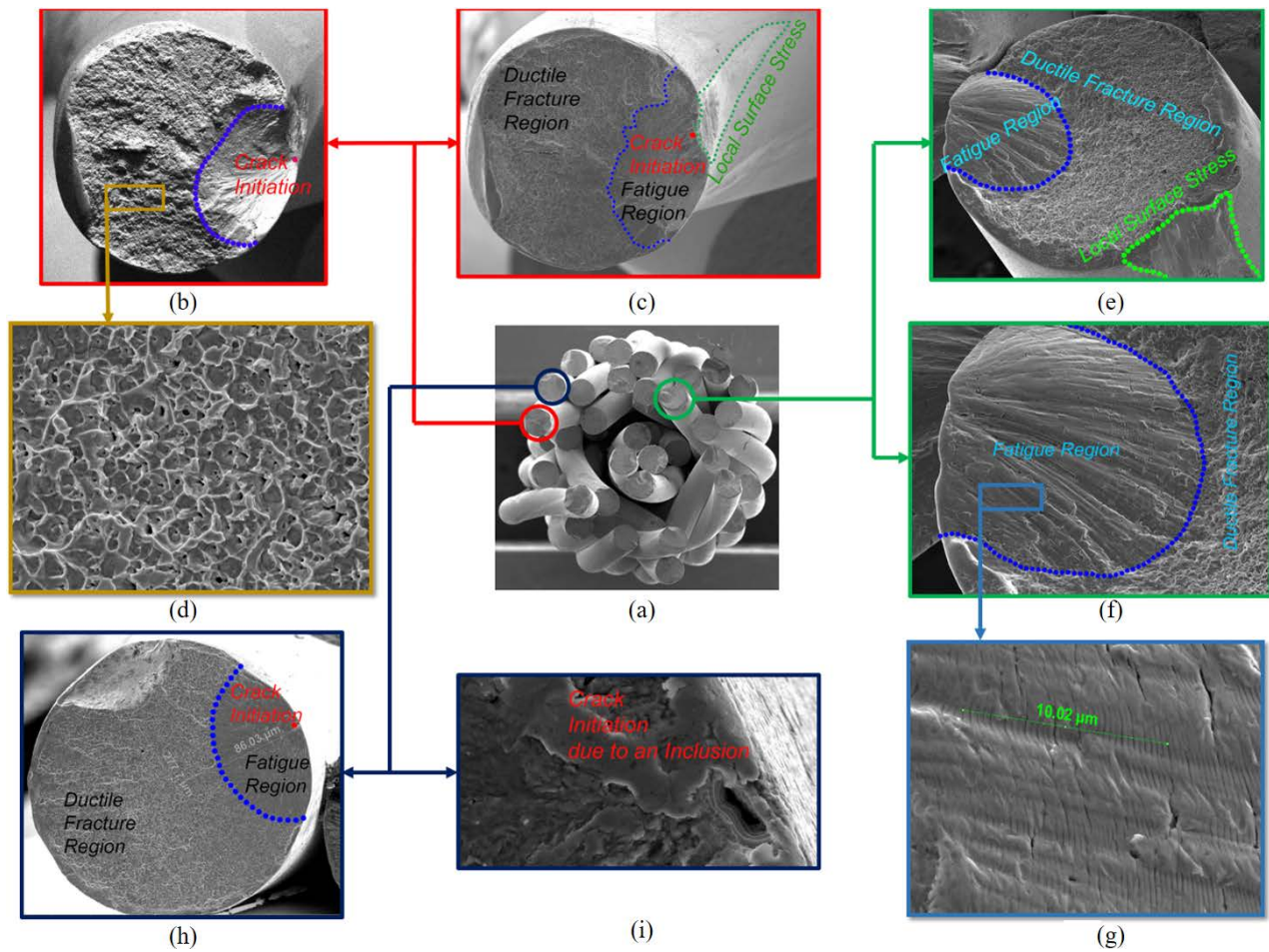


Figure 3-21. SEM images for the second cable: (a) inner core and first outer layer zoomed at 30X; (b) topographic imaging of the first wire zoomed at 255X; (c) secondary imaging of the first wire zoomed at 255X; (d) ductile fracture region of first wire zoomed at 2500X; (e) topographic imaging of the second wire zoomed at 300X; (f) fatigue region of the second wire zoomed at 700X; (g) secondary imaging of fatigue region zoomed at 5000X; (h) topographic imaging of the third wire zoomed at 300X; and (i) crack initiation due to an inclusion for the third wire zoomed at 5000X

3.9 Thermal Response

Figure 3-22 shows the variation of temperature along the length of the first cable during loading and unloading. Because the exothermic responses are generated during loading and the endothermic responses are generated during unloading by the stress-induced phase transformations, the temperature of the cable increases during forward-phase transformations and decreases during reverse-phase transformations. The uniform temperature distributions on the surface of the cable confirm the homogeneity of martensite development. In addition, the heat emission and absorption are observed to be symmetric during forward- and reverse-phase transformations.

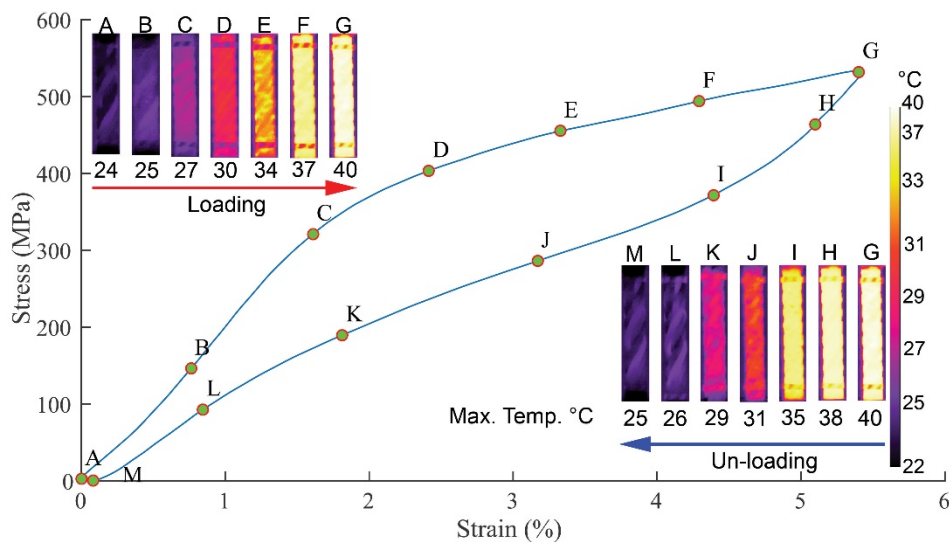


Figure 3-22. Typical temperature variation for the first cable subjected to a cyclic loading at a strain amplitude 5.4%

Figure 3-23 shows the temperature increase in the first cable specimen as a function of strain amplitude. Thermal contours of the specimen at the end of the loading curve, which illustrate the maximum temperature, are also included in the plot for different strain amplitudes. It is shown that the surface temperature of the cable increases because of the delayed heat release during forward phase transformation with the increase strain amplitude.

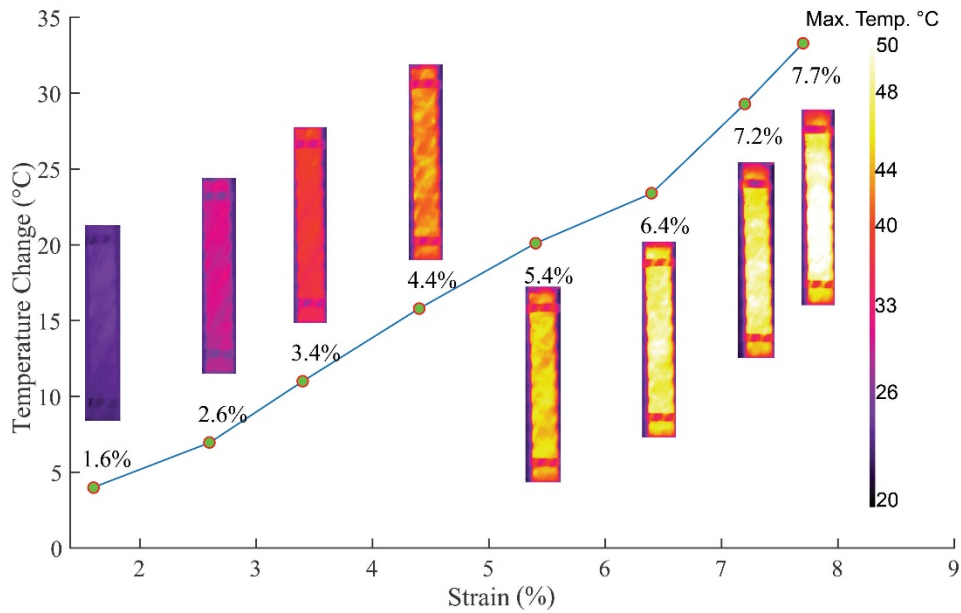


Figure 3-23. Maximum temperature profile of the first cable as a function of strain amplitude

High loading frequencies do not allow the material to transfer delayed heat to the environment. As a result, the temperature of the material changes and this, in turn, alters the transformation stresses. To better describe this effect, the temperature distributions at the specimen's surface along the length of the cable at three loading frequencies 0.05, 0.1 and 0.5 Hz are provided in Figure 3-24a-c, respectively. At higher loading rates, the latent heat released during loading did not have enough time to transfer out completely, leading to a higher and more non-uniform temperature rise at the start of unloading. Therefore, the reverse transformation stresses increase with the increase of the loading rate.

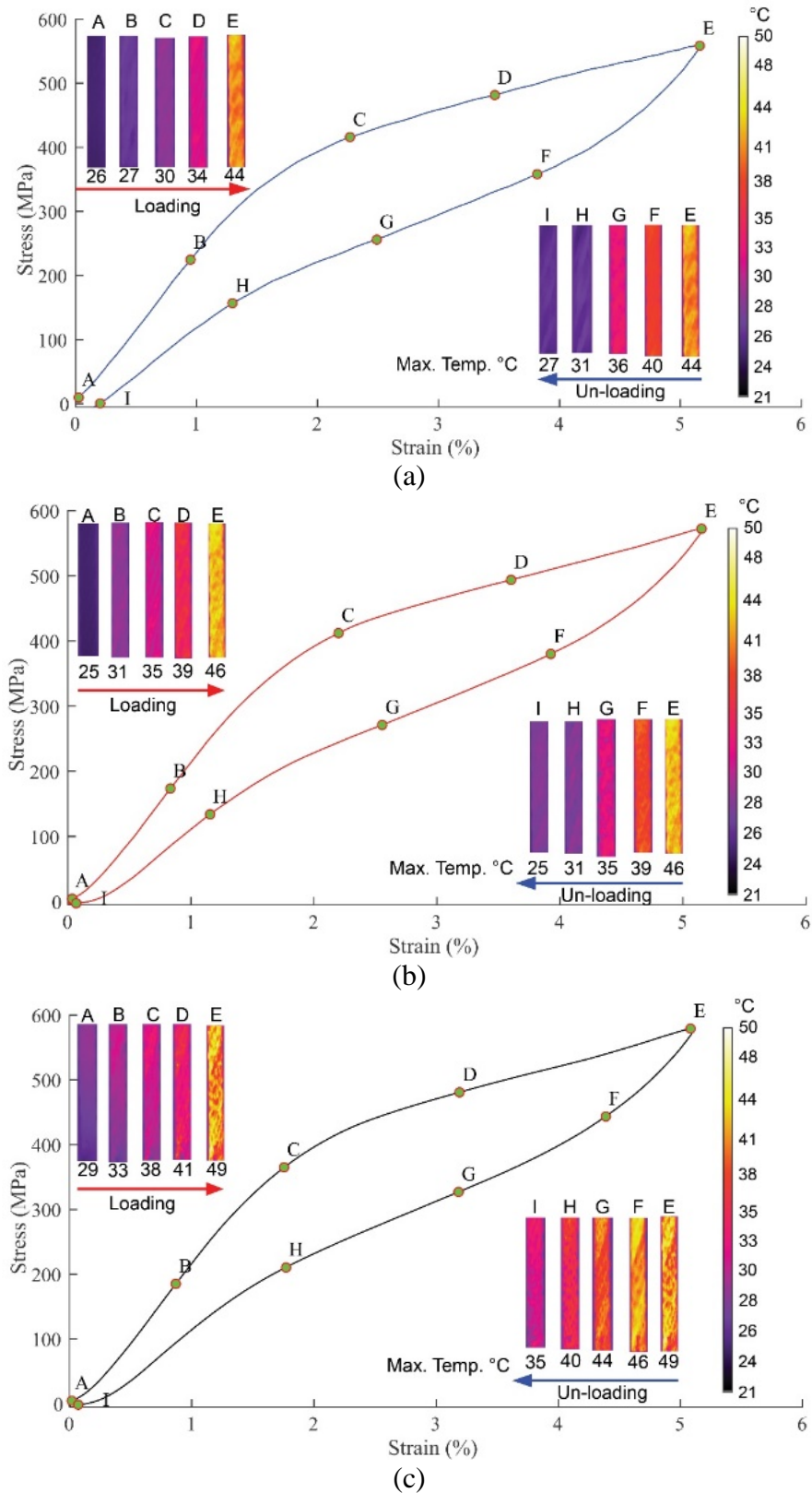


Figure 3-24. Variation of temperature morphology along the length of the first cable at (a) 0.05Hz; (b) 0.1Hz; and (c) 0.5Hz cyclic loading

In the second phase, Due to the small diameter of the strand and the nominal changes in the temperature profile with the changes of the applied strain, thermal cameras may not provide accurate thermal images that would allow for conclusive results. However, the NiTi SMA second cable is composed of multiple wires and hence has a larger diameter, which would allow for the generation of a visible change in the temperature profile with the applied strains/stress. Figure 3-25 displays the variations in the full-field temperature profile. During the loading stage, and due to the forward phase transformation from austenite to martensite (an exothermic reaction), the mean temperature of the cable increases. On the other hand, during the unloading stage, the reverse phase transformation from martensite to austenite (an endothermic reaction) is observed, and the mean temperature of the cable decreases. The thermal profile at the end of the loading curve, which corresponds to the maximum temperature, is represented by point F in Figure 3-25 for all strain amplitudes. The thermal contours illustrate that the SMA surface temperature increases with the increase of strain amplitudes due to the release of latent heat during the forward phase transformation.

This is evident based on the temperature changes that are observed in the temperature profile. During the loading phase from zero stress (point A) to the start of the forward transformation (i.e. point D for strain amplitudes of 3% and 4%, and point C for strain amplitudes ranging from 4% to 7%), the temperature change is very limited. On the other hand, the increase in the temperature was mostly observed during the phase transformation (i.e. from the start of forward transformation to the end of the loading protocol/maximum applied strain). Also, the temperature reduction was mostly observed within the unloading protocol and during the reverse phase transformation (i.e. maximum applied strain to the end of the reverse transformation that is represented by point I for strain amplitudes of 3% and 4%, and point J for strain amplitudes ranging from 4% to 7%). Beyond the end of reverse transformation and to the zero stress position, the temperature approximately returns to room temperature (22°C) except for the strain amplitude of 7%. After the unloading of the 1st cycle for the specimen subjected to 7% strain amplitude, the temperature returns to 23°C. This can be attributed to the excessive loading of the cable.

In general, the SMA second cable had a uniform temperature distribution on the surface, which may reflect the homogeneity of starting the phase transformation, i.e., the phase transformation is occurring at all components on the surface of the cable. This was fully observed for specimens with target strains of 3% and 4%. Limited non-uniformities that occurred at 5%

strain amplitudes. For the specimen with 6% and 7% strain amplitudes, the temperature profile was irregular, which indicates that the phase transformation at large strains occurred at different stages due to the different lengths of wires and geometrical irregularities of the multi-layered strand composition of the cable.

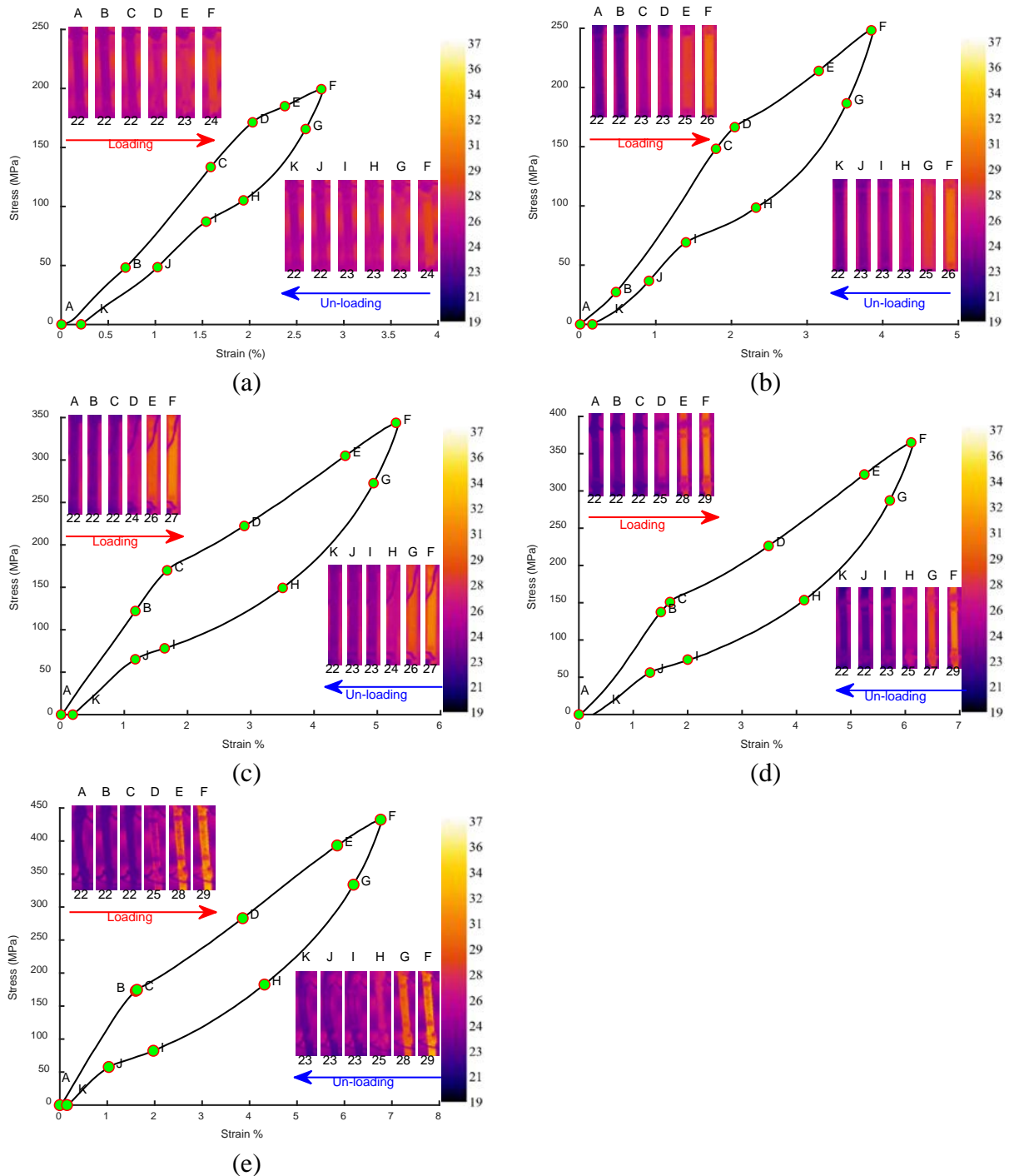


Figure 3-25. Temperature variations of the second cable for the 1st cycle with the corresponding full-field temperature profile for strain amplitudes of (a) 3%, (b) 4%, (c) 5%, (d) 6% and 7% strains

The temperature corresponding to the applied strain and the maximum recorded stress for each test of the second cable are illustrated in Figure 3-26a and b, respectively. A linear equation was used to fit the data. The linear equation corresponding to the temperature-strain is given as: $\varepsilon = 0.82 \times \Delta T + 1.247$, with a r-square of 0.97. The equation indicates that a temperature change will not occur or detected for applied strain lower than 1.25%. The equation for the temperature-stress correlation is expressed as: $\sigma = 45.3 \times \Delta T + 111.6$ and has r-square of 0.91. This correlation indicates that a temperature change will not take place for stresses less than 112MPa.

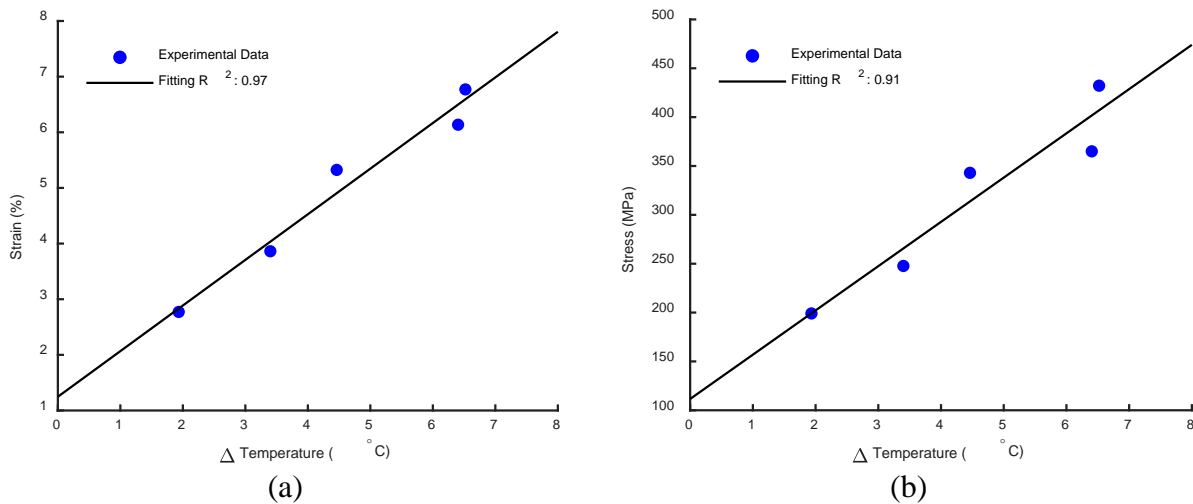


Figure 3-26. Correlation of (a) applied strain, and (b) maximum tensile stress response with the temperature change for the second SMA cable

Figure 3-27a displays the evolution of the temperature for the second cable specimen subjected to a 3% target strain. It represents the changes of the temperature under the condition of cyclic loading. The upper limit of the temperature evolution corresponds to the maximum strain/stress applied, while the lower limit corresponds to the zero-stress after the end of each cycle. In the first 100 loading cycles, it is observed that the mean temperature of the cable increases until reaching a stable temperature. Zhang et al. have reported a similar phenomenon for a wire with a 1 mm diameter that was subjected to 20 loading cycles [329]. Post the stability of the mean temperature, the upper limit decreases and the lower limit increases (i.e. the change in temperature between the zero-stress state and maximum applied strain/stress decreases).

Figure 3-27b illustrates the change in temperature between the zero-stress state and maximum applied strain for all loading cycles of specimens subjected to target strains ranging from 3% to 7%. The decrease in the change of temperature followed the same pattern of the increase of the

residual strains, revealing a possibility of a direct correlation between the decrease in temperature change and the increase of residual strains. This is apparent with the specimen subjected to 7% target strains, especially that a nearly stable change in temperature was visible from the 10th cycle to the 2500th cycle. Post the 2500th cycle to the 4000th cycle, the change of temperature was decreased in a linear fashion, which is similar to the increase of residual strains during the same period. This also indicates possible ruptures in single wires. Post the 4000th cycle, the change in the temperature dropped to zero, which also corresponded to a sudden increase in residual strain as displayed in Figure 3-17. This indicates that the inner core of the second cable has completely ruptured.

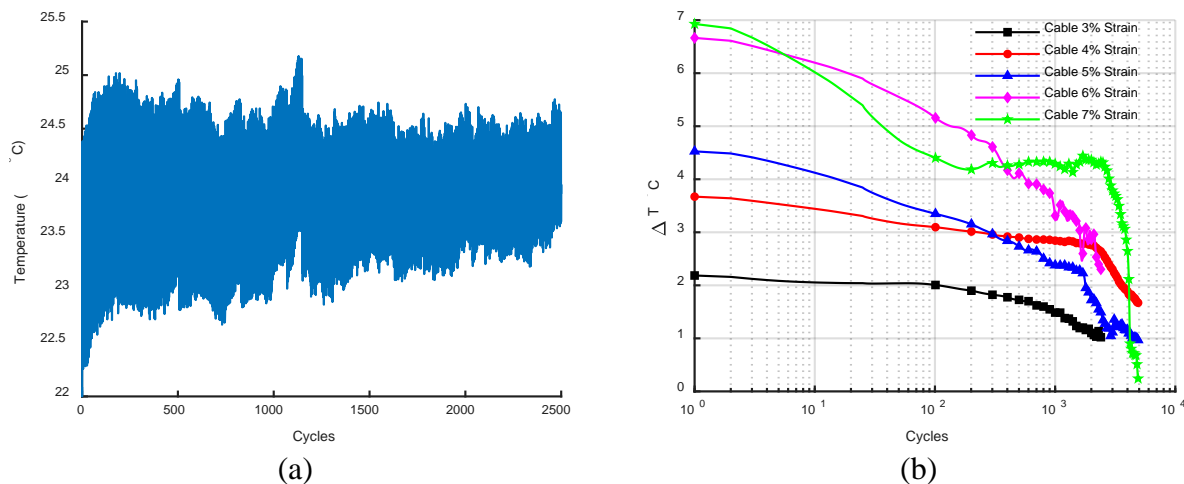


Figure 3-27. (a) Temperature evolution during the cycling loading of the second cable specimen with a 3% target strain, and (b) change in temperature with the number of cycles

3.10 Electrical Resistivity

Figure 3-28a illustrates the normalized change in resistance during the 1st cycle of the strand and the second cable subjected to 7% target strain. It represents the profile of normalized change in resistance for the other target strains. No correlation between the applied strain and the recorded change in resistance of the cable is observed. The resistance of the cable increases up to a certain point (in this case, it is up to 0.2 of the cycle) after which the resistance decreases to a stable plateau from 0.4 to 0.6 of the cycle. Beyond 0.6 of the cycle (i.e. in the unloading portion of the cycle protocol), the resistance increases until reaching 0.7 of the cycle, after which it decreases. The irregular shape of the change of resistance represents the global change in resistance of the cable. Its irregularity is due to the non-uniform strain distribution of the wires in the cable that is due to the various lengths of the wires and multi-layering structure of the cable.

However, for the typical strand configuration (1×7), the change in resistance profile can be correlated to the loading and unloading protocols. The resistance increases with the increase of the strains and decreases with the reduction of the applied strains. A direct correlation is achieved due to uniform length used for the assembling of the strand and the uniform distribution of the applied strains over the cross-sectional area of strand.

Figure 3-28b illustrates the recorded changes in resistance with the applied strains for all cable specimens subjected to target strains ranging from 3% to 7% strains. The scattered points show a direct correlation between the change of resistance and the applied strains. The data was fitted to obtain a prediction of the change of resistance with the applied strain and is given by the following equation: $\Delta R = 0.06038 \times \varepsilon + 0.01858$ with r-square value of 0.95. The stress-strain and stress-resistance response of the strand subject to a target strain of 6% are illustrated in Figure 3-28c and d, respectively. It is interesting to observe that due to the direct correlation between the change in resistance with applied strain, the typical flag shape is conserved even when the stress is plotted against the recorded change in strain. This consolidates the understanding that the change in resistance is directly correlated to the applied strain.

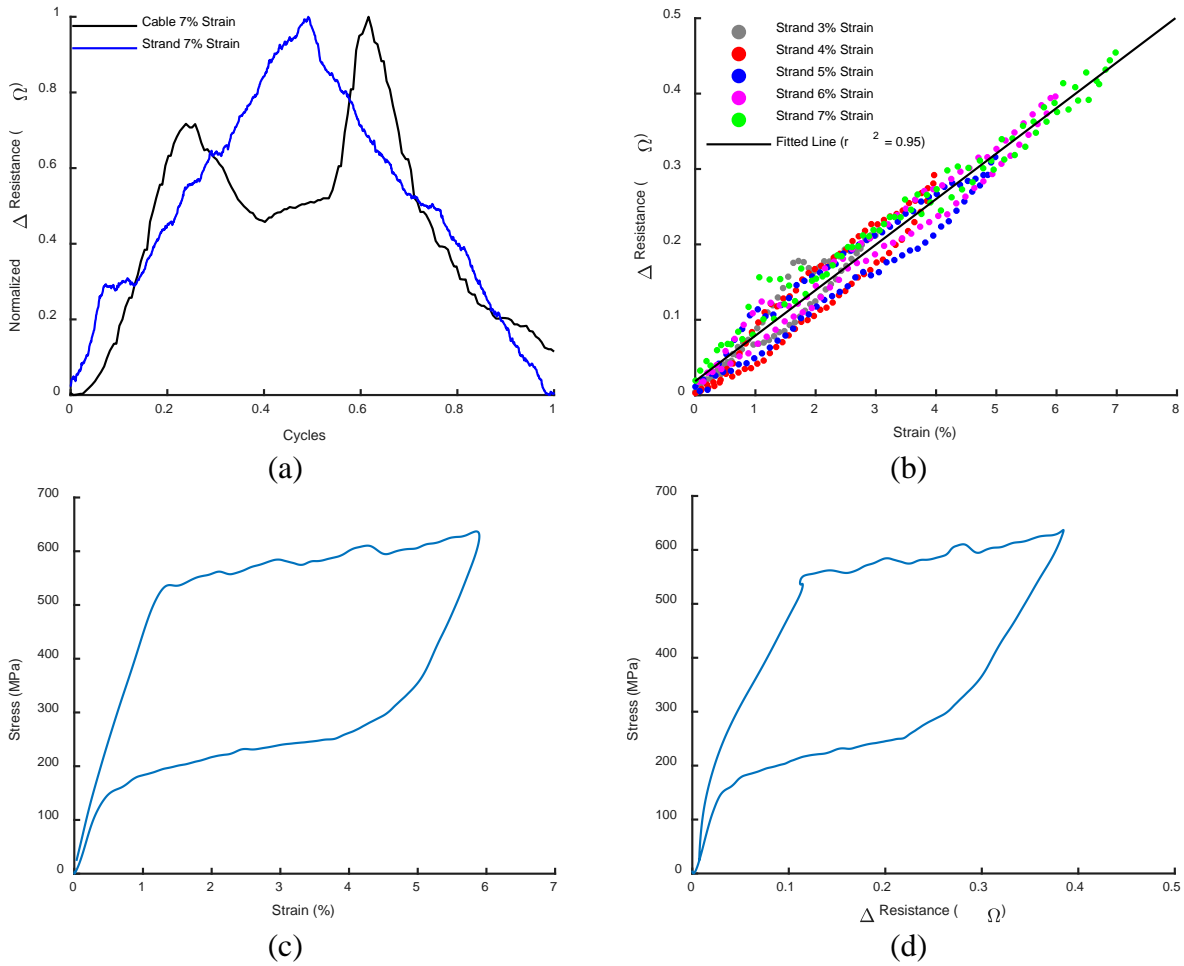


Figure 3-28. (a) Normalized change in resistance of both strand and the 2nd cable subjected to 6% target strain, (b) Scatter plot of change in resistance with the applied strain, (c) stress-strain curve of the strand subjected to 6% target strain, and (d) stress-resistance curve of the strand subjected to 6% target strain

3.11 Fabrication of a SMA Cable-based Control Device

Based on the previous discussions on the tensile characterization and functional fatigue of superelastic NiTi cables, it was concluded that SMA cables possess good energy dissipation and high tensile strength associated with low manufacturing cost. This has led to the manufacturing and experimental investigation of superelastic viscous damper (SVD) that was proposed and numerically investigated by Silwal et al. [57]. The proposed SVD is a hybrid device that consists of superelastic cables and high damping butyl elastomers. The elastomer compound would provide the energy dissipation required, while the superelastic cable will provide the re-centering capabilities. Figure 3-29a-c, illustrate the force-displacement behavior of the superelastic SMA, the shear behavior of the elastomer, and the expected behavior of the SVD, respectively.

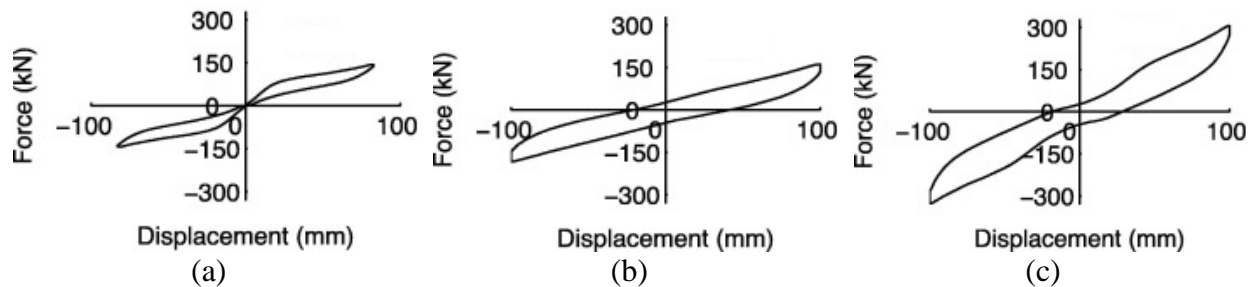


Figure 3-29. Force-displacement curves of the sub-components (a) SMA, and (b) elastomer compound, and (c) the hybrid behavior (superelastic viscous damper)⁵⁷

Figure 3-30a and b, represent a 3D rendering of the proposed SVD and a schematic diagram of SVD at its un-deformed and deformed positions, respectively. The SVD consisted of elastomer compounds placed in-between three steel plates. The SMA cable was wrapped around the top and bottom steel plates. The top and bottom steel plates were fixed, while the middle plate is allowed to move, and will always apply a tensile force on the SMA cable.

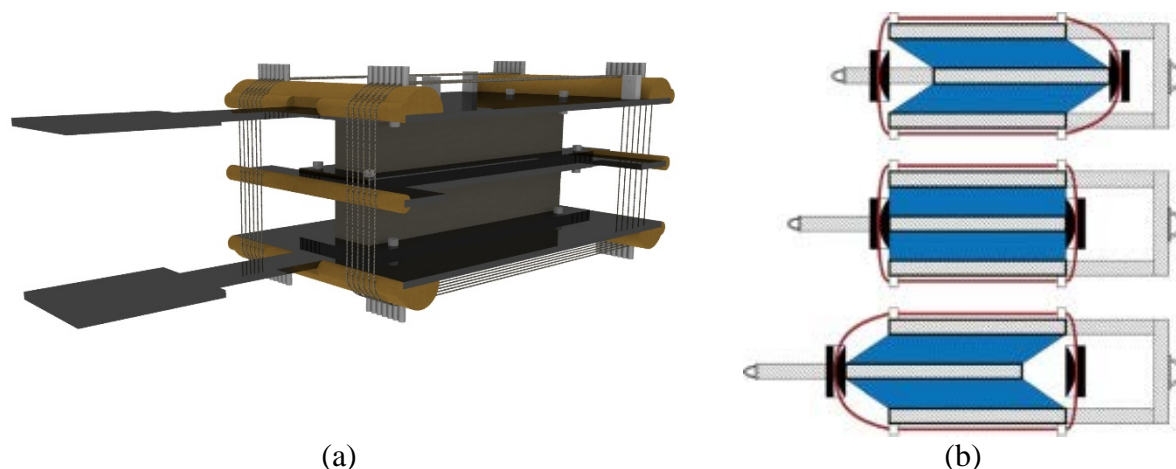


Figure 3-30. (a) 3D rendering of SVD, and (b) schematic drawing at its un-deformed and deformed positions⁵⁷

A prototype SVD was designed based on the cable cross-section area, tensile behavior of the SMA cable, and the shear behavior of the elastomer compound. The cable for the SVD had a 7×7 configuration with each individual wire consisting of a diameter of 0.267 mm and a total diameter of 2.40 mm. Special considerations were made to limit the maximum strains applied to the cable to be around 7%, as the cables can handle large strains without an immediate failure. Even though, the elastomer compound can reach 300% of shear strains, the thickness of the elastomer compound was calculated based on a maximum 200% of shear strains for the maximum displacement capacity which was set to 100 mm.

The manufacturing of the SVD consisted of several stages to assemble the multiple components. The first stage included the bonding of the elastomer compound to steel plates at the bottom and top face of the elastomer, using the 3M DP190 epoxy. The epoxy was applied to the bottom steel plate, and the elastomer was then placed. Another layer of the epoxy was added to the top of the elastomer and the top steel plate was placed. A small compressive force was applied to eliminate any excessive epoxy that might affect the viscoelastic properties of the elastomer component. Figure 3-31a and b display the dimensions of a single elastomer pad bonded to the steel plates and the location of bolt holes in the steel plates, respectively.

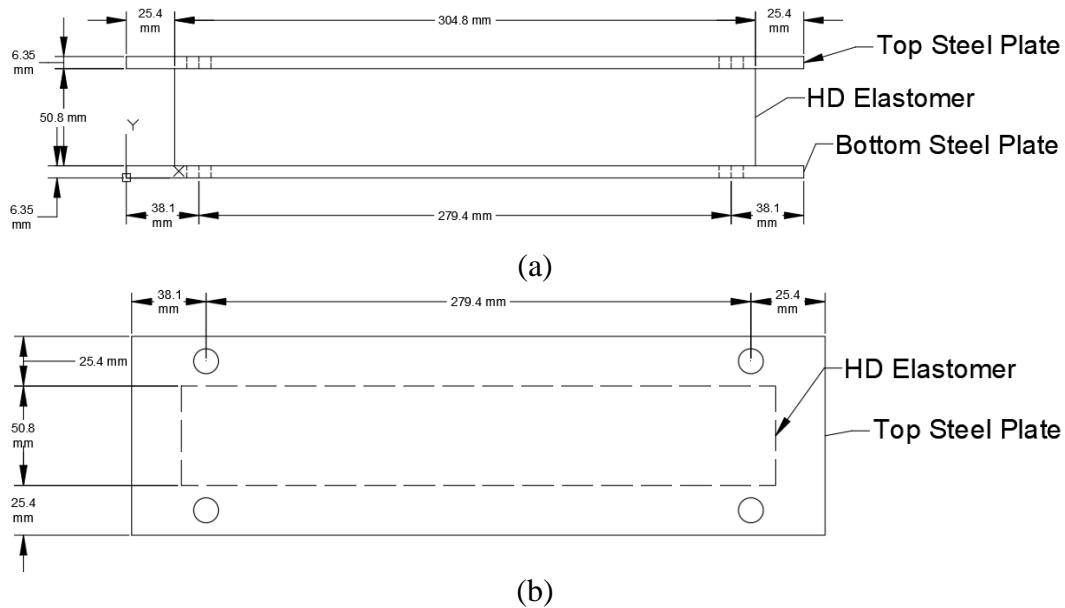


Figure 3-31. (a) Side view of the elastomer with steel plates, and (b) top view section of the elastomer with the bolt holes location of the steel plates

The second stage included the attachment of delrin rod to the middle, top and bottom steel plates. In general, the delrin rods are required to have a smooth contact and low friction between the steel plate and SMA cable. The top steel plates had two sets of delrin rods. The first set had a radius of 22 mm and was attached on the top side of the steel plate. This set is necessary to increase the total height of the damper, which increases the length of the loops of the SMA cables, that results in limiting the maximum strains which corresponds to the maximum displacement capacity. The second set of rods had a radius of 8 mm which was attached to the left and right sides of the steel plate. The bottom steel plate had a similar configuration to that of the top plate. The middle plate had a set of rods similar to the second set of delrin rods of the top and bottom steel plates. Figure 3-32a and b display a schematic diagram for the side view of the top and middle steel plates with the delrin rods. The third stage involved the attachment of the elastomers to the top, middle and bottom steel plates. The fourth stage included the wrapping of the SMA cable around the damper. Figure 3-32c illustrates the final product from a side view.

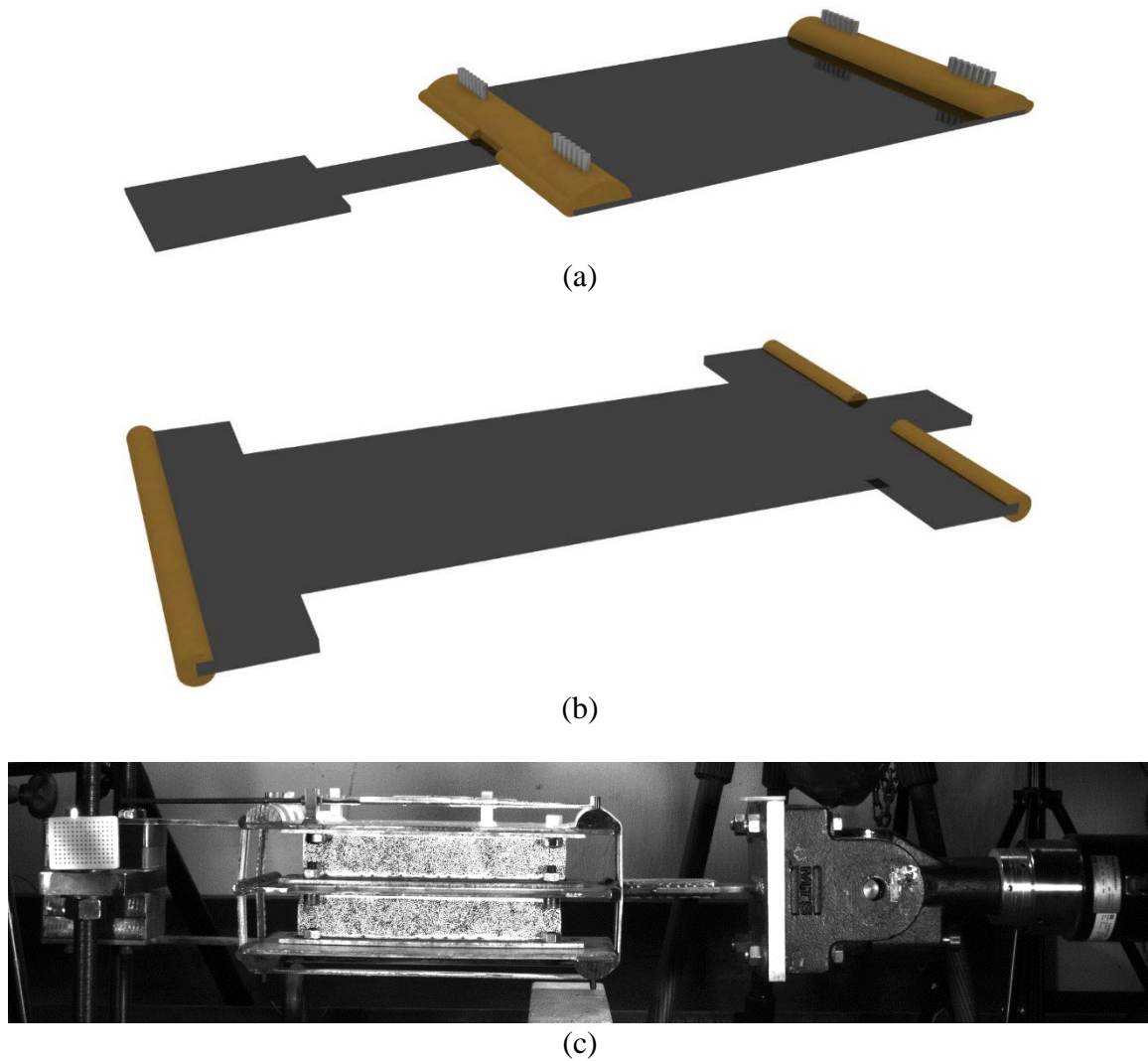


Figure 3-32. Schematic drawing for (a) top steel plates, (b) middle steel plates with delrin rods, and (c) the complete assembly of the superelastic viscous damper

The superelastic viscous damper was subjected to three cycles with various loading frequencies ranging from 0.1Hz to 2.0Hz, and displacement amplitudes ranging from ± 12.7 mm to ± 101.6 mm. The displacement amplitude of 12.7 mm corresponds to 3.0% tensile strains in the cable and 25% shear strains in the elastomer compound. While the displacement of 101.6 mm corresponds to 7.0% tensile strains in the cable and 200% shear strains in the elastomer compounds. Low and high speed cameras were used to monitor the full-field strains and displacement in the SMA cable and elastomer compounds. Furthermore, a thermal camera FLIR A615 was used to monitor the full temperature profile change in the viscoelastic and SMA cable. Figure 3-33a displays the test setup for the superelastic viscous damper with low- and high-speed camera and thermal camera FLIR A615.

During the testing of the superelastic viscous damper under a loading frequency of 0.1Hz and strain amplitudes of ± 12.7 mm, ± 25.4 mm, and ± 50.8 mm, multiple undesired behaviors were observed after which the testing protocol was suspended. The major concern was related to the bond between the elastomer compound and steel plates, and its failure was due to the excessive shear displacement. By the end of the 3rd cycle with a strain amplitude of ± 50.8 mm, it was obvious that the rubber was de-bonding from the steel plates and a failure in the epoxy was observed. Another alarming concern was the bending of the top and bottom plates at the free end which may have led to weakening the bond between the elastomer compound and steel plates as well as reducing the strains experienced by the SMA cable. Also minor displacement at the fixed end was observed which indicated the need for strengthening the fixed support.

Figure 3-33b displays the force-displacement response obtained for the 1st cycle with a loading frequency of 0.1Hz and displacement amplitudes of ± 12.7 mm, ± 25.4 mm, and ± 50.8 mm. A good hysteretic response was obtained from the testing of the device but the bond between rubber and steel plate needs to be improved to fully characterize the response of the damper in future work.

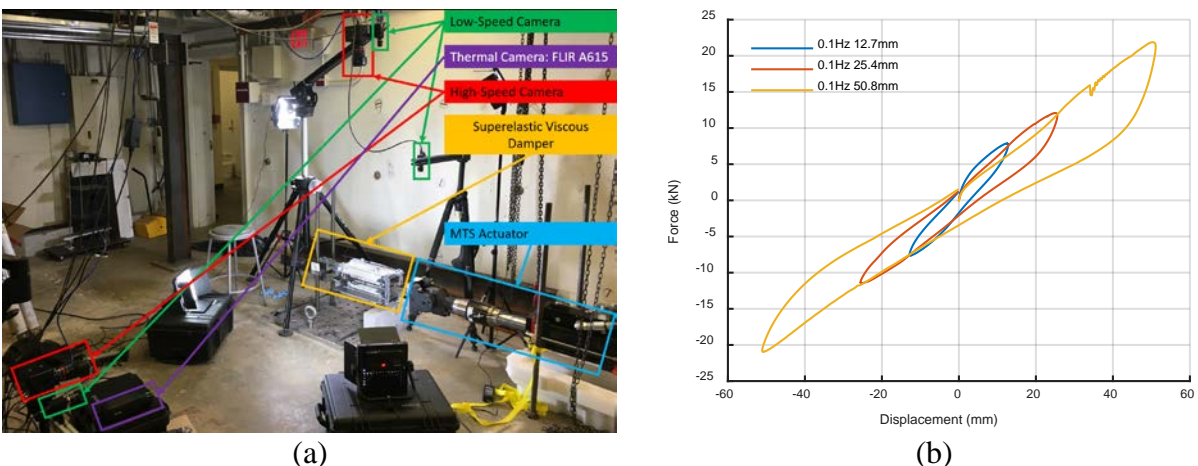


Figure 3-33. (a) Test setup of the superelastic viscous damper including low-, high-speed cameras and thermal camera FLIR A615, and (b) Test results for displacement amplitudes of ± 12.7 mm, ± 25.4 mm, and ± 50.8 mm at a loading frequency of 0.1Hz

3.12 Summary

In the first part of this section, uniaxial tensile behavior of a large diameter SMA cable was investigated. Experimental tests were conducted at various strain amplitudes and loading frequencies. The results indicated that SMA cables can undergo deformations of up to 6% strain with no residual deformation. The low-cycle fatigue response of the cable was investigated. In

general, the hysteresis loops narrow and residual strains are accumulated with the increasing number of loading cycles. The influence of number of loading cycles on the behavior of the SMA cable were more apparent in early cycles and tends to diminish, especially after the first 40 cycles. In addition, the increasing loading rates result in an upward shift in the reverse transformation stress levels although they do not considerably alter the forward transformation levels. As a result, a decrease in the amount of energy dissipated per cycle occurs when the SMA cable is loaded at higher rates.

Second, the tensile response and the functional fatigue characteristics of a non-conventional superelastic NiTi cable was explored. The cable specimen were subjected to cyclic tensile loads for a minimum of 2500 loading and unloading cycles under various loading strain amplitudes. Next, the thermal and electrical response of the SMA cable subjected to fatigue loading was investigated. The findings of the functional fatigue tests can be summarized as follows:

- The results of the tensile tests confirmed that the SMA cables exhibit superelastic behavior with no or minimal residual deformations up to 6% strain and a maximum of a 0.76% residual strain for a strain of 10%.
- A high positive stress-strain slope over forward transformation range was observed, which might be due to a non-uniform transformation initiation in the individual wires of the cable.
- Cyclic loading tests under different strain amplitudes revealed a very high functional fatigue life for the NiTi cable. The influence of the number of loading cycles on the superelastic properties of the SMA cable was more apparent for the first 100 cycles.
- The peak residual strain was only 0.8% by the end of the 2500th cycle for a loading strain of 3%, while the specimens tested under loading strain of 4% and 5% exhibited residual strains of 2% and 2.18%, respectively, by the end of the 5000th cycle.
- Under a loading strain of 6%, the stress-induced martensite transformations were still apparent by the end of the 2500th cycle, while there was about 2.6% residual strain.
- The specimen subjected to 7% strain had a complete fracture of the inner core as well as the first outer layer above cycle 3650, but showed a flag-shaped hysteresis until loading cycle number 1250.
- In terms of energy dissipation, the cable exhibited the highest dissipated energy and equivalent viscous damping ratio under 5% loading strain when a high number of loading cycles was applied.

- SEM images taken from the cross-section of the cable failed under 7% strain fatigue loading illustrated minor local stresses due to the configuration of the cables and re-orientation of wires.
- Thermal imaging can be used to monitor the strains and stresses experienced by cables due to the exothermic and endothermic reactions that occur during the loading and unloading protocols, respectively. However, thermal imaging may not be appropriate for small diameter strands as they provide minimal latent heat during the phase transformation.
- Thermal imaging can also be used to monitor the degradation of SMA cables in their functionality (i.e. energy dissipation and residual strains), due to the correlation between the decrease of temperature change, the decrease of energy dissipation, and the increase of residual strains.
- The global change in resistance of the multi-layered SMA cable is not effective in determining the strain/stress state, due to the non-uniform strain distribution and phase transformation along the cross-sectional area and the outer surface of the cable. However, for a conventional strand with a 1×7 configuration can be used for self-sensing application.

Finally, the fabrication of a SMA cable-based control device was discussed. An experimental matrix was implemented to investigate the energy dissipation and re-centering capabilities of the SMA cables under cyclic loadings. Even though the developed device showed promising response, some modifications such as the enhancement of the bond between the steel plates and the rubber compound need to be considered. Also, the bending of the top and bottom plates should be limited to apply high strains on the SMA cables and achieve the re-centering capabilities.

This section illustrates that SMA cables exhibit excellent superelastic behavior similar to thin SMA wires. Considering their very good mechanical properties and cost advantages over a same size monolithic SMA bar, SMA cables can potentially accelerate the implementation of shape memory materials in real-world structural applications.

4 Fiber Reinforced Cementitious Composites

(Most of the discussions presented in this section were published in the following conference and journal papers [330-332])

4.1 Overview

In this section, the behavior of mortar and concrete mixtures with randomly distributed superelastic shape memory alloy (SMA) fibers was investigated. SMA-fiber reinforced mortar and concrete with varying fiber volume fractions and fiber aspect ratio were investigated. The performance of SMA fiber reinforced specimens were compared against those of control specimens as well as hybrid fiber systems which included a combination of steel and SMA fibers for concrete specimens. Flexural cyclic tests were conducted on both mortar and concrete beam specimens. Digital image correlation systems were used to measure full-field deformations and monitor the damage evolution on the surface of the specimens. Test results were analyzed in terms of flexural strength capacity, deflection capacity, crack width as well as re-centering and crack recovery ratios for each specimen. Furthermore, acoustic emission sensors were attached to the mortar and concrete specimens to further characterize crack development.

4.2 SMA Fiber Reinforced Mortar

4.2.1 Material and Specimen Preparation

The mortar mixture design and specimen preparation were based on the ASTM C348: Standard Test Method for Flexural Strength of Hydraulic-Cement Mortars. A total of five different mixtures, including plain mortar as a control mixture, were prepared as shown in Table 4-1. Conventional Portland cement (ASTM Type I/II based on ASTM D1193: Standard Specification for Reagent Water) and a natural sand fine aggregate were used for all specimens. SMA strands with a diameter of 0.351 mm were used as fibers in all SMA fiber reinforced mortar specimens. Each strand consisted of seven NiTi wires with a diameter of 0.117 mm as shown in Figure 4-1. The strand construction included one straight core wire and six outer helical wires. The chemical composition of NiTi strands in atomic percentage is given in Table 4-2.

Table 4-1. Mortar mix design

Mixture	Sand/Cement	Water/Cement	SMA Fiber Volume Ratio (%)	SMA Fiber Length (mm)	Number of Specimens
1 (M-Control)	2.75	0.48	-	-	3
2 (M-SMA-1)	2.75	0.48	0.30	20	3
3 (M-SMA-2)	2.75	0.48	0.30	30	3
4 (M-SMA-3)	2.75	0.48	0.50	30	3
5 (M-SMA-4)	2.75	0.48	1.00	30	3



Figure 4-1. Cross-sectional and longitudinal view of SMA fibers

Table 4-2. Chemical composition of NiTi strands in atomic percentage

C	Cr	Ni	Ti	Fe	Cu	Co	O	Others
0.0272	0.0003	56.03	43.91	0.0087	0.0005	0.0005	0.0214	0.0014

Figure 4-2a shows the monotonic tensile behavior of SMA strands up to failure, while Figure 4-2b illustrates the response of SMA strands to a loading of up to 6% strain and subsequent unloading. The NiTi strand had a tensile strength of 915MPa at 9.5% total elongation with an austenite (initial) elastic modulus of 30.5GPa. The forward phase transformation stress was encountered at 350MPa, while the reverse phase transformation stress was observed at 130 MPa. The transformation temperatures were -20.9°C for A_s (austenite start) and -11.6°C for A_f (austenite finish), ensuring a superelastic behavior at room temperature. Three different SMA fiber ratios, namely 0.3%, 0.5% and 1.0% by volume of the mortar, were evaluated. Each SMA fiber had a length of 30 mm and an aspect ratio of 86. To assess the effect of SMA fiber length on the performance of the composite, an additional SMA fibers with a length of 20 mm and an aspect ratio of 57 were used at 0.3% fiber volume ratio. Three prismatic specimens with dimensions of $40 \times 40 \times 160$ mm were casted for each mixture. Three 50 mm cubic specimens were also prepared for compressive testing of plain mortar mixture. The mixing procedure of the SMA fiber reinforced

mortar consisted of weighing the required mortar material for each volume fraction and fiber length. The cement, sand and water were mixed and then fibers was added to the mortar base and mixed once again until the composite material achieved homogeneity. All samples were consolidated using a vibrating table and covered with plastic and insulated inside styrofoam containers for the first 24 hours. The samples were removed from the molds and cured inside a moisture room at above 95% relative humidity and air temperature of $23 \pm 1.5^\circ\text{C}$ for 28 days.

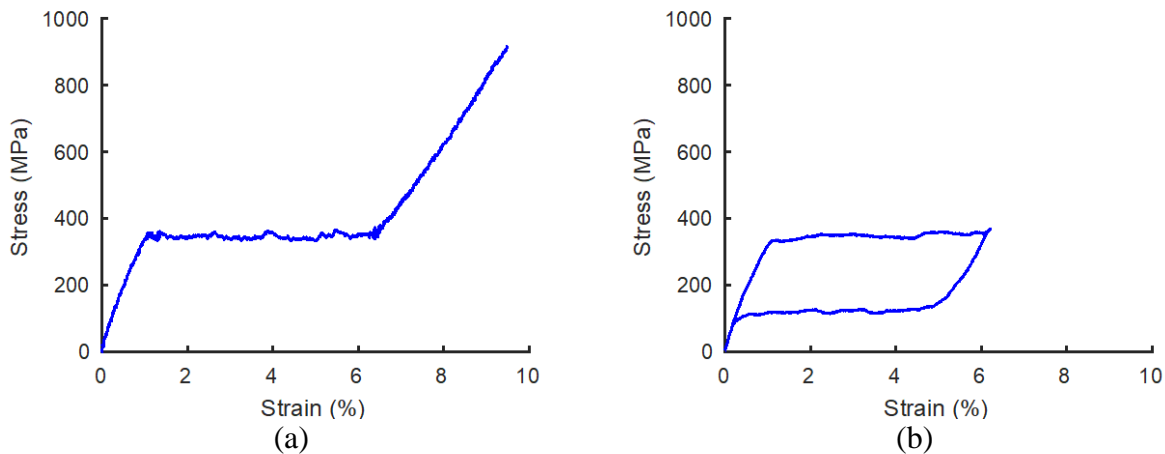


Figure 4-2. Stress-strain curve of SMA strand: (a) Monotonic response until failure; and (b) Hysteresis loop for 6% strain

4.2.2 Test Plan and Setup

A three-point (central) loading cyclic bending test, configured in displacement-control, was conducted to evaluate the performance of SMA fiber-reinforced mortar specimens. The clear span length of the beam specimens was 135 mm. MTS loading frame with a capacity of 1000kN was used for the flexural tests. The cyclic loading procedure, which included 13 cycles, utilized a zero to peak loading regime with successive cycles incremented by 0.1 mm to a total displacement of 1.3 mm (Figure 3-7a). Both the loading and unloading rates were set to be 1.0 mm/min.

DIC was used during the experiments to monitor strain evolution and deformation fields. The DIC system was also used to monitor crack propagation and crack width. To enable the DIC measurements, the surface of specimens need to be textured with a random speckle pattern. In this work, a single camera with 12 mm lens was used for 2D-DIC as there was no significant out-of-plane movement. The camera resolution was 2448×2048 pixels with a CCD sensor that has a format of 2/3in. The maximum frame rate for the camera was 15 frames per second. In addition to the DIC measurements, a laser extensometer was used to monitor the specimen deflection on the

tension side. The acoustic emissions of the specimens were monitored by attaching an acoustic emission sensor at one end of the specimen. Figure 3-7b displays the test setup for the flexural testing of mortar specimens.

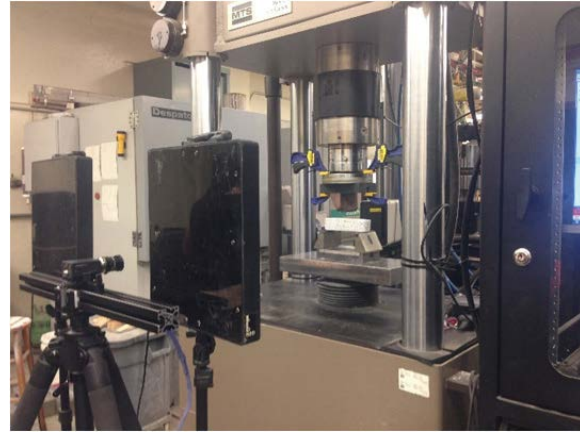
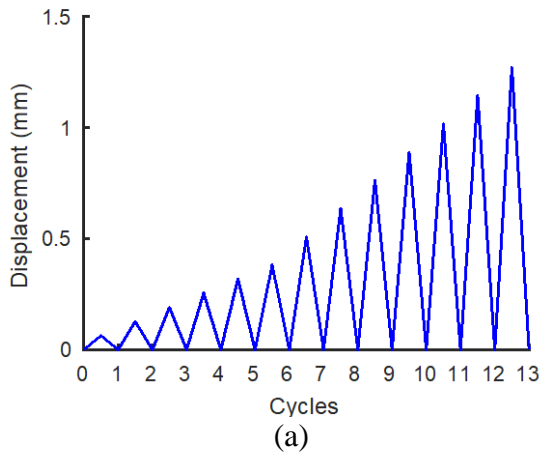


Figure 4-3. (a) Mortar cyclic displacement protocol; and (b) test setup for mortar testing

Acoustic emission (AE) is the generation of transient elastic waves that are caused by the release of energy from localized sources within a specimen. Acoustic emissions testing can be used as a non-destructive method to evaluate and monitor structural integrity of members [334-337]. The acoustic waves within a material matrix can be detected by attaching one or more AE sensors, made of piezoelectric material [338, 339]. The transducers record electric waveform response caused by an energy release event in the system. The analysis of the waveforms properties provides information about the crack propagation, density of cracks, and failure mechanism.

A typical AE signal with its properties is illustrated in Figure 4-4. In AE testing, a “threshold” voltage level is set by the user to disregard the AE signals that are below a certain magnitude and might be encountered due to noise generated by the surrounding environment. The maximum voltage exhibited at the highest peak of the waveform is called an “Amplitude” of a signal. The “Duration” represents the time span between the first and last threshold crossing in a signal. The “Counts” or “Hits” refer to the number of times the signal have crossed the threshold level. The time span that elapsed from the first count to the amplitude of the signal is known as the “Rise Time (RT)”. Other important acoustic parameters include the “Average Frequency (AF)” and the “Rise Amplitude (RA)”. The AF is computed as the number of counts (hits) divided by the duration of the signal, whereas the RA is defined as the ratio of rise time to amplitude.

The scale of a crack depends on the energy emitted at the source and can be identified by the amplitude of AE. Small strains (micro-cracking) emit waves of low energy and low amplitudes, while a crack propagation generates a higher amount of energy and large amplitudes. The failure mechanisms in cementitious material can be primarily described by two failure modes: tensile and shear. A tensile mode is a motion perpendicular to the sides of each crack face, while the shear mode is a motion parallel, but opposite in direction, at the crack face. A tensile mode of failure, such as matrix cracking, has a high average frequency and a high rise angle (low rise amplitude). On the other hand, a shear failure mode, such as delamination and fiber pull-out, would produce signals with long durations, i.e., a low average frequency, low rise angle, and high rise amplitude [340]. Figures 2(a) and (b) illustrate a typical acoustic signal for tensile mode (mode I) and shear mode (mode II), respectively.

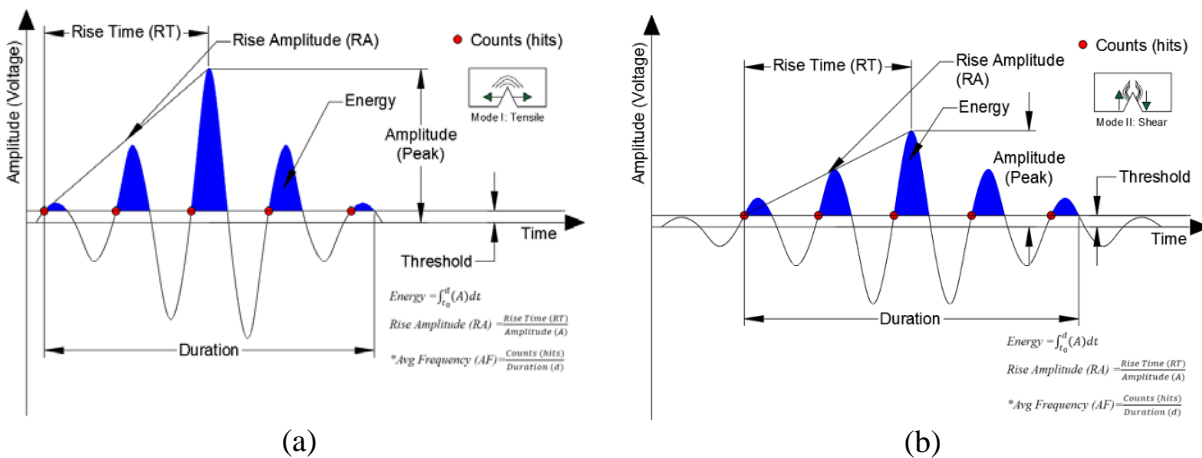


Figure 4-4. A typical AE signal for (a) tensile mode (mode I) and shear mode (mode II)

The correlation between average frequency and rise amplitude can be used to identify cracking and recovery mechanisms of the SMA fiber reinforced specimens; i.e. the failure type (shear or tensile failure), and the recovery type (macro or micro-crack recovery). Figure 4-5 illustrates the identification of the failure event using the average frequency and rise amplitude. Ohtsu et al. recommended a crack classification technique based on the correlation between average frequency and rise amplitude [341]. It was proposed that the type of cracking can be distinguished by observing a borderline of a ratio of 50 (i.e. $AF = 50 \times RA$). Events that lie above the line represents a tensile crack, and events that occur below the line represents a shear crack. The ratio of 50 is recommended based on a moment tensor analysis performed by Ohno et al. [342]. Recently,

Benard et al. conducted a study about the characterization of the crack in concrete structures using AE and DIC techniques [343].

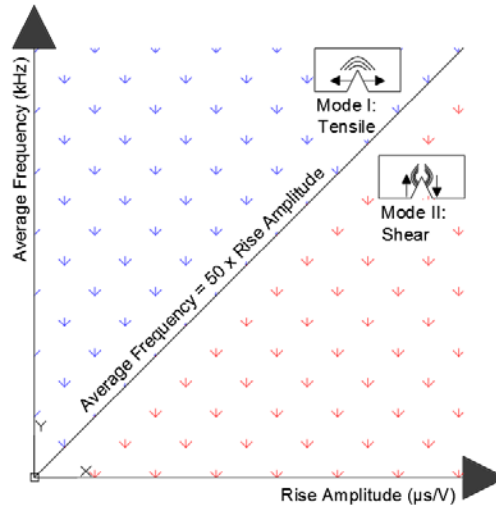


Figure 4-5. Identification of failure mode using acoustic emission parameters

4.2.3 Force-Displacement Curves

The force-displacement curves describe the response of the mortar specimens to cyclic loading and provide basis for assessing the flexural behavior and re-centering capabilities. Figure 4-6 illustrates the cyclic force-displacement curves of the four SMA fiber reinforced mortar mixtures as well as that of the control mortar. A representative specimen response is presented in Figure 4-6 for each mixture type, while the average and standard deviation results for the peak strength and residual strength are given in Figure 4-7. In Figure 4-6, the plain mortar specimen (M-Control) deflected elastically until the stress at the bottom of the beam reached its tensile strength capacity. The tensile strength of the mortar can be calculated as $0.7\sqrt{f'_c}$, where f'_c is the compressive strength of the mortar. The average compressive strength was 35 MPa for three tested cubic mortar specimens, which yielded a tensile strength of 4.1 MPa for the mortar. The specimen failed during 7th loading cycle at a displacement of 0.10 mm and a peak load of 1.47 kN. The modulus of rupture for a beam with center loading can be calculated as $\sigma_r = \frac{3PL}{2bd^2}$, where P is the applied load, L is the span length, b and d are the width and depth of specimen, respectively. For the failure load of 1.47 kN, the modulus of rupture is calculated to be 4.6 MPa, which is higher than the tensile capacity of the mortar.

The SMA fiber reinforced mortar specimens exhibited post-cracking flexural strength, i.e., residual strength, indicating a ductile failure pattern. The residual strength observed in the specimens with 0.3% of fiber volume ratio (M-SMA-1 and M-SMA-2) followed a deflection softening behavior, i.e., the residual strength had a lower ultimate peak force than the first-peak force. The specimen with 0.3% of 20 mm long SMA fibers (M-SMA-1) attained its peak force of 1.58 kN during the 9th loading cycle at a displacement of 0.30 mm. The flexural strength of the beam decreased significantly for the subsequent loading cycles due to cracking. After concrete cracking, only SMA fibers carry the tensile loads at the bottom of the specimen. During subsequent loading cycles, the load on the SMA fibers increased and SMA fibers exhibited superelastic transformations, which produce re-centering and crack recovery effects as will be discussed later. With further loading, the pull-out of the fiber occurred. The test was terminated after cycle 13.

Similarly, the ultimate strength for the specimen with 0.3% of 30 mm long SMA fibers (M-SMA-2) was reached during the 8th loading cycle at a displacement of 0.53 mm and an ultimate force of 1.72 kN. The residual strength of the M-SMA-2 specimen was 97% higher than that of M-SMA-1 in the cycles following post-peak strength. The specimen with 0.5% of 30 mm long SMA fibers (M-SMA-3) kept its ultimate strength level at almost the same level as the first peak strength at the 12th cycle. The first-peak force for the M-SMA-3 specimen was 1.72kN that occurred during the 8th loading cycle at a displacement of 0.53 mm. M-SMA-3 exhibited an ultimate strength at the 13th cycle of 1.75 kN. The specimens with 1.0% of 30-mm SMA fibers (M-SMA-4) exhibited a deflection hardening behavior, i.e., displaying higher post-cracking residual strength than the first-peak strength. The increase in residual strength as compared to the first-peak strength was 26% on average for the three M-SMA-4 specimens. The loading procedure consisted of a total of 13 cycles for all specimens but both the M-SMA-3 and M-SMA-4 reached higher strength at subsequent loadings. All of the SMA-fiber reinforced specimens exhibited a post-cracking residual strength with a minimum of 17% of its first-peak strength for the M-SMA-1 specimens and a maximum of 126% of its first-peak strength for the M-SMA-4 specimens as shown in Figure 4-6.

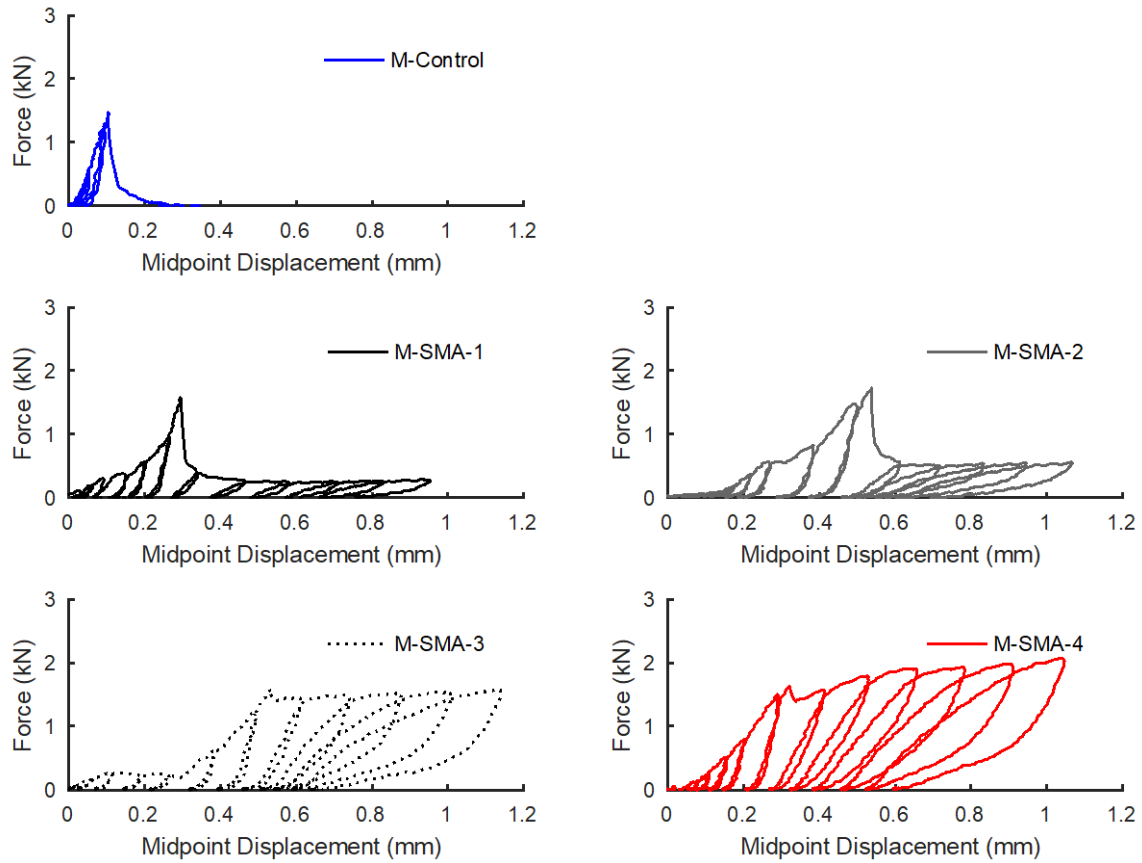


Figure 4-6. Cyclic force-displacement curves for mortar specimens

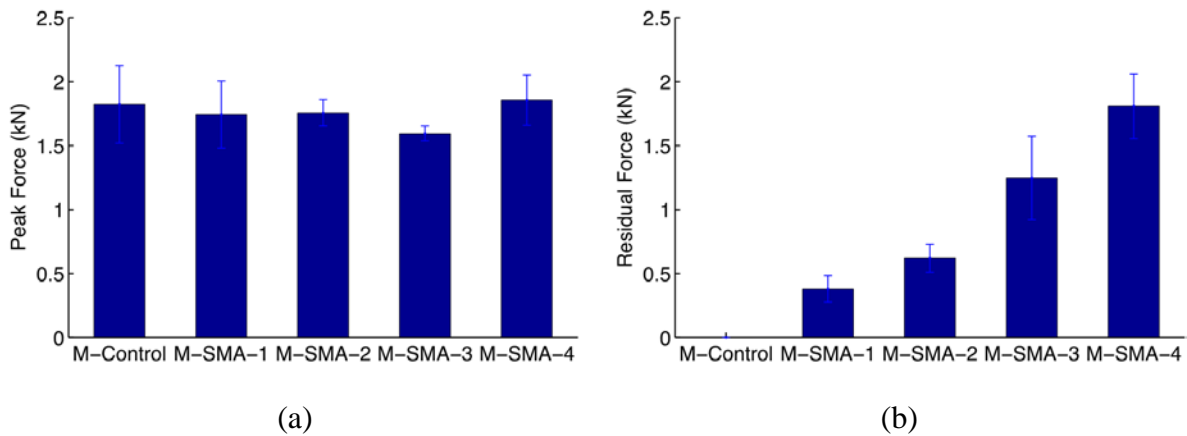


Figure 4-7. Average strength of mortar specimens (a) peak strength; and (b) residual strength

4.2.4 Re-Centering Capabilities

The midspan displacement of the specimens was monitored during the cyclic tests. The average deflections at the end of loading and unloading cycles for each mixture type are plotted in Figure 4-8. Figure 4-8 also illustrates the re-centering ratio for each cycle, which is defined as:

$$R = \frac{D_{max} - D_{residual}}{D_{max}} \quad (5)$$

where D_{max} is the maximum displacement for each loading cycle and $D_{residual}$ is the residual displacement at the end of each loading cycle. It is observed that the SMA-fiber reinforced specimens had a minimum of 26% recovery at the end of each cycle. After several initial elastic cycles, residual deflections started to occur in the specimens. However, the SMA-fiber reinforced specimens recovered most of their deformations occurred at a given loading cycle at large displacement amplitudes. This can be attributed to the superelastic strains developed in the SMA fibers. The M-SMA-2, M-SMA-3 and M-SMA-4 displayed approximately stable re-centering capabilities after cycle 4; while for the M-SMA-1 specimens, the re-centering ratio gradually decreased with the increase of the number of cycles. That might be due to the shorter SMA fiber lengths in M-SMA-1 specimens, which may have induced large unrecoverable strains in the SMA fibers at larger deformation levels.

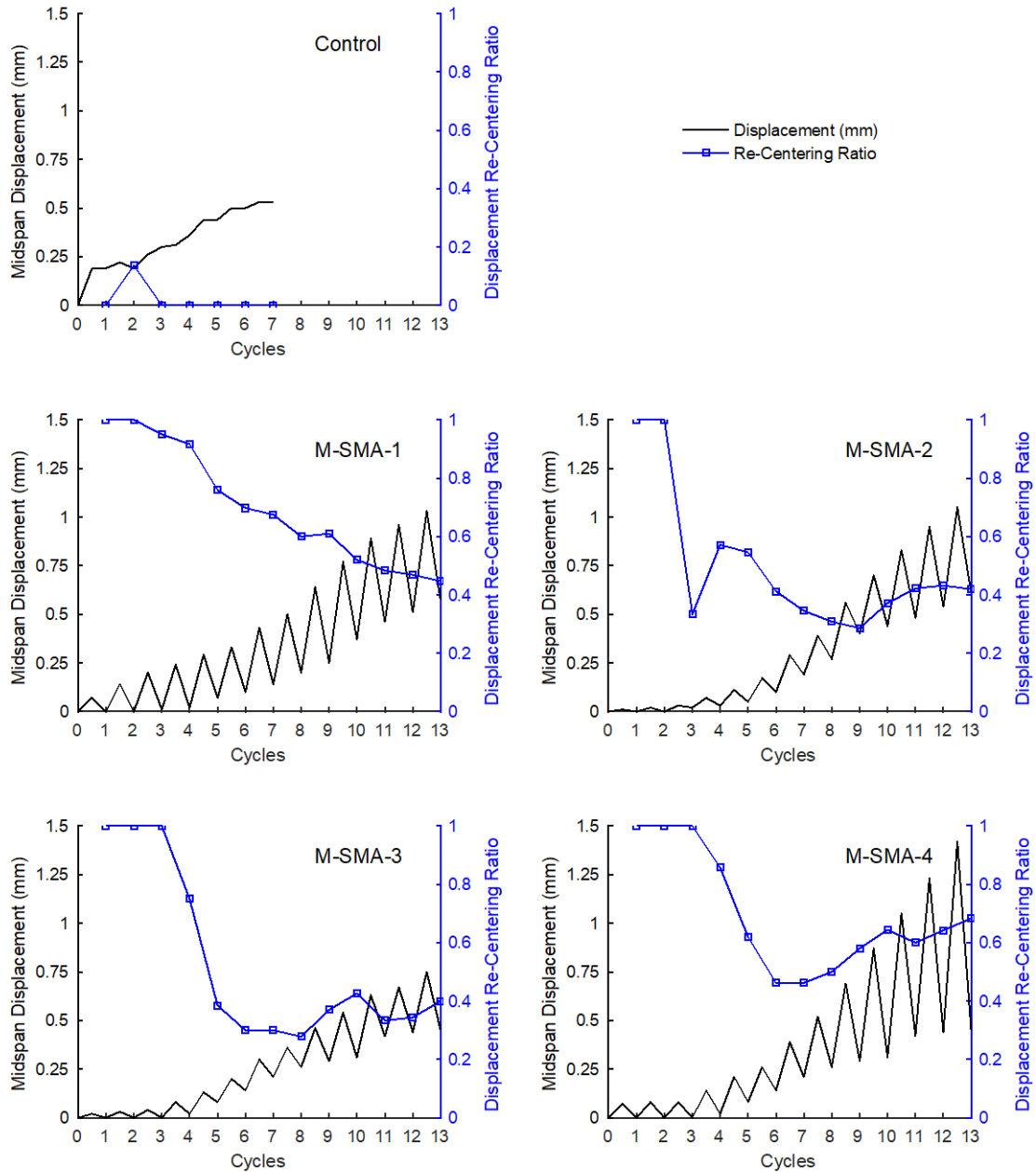


Figure 4-8. Mid-span displacement history and recovery ratio for mortar specimens

The re-centering capabilities of SMA fiber reinforced mortars are presented in Figure 4-9. It shows the force-displacement curves for the last two loading cycles (cycles 12 and 13) for the SMA fiber reinforced mortar specimens with 0.5% (M-SMA-3) and 1% fiber (M-SMA-4) volume ratios. It can be seen that the M-SMA-3 specimen recovered 0.42 mm and 0.50 mm deformations for the last two cycles upon unloading. The residual displacement was only 0.05 mm for both loading cycle. Similarly, the M-SMA-4 experienced 0.38 mm and 0.52 mm mid-span displacements in the last two cycles and recovered most of these deformations (0.32 mm and 0.45 mm, respectively) upon unloading.

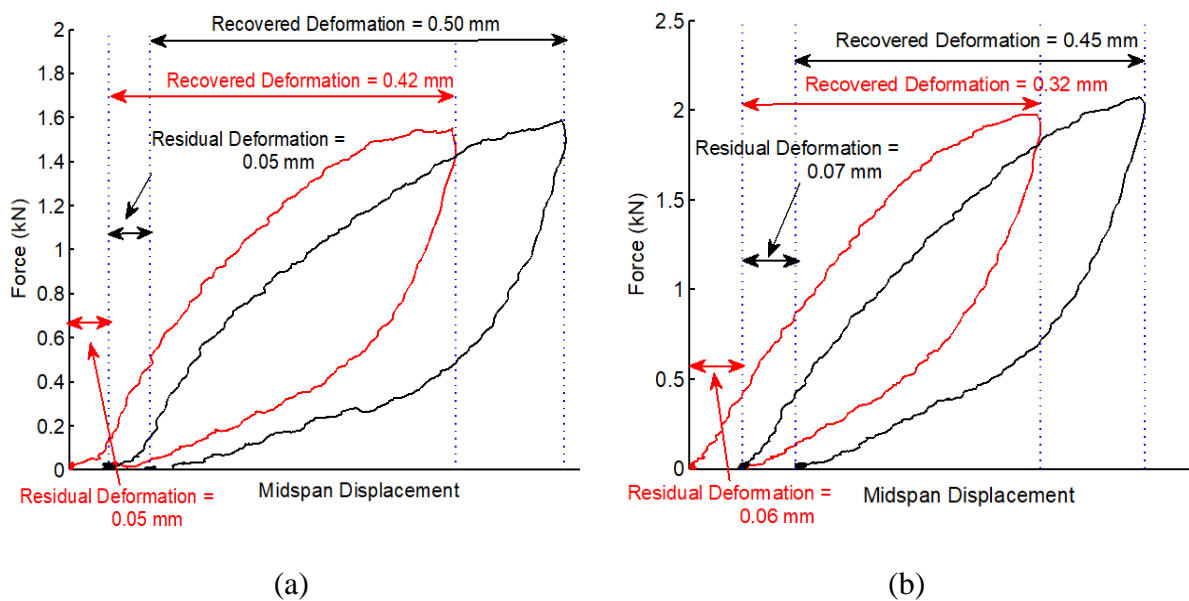


Figure 4-9. Force-displacement curves for the last two cycles for (a) M-SMA-3; and (b) M-SMA-4

4.2.5 Crack Recovery

DIC was used to monitor the strain evolution and crack width propagation in the mortar specimens. Figure 4-10 illustrates the evolution of the longitudinal strain contours for the SMA fiber reinforced mortar specimens at four stages of the test: (a) at the first crack, (b) at the peak load, (c) at the peak load of the last loading cycle, and (d) at the end of the testing procedure (i.e. after the unloading of the last cycle). It can be seen that the M-SMA-1 specimen experienced larger and more widely distributed strains at each phase of the loading as compared to other SMA fiber reinforced specimens. At the peak load of the last (13th) cycle (c), the strain distribution across the

M-SMA-1 specimen was the highest, followed by the M-SMA-3, M-SMA-2, and M-SMA-4, respectively.

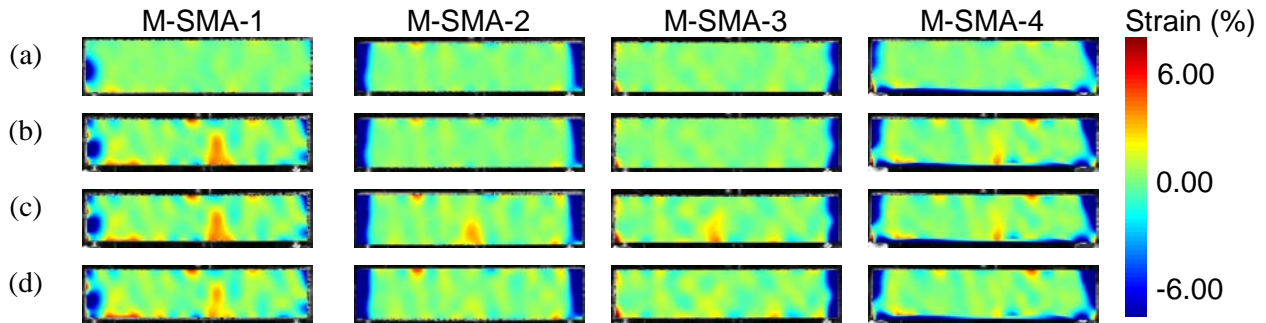


Figure 4-10. Full-field strain measurement of SMA fiber reinforced mortar with 2D-DIC (a) at the first cracking; (b) at the peak load; (c) at the peak load of the 13th cycle; and (d) at the end of the cyclic loading protocol

Figure 4-11 shows the average crack propagation history and crack recovery ratio (i.e. the ratio of the crack width at the end of the cycle to the maximum crack width during the same cycle) for various mortar mixture types. All specimens experienced one main crack. It can be seen that no crack recovery occurred in the control mortar while the SMA-fiber reinforced mortar specimens showed crack-closing capability at large displacement levels (i.e. after the 7th cycle). The largest average crack width during overall cyclic procedure was observed for the M-SMA-3 specimens with a value of 6.4 mm. However, the M-SMA-3 specimens showed about 30% crack recovery and possessed a crack width of 4.7 mm at the end of last loading cycle. The largest average crack width at the end of cyclic procedure was observed in the M-SMA-1 specimens, while the smallest crack width was observed in the M-SMA-2 specimens. M-SMA-1 and M-SMA-2 specimens experienced average crack widths of 5.2 mm and 3.3 mm, respectively at the end of 13th cycle. The M-SMA-2 specimens also had the highest crack recovery percentage, with a maximum of 36% at the last cycle. When all cycles are considered, the M-SMA-4 specimens experienced the smallest cracks at the peak loading of each cycle as compared to other SMA-fiber reinforced specimens. They also had an average crack recovery ratio between 20% and 28% after the 7th cycle.

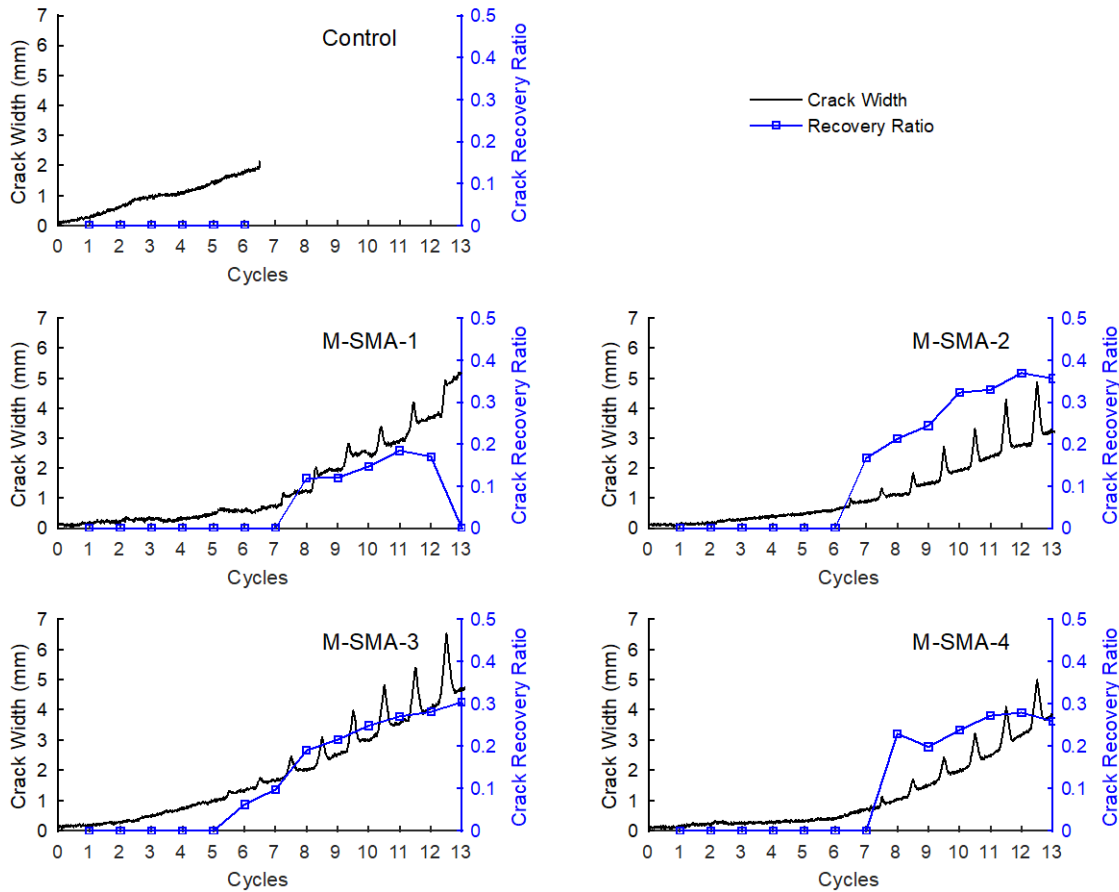


Figure 4-11. Crack width history and crack recovery ratio for mortar specimens

4.2.6 Energy Dissipation Capacity

Energy dissipation per individual cycle and the cumulative of accumulated energy dissipation for SMA fiber reinforced specimens after each cycle were computed. The dissipated energy at each individual cycle for different SMA fiber reinforced mixtures is illustrated in Figure 4-12a, while the cumulative energy dissipation after each cycle is shown in Figure 4-12b. Specimens with 0.3% of SMA fibers dissipated energy at each cycle until the specimens reached their ultimate strength. The peak dissipated energy was 80.4 J and 141.4 J for the M-SMA-1 and M-SMA-2 specimens, respectively. A significant decrease is observed in the dissipated energy for the cycles after the peak strength cycle as the residual flexural strength of these specimens are considerably lower than that of the first-peak strength. On the other hand, for the specimens with 0.5% and 1.0% SMA fibers, the energy dissipation constantly increased with the increase of loading cycles. This can be attributed to the deflection hardening behavior observed in these specimens. The M-SMA-

3 and M-SMA-4 specimens showed a maximum energy dissipation of 351.2 J and 390.4 J, respectively.

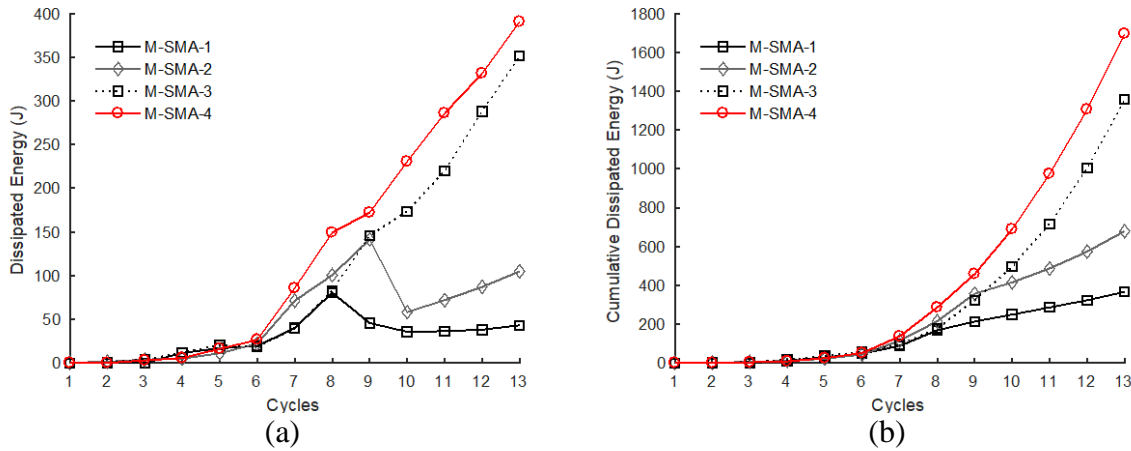


Figure 4-12. (a) Energy dissipation per individual cycle; and (b) cumulative energy dissipation after each cycle for SMA fiber-reinforced mortar specimens

4.2.7 Acoustic Emissions Analysis

The distribution of acoustic events as a function of average frequency was calculated for each mortar mixture and shown in Figure 4-13a for each individual cycle (except the first cycle). In addition, Figure 4-13b illustrates the distribution profile of average frequency for all 13 cycles for fiber reinforced specimens and for the first seven cycles for the control specimen as it failed during cycle 7. Although SMA fiber reinforced mortar specimens have different fiber contents, the general shape of the average frequency profiles was similar for all fiber reinforced mortar specimens as well as the control specimen. However, a slight decrease in the peak AF (which corresponds to the maximum number of events) can be observed with the addition of fibers. The acoustic events due to micro-cracking or fiber pull-out occur at relatively lower average frequencies. That might be the reason of a slight decrease in peak AF in fiber reinforced specimens. In addition, it can be noticed that mortar specimens with higher SMA fiber volume ratios have more acoustic events at the full spectrum of frequency. The increase in acoustic events in the specimens is related to the fiber volume ratio content. For the specimens with 0.3% fiber volume ratio, the specimen with 20-mm long SMA fibers had more fibers than that with 30-mm long SMA fibers. However, more acoustic events are observed in the specimen with 30-mm long SMA fibers. This might be due to better crack-closing behavior (i.e. more acoustic event during unloading) observed in the specimens with longer fibers as can be seen in Figure 4-11.

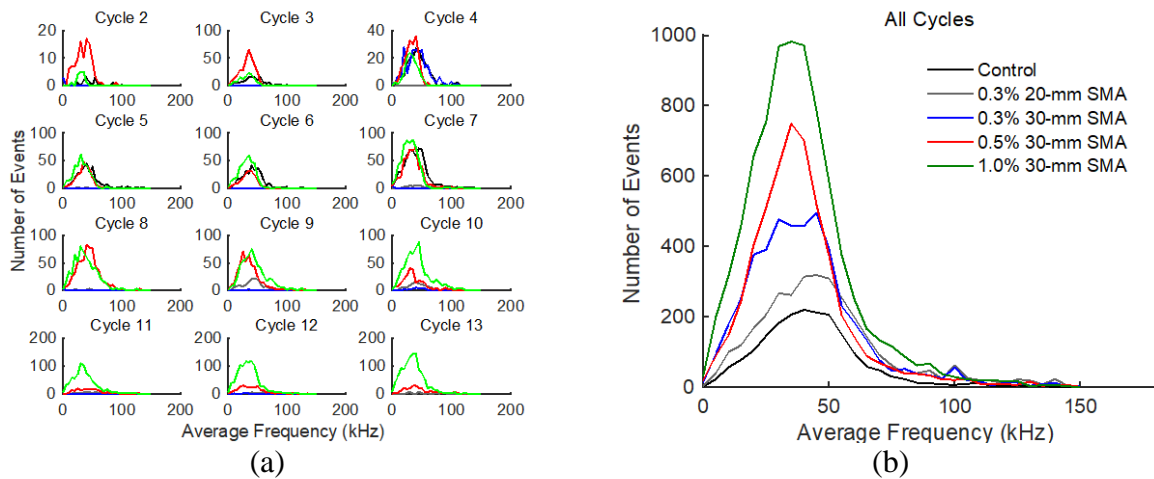


Figure 4-13. Average frequency distribution of acoustic events for different mortar specimens: (a) individual loading cycles, and (b) complete loading protocol

The events in terms of duration of the AE signal are plotted for each cycle in Figure 4-14 for the control specimen and SMA fiber reinforced specimen with 1.0% fiber volume ratio. Although the results are presented only for the SMA fiber reinforced specimens with 1.0% fiber volume ratio, similar observations were made for the other SMA fiber reinforced mortar specimens. The duration plots for the control specimen show minimal acoustic events at the unloading phase, indicating a limited degradation in the mortar matrix during unloading. On the other hand, for the SMA fiber reinforced specimen, there is an increase in the number of events occurring during the unloading phase after cycle 7, becoming similar to those during the loading phase at cycles 12 and 13. This can be attributed to the crack-closure mechanism observed in the SMA fiber reinforced mortar upon unloading. As discussed above, no crack recovery was observed in the control mortar while the SMA-fiber reinforced mortar specimens exhibited crack-closing capability after cycle 7.

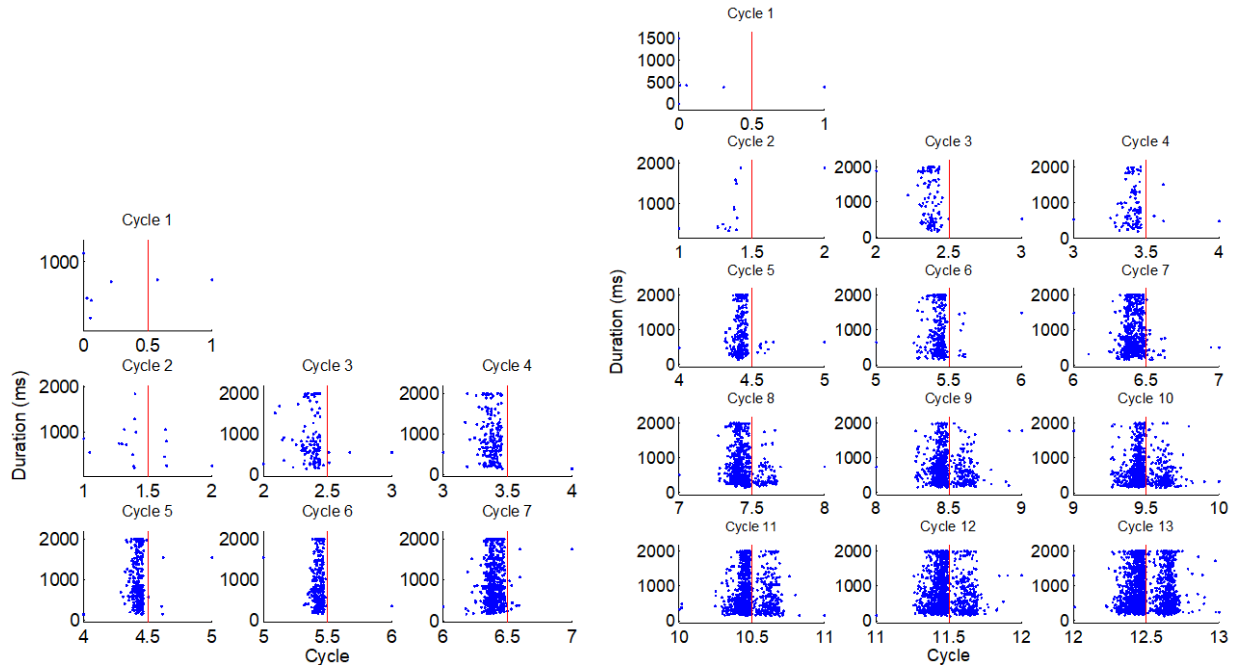


Figure 4-14. Acoustic emissions durations for (a) control specimen, and (b) fiber reinforced mortar specimen with 1.0% SMA fibers

To further investigate this finding, the energy content of the acoustic events in both control and SMA fiber reinforced mortar specimens were analyzed. Figure 4-15 illustrates the evolution of cumulative energy at each loading-unloading cycle in the control specimen and specimen with 1.0% of SMA fibers. The released energy was significantly lower in the early cycles as compared to the later cycles for both specimens, since an increasing displacement testing protocol was implemented. For the control specimen, the cumulative energy rapidly increases when the load gets close to its peak value (i.e. the mid-point of the cycle) and then remains mostly constant during the unloading for a given cycle. The increase in the cumulative energy at the peak load can be attributed to cracking in the mortar matrix. A similar cumulative energy response can be seen for the SMA fiber reinforced mortar specimen up to cycle 7. However, starting from cycle 8, an increase in cumulative energy was observed during the unloading segments of each cycle (i.e. second half of the cycle). The presence of acoustic events in the unloading phase can be attributed to the shape recovery of SMA fibers and closure of cracks.

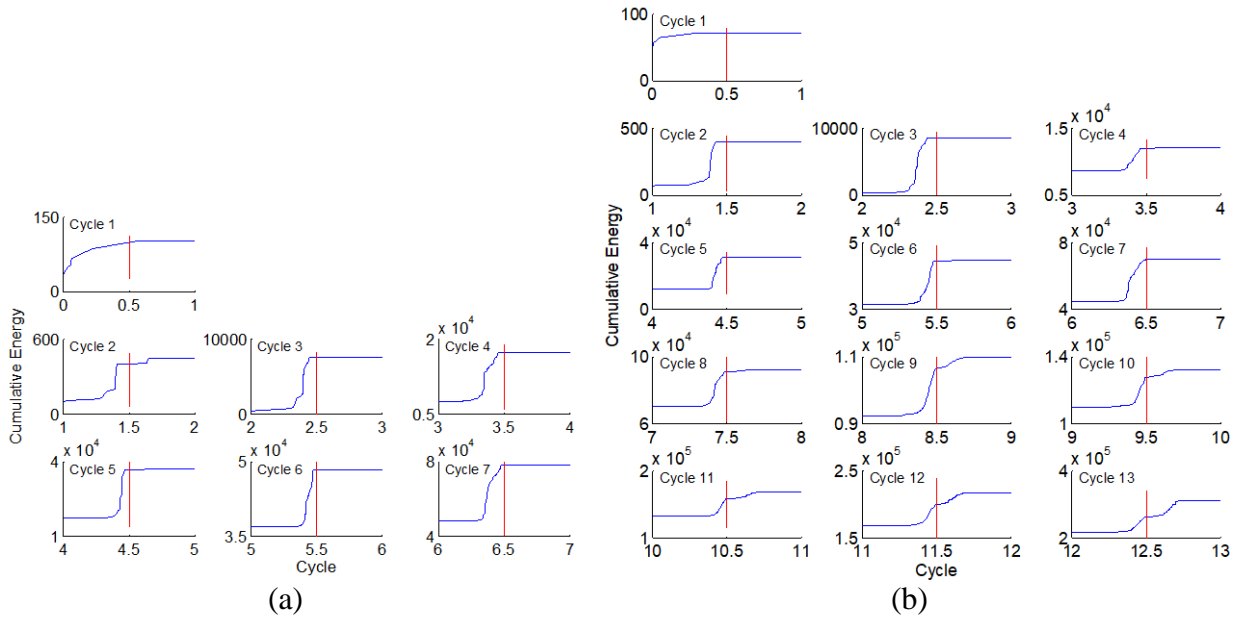
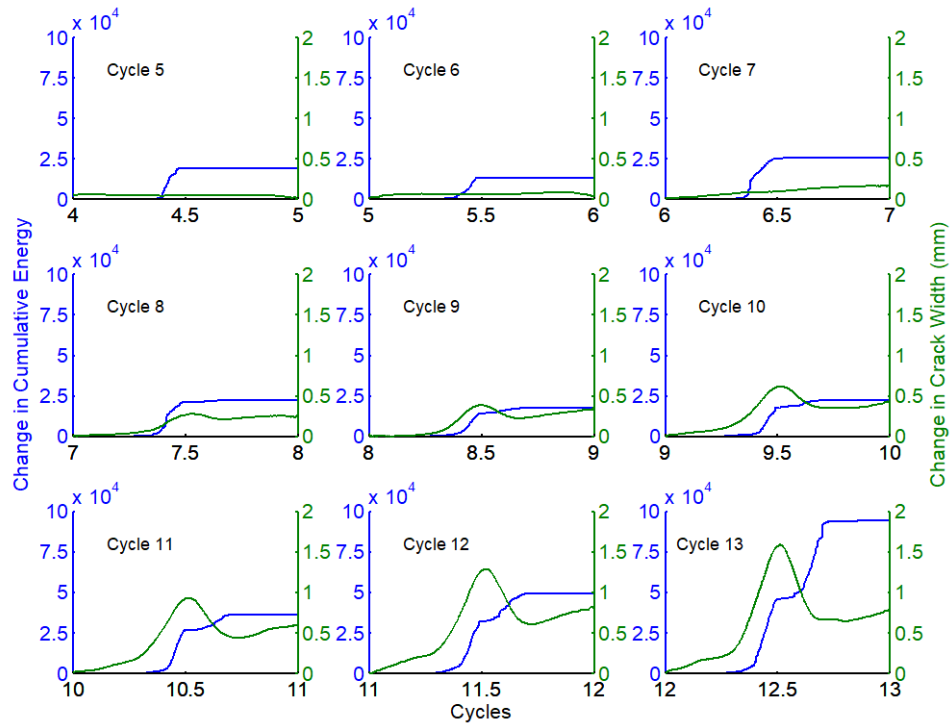
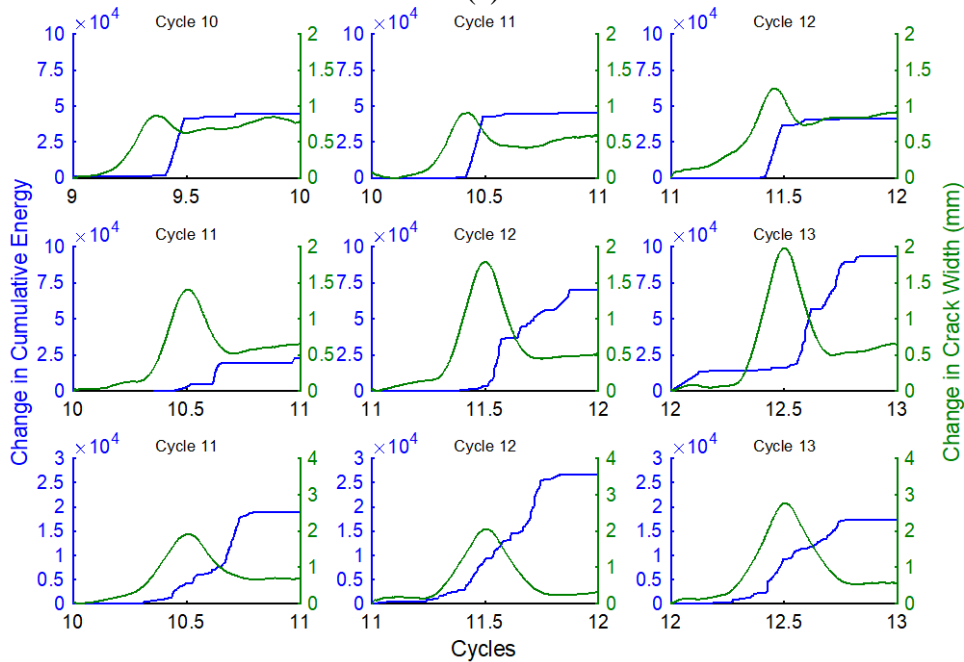


Figure 4-15. Cumulative energy evolution for (a) control specimen, and (b) fiber reinforced mortar specimen with 1.0% SMA fibers

The relation between the increase in energy and crack width propagation was investigated. Figure 4-16a illustrates the changes in cumulative energy and crack width for cycles 5 to 13 for the SMA fiber reinforced mortar with 1.0% fiber volume ratio. For early cycles (cycles 5 to 7), the cumulative energy suddenly increased as the load reached its peak value (midpoint of the cycle) and remained almost constant during unloading. There was no considerable increase in the crack width during these cycles. For the later cycles, there was a visible increase in the crack width profile at the midpoint of the cycle, which was also associated with an increase in the cumulative energy. However, crack recovery was observed upon unloading, especially in later cycles (cycles 10 to 13). The crack recovery was accompanied by an increase in cumulative energy, the end of which corresponds to a flattening cumulative energy profile. Therefore, the increase in the energy profile during the unloading can be attributed to the re-centering behavior of SMA fibers and closing of the cracks. Similar profiles were observed for the other fiber reinforced mortar specimens. Figure 4-16b illustrates the change in cumulative energy correlated to the change in crack width for the last 3 cycles for the specimens with 0.3% and 0.5% SMA fiber volume ratios. It should be noted that stronger correlation between the change in cumulative energy and crack width was observed for the specimens with higher SMA fiber volume ratio.



(a)



(b)

Figure 4-16. Changes in cumulative energy and crack width for (a) specimen with 1.0% of 30 mm SMA fibers for cycles 5 to 13, and (b) specimens with 0.3% of 20 mm, 0.3% of 30 mm and 0.5% of 30 mm long SMA fibers for the last three cycles

Finally, the moving average of 30 acoustic events (in terms of hits and average frequency) was computed and plotted together with crack width history in Fig. 12, for both the control specimen and the SMA fiber reinforced specimen with 1.0% fiber volume ratio. The moving average could not be computed for the first two cycles due to the limited amount of acoustic events at these cycles. For the control specimen, the number of AE hits increased suddenly at the midpoint of each cycle, where the displacement reached its peak value. The increase in the AF at the same points indicates a tensile mode of cracks, i.e., matrix cracking. With the progression of loading cycles, the crack width increased and the specimen failed at cycle 7. For the SMA fiber reinforced mortar, it can be seen that the largest number of hits occurred when the main crack was formed during cycle 8, accompanied by a sudden increase in AF at the peak load, indicating matrix cracking (tensile mode). Similar increases in the AF were observed around the peak deflection at cycles 9 and 10, followed by decreasing AF when the load reached its peak value. A decrease in AF was also observed during the loading portions of cycles 11, 12 and 13. These decreases in AF likely indicate fiber friction and pull-out events, which are representative of shear failure mode.

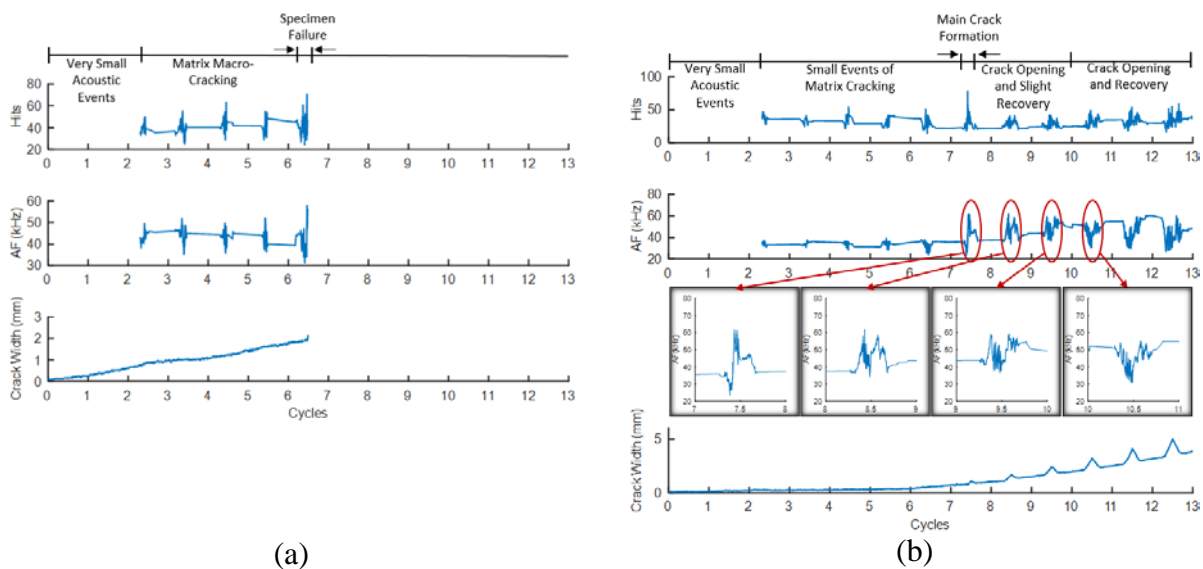


Figure 4-17. Moving average of hits and average frequency as well as crack width history for (a) control specimen, and (b) fiber reinforced mortar specimen with 1.0% SMA fibers

Figure 4-18 shows the moving average of AF during unloading portion of the cycles for control and SMA fiber reinforced specimens with 1% fiber volume ratio. For the SMA fiber reinforced specimen, the crack width history was also plotted in Figure 4-18. It can be seen that the AF remained almost constant during unloading for the control specimen as well as SMA fiber reinforced specimen until cycle 8. However, for the later cycles, the AF increased during early portions of unloading, where crack width reduction was also seen. The increase in AF indicates a tensile mode event, meaning matrix crack recovery. The crack width history plot confirms this finding.

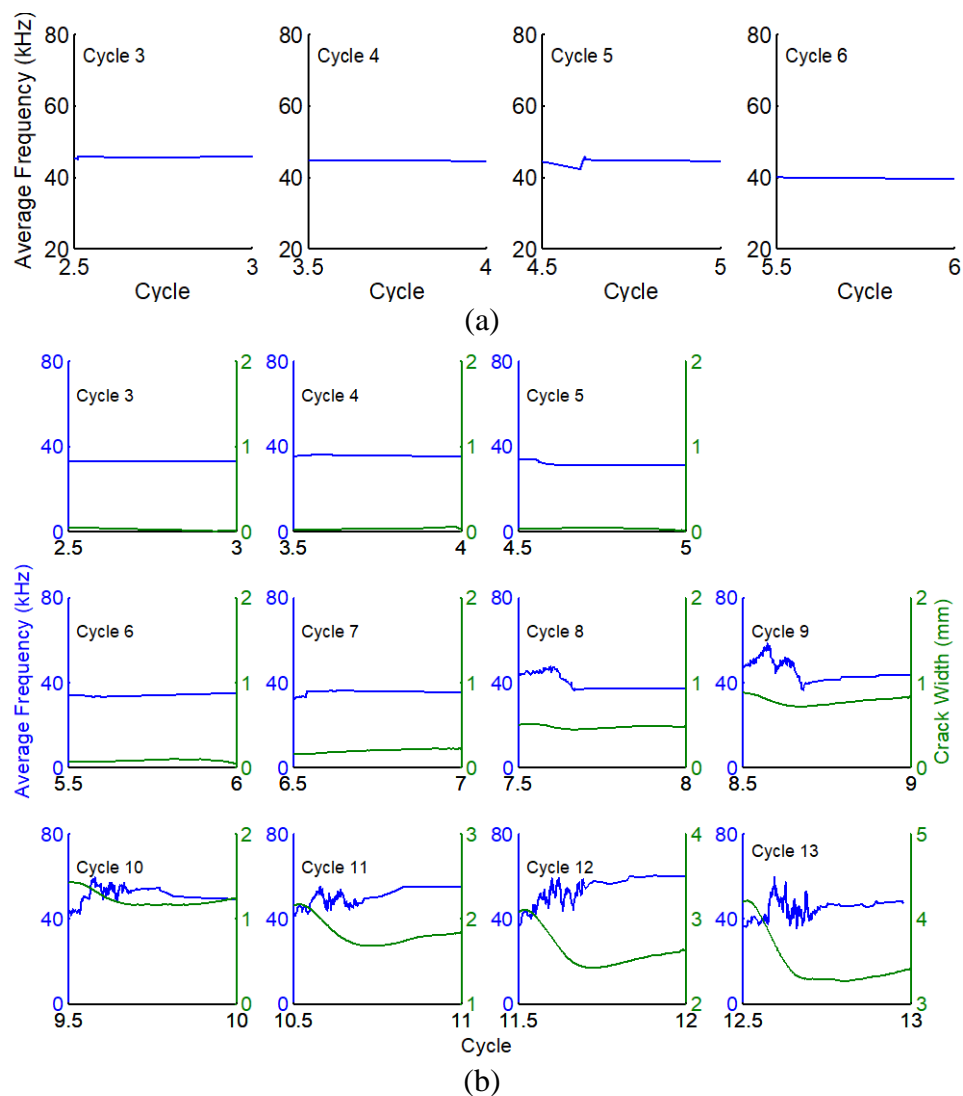


Figure 4-18. Moving average of average frequencies during unloading for (a) control specimen, and (b) alongside with crack width history for fiber reinforced mortar specimen with 1.0% SMA fibers

4.3 Hybrid Fiber Reinforced Concrete

4.3.1 Material and Specimen Preparation

The concrete mixture was designed using a water to cement ratio (w/c) of 0.48, a fine aggregate to cement ratio of 2.50, and a coarse aggregate to cement ratio of 2.64. The cement used in all concrete mixture was ordinary Portland cement (ASTM Type I/II). The coarse aggregate consisted of 12.7 mm of nominal maximum size, and natural sand with a fineness modulus of 2.9 was used as fine aggregates. A high-range water-reducing admixture and an air-entraining agent that are in conformance with ASTM standards were used to achieve the desired workability and fresh concrete properties. Steel and NiTi superelastic SMA fibers were randomly distributed in the concrete mixture. Commercially available Dramix 5D steel fibers, with a diameter of 0.90 mm, a length of 60 mm and an aspect ratio of 65, were used as steel fiber reinforcement. The steel fibers had a tensile strength of 2,300 MPa, a yield strength of 2,100 MPa, an elastic modulus of 210,000 MPa and ductility of 6.0%. Roughened superelastic NiTi alloy fibers with a diameter of 0.58 mm and a length of 60 mm were used as SMA fibers. The NiTi wire had a tensile strength of 1,070 MPa at 10.0% total elongation with an elastic modulus of 75,000 MPa. The forward transformation stress was 380 MPa at 2.0% strain.

Preliminary work with steel fiber reinforced concrete indicated that a 0.60% fiber volume ratio is critical to achieve high strength and deflection hardening behavior. To investigate the effect of SMA fibers on the flexural behavior of concrete specimens, the fiber volume ratio was set as 0.60% for all the mixtures. Fiber reinforced concrete was casted into prismatic specimens with dimensions of 76×76×292 mm. Five different fiber volume ratios were used to evaluate the SMA fiber performance in flexural testing. A plain concrete specimen without fibers (C-Control) was prepared as a control specimen. C-Steel mixture included only steel fibers with 0.60% of fiber volume ratio, while C-SMA included SMA fibers with 0.60% of fiber volume ratio. Two hybrid fiber reinforced concrete specimens with a total of 0.60% fiber volume ratio were casted with a combination of steel and SMA fibers. C-Hybrid-1 had 0.45% of steel and 0.15% SMA fiber, while C-Hybrid-2 had 0.30% of steel and 0.30% of SMA fibers. Table 4-3 shows the constituents and the proportions of each mixture.

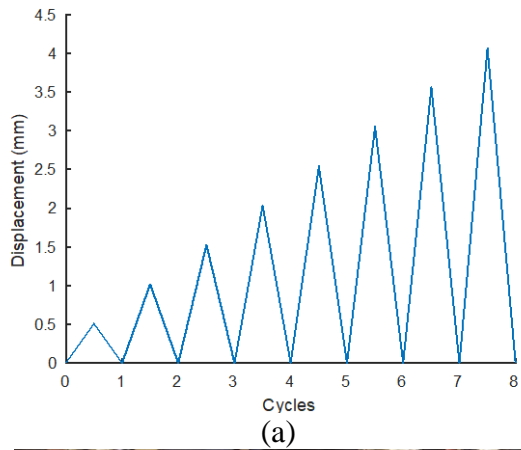
Table 4-3. Concrete Mixture Design

Mixture ID	Fly ash/ cement	Sand/ cement	Coarse aggregate/ cement	Water/ cement	Plasticizer ml/kg (oz/cwt)	Fiber volume ratio (%)	
						Steel	SMA
C-Control	0.25	2.50	2.64	0.48	2.4 (3.74)	-	-
C-Steel	0.25	2.50	2.64	0.48	2.4 (3.74)	0.60	-
C-Hybrid-1	0.25	2.50	2.64	0.48	2.4 (3.74)	0.45	0.15
C-Hybrid-2	0.25	2.50	2.64	0.48	2.4 (3.74)	0.30	0.30
C-SMA	0.25	2.50	2.64	0.48	2.4 (3.74)	-	0.60

To prepare the specimens, all concrete ingredients, except the fibers, were mixed in a large mixer first. Using a smaller mixer, the required fiber content was then added to the base concrete material and mixed again to achieve a random distribution without any visible clumping of fibers. The samples were demolded after the first 24 hours and cured in a moisture room with a relative humidity above 95% and an air temperature of 23 ± 1 °C for 28 days before testing.

4.3.2 Test Plan and Setup

A four-point cyclic bending test, configured in displacement-control, in accordance with ASTM C1609 [344], was used to evaluate the performance of fiber-reinforced concrete specimens. The cyclic procedure included an incremental increase of 0.51 mm in displacement with a total of 8 cycles to reach a total displacement of 4.08 mm. The loading and unloading rates were both set at 0.66 mm/min under displacement control. Figure 4-19a illustrates the displacement protocol applied in the experimental testing. A 2D-DIC configuration was used to monitor crack evolution on concrete specimens. The specimens were textured with random speckle pattern using spray paint to enable DIC measurements as shown in Figure 4-19b. Figure 4-19c displays the test setup for the flexural testing of fiber reinforced concrete specimens.



(b)



(c)

Figure 4-19. (a) Concrete cyclic displacement procedure; (b) speckle pattern on the fiber reinforced concrete; and (c) test setup for concrete testing

4.3.3 Force-Displacement Curves

Figure 4-20 illustrates the cyclic force-displacement curves for each mixture. All concrete specimens deflected elastically in the first cycle without experiencing any residual displacements. C-Control (plain concrete) failed during the second loading cycle with an ultimate force of 9.2 kN. C-Steel and C-SMA reached an ultimate strength of 10.7 kN and 11.3 kN, respectively, during the second cycle. Hybrid fiber reinforced concrete specimens, C-Hybrid-1 and C-Hybrid-2, had a peak strength of 10.8 kN and 9.7 kN during the second cycle and an ultimate strength of 11.9 kN and 12.5 kN during the third cycle, respectively. All specimens exhibited a main localized crack on the tension side and some of them developed small secondary cracks.

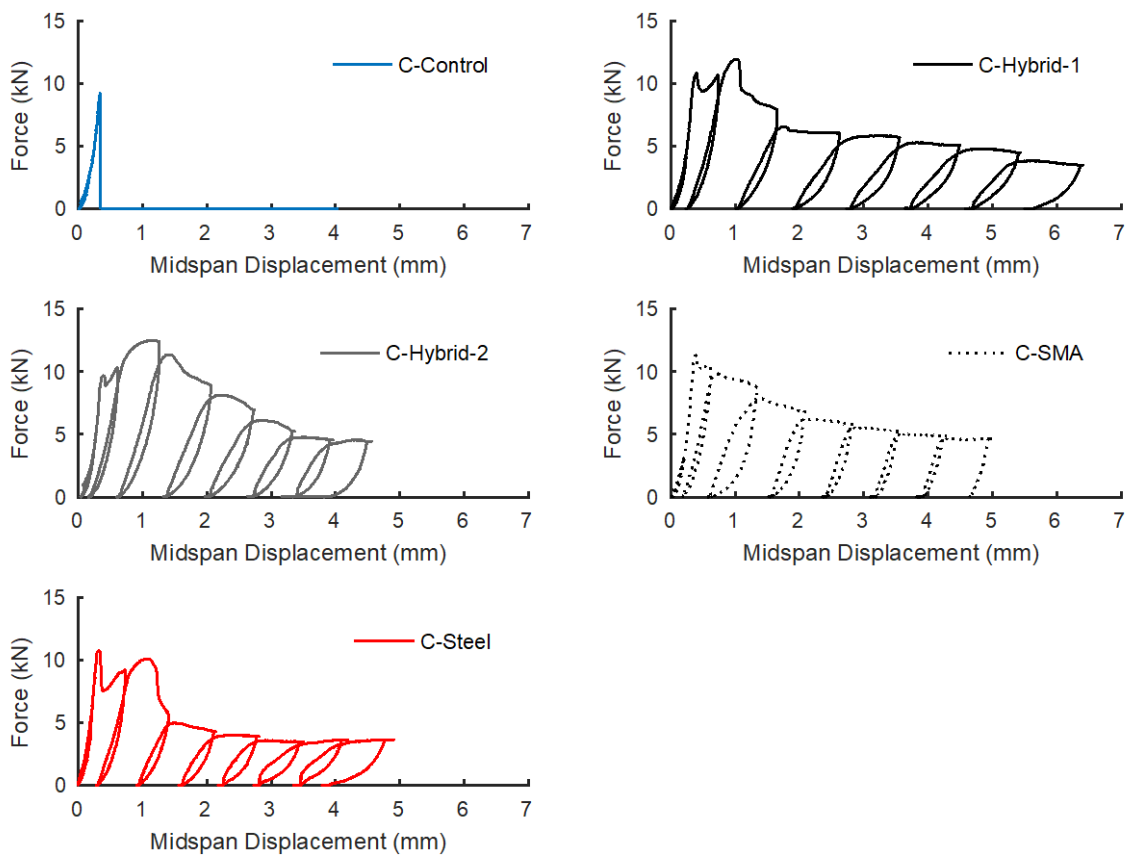


Figure 4-20. Cyclic force-displacement curves for fiber reinforced concrete specimens

Figure 4-21 summarizes the ultimate and residual strengths for the fiber reinforced concrete specimens. The addition of fibers to the concrete mix increased the flexural strength of the specimens by at least 17% (for C-Steel specimen) as compared to the plain concrete. C-Hybrid-1, C-Hybrid-2, and C-SMA specimens exhibited an increase in ultimate strength of 29%, 35%, and 22%, respectively. The C-Hybrid-2 specimen had the highest increase in load carrying capacity after the first-peak and the highest ultimate strength. At the last cycle, the C-Steel specimen exhibited a residual strength equivalent to 34% of its peak strength. On the other hand, the residual strengths were 29%, 35%, and 41% of the peak strength for the C-Hybrid-1, C-Hybrid-2, and C-SMA, respectively. C-SMA had the highest residual strength which might be attributed to the ability of SMA fibers to withstand large magnitudes of elastic strain as compared to its counterpart steel fibers.

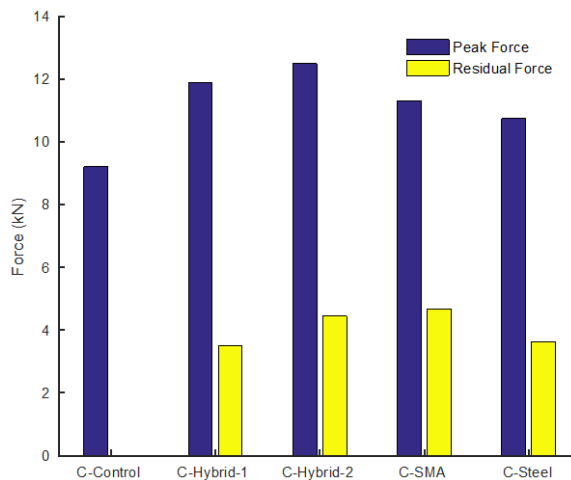


Figure 4-21. Fiber-reinforced concrete peak and residual flexural strength

4.3.4 Re-Centering

Figure 4-22 displays the mid-span displacements and re-centering ratios at the end of each loading and unloading cycles. The C-Control specimen failed during the second loading cycle at a displacement of 0.30 mm. It can be observed that the fiber reinforced concrete specimens exhibited similar behavior, with no obvious demonstration of additional re-centering capability with the use of SMA fibers. In contrast, the specimen with all SMA fibers (C-SMA) exhibited a lower average re-centering ratio as compared to all other specimens. A possible explanation for this observation is that the straight SMA fibers did not develop good bond with concrete mixture and were pulled-out when subjected to the cyclic loading.

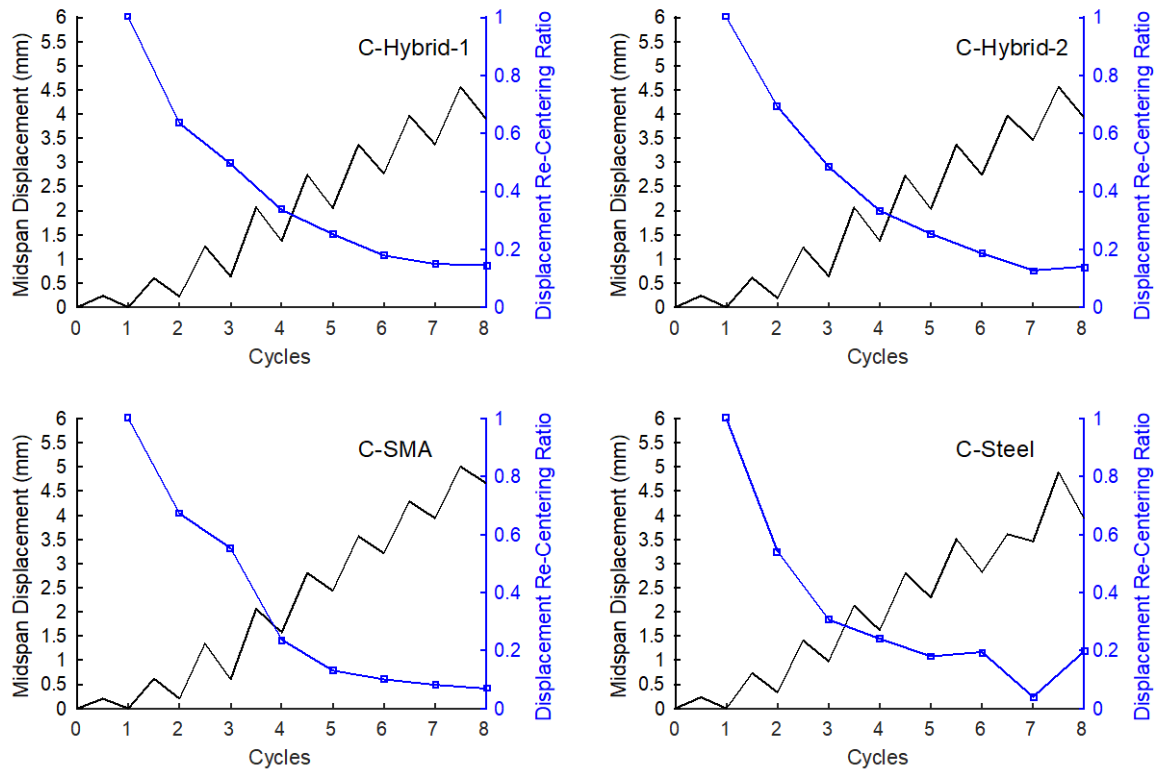


Figure 4-22. Mid-span displacement history and recovery ratio for fiber reinforced mortar specimens

4.3.5 Crack Recovery

Figure 4-23 shows the longitudinal strain contours for the fiber reinforced concrete specimens at four stages of the test; namely, (a) at the first crack during the second loading cycle, (b) at the ultimate load, (c) at the peak load of the last (eighth) loading cycle, and (d) at the end of the testing procedure. The full-field strain contours indicate that the C-Steel specimen developed the largest crack at the end of the last loading cycle as compared to the samples with SMA fibers. The specimens with SMA fibers had a smaller crack width and the crack had a sloped inclination; indicating the combination of both shear and tension failure due to the fiber distribution. C-Hybrid-2 specimen had the smallest crack slopes, indicating shear and tension failure mechanisms. Furthermore, C-Hybrid-2 specimen had multiple cracks, which facilitated the distribution of energy over multiple fracture locations, leading to a higher flexural strength by the matrix composition.

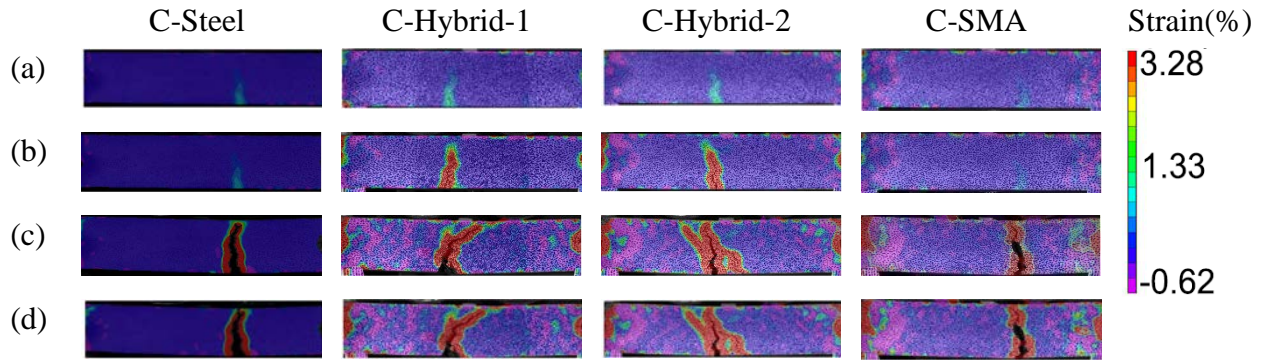


Figure 4-23. Full-field strain measurement of fiber reinforced concrete with 2D-DIC (a) at the first cracking load; (b) at the peak load; (c) at the peak load of the 8th cycle; and (d) at the end of the loading protocol

Figure 4-24 illustrates the crack width development and crack recovery ratio as a function of loading cycles. Specimens with steel fibers (only steel fiber or the combination of SMA and steel fibers) displayed a better crack width recovery as compared to C-SMA. The results indicated a poor bond behavior between the SMA fibers and the mortar matrix. The C-Steel specimen displayed the largest crack width of 8mm at the peak load point of the last loading cycle; however, a crack width recovery of about 14% was observed upon unloading, reducing the final crack width to 6.1mm. The hybrid specimens had similar crack propagation history. The average crack recovery ratios for C-Hybrid 1, C-Hybrid-2, and C-Steel specimens after cycle 4 were about 12%, 16%, and 13%, respectively. To the contrary, C-SMA displayed smaller crack width with a lower propagation rate as compared to C-Steel during the loading protocol. Similar to C-SMA, the C-Hybrid-2 had small cracks and demonstrated a crack recovery capability.

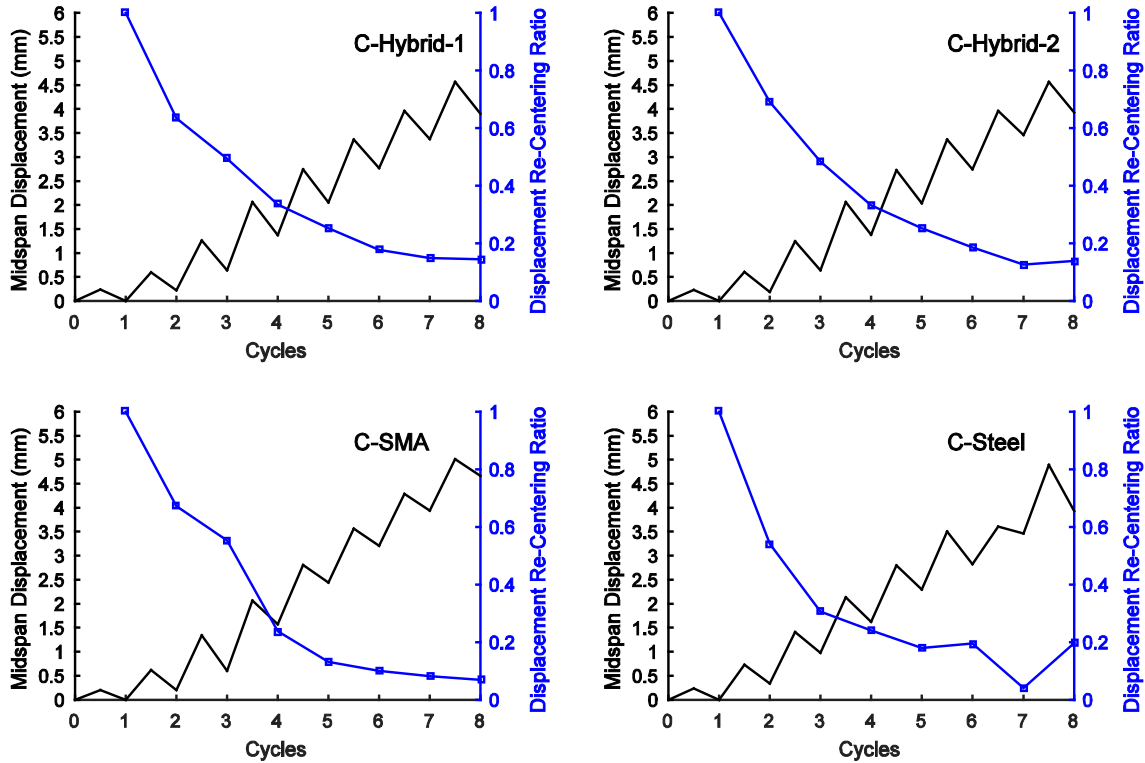


Figure 4-24. Crack width history and crack recovery ratio for mortar specimens

4.3.6 Energy Dissipation Capacity

The energy dissipation that occurred during each loading and unloading cycle for fiber reinforced concrete specimens was calculated. Figure 4-25 illustrates the dissipated energy with the cycles for each mixture. The maximum dissipated energy produced by C-Control was 1.14kJ. The fiber reinforced concrete specimens had a higher maximum energy dissipation of 6.52kJ and 7.92kJ for C-Steel and C-SMA, respectively. The hybrid fiber reinforced concrete specimens had the highest energy dissipation of 9.17 kJ and 9.55 kJ for C-Hybrid-1 and C-Hybrid-2, respectively. The C-Steel fiber reinforced concrete specimens reached a plateau of 2.87 kJ for energy dissipation after the fifth cycle. Specimens with SMA fibers had a higher energy dissipation than the specimen with only steel fibers (C-Steel) after the second cycle. C-Hybrid-1 had the highest energy dissipation with 4.43 kJ at the end of the eighth cycle. In general, the incorporation of SMA fibers increased the energy dissipation. However, the use of hybrid fibers, i.e. a mixture of SMA and steel fibers, could increase the energy dissipation at large displacements cyclic loading.

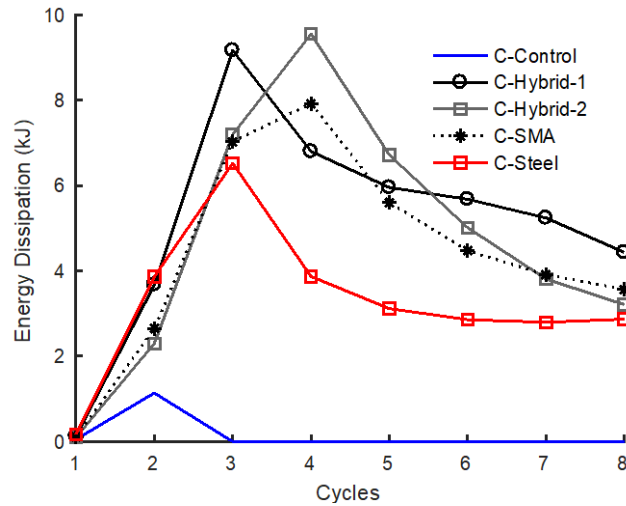


Figure 4-25. Energy dissipation per cycle for each SMA fiber-reinforced concrete specimens

4.3.7 Acoustic Emissions Analysis

The acoustic emissions signal data was acquired using two transducers placed at each end of the specimens. Parameters that define the AE signal include energy, duration, hits, and amplitude. The cumulative energy history plot can identify a loading stage of an acoustic event and its intensity. Figure 4-26a and b display the cumulative energy history for C-Control and C-Hybrid-2, respectively. For C-Control specimens, the increase of cumulative energy is visible in the loading stage only, indicating no activity during the unloading stage. However, the increase in cumulative energy is apparent for C-Hybrid specimens during the loading and unloading stages of all cycles except for the first cycle, where the increase in cumulative energy only occurs in the loading stage. Increase in cumulative energy during the unloading stages can be explained by the occurrence of crack closure, where the elastic fibers engage to apply a closing force and release acoustic energy.

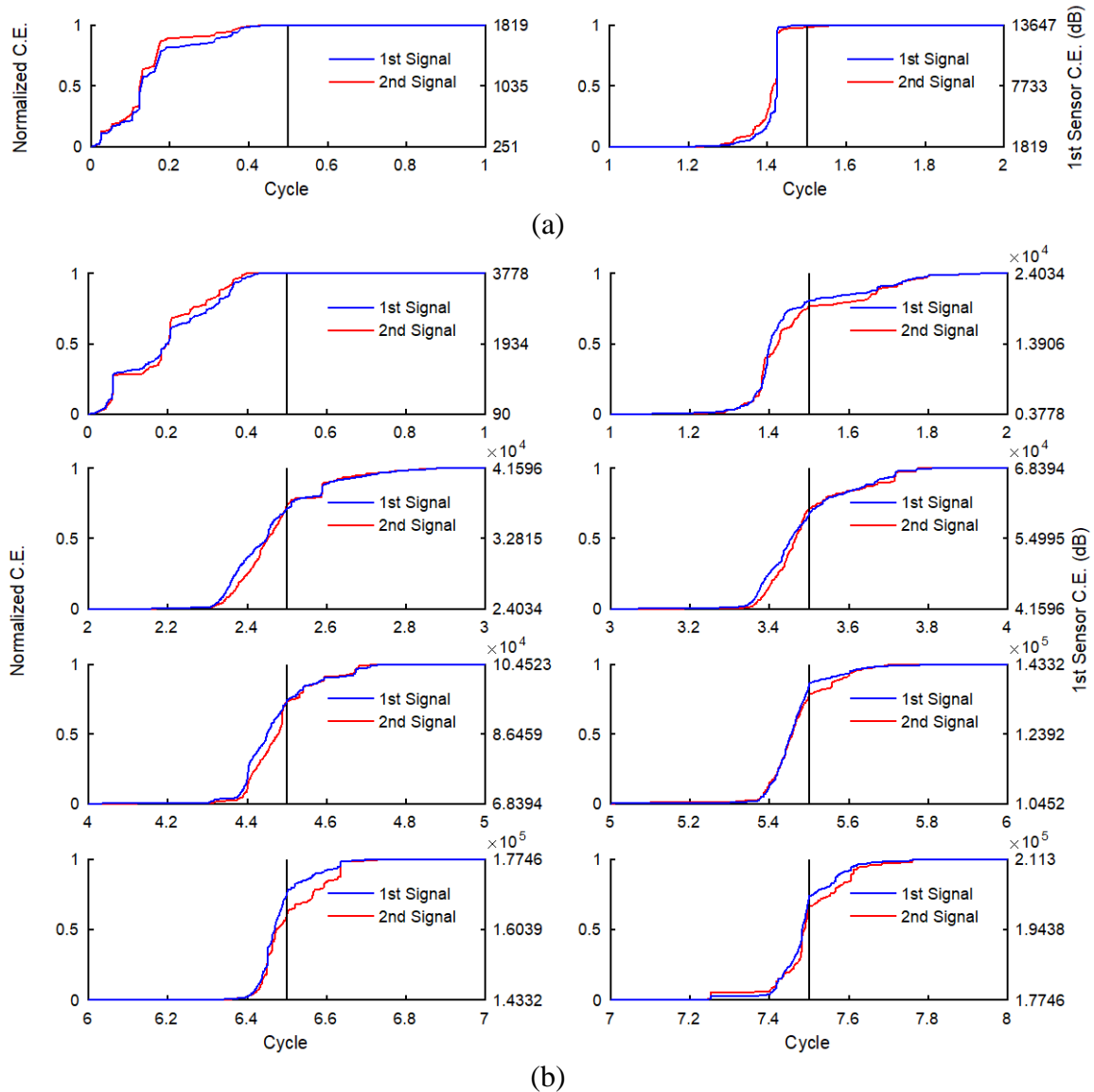


Figure 4-26. Cumulative energy evolution for (a) C-Control, and (b) C-Hybrid-2

Figure 4-27 displays the cumulative acoustic energy released by the fiber reinforced concrete as compared to the growth of the primary crack during a given cycle. The slope indicates the energy that is required to be released for a certain crack width to occur. C-Hybrid-2 had the steepest slope followed by C-Hybrid-1. This confirms the crack-width history plots as C-Hybrid-2 had the smallest crack width followed by C-Hybrid-1. C-Steel had a shallow slope, which is in agreement with the specimen having the largest crack width. In contrast, C-SMA had a small slope similar to C-Steel; while producing small crack width as compared to hybrid specimens. This can be attributed to the insignificant crack recovery exhibited by C-SMA.

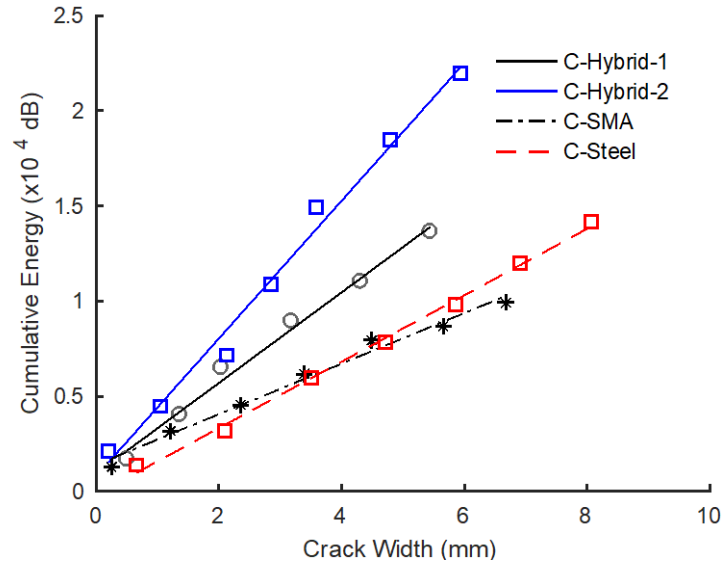


Figure 4-27. Cumulative energy as a function of crack width

In addition, the correlation between the increase in the cumulative energy monitored by acoustic emissions and the crack width growth monitored by DIC was investigated. Figure 4-28 displays the change in the cumulative energy with respect to the crack width for all cycles of the C-Hybrid-2. Cycle 1 exhibited a sudden increase in the cumulative energy as the load increased and remained constant during unloading. No cracks were initiated during the first cycle, indicating that the specimen was in the elastic region. In the later cycles (Cycles 2 through 8), cracks were initiated and their widths continued to increase and the associated cumulative energy increased. Crack recovery was observed upon unloading. Crack recovery was accompanied by an increase in cumulative energy that flattens as the crack recovery phase ends. Therefore, the increase in cumulative energy might be considered representative of crack propagation during the loading stage, and crack recovery during unloading stage.

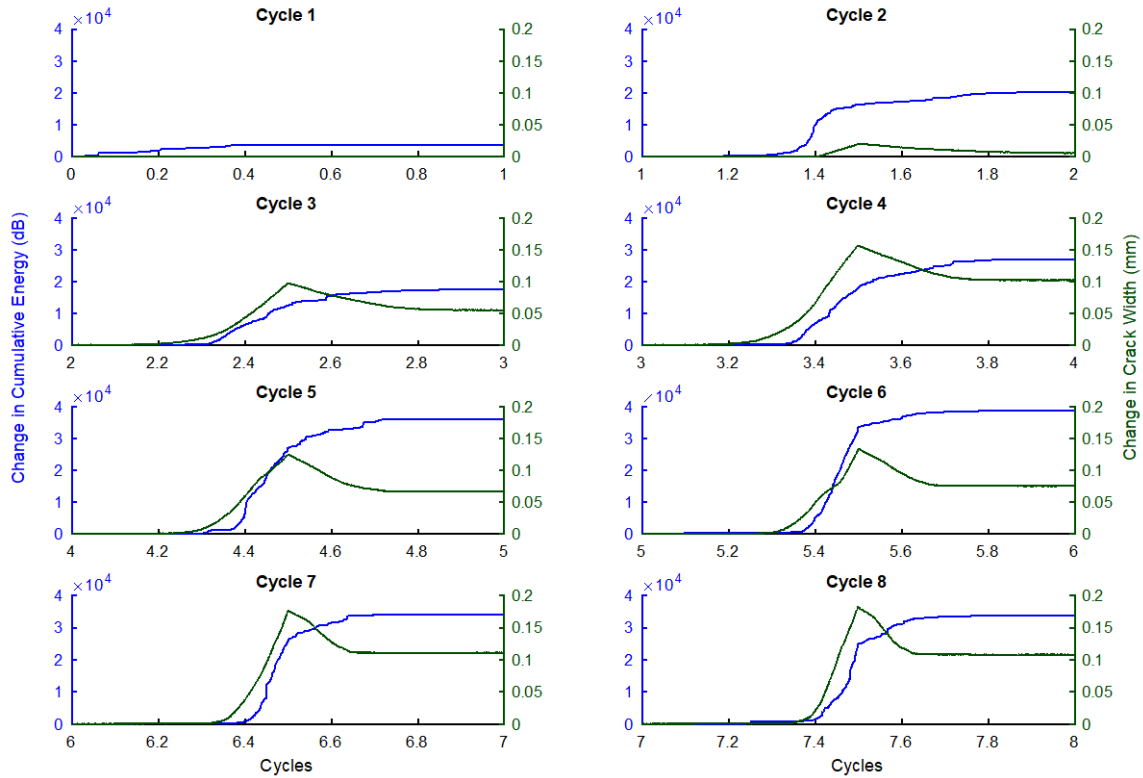


Figure 4-28. Increase in cumulative energy and crack width for C-Hybrid-2

Figure 4-29a and b display the distribution of the frequency profile of the acoustic emissions for all specimens for each individual loading cycle and for total loading protocol, respectively. The results showed that the addition of fibers to the concrete mixture have altered the frequency distribution spectrum. The frequency distribution for the C-Control was between 0-100 KHz, while the fiber reinforced concrete specimens had a frequency distribution between 0-150 KHz. The increase of the average frequency of the acoustic events is due to the increase in mode I tensile cracking (macro-cracking) which is associated with the large displacements that were applied. Overall, the fibers increased the number of events across the full frequency spectrum. However, C-Hybrid-2 clearly had a higher number of events among the fiber reinforced concrete specimens indicating better crack control and recovery, which is in agreement with the crack history data captured by the DIC.

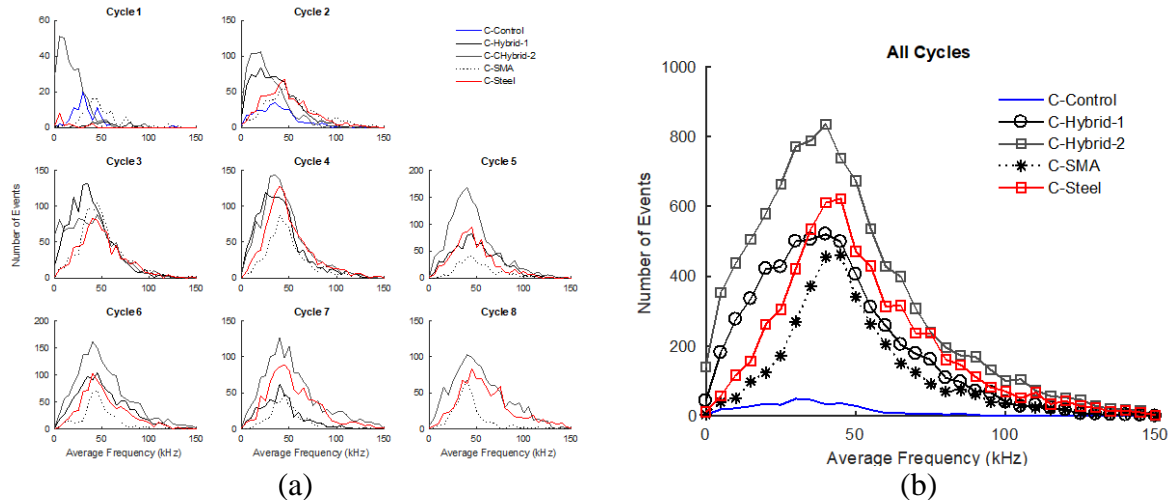


Figure 4-29. Average frequency distribution of acoustic events for different concrete specimens: (a) individual loading cycles, and (b) complete loading protocol

The correlation between the average frequency and rise amplitude of the acoustic emissions is an indicator of whether an event occurred due to shear (micro-cracking) or tensile (macro-cracking) failure. The results indicate that all specimens had a tensile dominating failure pattern during all loading cycles. The relationship between average frequency and rise amplitude for C-Hybrid-2 specimen is illustrated in Figure 4-30a as a representative sample for fiber reinforced concrete specimens under the loading portion of the last three cycles. Figure 4-30b illustrates the average frequency as a function of rise amplitude for the fiber reinforced concrete specimens for the unloading segments. The C-Control specimen exhibited minor acoustic events during unloading due to the absence of any crack recovery mechanisms. The C-SMA specimen had minor acoustic events indicating a trivial crack recovery. The C-Hybrid-2 specimen had the most acoustic emissions during unloading indicating considerable crack-recovery behavior. The same behavior was observed for C-Steel and C-Hybrid-1. However, C-Hybrid-1 and C-Hybrid-2 specimen displayed micro-crack recovery, which contributed to crack control. The results of the average frequency correlation with the rise amplitude indicated that macro-cracking was the main failure event. Furthermore, recovery of the macro-cracks for C-Hybrid-2, C-Hybrid-1 and C-Steel took place. These results were in agreement with the crack history captured by DIC.

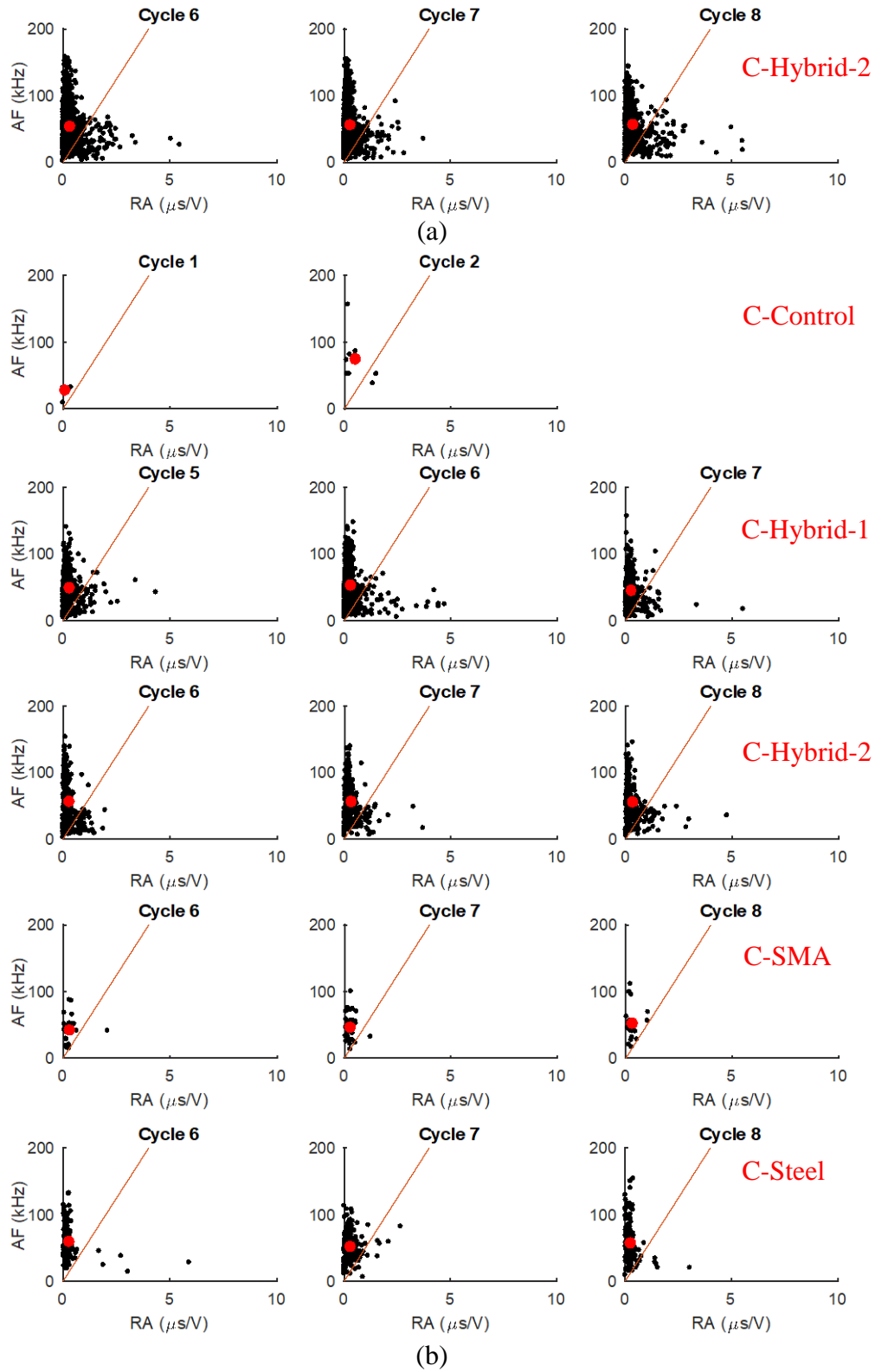


Figure 4-30. Average frequency as a function of rise amplitude during the last capture three cycles during: (a) loading, and (b) unloading

4.4 Summary

The performances of SMA-fiber reinforced mortar and concrete materials under flexural cyclic loading were investigated. For mortar composites, the SMA fibers were added at 0.3%, 0.5% and 1.0% volume ratios. For fiber reinforced concrete mixtures, the use of SMA fibers alone, as well as the hybrid use of SMA fibers together with steel fibers were considered. A fixed fiber volume ratio of 0.6% was used in all fiber reinforced concrete specimens. Flexural cyclic loading tests were conducted on both mortar and concrete beam specimens. During testing, a digital image correlation system was used to monitor the full strain and displacement fields as well as crack propagation. To better understand the behavior of the SMA fiber reinforced composites, acoustic emissions were monitored and characterized. The findings of the experimental tests can be summarized as follows:

- The addition of the SMA fibers increased the overall ductility of the mortar composites. The specimens with 1.0% SMA fibers exhibited deflection hardening behavior, with residual strength up to 26% of their peak strength. All other types of the SMA-fiber reinforced mortars exhibited deflection softening behavior.
- The specimens with 30-mm long SMA fibers showed good re-centering capability at high deformation levels. Increasing the SMA fiber volume ratio from 0.3% to 0.5% considerably improved the flexural performance and re-centering ability of the samples. However, a further increase of the SMA fiber volume ratio to 1.0% did not significantly affect the re-centering behavior. Nevertheless, the specimens with 1.0% of SMA fibers by volume exhibited the highest re-centering ratio, with a minimum of 29% for each loading cycle.
- The specimens with 1.0% of SMA fibers by volume displayed the smallest crack propagation and the highest crack recovery ratio.
- The addition of SMA fibers into concrete mixtures did not significantly improve the re-centering or crack-closing capabilities as compared to steel fiber reinforced concrete. This is attributed to the straight shape configuration of the used SMA fibers. The lack of mechanical anchorage due to hooked ends or friction resistance due to textured surface caused poor bond behavior and pull-out of the SMA fibers was observed.
- The combination of SMA and steel fibers showed potential for further investigations as the concrete specimens with the hybrid fibers had the highest increase in load carrying

capacity, the least residual mid-span displacement and the best control of crack propagation.

- Few acoustic events were observed during unloading for the control specimen and for the early loading cycles of the SMA fiber reinforced mortar specimens. However, large number of acoustic events with scattered durations were present during unloading phase of latter cycles in SMA fiber reinforced specimens.
- Cumulative energy histories showed that the energy remains constant during unloading for all loading cycles of control specimen and the early cycles (cycles 1 to 8) of SMA fiber reinforced mortar. An increase in the cumulative energy was observed in SMA fiber reinforced specimens at the latter loading cycles. It was demonstrated that the increase in energy can be correlated with crack-closure.
- The acoustic emission confirmed the experimental results obtained by the DIC and a direct correlation between the crack width propagation and the cumulative energy was established.

These results illustrated the potential of using SMAs as a fiber-reinforced mechanisms. However additional work is needed to study the performance of SMA fibers in mortar and concrete materials and determine optimum fiber geometry and fiber volume ratio. The use of SMA fibers with hooked ends or irregular or crimped surface may provide better mechanical interlock and bond to the concrete and mortar materials as compared to straight fibers. The enhanced bond between the SMA fibers and matrix will likely improve the overall performance of SMA-based cementitious composite systems.

5 Self-Post-Tensioning of Concrete Members Using SMAs

(Most of the discussions presented in this section were published in the following conference and journal papers [345-347])

5.1 Overview

This section investigates the feasibility of self-post-tensioned (SPT) concrete elements by activating the SME of NiTiNb, a class of wide-hysteresis SMAs, using the heat of hydration of grout. First, the process of self-post-tensioning with SMA tendons and the required conditions on the transformation temperatures of the SMAs were discussed. The microstructure characterization of the NiTiNb wide-hysteresis shape memory alloys was reported then. The tensile stress-induced martensitic transformations in NiTiNb SMA tendons were studied. Next, the temperature increase due to the heat of hydration of four commercially available grouts was investigated. Pull-out tests were also conducted to investigate the bond between the grout and SMA bar.

5.2 Proposed Self-Post-Tensioning Mechanism

As discussed earlier, SMAs have four characteristic temperatures at which phase transformations occur: (1) the austenite start temperature A_s , where the material starts to transform from twinned martensite to austenite, (2) austenite finish temperature A_f , where the material is completely transformed to austenite, (3) martensite start temperature M_s , where austenite begins to transform into twinned martensite, and (4) martensite finish temperature M_f , where the transformation to martensite is completed. If the temperature is below M_f , the SMA is in its twinned martensite phase. When a stress above a critical level is applied at a temperature below M_f , the twinned martensitic material converts into de-twinned martensite phase and retains this phase upon the removal of the load. It can regain its initial shape when the SMA material is heated to a temperature above A_f . Heating the material above A_f results in the formation of the austenite phase and, in the ideal case, a complete shape recovery. By a subsequent cooling, the SMA transforms to initial twinned martensite phase without any residual deformation.

During the hardening of cementitious composites, significant heat is generated due to the hydration of cement products. Numerous factors such as the type and composition of cement, the proportion of the mix, and the ambient temperature affect the heat evolution during the hydration process. In concrete structures, internal temperatures of 70 °C are not uncommon [348]. Since grout

is generally composed of very high portion of cement, temperature increases can also be observed during grouting applications. Therefore, hydration heat of grout can be used to trigger the SME of SMAs to obtain SPT concrete members. Figure 5-1 shows the process for development of the SPT concrete beams using SMAs. First, the SMA tendons, in the martensitic state, are pre-stretched. Then, concrete is poured and the SMA tendons are installed in post-tensioning ducts after concrete hardening. The void between the duct and the SMA tendons is filled with grout. Due to the heat of hydration of grout, the temperature of the SMA tendons increases, which induces the transformation of the material to austenite when the temperature is above that of the A_s . A complete transformation to austenite phase occurs when the temperature reaches the A_f . As the SMA tendons attempt to return back to their original shorter length, while being constrained at both ends, a tensile stress is produced in the tendons, causing pre-stress in the concrete beam.

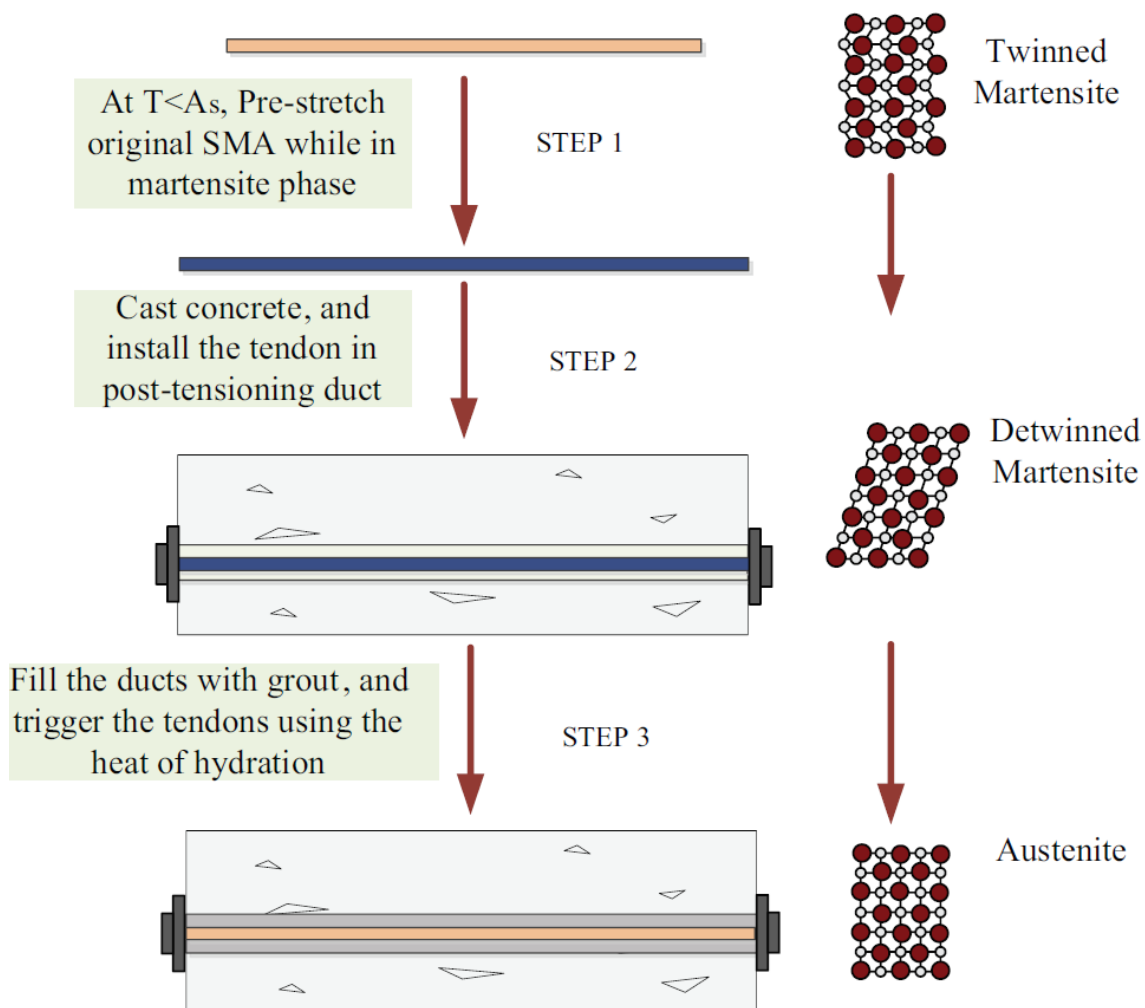


Figure 5-1. Self-post-tensioning process

The conditions on the phase transformation temperatures and the required temperature window (service temperature) for self-stressing application are shown in Figure 5-2. First, the A_s should be higher than the highest possible ambient temperature as the pre-strained SMA tendons must stay in the martensite state at ambient temperature. This will prevent pre-stretched SMA tendons from recovering their deformations at the storage temperature or during the installation of tendons to the concrete member. Second, the M_s should be below the lowest possible ambient temperature. This will ensure that the heated SMA tendons maintain their recovery stress after cooling to the ambient temperature. If the temperature of the SMA tendons becomes lower than the M_s , the SMA tendons will lose their recovery stress due to a phase transformation to martensite. This requirement for M_s coupled with the aforementioned requirement for A_s necessitates the use of the current NiTiNb class of wide-hysteresis (i.e. $\Delta T_H = A_s - M_s$) SMAs. The ternary alloying with Nb facilitates hysteresis ranges from 130 °C to 150 °C as compared to 30 °C in binary NiTi alloys [349, 350]. Furthermore, the A_f should be as close as possible to the A_s , which requires minimizing the differential $\Delta T_R = A_f - A_s$, to complete the phase transformation using the hydration heat. When the temperature rises above the A_s , the SMA tendons start to transform to austenite, and thus, recovery stresses are induced. However, the maximum recovery stress will not be obtained until the microstructure is completely austenitic, at a temperature above the A_f .

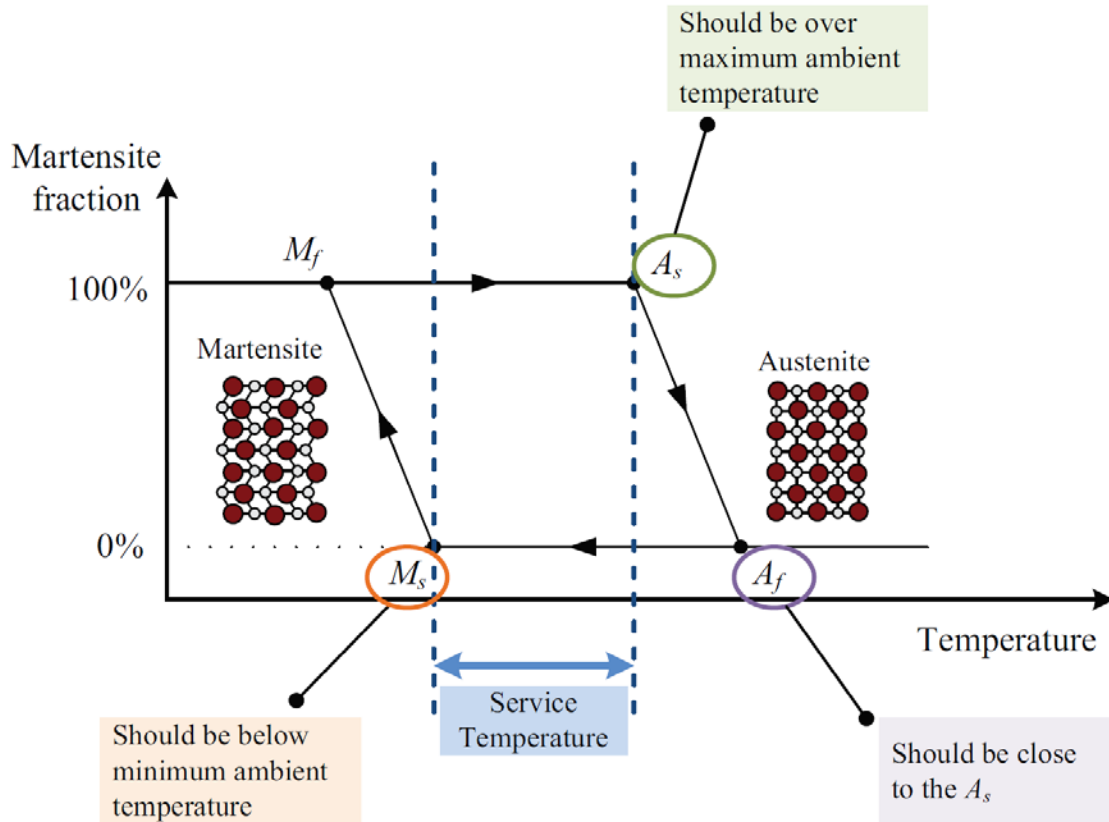


Figure 5-2. Phase transformation temperatures of SME SMAs

5.3 Materials Characterization

The phase transformation temperatures A_s and A_f and their differential $\Delta T_R = A_f - A_s$ depend on the microstructure of the NiTiNb alloy, that is, the composition and the micro-constituent morphology. The influence of Nb addition has been systematically investigated with respect to the microstructure and transformation temperatures [351, 352]. A common ternary alloy composition for widening the thermal hysteresis ($M_s - A_s$) while providing useful SME recovery behavior is Ni₄₇Ti₄₄Nb₉ (%) [353]. Tailoring the micro-constituent morphology via deformation processing is the fundamental means to control the phase transformation temperatures [352]. The alloys are typically cast and further cold- or hot-worked into final forms for practical application.

In this work, the microstructure of a cast and deformation-processed (sheet) alloy with similar compositions are reported. Atlantic Metals and Alloys LLC supplied a cast alloy with the composition of Ni_{47.3}Ti_{44.1}Nb_{8.6} (%). Medical Metals LLC supplied a deformation-processed sheet that was 6 mm wide and 0.25 mm thick with the composition of Ni_{47.7}Ti_{43.5}Nb_{8.8} (%). The compositions of both alloys are nearly equal to Ni₄₇Ti₄₄Nb₉ (%), which is the recommended ternary

composition for wide-hysteresis applications above. The grain sizes for the cast and sheet material were determined as 300 μm and 300 nm, respectively, using the Intercept Procedure from ASTM E112-12. Texture is rarely reported [355] and it is likewise beyond the scope of this work. The impact of differential thermo-mechanical processing was contrasted by studying an extruded rod material (3.45 mm diameter) provided by Memory Corporation with the composition of $\text{Ni}_{44.6}\text{Ti}_{42.8}\text{Nb}_{12.6}$ (%). Specimens for mechanical testing and microstructure analysis were wire electro-discharge machined from the rod material with an 8 mm gage length and $1.1 \times 0.5 \text{ mm}^2$ cross-section and from the sheet material with a 10 mm gage length and $3 \times 0.25 \text{ mm}^2$ cross-section.

The microstructure was characterized along with the characteristic thermally induced martensitic transformation temperatures and mechanical properties. The cast microstructure consists of a net-like arrangement of a characteristic eutectic micro-constituent encompassing a NiTiNb matrix. A scanning electron microscopy (SEM) image is shown in Figure 5-3a. The martensitic transformation occurs in the matrix regions. The as-cast microstructure is representative of the microstructure prior to thermo-mechanical processing. The SEM image in Figure 5-3b shows the typical eutectic micro-constituent, which is made up of β -Nb-rich particles and α -NiTiNb matrix [352, 356, 357]. Deformation processing breaks up the net-like structure [352, 355, 356]. The micro-constituent morphology for the sheet material is shown in Figure 5-3c. The image revealed a composite like microstructure with β -Nb-rich particles (appearing as the lighter streaks) that are elongated and discontinuous fiber-like reinforcements aligned in the primary processing direction within the NiTiNb matrix.

It is well known that the unique stabilization of martensite, which is the cornerstone of NiTiNb shape memory behavior, is attributed to the micro-constituent morphologies [355-360]. The microstructure images in Figure 5-3c and Figure 5-3d underscore differential micro-constituent morphologies that resulted from different thermo-mechanical processing done by the different companies, which showed the sheet and rod materials, respectively. The images revealed a composite-like microstructure with β -Nb-rich particles (appearing as the lighter streaks) that were elongated and discontinuous fiber-like reinforcements aligned in the primary processing direction within the NiTiNb matrix. The area fractions of the second particles were estimated using a digital image pixel thresholding technique [361, 362], which takes advantage of the dark and light contrasts of the matrix and particles, respectively, and uses the average of several SEM images.

The particle average area fraction for the rod microstructure was 18%. Consistent with the similar compositions, the fractions for the cast and sheet materials were 10%. The average inter-particle spacing was determined from cross-sectional SEM images. For the sheet material, the inter-particle spacing was about 100 nm and it was 500 nm for the rod material. These findings conveyed a refined micro-constituent morphology for the sheet compared to the rod. Moreover, the microstructure characterization illustrated that deformation processing after castings affords the ability to tailor the microstructure, via orienting the micro-constituents and inter-particle spacing.

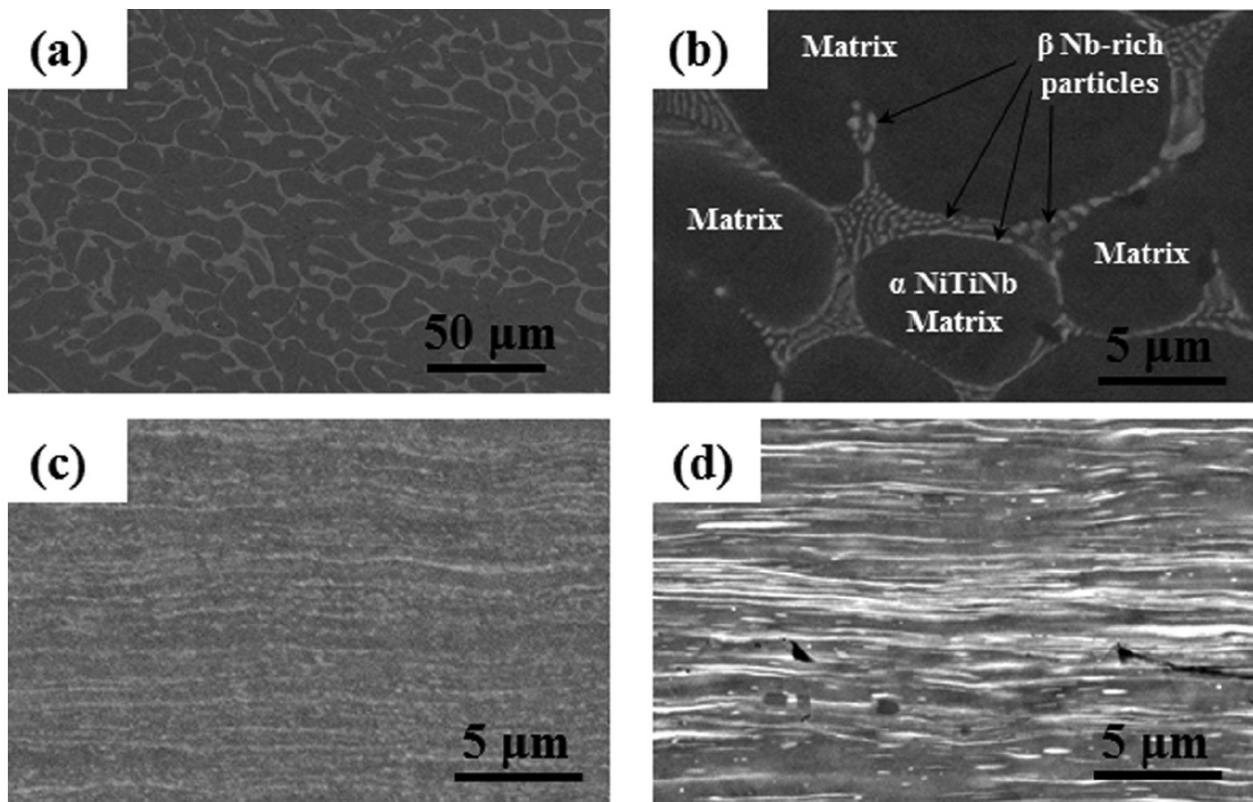


Figure 5-3. SEM images showing (a) the microstructure in a cast $\text{Ni}_{47.3}\text{Ti}_{44.1}\text{Nb}_{8.6}$ (%) alloy; (b) the micro-constituents in a cast $\text{Ni}_{47.3}\text{Ti}_{44.1}\text{Nb}_{8.6}$ (%) alloy; (c) the microstructures of the $\text{Ni}_{47.7}\text{Ti}_{43.5}\text{Nb}_{8.8}$ (%) alloy sheet; and (d) the microstructure of $\text{Ni}_{44.6}\text{Ti}_{42.8}\text{Nb}_{12.6}$ (%) alloy rod

Differential Scanning Calorimetry (DSC) analysis was carried out to determine transformation temperatures using a power compensated Perkin-Elmer DSC8500. The temperature scan rate was 40°C/min. The methodology involved the following steps: (1) heat the sample from 50°C to 100°C, (2) hold for 1 min at 100°C, (3) cool to -120°C, (4) hold at -120°C for 1 min, (5) reheat to 200°C, (6) hold at 200°C for 1 min, and (7) cool to 50°C. The transformation temperatures for the cast alloy were $M_s = -64^\circ\text{C}$, $M_f = -106^\circ\text{C}$, $A_s = -81^\circ\text{C}$, and $A_f = 11^\circ\text{C}$. For deformation processed NiTiNb

alloys, endothermic and exothermic events did not arise in DSC measurements down to liquid nitrogen temperature. Thermal cycling under constant bias load is typically employed to determine characteristic transformation temperatures for processed NiTiNb materials [360, 363]. Constant bias loads were increased from 10MPa up to a load that facilitated measurable transformation strain. Biasing with a constant stress of 150MPa revealed the thermally induced transformation. The transformation temperatures for the sheet were $M_s = -64^\circ\text{C}$, $M_f = -75^\circ\text{C}$, $A_s = -29^\circ\text{C}$, and $A_f = -6^\circ\text{C}$, and those for the rod were $M_s = -52^\circ\text{C}$, $M_f = -71^\circ\text{C}$, $A_s = -29^\circ\text{C}$, and $A_f = -1^\circ\text{C}$.

The strength properties were determined from uniaxial tension loading until failure. The stress–strain responses are shown in Figure 5-4. The uniaxial tension test for each material was determined at room temperature (23°C) with the material in the austenite state and thus the martensitic transformation is stress induced. The tests were conducted in displacement control using an equivalent strain rate of $2.0 \times 10^{-4}/\text{s}$. Strain was measured via a miniature extensometer within the gauge length and computed via DIC. The material properties are summarized in Table 5-1. The moduli for the deformation-processed materials were greater than that for the cast material. Deformation processing improved ductility and the fracture strain increased when compared to the cast material. For the cast and rolled sheet materials with similar composition, deformation processing improved the mechanical strength. The martensitic sheet exhibited higher strength properties and failure strain.

Table 5-1. Mechanical properties for the NiTiNb alloys

Composition (%)	Modulus (GPa)	Austenite Critical Stress (MPa)	Martensite Yield Stress (MPa)	Ultimate Tensile Strength (MPa)	Failure Strain
Cast Ni _{47.3} Ti _{44.1} Nb _{8.6}	63	330	-	-	9.4%
Sheet Ni _{47.7} Ti _{43.5} Nb _{8.8}	70	640	740	980	42.2%
Rod Ni _{44.6} Ti _{42.8} Nb _{12.6}	54	500	600	710	29.1%

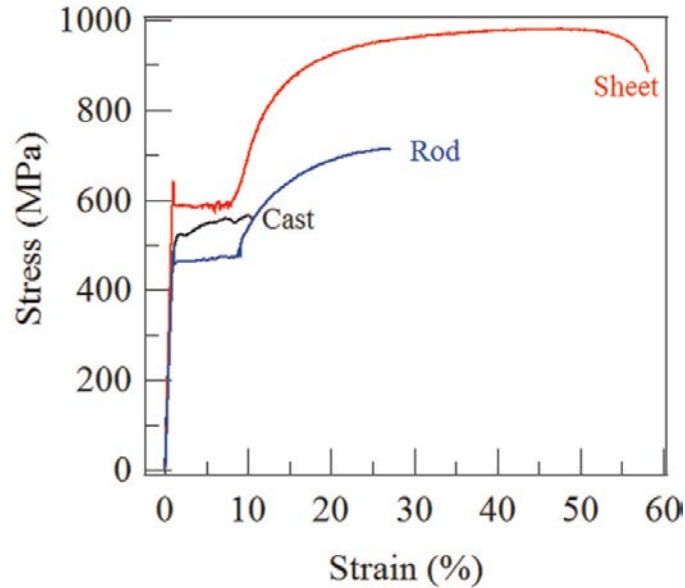


Figure 5-4. Tensile stress-strain response of the NiTiNb Alloy

5.4 Pre-Straining and Strain-Recovery

The pre-strain experiments were conducted on an MTS 810 servo-hydraulic load frame and at room temperature, which averaged about 23°C and was well above the A_f temperatures. Therefore the starting microstructure was austenitic. Pre-strain for binary NiTi SMAs is typically carried out in the martensitic state and martensite reorientation takes place rather than the stress-induced austenite-to-martensite transformation [356-358, 364]. In this work, the martensite was stress-induced, which is made possible by the Nb addition in the ternary NiTiNb SMAs. The specimens were loaded in displacement control at an average strain rate of about $2.0 \times 10^{-4}/s$ and were unloaded upon reaching the desired pre-strain level. Residual strain remained after unloading. To assess the recovery ratio of residual strain, specimens were heated at zero load (referred to as free recovery). Thermo-mechanical experiments were conducted for the current work on an MTS 810 servo-hydraulic load frame equipped with a custom thermal cycling set-up. The specimens were heated via induction heating. The temperature was measured via a thermocouple affixed to the specimen. The induction coil design minimized thermal gradients in the specimen [365]. Heating and cooling rates were controlled so that they were maintained around 10°C/min to 15°C/min. Specimens were allowed to cool in the ambient back to room temperature. Preliminary free recovery experiments were conducted on both deformation-processed material in order to assess the material response of the differential composite-like microstructures.

For the sheet and rod materials, free recovery was contrast for the pre-straining stress–strain response shown in Figure 5-5a. After unloading, there was a residual strain ε_{res} . The strain recovery began at the A_s^* temperature, Figure 5-5b. The strain saturated at a temperature A_f^* when the reverse transformation was complete. Since saturation was achieved, the reverse transformation temperature interval $\Delta T_R^* = A_f^* - A_s^*$ fully activated the SME. As shown in Figure 5-5b, not all the strain was recovered during heating and there was a permanent irrecoverable strain ε_{perm} . The strain that was recovered during heating is shown as ε_{rec}^{full} . The percentage of residual strain that was recovered via free SME recovery is defined as the recovery ratio $\varepsilon_{rec}^{full} / \varepsilon_{res} \times 100\%$. The recovery ratio was 58% for the sheet material which was higher than that of the rod with a recovery ratio of 49%. The recovery will be incomplete if the temperature was raised by a fraction of ΔT_R^* ; therefore, the material will be partially activated. In order to achieve full activation, as well as to maximize the recovery ratio, the material microstructure must be designed such that ΔT_R^* matches the heat of hydration of the grout.

The recovery behavior can be further characterized based on heating strain–temperature ($\varepsilon - T$) curves. A dotted line was drawn tangent to the curves in Figure 5-5b, demonstrating the extent of strain recovery within a select temperature range. The strains of the sheet and rod, respectively, recovered with temperatures at 0.12%/°C and 0.09%/°C. Contrasting the initial slopes, the sheet exhibited a higher recovery ratio over a smaller temperature interval, which may better match the possible heat of hydration. After the initial slope, the strain recovered gradually with a $\Delta T_R^* = 49^\circ\text{C}$ and $\Delta T_R^* = 57^\circ\text{C}$ for the sheet and rod, respectively. However, it can be seen that when the temperature was increased to 50°C, which corresponded to a 26°C increase from the pre-straining temperature, 91% and 77% of ε_{rec}^{full} were achieved for the sheet and rod, respectively. The lower temperature interval and higher recovery ratio of the sheet as compared to the rod confirm that the extent of deformation experienced by sheet material resulted in a more promising microstructure for activation via heat of hydration of the grout. Thus, understanding the microstructure property relationships can enable tailoring the eutectic micro-constituent orientation (giving rise to an apparent elongation in Figure 5-3d as compared to Figure 5-3c) and inter-particle spacing in order to tune the activation strain and ΔT_R^* . The following section focuses on stress generation during heating with a fixed displacement constraint for the sheet material, as the martensite exhibited

higher strength and fracture strain and the recovery ratio was substantial above the lower temperature interval.

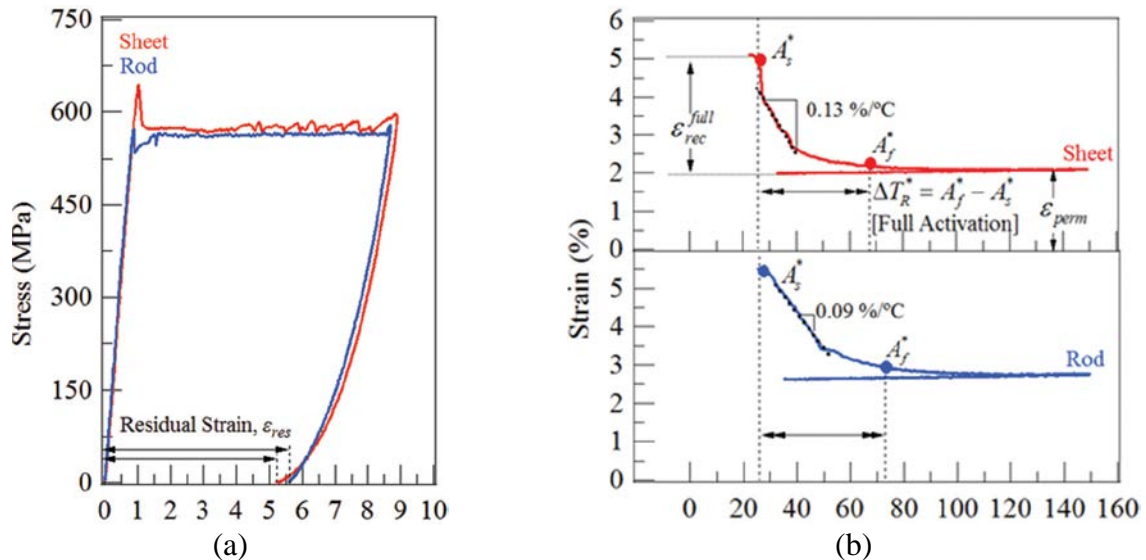


Figure 5-5. (a) Stress-strain curves for pre-straining of sheet and rod; and (b) the subsequent strain-temperature ($\epsilon - T$) response during shape memory recovery for sheet and rod materials

5.5 Assessment of Pre-Straining and Pre-Stressing

The stress-strain responses for the pre-straining of the sheet material are shown in Figure 5-6. Pre-strain levels of more than 12% are commonly suggested by Otsuka et al. [353]. In this work, pre-strain levels exceeded 12%. The pre-strain levels were 5.4%, 8.8%, 10.1%, 12.2%, and 16.1% in order to deform martensite to different extents of the stress-strain response. During loading, the curve exhibited an initial linear-elastic response was observed up to a stress peak, followed by a stress drop. Then, a stress plateau indicative of the phase transformation was observed. The evolution of the morphology depends on whether the pre-strain in Figure 5-6 is within the plateau region, at the completion of the plateau, within the linear-elastic response of martensite after the plateau, or within the strain-hardening type behavior of martensite after the elastic response. For the 5.4% pre-strain level, the microstructure was a mixture of martensite and austenite. The martensite volume fraction increased throughout the plateau and the material completely achieved the martensitic status at the 8.8% pre-strain. Beyond the plateau, the martensite deformed for the 10.1% pre-strain and the stress-strain response exhibited a linear-elastic type response. The

highest pre-strain levels (12.2% and 16.1%) were within the non-linear response and the martensite likely yielded.

Residual strain remained after unloading in Figure 5-6 and the corresponding displacement was fixed during heating which constrained SME recovery and generated recovery stresses. The stress generation experiments utilized the heating set-up described in the previous section. The displacement sensor of the MTS machine measures the change in actuator position and thus the change in length of the specimen and the grips. However, in this work it was not possible to mount an extensometer on the thin sheet specimens. Hence, the displacement was used for stable feedback that maintained the constant constraint and avoided damaging the extensometer. Note that ASTM standard E328 outlines Standard Test Methods for Stress Relaxation for Materials and Structures at constant temperature and recommends mounting an extensometer within the gage section to fix/constrain the strain [354]. Using the extensometer measurements to maintain a fixed strain constraint can fix the sample length, as the grips would be excluded from the constraint, and the impact on the results can be considered in future work. The current experiments represented the constraining conditions for pre-stressing via heat of hydration of the grout. During heating, the displacement was programmed so that it was fixed at the residual strain after pre-straining and the stress generation results are reliable for the context of the discussion in this work.

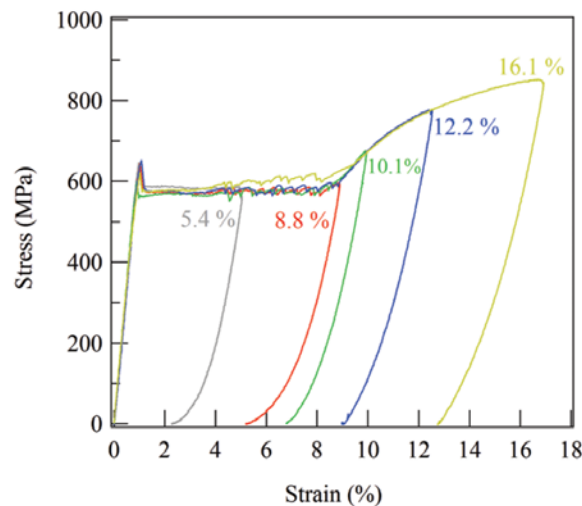


Figure 5-6. Tensile stress-strain curves for the sheet pulled to increasing pre-strain levels at room temperature

The recovery stress was plotted as it evolves throughout heating in Figure 5-7. The stress generation began at the onset of heating and thus approached the test temperature. For the lowest

pre-strain in Figure 5-7a, the recovery stress reached a maximum/peak and dropped. For the higher pre-strain levels in Figure 5-7b and Figure 5-7c, the recovery stress increased to a maximum and then decreased slightly up to the maximum temperature. The temperature at the maximum stresses generated during heating should correspond to the temperature at which Stress-Induced Martensite (SIM), which was stabilized during pre-straining deformation, recovers deformation. Note that the deformation recovery mechanism may be attributed to de-twinned SIM reverting to twinned martensite to recovery of reoriented SIM or deformation-induced martensite to the conventional reverse martensite-to-austenite transformation [350, 366, 367]; or to multiple mechanisms occurring in different volume fractions of martensitic material. Hence, in Figure 5-7, that temperature was designated as A_f^{**} (associated with constrained residual strain recovery). Recovery stresses reaching maximum values during heating have been observed for NiTiNb and a Fe-based SMA [356, 368]. For each pre-strain level, recovery stress accrues after heating is complete as the temperature decreases to room temperature. Recovery stresses increased during cooling for the Fe-based SMA [368]. The observations that the generated stress reached a maximum value during heating and that it increased during cooling merit further study beyond the scope of the current work. The findings pertinent to the pre-stressing application, which are presented later in the concluding remarks, indicate that the maximum recovery stresses were generated under constraint after straining to 12.2% and the resulting transformation temperature interval is $\Delta T_R^{**} = A_f^{**} - A_s^{**}$.

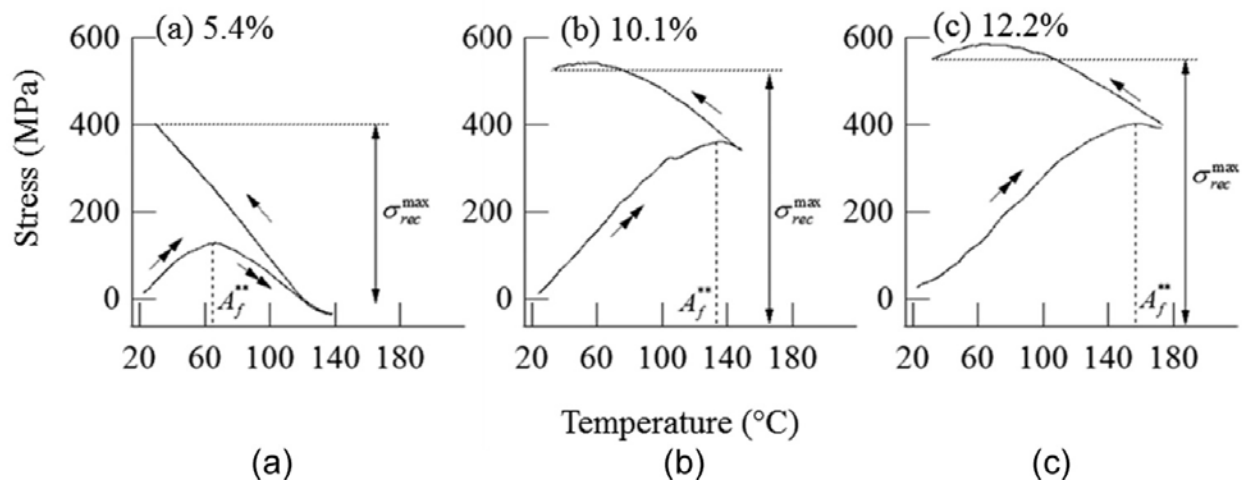


Figure 5-7. Stress-temperature response during constrained heating and cooling of specimens that have been pre-strained to (a) 5.4%; (b) 10.1%; and (c) 12.2%. The double arrows indicate heating, and the single arrows indicate cooling

5.6 Heat of hydration of grout

Portland cement and potable water along with any admixtures to obtain required properties are the basic grout materials. The chemical reaction between Portland cement and water is exothermic, i.e., producing heat. This heat is called the heat of hydration. In order to determine the temperature increase during grouting post-tensioning ducts, four commercially available tendon grouts were tested. All grouts were prepackaged and approved by Virginia Department of Transportation for post-tensioning applications. The water-to-grout ratios for each commercial grout were set per manufacturer's direction and are given in Table 5-2. To prepare test specimens with each grout, a mixing cylinder was cleaned, a bag of selected grout, and the required water were placed in the cylinder. The contents were mixed in the cylinder for 3 min with a variable speed high shear mixer and the resulting grout mixture was poured into a 102 × 203 mm (4 × 8 in) cylinder with a thermocouple attached to a single tendon placed in the center. The thermocouple was connected to a data logger that monitored the temperature of the curing grout every minute for 48h.

Time versus grout temperature plots for each specimen as well as ambient temperature are given in Figure 5-8. Three specimens were prepared and tested for Grout I and Grout II on three different days. The results for Grout I were consistent for each specimen. The highest temperature recorded during curing is 41°C, which indicated a temperature increase of 19°C - 20°C from initial temperature of 21°C - 22°C due to the heat produced by the cement hydration. The temperature of Grout II reached 48°C for two specimens and 51°C for one specimen. At three different tests of Grout II, the average temperature increase was 28°C. The peak temperature and average increase in temperature for Grout III and Grout IV were similar to the results obtained from Grout I. For Grout IV, two samples at two different water-to-grout ratios were tested. It is observed that the peak temperature is slightly higher and occurs a few hours earlier when a lower water-to-grout ratio was used as shown in Figure 5-8d. The grout temperature reached its peak value at 10 - 18h after casting for Grout I, Grout II, and Grout IV, whereas the peak temperature occurred at 2.5h after casting for Grout III. For all specimens, the grout temperature reduced to values between 22°C and 24°C near 30h after casting and remained almost constant thereafter. The results of experimental tests conducted to characterize the grout temperature during curing are summarized in Table 5-2. These results suggested that a commercially available tendon grout (Grout II) can

provide an average of 28°C increase in temperature during the hydration process, which can be used to activate SMA tendons.

Table 5-2. Summary of grout temperature test results

Specimen	Grout	Water-to-grout ratio	Initial temperature (°C)	Maximum temperature (°C)	Temperature increase (°C)
S1	Grout I	0.25	21	41	20
S2	Grout I	0.25	22	41	19
S3	Grout I	0.25	21	41	20
S4	Grout II	0.24	21	48	27
S5	Grout II	0.24	22	53	31
S6	Grout II	0.24	21	48	27
S7	Grout III	0.25	22	41	19
S8	Grout III	0.25	22	41	19
S9	Grout IV	0.27	22	41	19
S10	Grout IV	0.27	22	41	19
S11	Grout IV	0.32	22	40	18
S12	Grout IV	0.32	22	40	18

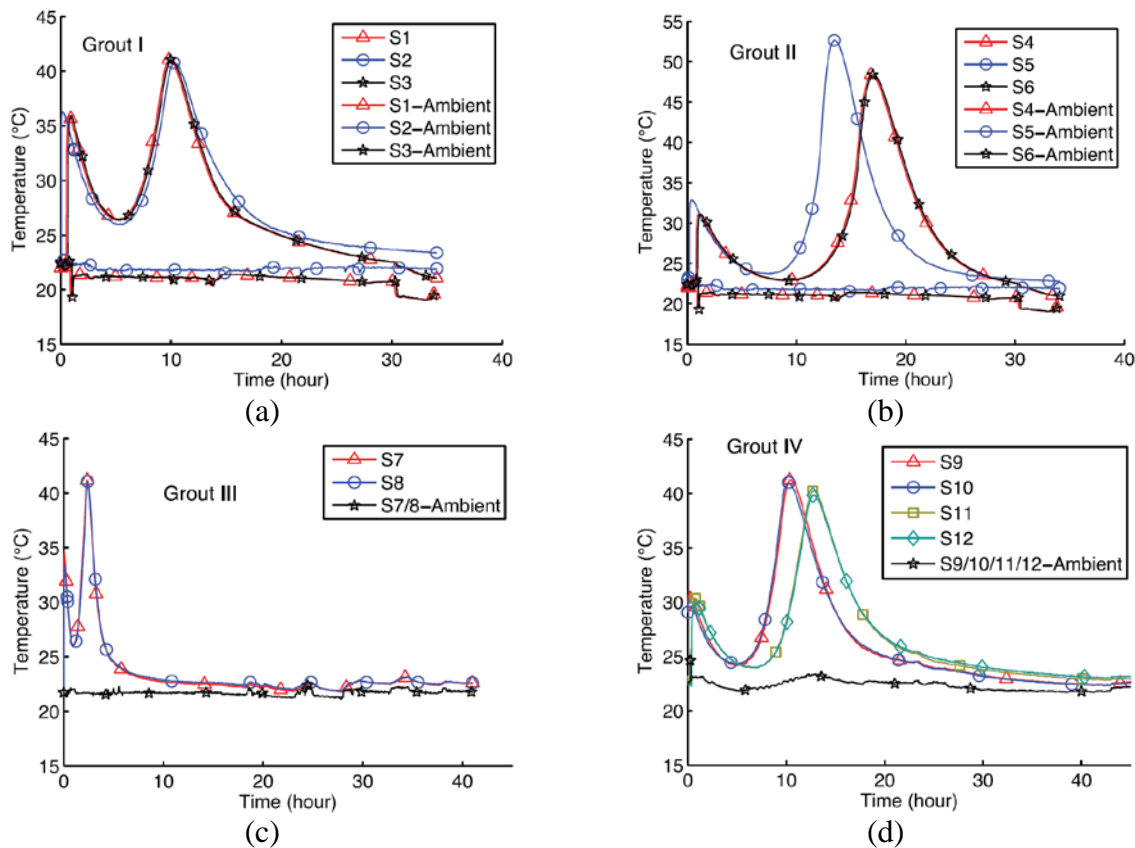


Figure 5-8. Temperature measured in different commercially available grouts during curing for: (a) Grout I; (b) Grout II; (c) Grout III; (d) Grout IV

5.7 SMA-Grout Bond Behavior

When the post-tensioning ducts are filled with grout after the tendon has been anchored at both ends, it is possible to obtain some degree of bond between the pre-stressing tendon and the concrete. The bond of pre-stressing tendon is important with regard to failure behavior, cracking, and the factor of safety. For pre-stressed concrete beams with well-bonded pre-stressing tendons, the ultimate tensile stress of tendon is an important factor that affects the strength of the member. However, if the bonding of the grout to the post-tensioning tendon is not satisfactory or the tendon is un-bonded, the tendon rarely reaches its ultimate resistance before the failure of concrete in compression. The insufficient bond will also result in a uniform distribution of tensile strains along the length of the tendon, which leads to the development of fewer but wider cracks in concrete [369]. In addition, in case of a ruptured tendon, good bonding between the grout and pre-tensioning tendon enables re-anchoring of ruptured tendon and contributes to the residual structural capacity [370].

To investigate the bond behavior of SMA bars with grout, pull-out tests were conducted. SMA bars with a diameter of 3.5 mm were cut into 220 mm segments using a cutoff wheel. Two 102 × 102 mm (4 × 4 in) cylindrical molds were used to manufacture pull-out specimens. Holes with a diameter of 3.5 mm were drilled at the center of the top and bottom of the molds to allow SMA to pass through. The SMA bar was secured at the bottom hole of each mold and Grout II was poured inside the mold. The specimens were left to cure for 3 days. Figure 5-9a shows a schematic diagram of the specimen used for the pull-out test.

Since it is difficult for standard grips to fully hold on to SMA bars because of their small diameter size, special aluminum sleeves were fabricated. Two 50 mm long sections were cut from a 10mm aluminum rod. These sections were then placed on a lathe, and a 3.5 mm hole was drilled all the way through. The sleeve was then attached to the specimen by means of twisting since the aluminum sleeve hole was a little bit smaller than the diameter of the SMA bar. The tight fit was useful to establish a mechanical interlock to help the SMA resist slippage out of the sleeve during testing.

The pull-out tests of the SMA bar was conducted using an MTS servo-hydraulic load frame. The specimen was held in place by a testing cage attached to the top head of the load frame by a large bolt. The load was applied to the SMA bar at a rate of 0.075mm/s and measured by a built-in load cell of the load frame. The slip of the SMA bar relative to grout was measured using DIC method at the loaded and free ends of the specimen. Two cards with a speckle pattern were attached to the loaded and free ends of the SMA bar. The bottom card was attached directly at the end of the grout cylinder to reduce any errors in the calculation of slippage due to strains in the SMA. The optical system captured the movement of speckle patterns on the cards and provided an output of the average vertical movements at each time step. Figure 5-9b shows pull-out test set-up.

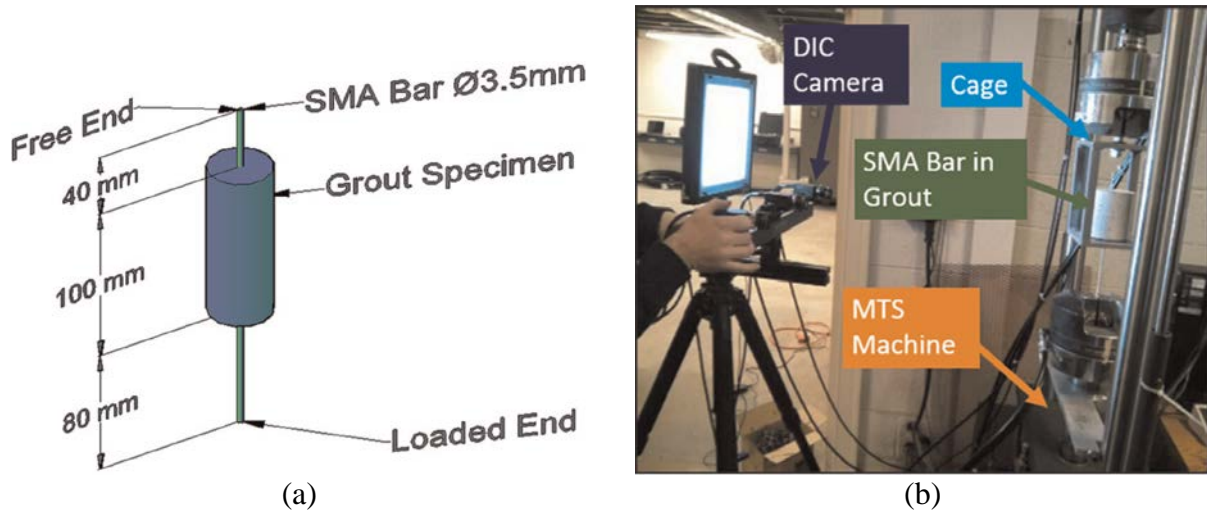


Figure 5-9. (a) Pull-out test specimen and (b) test setup

Two specimens were tested and the applied tensile force and the slip of the bar were recorded. Bond strength is defined as the shear force per unit surface area of the bar and calculated by the following equation:

$$\tau = \frac{T_b}{\pi d_b l_b} \quad (6)$$

where T_b is the tensile load on the SMA bar, d_b is the nominal bar diameter, and l_b is the embedment length of the bar. Figure 5-10 illustrates bond stress-slip curves both at the loaded and free ends of the SMA bar. The bond behavior is characterized by an initial increase in the bond stress up to 1.2 MPa for the first specimen and up to 1.4 MPa for the second specimen, and with insignificant slippage and a softening thereafter. Since SMA bars had a very smooth surface, mechanical bearing

forces were very low and the load transfer was primarily provided by friction. Maximum pull-out load was found to be 1.4 and 1.6 kN for the two specimens.

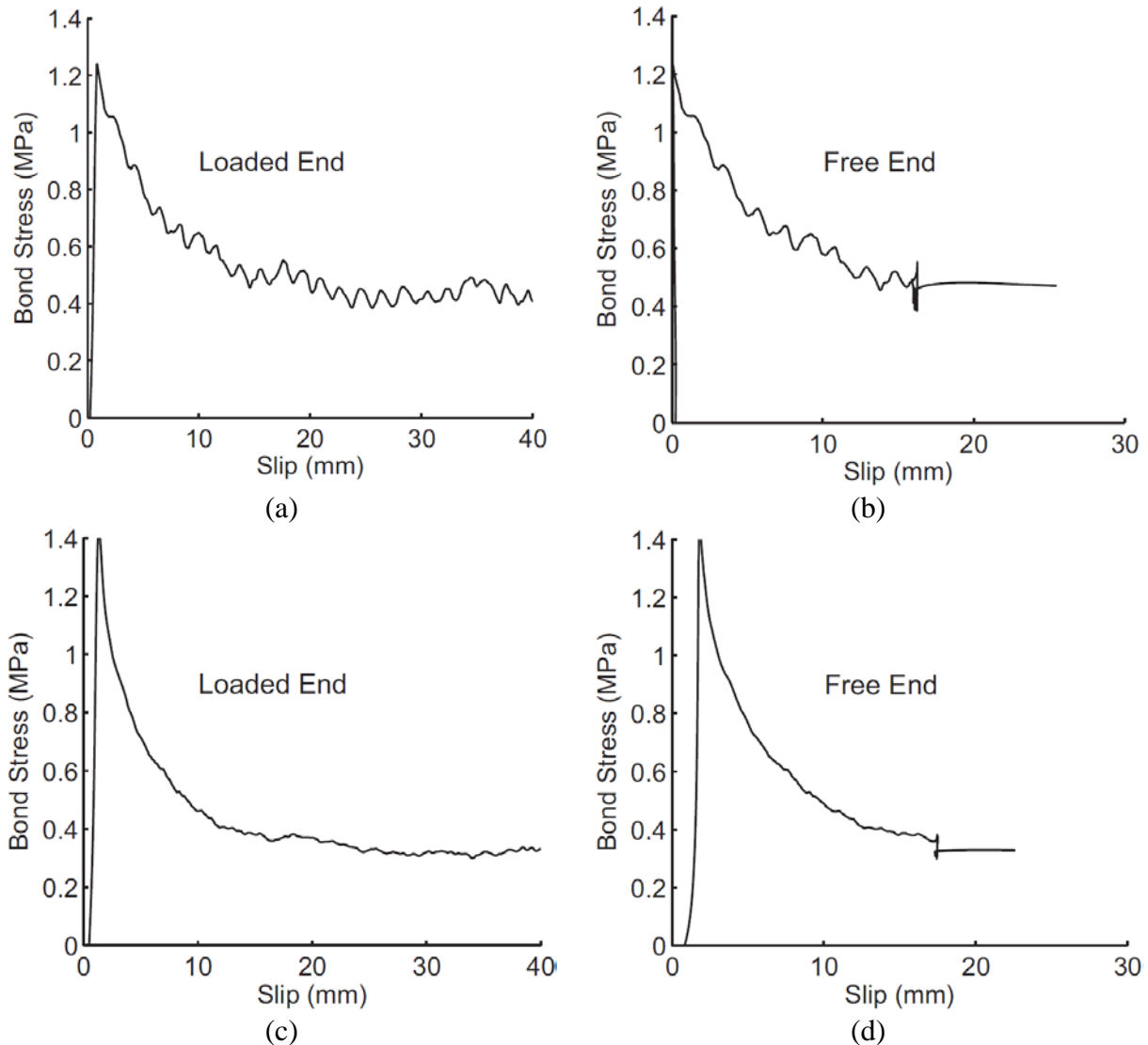


Figure 5-10. Bond stress-slip relationship for SMA bars for specimen 1 at (a) loaded end and (b) loaded end; and for specimen 2 at (c) loaded end and (d) free end

5.8 Feasibility of SPT

The comparison of the rod and sheet material demonstrated the importance of microstructure to tailor ΔT_R to the thermal inputs that the heat of hydration can provide. It has been postulated that the increase in reverse transformation temperatures after pre-straining in these alloys is related to the interaction of the martensitic transformation with the β -Nb-rich particles [364, 371, 372]. The deformation of these particles could lead to the stabilization of transformed martensite in the

surrounding matrix. Stabilization refers to the reverse martensitic transformation requiring a higher thermal driving force, which facilitates an increase in the reverse transformation temperatures [373]. Pre-strain for NiTi-based SMAs is typically carried out at temperatures between M_s and A_s ; the stress-induced austenite-to-martensite transformation is expected to remain after unloading and thus, heating facilitates recovery via SME [356, 358, 359, 364]. This work demonstrated that SIM remained after pre-strain deformation at a constant room temperature, which was well above A_f determined via the thermal cycling, can be partially recovered. The sheet micro-constituent morphology appeared refined in SEM images as compared to the rod. The results reflected that the sheet exhibited the highest activation strain and improved martensite strength properties. Hence, the findings confirmed that the material response can be tuned via tailoring Nb concentration and deformation processing after casting in order to refine the inter-particle spacing and volume fraction of the micro-constituent morphology.

The grout temperature characterization tests revealed that it is possible to increase the temperature of a posttensioning tendon up to about 50°C when a posttensioning duct is filled with a commercially available grout. When the SMA sheet material is pre-strained at different levels, the strain remained after unloading, and recovered upon a temperature increase to 50°C, which can be reached through hydration heat. Table 5-3 provides the strain recovered after fully activating the material (heating above A_f^*). Note that A_f^* is stress dependent and it increased under applied stress as shown in Table 5-3. The material should be heated above the A_f^* under generated stress to achieve maximum strain recovery. It can be seen that a great percentage of the maximum recoverable strain can be activated when the temperature reached 50°C. For instance, a temperature increase to 50°C will achieve 91% of recoverable strain during free recovery experiments for an SMA tendon with a 10.1% pre-strain.

Table 5-3. Characteristic metrics for pre-strain deformation of NiTiNb alloy sheet material

Pre-strain (%)	Applied stress (MPa)	Strain remaining after unloading (%)	Strain recovered up to 50°C (%)	Free recovery A_f^* (°C)	Strain recovered after heating to A_f^* (%)
5.4	590	2.3	1.0	63	1.1
8.8	630	5.2	2.7	75	3.0
10.1	720	6.8	4.1	80	4.5
12.2	800	9.0	1.3	111	5.3
16.1	860	12.7	0.5	123	4.8

Figure 5-11 shows the dependence of the reverse transformation temperature interval $\Delta T_R^* = A_f^* - A_s^*$ and recovery ratio on the pre-strain for the free recovery experiments. The ΔT_R values continually increase while the recovery ratio reached a maximum for the 10.1% pre-strain and decreased thereafter. The increasing ΔT_R^* and the achievement of maximum pre-strain reflected the role of the Nb-rich particles in the composite-like microstructure. Particles can have a stabilizing effect and prohibit the reverse martensitic transformation and thus, the thermal energy and A_f must increase to complete (or fully activate) the recovery [364].

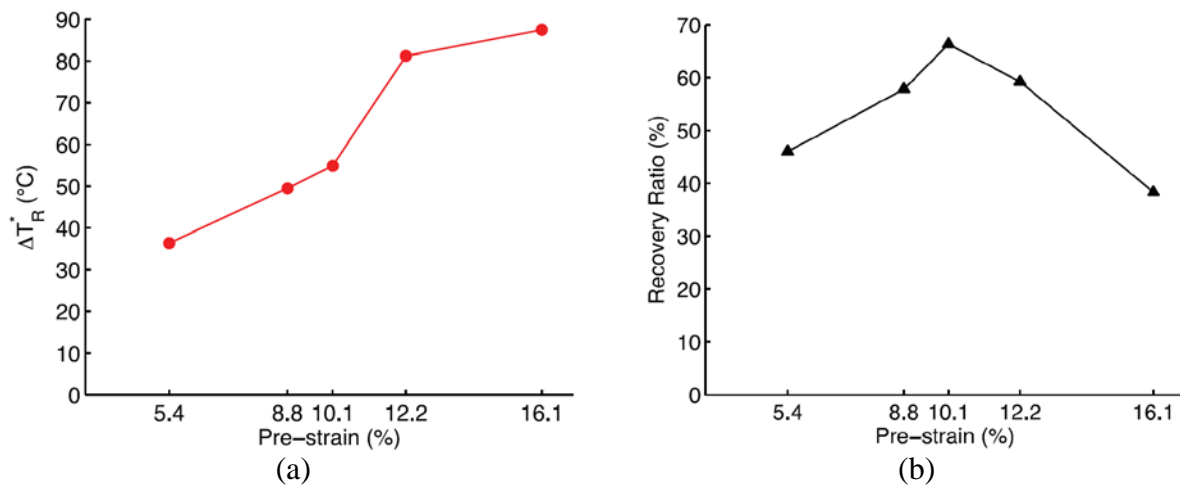


Figure 5-11. Variation of (a) ΔT_R^* and (b) recovery ratio with pre-strain level for free recovery experiments

Figure 5-12 shows the variation of the ΔT_R^{**} and recovery stress with the pre-strain for the constrained recovery experiments. For the pre-strain level of 10.1% and 12.2%, the stresses generated during constrained recovery are 530 and 550 MPa, respectively. The temperature intervals under constrained recovery are, in general, larger than the ΔT_R^* during free recovery, especially when the pre-strain level is greater than 8.8%. Presumably, the constraining stress augments the stabilization effect. This disparity needs to be considered when designing such alloys.

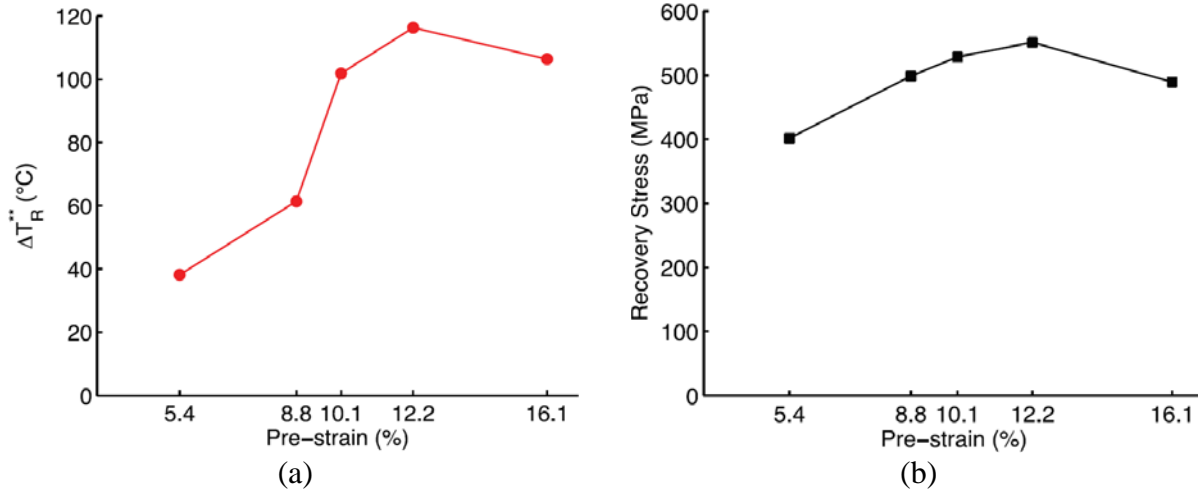


Figure 5-12. Variation of (a) ΔT_R^{**} and (b) recovery stress with pre-strain level for constrained recovery experiments

The results obtained from free and constrained recovery tests showed that pre-stressing significantly affects the transformation temperatures and shape recovery. Figure 5-13a showed the amount of strain recovered per unit temperature increase for free recovery experiments at different pre-strain levels. It can be seen that the optimum pre-strain level that results in maximum strain recovery for a unit temperature increase is 10.1%. Pre-strain level also provided the maximum recovery ratio as can be seen from Figure 5-11b.

On the other hand, for constrained recovery, the recovery stress developed per unit temperature increase declined with the increase of pre-strain level as shown in Figure 5-13b. However, the maximum recovery stress increased with the pre-strain level up to 12.2% pre-strain and decreased thereafter as shown in Figure 5-12b. Therefore, if the SMA tendons will be activated partially with limited temperature increase, a relatively low level of pre-strain (6%–9%) can be more favorable. If the SMA tendons will be fully activated with sufficient heat, then a pre-strain level that was just beyond the plateau region (10%–12%) is more preferable.

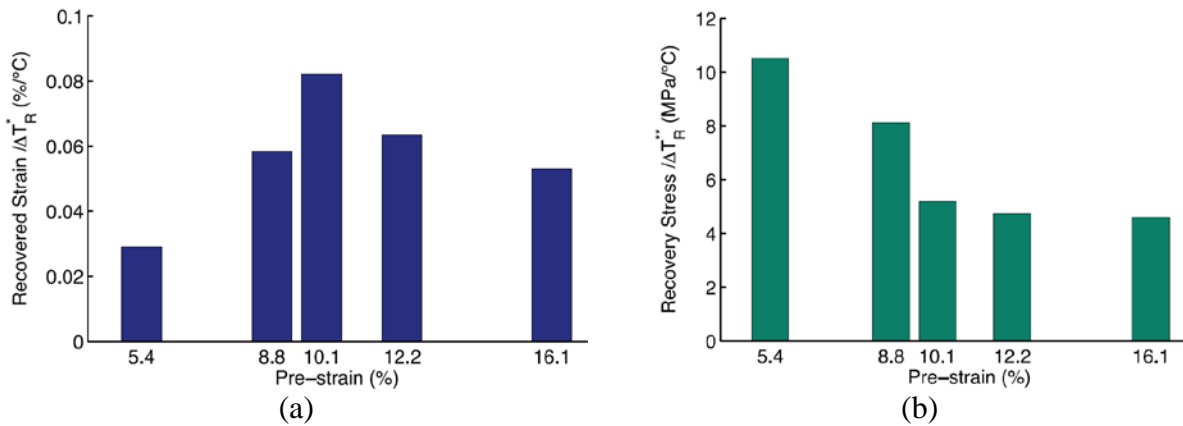


Figure 5-13. (a) Strain recovered per unit temperature increase as a function of pre-strain level, and (b) recovery stress per unit temperature increase as a function of pre-strain level

It should also be noted that only four types of grouts approved by the state transportation agency were considered here. The hydration heat of grout was a result of a number of exothermic chemical reactions that can be influenced by several factors such as water/cement ratio, air entrainment, chemical admixtures, cement type, cement fineness, and ambient temperature. Therefore, further studies can be conducted to obtain larger hydration heat (i.e. higher increases in temperature) by altering some of these factors. However, this needs to be done carefully since excessive hydration heat can cause other problems during grouting and adversely affect the performance of the grout.

Pull-out tests showed that the bond between the SMA bars and the grout is low. However, it was comparable to the bond strength (<1 MPa) between a single steel bar and grout and the bond strength (<2 MPa) between smooth pre-stressing bars and normal strength concrete. In self-post-tensioning with SMAs, the pre-stress is transferred to the concrete element by the end anchorages. Therefore, the recovery stresses in the SMA bar will be transferred through the anchorage system at the end of the beam despite the low bond strength. Nonetheless, as discussed earlier, good bonding is still favorable for better cracking behavior and ultimate strength response. The use of SMA strands instead of a single SMA bar can provide better bond performance as higher bond strength was reported for steel strands compared to steel bars in the literature. Superelastic SMAs in the strand or cable form have recently been developed and studied by several researchers. When SMA strands with SME properties are developed, they can be used in pre-stressing applications with better bond characteristics.

5.9 Summary

This section explored the feasibility of activating SMA tendons using heat of hydration of grout in order to develop SPT concrete elements. Material characterization tests were conducted on NiTiNb SMAs. In particular, the influence of differential thermo-mechanical processing on shape memory behavior is assessed for a rolled sheet and extruded rod. The recovery behavior of the material was studied during free and constrained recovery experiments. The increase in temperature during the hydration of four commercially available grouts was evaluated. A typical cylinder specimen was filled with the grout and a thermocouple and a data acquisition system were employed to measure the temperature during 48h. In addition, two pull-out tests were conducted on cylindrical specimens to investigate the bond between the grout and SMA bar. The major findings can be summarized as follows:

- Tailoring deformation processing after casting, such that the eutectic micro-constituent is oriented and closely spaced, can facilitate tuning the activation strain and reverse transformation interval.
- Pre-strain level considerably influences the reverse transformation interval and recovery ratio or stress.
- For free recovery experiments, reverse transformation interval increases with the increasing pre-strain level while recovery ratio reaches a maximum value and then decreases.
- For constrained recovery experiments, both reverse transformation interval and recovery stress increase up to 12.2% strain and then slightly decrease with the increasing pre-strain. A recovery stress more than 550MPa could be achieved after cooling to ambient temperature.
- An average of 28°C temperature increase was observed during hydration of a prepackaged grout material.
- The temperature increase due to heat of hydration of the grout can activate most substantial percentage of recoverable strain during a free recovery experiment. However, for constrained recovery, higher temperature increases are needed to fully activate the SMA material.
- Bond strength between plain SMA bars and grout material is found to be about 1.3 MPa. To achieve higher bond strength, the surface of SMA bars can be sand-blasted.

Although this feasibility study indicated that the concrete elements can be pre-stressed by partially activating NiTiNb SME bars using hydration heat of the grout, pre-straining in the austenitic state via the SIM transformation has limited potential. Decreasing prestrain deformation temperatures below room temperature down to M_s and below M_f can facilitate lower critical stress levels and differential reverse transformation intervals for SME recovery as well as higher recoverable strains and recovery stresses. Hence, a similar systematic study for pre-straining NiTiNb in the martensitic state is warranted. Further research is needed to investigate other SMA materials that possess more favorable phase transformation ranges for self-stressing and higher recovery stresses. Potential of achieving higher temperature increases during the hydration of grout can also be explored. Furthermore, long-term pre-stress losses, the use of larger size SMA tendons, and the effects of field conditions need to be examined.

6 Summary, Conclusions and Recommendations

6.1 Summary

Concrete represents the most common material that is being used in the vast majority of civil structures at the global level. However, traditional cementitious materials are subject to cracking and have limited or no functional properties. The vulnerability and exposure of concrete structures to rapid deterioration due to cracking, rebar corrosion, seismic events, and extreme weather conditions have always been a concern in the engineering community. In addition, extreme weather events including hurricanes, tropical storms, and prolonged intense temperatures have been encountered more frequently in recent years.

Shape Memory Alloys (SMAs) are smart materials that can recall and restore their original shapes upon being deformed. Their shape recovery ability is attributed to reversible phase transformations between two different solid phases of the material. SMAs are classified into two main groups: shape memory effect SMAs and superelastic SMAs. The shape recovery in shape memory effect SMAs occurs due to thermal activation; while for the superelastic SMAs shape recovery is mechanically (stress) induced. Due to their excellent re-centering and good energy absorbing capabilities, superelastic SMAs have received a great interest for applications in concrete structures.

This dissertation explored the development and characterization of shape memory alloy materials and composites to enhance resilience and sustainability of concrete structures. The first SMA material investigated in this research was relatively large-diameter NiTi SMA cables. The complete characterization of these cables was carried out in this work. To illustrate their potential use as a component of seismic control device that can be installed in concrete structures for dynamic response mitigation, a passive control device was fabricated and tested. Secondly, the development of SMA fiber reinforced cementitious composites was studied. In particular, the behavior of cementitious composites that contains short distributed SMA fibers was systematically evaluated. Another SMA material studied in this research was wide-hysteresis NiTiNb shape memory effect SMAs. The feasibility of self-pre-stressing concrete members using this SMA materials was evaluated.

The dissertation is composed of six sections. Section one provides a review of the innovative technologies and methodologies that have been reported in the literature and investigated by different researchers to mitigate the deficiencies of concrete structures. The motivation of

conducting this research work and its scope are presented. Section two provides an overview of the discovery and composition of SMAs and elaborates the development and mechanical response of SMAs and their applications in concrete and steel structures. A comprehensive review of fiber reinforced cementitious composites and the latest research activities in the field of SMA fiber reinforced cementitious composites are presented. The use, and different applications, of shape memory effect SMAs in pre- and post-stressing concrete members are discussed.

Section three is devoted to the characterization of superelastic SMA Cables. It investigates the mechanical response of superelastic cables and strands subjected to various strain amplitudes and rates under tensile loading protocols. The stress-strain response and the degradation of various properties of the superelastic SMAs under fatigue loading are examined. The thermal and electrical response are investigated and SEM images of the fracture of a superelastic SMA cable due to fatigue loading are presented. At the end of this Section, the manufacturing, testing and preliminary results of a superelastic viscous damper are presented and discussed.

Section four focuses on fiber reinforced cementitious composites. It discusses the use of randomly distributed superelastic SMA fibers in mortar and concrete beams to resist flexural loads. The enhancement of various properties such as, flexural strength, residual deformations, and crack recovery are also investigated. The energy dissipation that would occur during each loading and unloading cycle for fiber reinforced concrete specimens is evaluated and the acoustic emissions signal data is acquired using two transducers placed at each end of the specimens. Section five is devoted to the study of self-post-tensioning of concrete members using SMAs. The mechanisms and material characterization of self-post-tensioning are discussed. The pre-straining and strain-recovery is presented. Finally, the heat of hydration of grout, the behavior of SMA-grout bond, and the feasibility of self-post-tensioning are elaborated and assessed.

Section six includes a summary of the conducted research and provides the main conclusions of the study. Recommendations for future work are also provided. A comprehensive list of relevant references that have been cited in this study is also attached.

6.2 Conclusions and Recommendations

The characterization of tensile tests of cables at different strain amplitudes and rates revealed that SMA cables are viable alternative that can be implemented in real-world structural applications. SMA cables have very good mechanical properties and have a lower production cost when compared to same size monolithic SMA bars. The uniaxial tensile tests, revealed that SMA cables exhibit excellent superelastic behavior similar to thin SMA wires. Also, the non-conventional complex configuration experienced minimal residual deformations when subjected to 6% strains, which represents the unique re-centering properties of SMAs. While, a maximum of 0.76% residual strain was observed when the cable was subjected to 10% strains. The influence of cyclic fatigue loads is apparent in the first 100 cycles (i.e. most of the degradations occur during the first 100 cycles). The residual strains of the cable were 2% and 2.18% at the end of the 5000th loading cycle for strain amplitudes of 4% and 5%, respectively.

In general, SMA cables provide high tensile forces, good energy dissipation, and redundancies which are advantageous properties for civil applications. The redundancy of the cable was observed for the cable subjected to 7% strain amplitudes fatigue loadings. By the end of the 5000th cycle, the inner core of cable fractured, but the outer cores were still intact. However, the complex geometrical configuration of the SMA cables influenced the tensile response, and reduced the transformation stresses, elastic modulus and the maximum tensile stress for the applied strain amplitude. This is mostly due to the non-uniform distribution of the applied strains on the cross-section of the cable. Therefore, the geometrical configuration of the SMA cables need to be tailored for a given application.

Moreover, preliminary experimental tests conducted on a SMA cable based control device illustrated a good hysteretic response which enabled a good dissipation of energy. Some modifications such as the enhancement of the bond between the steel plates and the rubber compound need to be considered. Also, the bending of the top and bottom plates should be limited to apply high strains on the SMA cables and achieve the re-centering capabilities.

The results of thermal imaging illustrated the feasibility of predicting the applied stress and strains, and a good correlation between the changes in temperature with the re-centering capabilities can be established. Also, the investigations concluded that there is a direct correlation between the electrical resistance and applied strains for a conventional strand configuration (1 × 7), but it revealed the complexity of sensing the applied strains for a multi-layered cable. The

thermal imaging and electrical resistance are essential capabilities that enhance the functionality of the SMAs for self-sensing applications. However, further research is needed to evaluate the effect of the strain rate on the thermal response.

The flexural results of the SMA fiber reinforced mortar revealed that the addition of the SMA fibers increased the overall ductility of the mortar composites. The specimens with 1.0% SMA fibers exhibited a deflection hardening behavior, with residual strength up to 26% of their peak strength. All other types of the SMA-fiber reinforced mortars exhibited a deflection softening behavior. Also, the specimens with 1.0% of SMA fibers by volume displayed the smallest crack propagation and the highest crack recovery ratio. Moreover, to better understand the behavior of the SMA fiber reinforced composites, acoustic emissions were monitored and characterized.

Few acoustic events were observed during unloading for the control specimen and for the early loading cycles of the SMA fiber reinforced mortar specimens. However, large number of acoustic events with scattered durations were present during the unloading phase of latter cycles in SMA fiber reinforced specimens. Cumulative energy histories showed that the energy remains constant during unloading for all loading cycles of control specimen and during the early cycles (cycles 1 to 8) of SMA fiber reinforced mortar. An increase in the cumulative energy was observed in SMA fiber reinforced specimens at the latter loading cycles. It was demonstrated that the increase in energy can be correlated to the crack-closure pattern. The events with higher average frequency, which indicate a tensile mode behavior, were observed when the mortar experiences crack closure. Results suggest that the AE cumulative energy and average frequency can be used to characterize crack width growth and recovery in SMA fiber reinforced mortars. However, further investigations are needed to confirm the exact nature of this relationship and reveal the correlation between the relative increase of cumulative energy during the loading and unloading stage and crack opening and closure (i.e., quantification of crack width increase/recovery).

The flexural response of the SMA fiber reinforced concrete confirmed that the addition of SMA fibers into concrete mixtures did not significantly improve the re-centering capabilities as compared to the steel fiber reinforced concrete. This is mainly attributed to the straight shape of the SMA fibers used in this study. The lack of mechanical anchorage, such as hooked ends or friction resistance of a textured surface, caused poor bond behavior. SMA fiber reinforced specimen suffered from excessive pullout offsetting the crack recovery or re-centering capabilities.

However, specimens with SMA fibers displayed a better crack-width control (i.e. smaller crack width) as compared to its counterpart steel fiber reinforced concrete specimen.

Hybrid fiber reinforced specimens displayed the least residual mid-span displacement, better crack-closure capabilities and a slightly higher flexural strength. The combination of SMA and steel fibers increased the energy dissipation for almost all loading cycles. Furthermore, the acoustic emission confirmed the experimental results obtained by the DIC and a direct correlation between the crack width propagation and the cumulative energy was established. Overall, the use of hybrid fibers in cementitious composites showed good potential and can be the subject matter of further investigations. In particular, the use of SMA fibers with mechanical anchorage needs to be studied.

The feasibility of the self-post-tensioning of concrete members was investigated. It was shown that a recovery stress of more than 500 MPa could be achieved after cooling to ambient temperature. Further studies are currently being conducted to optimize the phase transformation temperatures for self-post-tensioning application. The record of temperature increase during the hydration of four commercially available grouts revealed that the highest temperature increase was for Grout II. At three different tests of Grout II, an average of 28°C temperature increase was observed. The increase of temperature increases in the other grouts were between 18°C and 20°C. The results indicated that commercially available grouts can provide considerable temperature increase during the heat of hydration of grout, which can be used to activate SMA tendons. In addition, the pullout tests concluded that the maximum pullout load is between 1.4 to 1.6 kN and the bond stress is between 1.2 and 1.4 MPa for 3.5-mm plain SMA bars.

The use SMA tendons, which possess high fatigue and corrosion resistance, as post-tensioning elements in concrete girders will provide a better performance, increase the service life, and allow for life-cycle cost savings for concrete bridges. The replacement of steel tendons with SMA prestressing tendons will prevent corrosion-induced deterioration of tendons in concrete structures. The use of heat of hydration of grout to activate the shape memory effect of SMA tendons will provide self-stressing capability. This will greatly simplify and facilitate the tendon installation. The need for jacking equipment or electrical source can then be eliminated. This will also enable to form the reinforcement in any shape in two or three-dimensional space without special devices. The use of SMA tendons will lead to a better control of the prestress and higher levels of effective prestress. During the service life of a bridge, heat-triggering the SMA tendons can repair possible damage observed in girders and reduce excessive deflections.

The presented dissertation established a framework for developing resilient and sustainable structures through extensive and thorough experimental investigations, backed up with critical analysis of the results. The study presented thorough experimental data and analysis needed to advance the work in this field. Future investigations may include the investigation of large scale structural components incorporating the shape memory alloys cables, bars and fibers. Furthermore, it is necessary to investigate the use of superelastic SMA fibers with hooked ends in a concrete matrix and their effects on the compressive, tensile and flexural strength of the composite. Further analysis is required to investigate the optimal strain amplitudes for achieving highest energy dissipations with the minimal degradation of the SMA cable under various strain rates. This would help to develop an effective SVD.

The interfacial bond between the high demand butyl compound and steel plates may need to be investigated and enhanced, to overcome the de-bonding issues under dynamic loading. The bending effect of the steel plates on the energy dissipation of the SVD should also be considered. Finally, a large scale experimental investigation might be carried out using the self-post-tensioning technique to investigate the actual pre-stressing forces in a conventional structure.

7 References

1. Zhang Y, Bai L. Rapid structural condition assessment using radio frequency identification (RFID) based wireless strain sensor. *Automation in Construction*. 2015 Jun 1; [54:1-1](#)
2. Leon RT, Gao Y. Resiliency of steel and composite structures. *Frontiers of Structural and Civil Engineering*. 2016 Sep 1; [10\(3\):239-53](#)
3. ASCE's 2017 Infrastructure Report Card. (2017). [Report Card History](#)
4. Nykyforchyn H, Kyryliv V, Maksymiv O, Slobodyan Z, Tsyurulnyk O. Formation of surface corrosion-resistant nanocrystalline structures on steel. *Nanoscale research letters*. 2016 Dec 1; [11\(1\):51](#)
5. Fernandez I, Herrador MF, Marí AR, Bairán JM. Structural effects of steel reinforcement corrosion on statically indeterminate reinforced concrete members. *Materials and structures*. 2016 Dec 1; [49\(12\):4959-73](#)
6. Kim IT, Dao DK, Jeong YS, Huh J, Ahn JH. Effect of corrosion on the tension behavior of painted structural steel members. *Journal of Constructional Steel Research*. 2017 Jun 1; [133:256-68](#)
7. Song ST, Wang CY, Huang WH. Earthquake damage potential and critical scour depth of bridges exposed to flood and seismic hazards under lateral seismic loads. *Earthquake Engineering and Engineering Vibration*. 2015 Dec 1; [14\(4\):579-94](#)
8. Rahmani M, Ebrahimian M, Todorovska MI. Time-wave velocity analysis for early earthquake damage detection in buildings: Application to a damaged full-scale RC building. *Earthquake Engineering & Structural Dynamics*. 2015 Apr 10; [44\(4\):619-36](#)
9. Barbosa AR, Ribeiro FL, Neves LA. Influence of earthquake ground-motion duration on damage estimation: application to steel moment resisting frames. *Earthquake Engineering & Structural Dynamics*. 2017 Jan 1; [46\(1\):27-49](#)
10. Zhang W, Cai CS, Pan F, Zhang Y. Fatigue life estimation of existing bridges under vehicle and non-stationary hurricane wind. *Journal of Wind Engineering and Industrial Aerodynamics*. 2014 Oct 1; [133:135-45](#)
11. Getter DJ, Davidson MT, Consolazio GR, Patev RC. Determination of hurricane-induced large impact loads on floodwalls using dynamic finite element analysis. *Engineering Structures*. 2015 Dec 1; [104:95-106](#)
12. Mooneghi MA, Irwin P, Chowdhury AG. Partial turbulence simulation method for predicting peak wind loads on small structures and building appurtenances. *Journal of Wind Engineering and Industrial Aerodynamics*. 2016 Oct 31; [157:47-62](#)
13. Su JZ, Xia Y, Zhu LD, Zhu HP, Ni YQ. Typhoon-and temperature-induced quasi-static responses of a supertall structure. *Engineering Structures*. 2017 Jul 15; [143:91-100](#)
14. [Engineeringchallenges.org](#). (2017). Grand Challenges - [Restore and Improve Urban Infrastructure](#)
15. Yu Y, Sun T, Wang Y. Bioactive titanium oxide coatings fabricated on NiTi SMA via thermal treatment for medical applications. *Procedia Engineering*. 2016 Jan 1; [141:115-20](#)
16. Frankel DJ. Design of Fatigue Resistant Heusler-strengthened PdTi-based Shape Memory Alloys for Biomedical Applications (Doctoral dissertation, Northwestern University) [2016](#)
17. Brandal G, Yao YL, Naveed S. Biocompatibility and corrosion response of laser joined NiTi to stainless steel wires. *Journal of Manufacturing Science and Engineering*. 2015 Jun 1; [137\(3\):031015](#)
18. Kaczmarek M, Kurtyka P. Corrosion Resistance of Surface Treated NiTi Alloy Tested in Artificial Plasma. *In Innovations in Biomedical Engineering 2017* (pp. 17-24). Springer, Cham
19. Gu Y, Perinpanayagam H, Kum DJ, Yoo YJ, Jeong JS, Lim SM, Chang SW, Baek SH, Zhu Q, Kum KY. Effect of different agitation techniques on the penetration of irrigant and sealer into dentinal tubules. *Photomedicine and laser surgery*. 2017 Feb 1; [35\(2\):71-7](#)
20. Tao L, Luo C, Li WX, Zhang YJ. Super-elastic behavior analysis of shape memory alloy vascular stent. *In Key Engineering Materials 2017* (Vol. 725, pp. 405-409). Trans Tech Publications
21. Xia M, Sun Q. Thermomechanical responses of nonlinear torsional vibration with NiTi shape memory alloy—Alternative stable states and their jumps. *Journal of the Mechanics and Physics of Solids*. 2017 May 31; [102:257-76](#)
22. Mani Y, Senthilkumar M. Shape memory alloy-based adaptive-passive dynamic vibration absorber for vibration control in piping applications. *Journal of Vibration and Control*. 2015 Jul; [21\(9\):1838-47](#)
23. Sultana P, Youssef MA. Seismic performance of steel moment resisting frames utilizing superelastic shape memory alloys. *Journal of Constructional Steel Research*. 2016 Oct 1; [125:239-51](#)
24. Wang W, Chan TM, Shao H. Seismic performance of beam–column joints with SMA tendons strengthened by steel angles. *Journal of Constructional Steel Research*. 2015 Jun 1; [109:61-71](#)

25. Yam MC, Fang C, Lam AC, Zhang Y. Numerical study and practical design of beam-to-column connections with shape memory alloys. *Journal of Constructional Steel Research*. 2015 Jan 1; [104:177-92](#)
26. Fang C, Yam MC, Ma H, Chung KF. Tests on superelastic Ni–Ti SMA bars under cyclic tension and direct-shear: towards practical recentring connections. *Materials and Structures*. 2015 Apr 1; [48\(4\):1013-30](#)
27. Alam MS, Nehdi M, Youssef MA. Seismic performance of concrete frame structures reinforced with superelastic shape memory alloys. *Smart Struct Syst*. 2009 Sep 1; [5\(5\):565-85](#)
28. Zafar A, Andrawes B. Seismic behavior of SMA–FRP reinforced concrete frames under sequential seismic hazard. *Engineering Structures*. 2015 Sep 1; [98:163-73](#)
29. Tazarv M, Saiid Saiidi M. Reinforcing NiTi superelastic SMA for concrete structures. *Journal of Structural Engineering*. 2014 Sep 15; [141\(8\):04014197](#)
30. Shahverdi M, Czaderski C, Annen P, Motavalli M. Strengthening of RC beams by iron-based shape memory alloy bars embedded in a shotcrete layer. *Engineering Structures*. 2016 Jun 15; [117:263-73](#)
31. Youssef MA, Alam MS, Nehdi M. Experimental investigation on the seismic behavior of beam-column joints reinforced with superelastic shape memory alloys. *Journal of Earthquake Engineering*. 2008 Oct 2; [12\(7\):1205-22](#)
32. Speicher MS, DesRoches R, Leon RT. Experimental results of a NiTi shape memory alloy (SMA)-based recentring beam-column connection. *Engineering structures*. 2011 Sep 1; [33\(9\):2448-57](#)
33. Padgett JE, DesRoches R, Ehlinger R. Experimental response modification of a four-span bridge retrofit with shape memory alloys. *Structural Control and Health Monitoring*. 2010 Oct 1; [17\(6\):694-708](#)
34. Debbarma SR, Saha S. Behaviour of concrete beams reinforced with SMA and steel bars under cyclic and monotonic load. *Magazine of Concrete Research*. 2014 Mar; [66\(6\):305-14](#)
35. Fang C, Wang W, He C, Chen Y. Self-centring behaviour of steel and steel-concrete composite connections equipped with NiTi SMA bolts. *Engineering Structures*. 2017 Nov 1; [150:390-408](#)
36. Abdulridha A, Palermo D, Foo S, Vecchio FJ. Behavior and modeling of superelastic shape memory alloy reinforced concrete beams. *Engineering Structures*. 2013 Apr 1; [49:893-904](#)
37. Shrestha KC, Araki Y, Nagae T, Koetaka Y, Suzuki Y, Omori T, Sutou Y, Kainuma R, Ishida K. Feasibility of Cu–Al–Mn superelastic alloy bars as reinforcement elements in concrete beams. *Smart Materials and Structures*. 2013 Jan 25; [22\(2\):025025](#)
38. Wierschem N, Andrawes B. Superelastic SMA–FRP composite reinforcement for concrete structures. *Smart materials and structures*. 2010 Jan 14; [19\(2\):025011](#)
39. Billah AM, Alam MS. Plastic hinge length of shape memory alloy (SMA) reinforced concrete bridge pier. *Engineering Structures*. 2016 Jun 15; [117:321-31](#)
40. Omar M. Comparative Study on Seismic Response of Reinforced Concrete Frames with SMA in Column and Beam Plastic Hinge Zones. In *Advanced Materials Research 2014* ([Vol. 1043, pp. 247-251](#)). Trans Tech Publications.
41. Andrawes B, DesRoches R. Unseating prevention for multiple frame bridges using superelastic devices. *Smart materials and structures*. 2005 May 26; [14\(3\):S60](#)
42. Andrawes B, Shin M, Wierschem N. Active confinement of reinforced concrete bridge columns using shape memory alloys. *Journal of Bridge Engineering*. 2009 Dec 15; [15\(1\):81-9](#)
43. Sherif MM, Tanks J, Ozbulut OE. Acoustic emission analysis of cyclically loaded superelastic shape memory alloy fiber reinforced mortar beams. *Cement and Concrete Research*. 2017 May 1; [95:178-87](#)
44. Casciati F, Faravelli L, Fuggini C. Cable vibration mitigation by added SMA wires. *Acta Mechanica*. 2008 Jan 1; [195\(1-4\):141-55](#)
45. Billah AM, Alam MS. Bond behavior of smooth and sand-coated shape memory alloy (SMA) rebar in concrete. *InStructures* 2016 Feb 1 ([Vol. 5, pp. 186-195](#))
46. Choi E, Park SH, Cho BS, Hui D. Lateral reinforcement of welded SMA rings for reinforced concrete columns. *Journal of Alloys and Compounds*. 2013 Nov 15; [577:S756-9](#)
47. Zaidi M. Experimental Testing and Reliability Analysis of Repaired SMA and Steel Reinforced Shear Walls (Doctoral dissertation, Université d'Ottawa/University of Ottawa).
48. Ameli MJ, Pantelides CP. Seismic analysis of precast concrete bridge columns connected with grouted splice sleeve connectors. *Journal of Structural Engineering*. 2016 Sep 19; [143\(2\):04016176](#)
49. Abo Alarab L, Ross BE, Poursae A. Corrosion Assessment of Coupled Steel Reinforcement with Ni–Ti–Based Shape Memory Alloy in Simulated-Concrete Pore Solution. *Journal of Materials in Civil Engineering*. 2016 Mar 16; [28\(8\):04016060](#)
50. Kim DJ, Kim HA, Chung YS, Choi E. Pullout resistance of straight NiTi shape memory alloy fibers in cement mortar after cold drawing and heat treatment. *Composites Part B: Engineering*. 2014 Dec 1; [67:588-94](#)

51. Shajil N, Srinivasan SM, Santhanam M. Self-centering of shape memory alloy fiber reinforced cement mortar members subjected to strong cyclic loading. *Materials and structures*. 2013 Apr 1; [46\(4\):651-61](#)
52. Shajil N, Srinivasan SM, Santhanam M. An experimental study on self-centering and ductility of pseudo-elastic shape memory alloy (PESMA) fiber reinforced beam and beam-column joint specimens. *Materials and Structures*. 2016 Mar 1; [49\(3\):783-93](#)
53. Li X, Li M, Song G. Energy-dissipating and self-repairing SMA-ECC composite material system. *Smart Materials and Structures*. 2015 Jan 14; [24\(2\):025024](#)
54. Ozbulut OE, Hurlbauss S, Desroches R. Seismic response control using shape memory alloys: a review. *Journal of Intelligent Material Systems and Structures*. 2011 Sep; [22\(14\):1531-49](#)
55. Dieng L, Helbert G, Chirani SA, Lecompte T, Pilvin P. Use of shape memory alloys damper device to mitigate vibration amplitudes of bridge cables. *Engineering Structures*. 2013 Nov 1; [56:1547-56](#)
56. Parulekar YM, Kiran AR, Reddy GR, Singh RK, Vaze KK. Shake table tests and analytical simulations of a steel structure with shape memory alloy dampers. *Smart Materials and Structures*. 2014 Oct 16; [23\(12\):125002](#)
57. Silwal B, Michael RJ, Ozbulut OE. A superelastic viscous damper for enhanced seismic performance of steel moment frames. *Engineering Structures*. 2015 Dec 15; [105:152-64](#)
58. Soul H, Yawny A. Self-centering and damping capabilities of a tension-compression device equipped with superelastic NiTi wires. *Smart Materials and Structures*. 2015 Jun 3; [24\(7\):075005](#)
59. Qiu C, Zhu S. Shake table test and numerical study of self-centering steel frame with SMA braces. *Earthquake Engineering & Structural Dynamics*. 2017 Jan 1; [46\(1\):117-37](#)
60. Nespoli A, Rigamonti D, Riva M, Villa E, Passaretti F. Study of pseudoelastic systems for the design of complex passive dampers: static analysis and modeling. *Smart Materials and Structures*. 2016 Sep 9; [25\(10\):105001](#)
61. Speicher MS, DesRoches R, Leon RT. Investigation of an articulated quadrilateral bracing system utilizing shape memory alloys. *Journal of Constructional Steel Research*. 2017 Mar 1; [130:65-78](#)
62. Choi E, Kim DJ, Youn H. Stiffness and Confinement Ratios of SMA Wire Jackets for Confining Concrete. *Journal of materials engineering and performance*. 2014 Jul 1; [23\(7\):2727-31](#)
63. Micelli F, Angiuli R, Corvaglia P, Aiello MA. Passive and SMA-activated confinement of circular masonry columns with basalt and glass fibers composites. *Composites Part B: Engineering*. 2014 Dec 1; [67:348-62](#)
64. Choi ES, Lee HS, Park JN, Cho BS. Hysteretic behavior of concrete cylinders confined by active confining SMA wire jackets. In *Materials Science Forum 2010 (Vol. 654, pp. 2099-2102)*. Trans Tech Publications.
65. Tran H, Balandraud X, Destrebecq JF. Improvement of the mechanical performances of concrete cylinders confined actively or passively by means of SMA wires. *Archives of Civil and Mechanical Engineering*. 2015 Jan 1; [15\(1\):292-9](#)
66. Choi E, Chung YS, Kim YW, Kim JW, 2011, Monotonic and cyclic bond behavior of confined concrete using NiTiNb SMA wires. *Smart Materials and Structures*; [20\(7\):075016](#)
67. Choi E, Cho BS, Park J, Park K. Inducing recovery stress of NiTiNb SMA wires using heat of hydration for confining concrete. *Journal of Intelligent Material Systems and Structures*. 2011 Nov; [22\(17\):1949-57](#)
68. Shahverdi M, Czaderski C, Motavalli M. Iron-based shape memory alloys for prestressed near-surface mounted strengthening of reinforced concrete beams. *Construction and Building Materials*. 2016 Jun 1; [112:28-38](#)
69. Daghast SM, Ozbulut OE. Bond-slip behavior of superelastic shape memory alloys for near-surface-mounted strengthening applications. *Smart Materials and Structures*. 2017 Feb 7; [26\(3\):035020](#)
70. Choi E, Nam TH, Chung YS, Kim YW, Lee SY. Behavior of NiTiNb SMA wires under recovery stress or prestressing. *Nanoscale research letters*. 2012 Dec 1; [7\(1\):66](#)
71. Yang ZY, Yuan TT, Liu J, Xi XH, Gao P. Experimental Study on the Mechanical Property of SMA Externally Prestressed Concrete Box Beam. In *Applied Mechanics and Materials 2015 (Vol. 778, pp. 50-54)*
72. Choi E, Kim DJ, Hwang JH, Kim WJ. Prestressing effect of cold-drawn short NiTi SMA fibres in steel reinforced mortar beams. *Smart Materials and Structures*. 2016 Jul 22; [25\(8\):085041](#)
73. Choi E, Hong HK, Kim HS, Chung YS. Hysteretic behavior of NiTi and NiTiNb SMA wires under recovery or pre-stressing stress. *Journal of Alloys and Compounds*. 2013 Nov 15; [577:S444-7](#)
74. Huang W. Shape memory alloys and their application to actuators for deployable structures [1998](#).
75. Lobo PS, Almeida J, Guerreiro L. Shape memory alloys behaviour: A review. *Procedia Engineering*. 2015 Jan 1; [114:776-83](#)
76. Ozbulut OE, Hurlbauss S. Neuro-fuzzy modeling of temperature-and strain-rate-dependent behavior of NiTi shape memory alloys for seismic applications. *Journal of Intelligent Material Systems and Structures*. 2010 May; [21\(8\):837-49](#)
77. Mansour NA, El-Bab AM, Assal SF, Tabata O. Design, characterization and control of SMA springs-based multi-modal tactile display device for biomedical applications. *Mechatronics*. 2015 Oct 1; [31:255-63](#)

78. Atasoy A, Toptas E, Kuchimov S, Kaplanoglu E, Takka S, Ozkan M. SMA actuated prosthetic finger design. InBiomedical Engineering Meeting (BIYOMUT), 2016 20th National 2016 Nov 3 ([pp. 1-3](#))
79. Ölander A. The crystal structure of AuCd. Zeitschrift für Kristallographie-Crystalline Materials. 1932 Dec 1; [83\(1-6\):145-8](#)
80. Greninger AB, Mooradian VG. Strain transformation in metastable beta copper-zinc and beta copper-Ti alloys. AIME TRANS. 1938; 128:337-69
81. Chang LC, Read TA. Plastic deformation and diffusionless phase changes in metals—the gold-cadmium beta phase. JOM. 1951 Jan 1; [3\(1\):47-52](#)
82. Buehler WJ, Gilfrich JV, Wiley RC. Effect of low-temperature phase changes on the mechanical properties of alloys near composition TiNi. Journal of applied physics. 1963 May; [34\(5\):1475-7](#)
83. Barbarino S, Flores ES, Ajaj RM, Dayyani I, Friswell MI. A review on shape memory alloys with applications to morphing aircraft. Smart Materials and Structures. 2014 Apr 10; [23\(6\):063001](#)
84. Di Cocco V, Iacoviello F, Natali S, Volpe V. Fatigue crack behavior on a Cu-Zn-Al SMA. Frattura ed Integrità Strutturale. 2014 Oct 1 (30):454
85. Omori T, Ando K, Okano M, Xu X, Tanaka Y, Ohnuma I, Kainuma R, Ishida K. Superelastic effect in polycrystalline ferrous alloys. Science. 2011 Jul 1; [333\(6038\):68-71](#)
86. Tejeda-Cruz A, Alvarado-Hernández F, Soto-Parra DE, Ochoa-Gamboa R, Castillo-Villa PO, Flores-Zúñiga H, Haro-Rodríguez S, Santos-Beltrán A, Ríos-Jara D. Microstructure, transformation temperatures, hardness and magnetic properties of $\text{Co}_{36.4+x}\text{Ni}_{33.3-x}\text{Ga}_{30.3}$ ferromagnetic SMA. Journal of Alloys and Compounds. 2010 Jun 11; [499\(2\):183-6](#)
87. Shimizu K, Tadaki T. Shape Memory Alloys, H. Gordon and Breach Science Publishers. 1987
88. Lexcelent C. Shape-memory alloys handbook. John Wiley & Sons; 2013 Apr 8
89. Hodgson DE, Ming WH, Biermann RJ. Shape memory alloys. ASM International, Metals Handbook, Tenth Edition. 1990; 2:897-902
90. Kaluvan S, Park CY, Choi SB. Bio-inspired device: a novel smart MR spring featuring tendril structure. Smart Materials and Structures. 2015 Nov 23; [25\(1\):01LT01](#)
91. Leon RT, DesRoches R, Ocel J, Hess G. Innovative beam column connections using shape memory alloys. InSmart Structures and Materials 2001: Smart Systems for Bridges, Structures, and Highways 2001 Jul 30 [Vol. 4330, pp. 227-238](#)
92. Wang W, Fang C, Liu J. Self-centering beam-to-column connections with combined superelastic SMA bolts and steel angles. Journal of Structural Engineering. 2016 Sep 19; [143\(2\):04016175](#)
93. Wang W, Fang C, Yang X, Chen Y, Ricles J, Sause R. Innovative use of a shape memory alloy ring spring system for self-centering connections. Engineering Structures. 2017 Dec 15; [153:503-15](#)
94. Oudah F, El-Hacha R. Joint performance in concrete beam-column connections reinforced using SMA smart material. Engineering Structures. 2017 Nov 15; [151:745-60](#)
95. McCormick J, DesRoches R, Fugazza D, Auricchio F. Seismic vibration control using superelastic shape memory alloys. Journal of Engineering Materials and Technology. 2006 Jul 1; [128\(3\):294-301](#)
96. Alipour A, Kadkhodaei M, Safaei M. Design, analysis, and manufacture of a tension-compression self-centering damper based on energy dissipation of pre-stretched superelastic shape memory alloy wires. Journal of Intelligent Material Systems and Structures. 2017 Sep; [28\(15\):2129-39](#)
97. Asgarian B, Salari N, Saadati B. Application of intelligent passive devices based on shape memory alloys in seismic control of structures. InStructures 2016 Feb 29 [Vol. 5, pp. 161-169](#)
98. Saedi S, Dizaji FS, Ozbulut OE, Karaca HE. Structural Vibration Control Using High Strength and Damping Capacity Shape Memory Alloys. InDynamics of Civil Structures, Volume 2 2017 (pp. [259-266](#))
99. Minorowicz B, Stefanski F, Sedziak D. Hysteresis modeling and position control of actuator with magnetic shape memory alloy. InCarpathian Control Conference (ICCC), 2016 17th International 2016 May 29 pp. [505-510](#)
100. Kuang Y, Ou J. Self-repairing performance of concrete beams strengthened using superelastic SMA wires in combination with adhesives released from hollow fibers. Smart Materials and Structures. 2008 Feb 19; [17\(2\):025020](#)
101. Billah AM, Alam MS. Seismic performance of concrete columns reinforced with hybrid shape memory alloy (SMA) and fiber reinforced polymer (FRP) bars. Construction and Building Materials. 2012 Mar 1; [28\(1\):730-42](#)
102. Shrestha KC, Saiidi MS, Cruz CA. Advanced materials for control of post-earthquake damage in bridges. Smart Materials and Structures. 2015 Jan 23; [24\(2\):025035](#)
103. Billah AM, Alam MS. Performance-based seismic design of shape memory alloy-reinforced concrete bridge piers. I: Development of performance-based damage states. Journal of Structural Engineering. 2016 Jul 22; [142\(12\):04016140](#)

104. Shin M, Andrawes B. Lateral cyclic behavior of reinforced concrete columns retrofitted with shape memory spirals and FRP wraps. *Journal of Structural Engineering*. 2010 Dec 29; [137\(11\):1282-90](#)
105. Cortés-Puentes WL, Palermo D. SMA tension brace for retrofitting concrete shear walls. *Engineering Structures*. 2017 Jun 1; [140:177-88](#)
106. Wang Y, Backer S, Li VC. A statistical tensile model of fibre reinforced cementitious composites. *Composites*. 1989 May 1; [20\(3\):265-74](#)
107. Öztaş A, Pala M, Özbay E, Kanca E, Caglar N, Bhatti MA. Predicting the compressive strength and slump of high strength concrete using neural network. *Construction and Building Materials*. 2006 Nov 30; [20\(9\):769-75](#)
108. Yıldırım G, Keskin ÖK, Keskin SB, Şahmaran M, Lachemi M. A review of intrinsic self-healing capability of engineered cementitious composites: Recovery of transport and mechanical properties. *Construction and Building Materials*. 2015 Dec 30; [101:10-21](#)
109. Bharatkumar BH, Narayanan R, Raghuprasad BK, Ramachandramurthy DS. Mix proportioning of high performance concrete. *Cement and Concrete Composites*. 2001 Feb 28; [23\(1\):71-80](#)
110. Frangopol DM, Furuta H. Life-cycle cost analysis and design of civil infrastructure systems. 2001
111. Mays GC, editor. Durability of concrete structures: investigation, repair, protection. CRC Press; 2002 Nov 1
112. Shaikh FU, Mihashi H, Kobayakawa A. Corrosion Durability of Reinforcing Steel in Cracked High-Performance Fiber-Reinforced Cementitious Composite Beams. *Journal of Materials in Civil Engineering*. 2014 Oct 9; [27\(8\):04014228](#)
113. Sandvik K, Eie R, Advocaat JD, Godejord A, Hæreid KO, Høyland K, Olsen TO. Offshore structures—a new challenge. In XIV national conference on structural engineering, Acapulco 2004
114. Ahn TH, Kim DJ, Kang SH. Crack self-healing behavior of high performance fiber reinforced cement composites under various environmental conditions. In *Earth and Space 2012: Engineering, Science, Construction, and Operations in Challenging Environments 2012* (pp. 635-640)
115. Neville A. Chloride attack of reinforced concrete: an overview. *Materials and Structures*. 1995 Mar 1; [28\(2\):63](#)
116. Montes P, Bremner TW, Lister DH. Influence of calcium nitrite inhibitor and crack width on corrosion of steel in high performance concrete subjected to a simulated marine environment. *Cement and Concrete Composites*. 2004 Apr 30; [26\(3\):243-53](#)
117. Hosseini F, Gencturk B, Lahpour S, Gil DI. An experimental investigation of innovative bridge columns with engineered cementitious composites and Cu–Al–Mn super-elastic alloys. *Smart Materials and Structures*. 2015 Jul 16; [24\(8\):085029](#)
118. Yunovich M, Thompson NG. Corrosion of highway bridges: Economic impact and control methodologies. *Concrete International*. 2003 Jan 1; [25\(1\):52-7](#)
119. Virmani YP, Clemena GG. Corrosion protection-concrete bridges. 1998 Sep.
120. Mather B, Warner J. Why do concrete repairs fail, interview held at University of Wisconsin, Department of Engineering Professional Development, Wis.
121. Astarlioglu S, Krauthammer T. Response of normal-strength and ultra-high-performance fiber-reinforced concrete columns to idealized blast loads. *Engineering structures*. 2014 Mar 1; [61:1-2](#)
122. Shah AA, Ribakov Y. Recent trends in steel fibered high-strength concrete. *Materials & Design*. 2011 Sep 30; [32\(8\):4122-51](#)
123. Serna P, Arango S, Ribeiro T, Núñez AM, Garcia-Taengua E. Structural cast-in-place SFRC: technology, control criteria and recent applications in Spain. *Materials and Structures*. 2009 Nov 1; [42\(9\):1233](#)
124. Tiberti G, Minelli F, Plizzari G. Reinforcement optimization of fiber reinforced concrete linings for conventional tunnels. *Composites Part B: Engineering*. 2014 Mar 31; [58:199-207](#)
125. Belletti B, Cerioni R, Meda A, Plizzari G. Design aspects on steel fiber-reinforced concrete pavements. *Journal of materials in civil engineering*. 2008 Sep; [20\(9\):599-607](#)
126. Xu Z, Hao H, Li HN. Experimental study of dynamic compressive properties of fibre reinforced concrete material with different fibres. *Materials & Design*. 2012 Jan 31; [33:42-55](#)
127. Jin C, Buratti N, Stacchini M, Savoia M, Cusatis G. Lattice discrete particle modeling of fiber reinforced concrete: Experiments and simulations. *European Journal of Mechanics-A/Solids*. 2016 Jun 30; [57:85-107](#)
128. Zhang W, Zhang N, Zhou Y. Effect of flexural impact on freeze–thaw and deicing salt resistance of steel fiber reinforced concrete. *Materials and Structures*. 2016 Dec 1; [49\(12\):5161-8](#)
129. Tiberti G, Minelli F, Plizzari GA, Vecchio FJ. Influence of concrete strength on crack development in SFRC members. *Cement and Concrete composites*. 2014 Jan 31; [45:176-85](#)
130. Nam J, Kim G, Lee B, Hasegawa R, Hama Y. Frost resistance of polyvinyl alcohol fiber and polypropylene fiber reinforced cementitious composites under freeze thaw cycling. *Composites Part B: Engineering*. 2016 Apr 1; [90:241-50](#)

131. Fantilli AP, Chiaia B. The work of fracture in the eco-mechanical performances of structural concrete. *Journal of Advanced Concrete Technology*. 2013 Oct 5; [11\(10\):282-90](#)
132. Müller HS, Haist M, Vogel M. Assessment of the sustainability potential of concrete and concrete structures considering their environmental impact, performance and lifetime. *Construction and Building Materials*. 2014 Sep 30; [67:321-37](#)
133. Di Prisco M, Plizzari G, Vandewalle L. Fibre reinforced concrete: new design perspectives. *Materials and Structures*. 2009 Nov 1; [42\(9\):1261-81](#)
134. Lee JY, Shin HO, Yoo DY, Yoon YS. Structural response of steel-fiber-reinforced concrete beams under various loading rates. *Engineering Structures*. 2018 Feb 1; [156:271-83](#)
135. Sun X, Zhao K, Li Y, Huang R, Ye Z, Zhang Y, Ma J. A study of strain-rate effect and fiber reinforcement effect on dynamic behavior of steel fiber-reinforced concrete. *Construction and Building Materials*. 2018 Jan 15; [158:657-69](#)
136. Hakeem IY. Characterization of an ultra-high performance concrete (Doctoral dissertation, King Fahd University of Petroleum and Minerals (Saudi Arabia))
137. Zhang W, Chen S, Liu Y. Effect of weight and drop height of hammer on the flexural impact performance of fiber-reinforced concrete. *Construction and Building Materials*. 2017 Jun 1; [140:31-5](#)
138. Hussein L, Amleh L. Structural behavior of ultra-high performance fiber reinforced concrete-normal strength concrete or high strength concrete composite members. *Construction and Building Materials*. 2015 Sep 15; [93:1105-16](#)
139. Karadelis JN, Lin Y. Flexural strengths and fibre efficiency of steel-fibre-reinforced, roller-compacted, polymer modified concrete. *Construction and Building Materials*. 2015 Sep 15; [93:498-505](#)
140. Yoo DY, Banthia N, Yoon YS. Impact resistance of reinforced ultra-high-performance concrete beams with different steel fibers. *ACI Structural Journal*. 2017 Jan 1; [114\(1\):113](#)
141. Dagenais MA, Massicotte B, Boucher-Proulx G. Seismic Retrofitting of Rectangular Bridge Piers with Deficient Lap Splices Using Ultrahigh-Performance Fiber-Reinforced Concrete. *Journal of Bridge Engineering*. 2017 Nov 21; [23\(2\):04017129](#)
142. Aoude H, Belghiti M, Cook WD, Mitchell D. Response of steel fiber-reinforced concrete beams with and without stirrups. *ACI Structural Journal*. 2012 May 1; 109(3):359
143. Imam M, Vandewalle L, Mortelmans F, Van Gemert D. Shear domain of fibre-reinforced high-strength concrete beams. *Engineering structures*. 1997 Sep 1; [19\(9\):738-47](#)
144. Al-Osta MA, Isa MN, Baluch MH, Rahman MK. Flexural behavior of reinforced concrete beams strengthened with ultra-high performance fiber reinforced concrete. *Construction and Building Materials*. 2017 Mar 1; [134:279-96](#)
145. Jiang C, Fan K, Wu F, Chen D. Experimental study on the mechanical properties and microstructure of chopped basalt fibre reinforced concrete. *Materials & Design*. 2014 Jun 30; [58:187-93](#)
146. Branston J, Das S, Kenno SY, Taylor C. Mechanical behaviour of basalt fibre reinforced concrete. *Construction and Building Materials*. 2016 Oct 15; [124:878-86](#)
147. Colombo C, Vergani L, Burman M. Static and fatigue characterisation of new basalt fibre reinforced composites. *Composite Structures*. 2012 Feb 29; [94\(3\):1165-74](#)
148. Zhao YR, Wang L, Lei ZK, Han XF, Shi JN. Study on bending damage and failure of basalt fiber reinforced concrete under freeze-thaw cycles. *Construction and Building Materials*. 2018 Feb 28; [163:460-70](#)
149. Fischer G, Li VC. Effect of fiber reinforcement on the response of structural members. *Engineering Fracture Mechanics*. 2007 Jan 31; [74\(1\):258-72](#)
150. Rasheed MA, Prakash SS. Mechanical behavior of sustainable hybrid-synthetic fiber reinforced cellular light weight concrete for structural applications of masonry. *Construction and Building Materials*. 2015 Nov 15; [98:631-40](#)
151. Stähli P, Van Mier JG. Manufacturing, fibre anisotropy and fracture of hybrid fibre concrete. *Engineering fracture mechanics*. 2007 Jan 31; [74\(1\):223-42](#)
152. Betterman LR, Ouyang C, Shah SP. Fiber-matrix interaction in microfiber-reinforced mortar. *Advanced Cement Based Materials*. 1995 Mar 1; [2\(2\):53-61](#)
153. Kwon S, Nishiwaki T, Kikuta T, Mihashi H. Development of Ultra-High-Performance Hybrid Fiber-Reinforced Cement-Based Composites. *ACI Materials Journal*. 2014 May 1; 111(3)
154. Banthia N, Sappakittipakorn M. Toughness enhancement in steel fiber reinforced concrete through fiber hybridization. *Cement and Concrete Research*. 2007 Sep 30; [37\(9\):1366-72](#)
155. Chi Y, Xu L, Zhang Y. Experimental Study on Hybrid Fiber-Reinforced Concrete Subjected to Uniaxial Compression. *Journal of Materials in Civil Engineering*. 2012 Dec 19; [26\(2\):211-8](#)

156. Qian CX, Stroeven P. Development of hybrid polypropylene-steel fibre-reinforced concrete. *Cement and Concrete Research*. 2000 Jan 31; [30\(1\):63-9](#)
157. Yao W, Li J, Wu K. Mechanical properties of hybrid fiber-reinforced concrete at low fiber volume fraction. *Cement and concrete research*. 2003 Jan 31; [33\(1\):27-30](#)
158. Ibrahim SM, Almusallam TH, Al-Salloum YA, Abadel AA, Abbas H. Strain Rate Dependent Behavior and Modeling for Compression Response of Hybrid Fiber Reinforced Concrete. *Latin American Journal of Solids and Structures*. 2016 Sep; [13\(9\):1695-715](#)
159. Horszczaruk E. Abrasion resistance of high-strength concrete in hydraulic structures. *Wear*. 2005 Jul 1; [259\(1-6\):62-9](#)
160. Wongprachum W, Sappakittipakorn M, Jiemvarangkul P. Resistance to Underwater Abrasion of Fiber Reinforced Cement Mortar. In *Key Engineering Materials 2017 (Vol. 728, pp. 379-383)* Trans Tech Publications
161. Ali MA, El-Salakawy E. Seismic performance of GFRP-reinforced concrete rectangular columns. *Journal of Composites for Construction*. 2015 Oct 30; [20\(3\):04015074](#)
162. Mohamed HM, Ali AH, Benmokrane B. Behavior of circular concrete members reinforced with carbon-FRP bars and spirals under shear. *Journal of Composites for Construction*. 2016 Aug 17; [21\(2\):04016090](#)
163. Mukhopadhyay S, Khatana S. A review on the use of fibers in reinforced cementitious concrete. *Journal of Industrial Textiles*. 2015 Sep; [45\(2\):239-64](#)
164. Ralegaonkar R, Gavali H, Aswath P, Abolmaali S. Application of chopped basalt fibers in reinforced mortar: A review. *Construction and Building Materials*. 2018 Mar 10; [164:589-602](#)
165. Nossoni G, Harichandran RS, Baiyasi MI. Rate of reinforcement corrosion and stress concentration in concrete columns repaired with bonded and unbonded FRP wraps. *Journal of Composites for Construction*. 2014 Dec 12; [19\(5\):04014080](#)
166. Capozucca R, Domizi J, Magagnini E. Damaged RC beams strengthened with NSM CFRP rectangular rods under vibration in different constrain conditions. *Composite Structures*. 2016 Oct 15; [154:660-83](#)
167. Seo SY, Lee MS, Feo L. Flexural analysis of RC beam strengthened by partially de-bonded NSM FRP strip. *Composites Part B: Engineering*. 2016 Sep 15; [101:21-30](#)
168. Alyousef R, Topper T, Al-Mayah A. Effect of FRP wrapping on fatigue bond behavior of spliced concrete beams. *Journal of Composites for Construction*. 2015 Jun 18; [20\(1\):04015030](#)
169. Sharaky IA, Reda RM, Ghanem M, Seleem MH, Sallam HE. Experimental and numerical study of RC beams strengthened with bottom and side NSM GFRP bars having different end conditions. *Construction and Building Materials*. 2017 Sep 15; [149:882-903](#)
170. Chen GM, Li SW, Fernando D, Liu PC, Chen JF. Full-range FRP failure behaviour in RC beams shear-strengthened with FRP wraps. *International Journal of Solids and Structures*. 2017 Oct 15; [125:1-21](#)
171. Banthia N, Zanotti C, Sappakittipakorn M. Sustainable fiber reinforced concrete for repair applications. *Construction and Building Materials*. 2014 Sep 30; [67:405-12](#)
172. Fantilli AP, Sicardi S, Dotti F. The use of wool as fiber-reinforcement in cement-based mortar. *Construction and Building Materials*. 2017 May 15; [139:562-9](#)
173. Mallat A, Alliche A. Mechanical investigation of two fiber-reinforced repair mortars and the repaired system. *Construction and Building Materials*. 2011 Apr 1; [25\(4\):1587-95](#)
174. Bentur A, Mindess S. *Fibre reinforced cementitious composites*. CRC Press; 2006 Nov 22
175. Dawood ET, Ramli M. The effect of using high strength flowable system as repair material. *Composites Part B: Engineering*. 2014 Feb 1; [57:91-5](#)
176. Hsie M, Tu C, Song PS. Mechanical properties of polypropylene hybrid fiber-reinforced concrete. *Materials Science and Engineering: A*. 2008 Oct 25; [494\(1-2\):153-7](#)
177. Banthia N, Chokri K, Ohama Y, Mindess S. Fiber-reinforced cement based composites under tensile impact. *Advanced Cement Based Materials*. 1994 Mar 1; [1\(3\):131-41](#)
178. Spadea S, Farina I, Carrafiello A, Fraternali F. Recycled nylon fibers as cement mortar reinforcement. *Construction and Building Materials*. 2015 Apr 1; [80:200-9](#)
179. Izaguirre A, Lanas J, Alvarez JI. Effect of a polypropylene fibre on the behaviour of aerial lime-based mortars. *Construction and Building Materials*. 2011 Feb 1; [25\(2\):992-1000](#)
180. Grdic ZJ, Curcic GA, Ristic NS, Despotovic IM. Abrasion resistance of concrete micro-reinforced with polypropylene fibers. *Construction and Building Materials*. 2012 Feb 1; [27\(1\):305-12](#)
181. Cavdar A. Investigation of freeze-thaw effects on mechanical properties of fiber reinforced cement mortars. *Composites Part B: Engineering*. 2014 Mar 1; [58:463-72](#)
182. Zanotti C, Banthia N, Plizzari G. A study of some factors affecting bond in cementitious fiber reinforced repairs. *Cement and Concrete Research*. 2014 Sep 1; [63:117-26](#)

183. Luo J, Li Q, Zhao T, Gao S, Sun S. Bonding and toughness properties of PVA fibre reinforced aqueous epoxy resin cement repair mortar. *Construction and Building Materials*. 2013 Dec 1; [49:766-71](#)
184. Dawood ET, Ramli M. High strength characteristics of cement mortar reinforced with hybrid fibres. *Construction and Building Materials*. 2011 May 1; [25\(5\):2240-7](#)
185. Iucolano F, Liguori B, Colella C. Fibre-reinforced lime-based mortars: A possible resource for ancient masonry restoration. *Construction and Building Materials*. 2013 Jan 1; [38:785-9](#)
186. Aziz MA, Paramasivam P, Lee SL. Prospects for natural fibre reinforced concretes in construction. *International Journal of Cement Composites and Lightweight Concrete*. 1981 May 1; [3\(2\):123-32](#)
187. Cook DJ, Pama RP, Weerasinghe HL. Coir fibre reinforced cement as a low cost roofing material. *Building and environment*. 1978 Jan 1; [13\(3\):193-8](#)
188. Uzomaka OJ. Characteristics of akwara as a reinforcing fibre. *Magazine of Concrete Research*. 1976 Sep; [28\(96\):162-7](#)
189. Ramakrishna G, Sundararajan T. Impact strength of a few natural fibre reinforced cement mortar slabs: a comparative study. *Cement and concrete composites*. 2005 May 1; [27\(5\):547-53](#)
190. Pacheco-Torgal F, Jalali S. Cementitious building materials reinforced with vegetable fibres: A review. *Construction and Building Materials*. 2011 Feb 1; [25\(2\):575-81](#)
191. Vajje S. Study on addition of the natural fibers into concrete. *International Journal of Scientific & Technology Research*. 2013 Nov 25; 2(11):213-8
192. Lewis G, Premalal M. Natural vegetable fibres as reinforcement in cement sheets. *Magazine of Concrete Research*. 1979 Jun; [31\(107\):104-8](#)
193. Xu G, Hannant DJ. Synergistic interaction between fibrillated polypropylene networks and glass fibres in a cement-based composite. *Cement and Concrete Composites*. 1991 Jan 1; [13\(2\):95-106](#)
194. Soroushian P, Tlili A, Alhozaimy A, Khan A. Development and characterization of hybrid polyethylene-fibre-reinforced cement composites. *Construction and Building Materials*. 1993 Dec 1; [7\(4\):221-9](#)
195. Walton PL, Majumdar AJ. Cement-based composites with mixtures of different types of fibres. *Composites*. 1975 Sep 1; [6\(5\):209-16](#)
196. Kim DJ, Naaman AE, El-Tawil S. Comparative flexural behavior of four fiber reinforced cementitious composites. *Cement and concrete Composites*. 2008 Nov 1; [30\(10\):917-28](#)
197. Soe KT, Zhang YX, Zhang LC. Impact resistance of hybrid-fiber engineered cementitious composite panels. *Composite structures*. 2013 Oct 1; [104:320-30](#)
198. Şahmaran M, Li VC. Durability of mechanically loaded engineered cementitious composites under highly alkaline environments. *Cement and Concrete Composites*. 2008 Feb 1; [30\(2\):72-81](#)
199. Funke H, Gelbrich S, Ehrlich A. Development of a new hybrid material of textile reinforced concrete and glass fibre reinforced plastic. *Procedia Materials Science*. 2013 Jan 1; [2:103-10](#)
200. Banthia N, Majdzadeh F, Wu J, Bindiganavile V. Fiber synergy in Hybrid Fiber Reinforced Concrete (HyFRC) in flexure and direct shear. *Cement and Concrete Composites*. 2014 Apr 1; [48:91-7](#)
201. Tosun-Felekoglu K, Felekoglu B. Effects of fibre hybridization on multiple cracking potential of cement-based composites under flexural loading. *Construction and Building Materials*. 2013 Apr 1; [41:15-20](#)
202. Li VC. Engineered cementitious composites-tailored composites through micromechanical modeling. 1998
203. Li VC. Engineered Cementitious Composites (ECC) Material, Structural, and Durability Performance. 2008
204. Li VC, Kong HJ, Bike SG. Fiber reinforced high performance concrete material. *High Performance Concrete-Workability, Strength and Durability*. 2000; 71-86
205. Kawamata A, Mihashi H, Fukuyama H. Properties of hybrid fiber reinforced cement-based composites. *Journal of Advanced Concrete Technology*. 2003; [1\(3\):283-90](#)
206. Li VC, Wang S. Flexural behaviors of glass fiber-reinforced polymer (GFRP) reinforced engineered cementitious composite beams. *Materials Journal*. 2002 Jan 1; 99(1):11-21
207. Fischer G, Li VC. Effect of matrix ductility on deformation behavior of steel-reinforced ECC flexural members under reversed cyclic loading conditions. *Structural Journal*. 2002 Nov 1; 99(6):781-90
208. Kesner KE, Billington SL. Experimental response of precast infill panel connections and panels made with DFRCC. *Journal of Advanced Concrete Technology*. 2003; [1\(3\):327-33](#)
209. Parra-Montesinos G, Wight JK. Seismic response of exterior RC column-to-steel beam connections. *Journal of structural engineering*. 2000 Oct; [126\(10\):1113-21](#)
210. Sakai K, Noguchi T. *The sustainable use of concrete*. CRC press; 2012 Aug 30
211. Fantilli AP, Chiaia B. Eco-mechanical performances of cement-based materials: An application to self-consolidating concrete. *Construction and Building Materials*. 2013 Mar 1; [40:189-96](#)

212. Kim J, Kim DJ, Park SH, Zi G. Investigating the flexural resistance of fiber reinforced cementitious composites under biaxial condition. *Composite Structures*. 2015 Apr 30; [122:198-208](#)
213. Kosa K, Wakita K, Goda H, Ogawa A. Seismic strengthening of piers with partial use of high ductility cement. *Advances in Construction Materials* 2007. 2007:269-77
214. Dehghani A, Nateghi-Alahi F, Fischer G. Engineered cementitious composites for strengthening masonry infilled reinforced concrete frames. *Engineering Structures*. 2015 Dec 15; [105:197-208](#)
215. Zhou J, Pan J, Leung CK. Mechanical behavior of fiber-reinforced engineered cementitious composites in uniaxial compression. *Journal of materials in civil engineering*. 2014 Jan 17; [27\(1\):04014111](#)
216. Zhang Y, Bai S, Zhang Q, Zhang X. Failure behavior of strain hardening cementitious composites for shear strengthening RC member. *Construction and Building Materials*. 2015 Mar 1; [78:470-3](#)
217. Hou L, Xu S, Liu H, Chen D. Flexural and interface behaviors of reinforced concrete/ultra-high toughness cementitious composite (RC/UHTCC) beams. *Journal of Advanced Concrete Technology*. 2015 Feb 23; [13\(2\):82-93](#)
218. Maalej M, Quek ST, Zhang J. Behavior of hybrid-fiber engineered cementitious composites subjected to dynamic tensile loading and projectile impact. *Journal of Materials in Civil Engineering*. 2005 Apr; [17\(2\):143-52](#)
219. Brandt AM. *Cement-based composites: materials, mechanical properties and performance*. CRC Press; 2009 Jan 29
220. Şahmaran M, Al-Emam M, Yıldırım G, Şimşek YE, Erdem TK, Lachemi M. High-early-strength ductile cementitious composites with characteristics of low early-age shrinkage for repair of infrastructures. *Materials and Structures*. 2015 May 1; [48\(5\):1389-403](#)
221. Yu JH, Chen W, Yu MX, Hua YE. The microstructure of self-healed PVA ECC under wet and dry cycles. *Materials Research*. 2010 Jun; [13\(2\):225-31](#)
222. Yang EH, Wang S, Yang Y, Li VC. Fiber-bridging constitutive law of engineered cementitious composites. *Journal of advanced concrete technology*. 2008; [6\(1\):181-93](#)
223. Li VC, Wang S. Microstructure variability and macroscopic composite properties of high performance fiber reinforced cementitious composites. *Probabilistic engineering mechanics*. 2006 Jul 31; [21\(3\):201-6](#)
224. Fan S, Li M. X-ray computed microtomography of three-dimensional microcracks and self-healing in engineered cementitious composites. *Smart materials and structures*. 2014 Dec 8; [24\(1\):015021](#)
225. Li VC, Mishra DK, Naaman AE, Wight JK, LaFave JM, Wu HC, Inada Y. On the shear behavior of engineered cementitious composites. *Advanced Cement Based Materials*. 1994 Mar 1; [1\(3\):142-9](#)
226. Maalej M, Hashida T, Li VC. Effect of Fiber Volume Fraction on the Off-Crack-Plane Fracture Energy in Strain-Hardening Engineered Cementitious Composites. *Journal of the American Ceramic Society*. 1995 Dec 1; [78\(12\):3369-75](#)
227. Li VC, Maalej M. Toughening in cement based composites. Part II: Fiber reinforced cementitious composites. *Cement and Concrete Composites*. 1996 Jan 1; [18\(4\):239-49](#)
228. Li VC, Wu HC, Maalej M, Mishra DK, Hashida T. Tensile behavior of engineered cementitious composites with discontinuous random steel fibers. *J Am Ceram Soc*. 1996; 79(1):74-8
229. Soe KT, Zhang YX, Zhang LC. Material properties of a new hybrid fibre-reinforced engineered cementitious composite. *Construction and Building Materials*. 2013 Jun 30; [43:399-407](#)
230. Cho CG, Kim YY, Feo L, Hui D. Cyclic responses of reinforced concrete composite columns strengthened in the plastic hinge region by HPFRC mortar. *Composite Structures*. 2012 Jun 30; [94\(7\):2246-53](#)
231. Kang SB, Tan KH, Yang EH. Progressive collapse resistance of precast beam-column sub-assemblages with engineered cementitious composites. *Engineering Structures*. 2015 Sep 1; [98:186-200](#)
232. Lepech M, Li VC. Water permeability of cracked cementitious composites 2005
233. Maalej M, Li VC. Introduction of strain-hardening engineered cementitious composites in design of reinforced concrete flexural members for improved durability. *Structural Journal*. 1995 Mar 1; 92(2):167-76
234. Yang EH, Yang Y, Li VC. Use of high volumes of fly ash to improve ECC mechanical properties and material greenness. *ACI materials journal*. 2007 Nov 1; 104(6):620-8
235. Mehta PK. High-performance, high-volume fly ash concrete for sustainable development. In *Proceedings of the international workshop on sustainable development and concrete technology 2004* May 20 (pp. 3-14). Ames, IA, USA: Iowa State University.
236. Li VC, Wang S, Wu C. Tensile strain-hardening behavior of polyvinyl alcohol engineered cementitious composite (PVA-ECC). *ACI Materials Journal-American Concrete Institute*. 2001 Nov 1; 98(6):483-92
237. Lee BY, Cho CG, Lim HJ, Song JK, Yang KH, Li VC. Strain hardening fiber reinforced alkali-activated mortar—a feasibility study. *Construction and Building Materials*. 2012 Dec 31; [37:15-20](#)

238. Park SH, Kim DJ, Ryu GS, Koh KT. Tensile behavior of ultra high performance hybrid fiber reinforced concrete. *Cement and Concrete Composites*. 2012 Feb 29; [34\(2\):172-84](#)
239. Ranade R, Li VC, Stults MD, Heard WF, Rushing TS. Composite Properties of High-Strength, High-Ductility Concrete. *ACI Materials Journal*. 2013 Jul 1; 110(4)
240. Singha K. A short review on basalt fiber. *International Journal of Textile Science*. 2012; 1(4):19-28
241. Choi JI, Lee BY. Bonding properties of basalt fiber and strength reduction according to fiber orientation. *Materials*. 2015 Sep 30; [8\(10\):6719-27](#)
242. Swamy RN. RILEM Symposium 1975 Fibre Reinforced Cement and Concrete. *Matériaux et Construction*. 1976 Sep 1; 9(5):375-7
243. Roumaldi JP, Batson GB. Mechanics of crack arrest in concrete. 2008
244. Van Chanh N. Steel fiber reinforced concrete. In *Faculty of Civil Engineering Ho chi minh City university of Technology. Seminar Material 2004* (pp. 108-116)
245. Kosa K, Naaman AE. Corrosion of steel fiber reinforced concrete. *Materials Journal*. 1990 Jan 1; 87(1):27-37
246. Li GY, Wang PM, Zhao X. Mechanical behavior and microstructure of cement composites incorporating surface-treated multi-walled carbon nanotubes. *Carbon*. 2005 May 31; [43\(6\):1239-45](#)
247. Musso S, Tulliani JM, Ferro G, Tagliaferro A. Influence of carbon nanotubes structure on the mechanical behavior of cement composites. *Composites Science and Technology*. 2009 Sep 30; [69\(11\):1985-90](#)
248. Konsta-Gdoutos MS, Metaxa ZS, Shah SP. Multi-scale mechanical and fracture characteristics and early-age strain capacity of high performance carbon nanotube/cement nanocomposites. *Cement and Concrete Composites*. 2010 Feb 28; [32\(2\):110-5](#)
249. Makar JM, Chan GW. Growth of Cement Hydration Products on Single-Walled Carbon Nanotubes. *Journal of the American Ceramic Society*. 2009 Jun 1; [92\(6\):1303-10](#)
250. Ferro G, Tulliani JM, Lopez A, Jagdale P. New cementitious composite building material with enhanced toughness. *Theoretical and applied fracture mechanics*. 2015 Apr 30; [76:67-74](#)
251. Cao M, Zhang C, Wei J. Microscopic reinforcement for cement based composite materials. *Construction and Building Materials*. 2013 Mar 31; [40:14-25](#)
252. Figarol A, Pourchez J, Boudard D, Forest V, Tulliani JM, Lecompte JP, Cottier M, Bernache-Assollant D, Grosseau P. Biological response to purification and acid functionalization of carbon nanotubes. *Journal of Nanoparticle Research*. 2014 Jul 1; [16\(7\):2507](#)
253. Ong KC, Basheerkhan M, Paramasivam P. Resistance of fibre concrete slabs to low velocity projectile impact. *Cement and Concrete Composites*. 1999 Dec 1; [21\(5\):391-401](#)
254. Kong HJ, Bike SG, Li VC. Constitutive rheological control to develop a self-consolidating engineered cementitious composite reinforced with hydrophilic poly (vinyl alcohol) fibers. *Cement and Concrete Composites*. 2003 Apr 30; [25\(3\):333-41](#)
255. Li VC, Wang S, Wu C. Tensile strain-hardening behavior of polyvinyl alcohol engineered cementitious composite (PVA-ECC). *ACI Materials Journal-American Concrete Institute*. 2001 Nov 1; 98(6):483-92
256. Said SH, Razak HA, Othman I. Flexural behavior of engineered cementitious composite (ECC) slabs with polyvinyl alcohol fibers. *Construction and Building Materials*. 2015 Jan 30; [75:176-88](#)
257. Dry C. Matrix cracking repair and filling using active and passive modes for smart timed release of chemicals from fibers into cement matrices. *Smart Materials and Structures*. 1994 Jun; [3\(2\):118](#)
258. Dry C. Procedures developed for self-repair of polymer matrix composite materials. *Composite structures*. 1996 Jul 1; [35\(3\):263-9](#)
259. Dry C, McMillan W. Three-part methyl methacrylate adhesive system as an internal delivery system for smart responsive concrete. *Smart Materials and Structures*. 1996 Jun; [5\(3\):297](#)
260. Li VC, Lim YM, Chan YW. Feasibility study of a passive smart self-healing cementitious composite. *Composites Part B: Engineering*. 1998 Nov 30; [29\(6\):819-27](#)
261. Motuku MJ, Vaidya UK, Janowski GM. Parametric studies on self-repairing approaches for resin infused composites subjected to low velocity impact. *Smart Materials and Structures*. 1999 Oct; [8\(5\):623](#)
262. Bleay SM, Loader CB, Hawyes VJ, Humberstone L, Curtis PT. A smart repair system for polymer matrix composites. *Composites Part A: Applied Science and Manufacturing*. 2001 Dec 31; [32\(12\):1767-76](#)
263. Pang JW, Bond IP. A hollow fibre reinforced polymer composite encompassing self-healing and enhanced damage visibility. *Composites Science and Technology*. 2005 Sep 30; [65\(11\):1791-9](#)
264. Nishiwaki T, Mihashi H, Jang BK, Miura K. Development of self-healing system for concrete with selective heating around crack. *Journal of Advanced Concrete Technology*. 2006; [4\(2\):267-75](#)
265. Thao TD, Johnson TJ, Tong QS, Dai PS. Implementation of self-healing in concrete—proof of concept. *The IES Journal Part A: Civil & Structural Engineering*. 2009 May 1; [2\(2\):116-25](#)

266. Joseph C, Jefferson AD, Isaacs B, Lark RJ, Gardner DR. Experimental investigation of adhesive-based self-healing of cementitious materials. *Magazine of Concrete Research*. 2010; [62\(11\):831-43](#)
267. Homma D, Mihashi H, Nishiwaki T. Self-healing capability of fibre reinforced cementitious composites. *Journal of Advanced Concrete Technology*. 2009 Jun 30; [7\(2\):217-28](#)
268. Nishiwaki T. Fundamental study on development of intelligent concrete with self-healing capability. Japan, Tohoku University, Master's thesis. 1997
269. White SR, Sottos NR, Geubelle PH, Moore JS, Kessler M, Sriram SR, Brown EN, Viswanathan S. Autonomic healing of polymer composites. *Nature*. 2001 Feb 15; [409\(6822\):794-7](#)
270. Boh B, Šumiga B. Microencapsulation technology and its applications in building construction materials. *RMZ–Materials and Geoenvironment*. 2008; 55(3):329-44
271. Huang H, Ye G, Leung C, Wan KT. Application of sodium silicate solution as self-healing agent in cementitious materials. In *International RILEM conference on advances in construction materials through science and engineering 2011 Sep 5* (pp. 530-536). RILEM Publications SARL: Hong Kong, China.
272. Van Tittelboom K, De Belie N, De Muynck W, Verstraete W. Use of bacteria to repair cracks in concrete. *Cement and Concrete Research*. 2010 Jan 31; [40\(1\):157-66](#)
273. Wiktor V, Jonkers HM. Quantification of crack-healing in novel bacteria-based self-healing concrete. *Cement and Concrete Composites*. 2011 Aug 31; [33\(7\):763-70](#)
274. Wang J, Van Tittelboom K, De Belie N, Verstraete W. Use of silica gel or polyurethane immobilized bacteria for self-healing concrete. *Construction and building materials*. 2012 Jan 31; [26\(1\):532-40](#)
275. Wang JY, Snoeck D, Van Vlierberghe S, Verstraete W, De Belie N. Application of hydrogel encapsulated carbonate precipitating bacteria for approaching a realistic self-healing in concrete. *Construction and building materials*. 2014 Oct 15; [68:110-9](#)
276. Kishi T, Ahn TH, Hosoda A, Suzuki S, Takaoka H. Self-healing behaviour by cementitious recrystallization of cracked concrete incorporating expansive agent. In *Proceedings of the First International Conference on Self-healing Materials*, 18-20 April 2007 Apr 18. Noordwijk aan Zee
277. Ahn TH, Kishi T. Crack self-healing behavior of cementitious composites incorporating various mineral admixtures. *Journal of Advanced Concrete Technology*. 2010 Jun 30; [8\(2\):171-86](#)
278. Sisomphon K, Copuroglu O, Koenders EA. Surface crack self-healing behaviour of mortars with expansive additives, [2011](#)
279. Sakai Y, Kitagawa Y, Fukuta T, Iiba M. Experimental study on enhancement of self-restoration of concrete beams using SMA wire. In *Smart Structures and Materials 2003: Smart Systems and Nondestructive Evaluation for Civil Infrastructures 2003 Aug 18* ([Vol. 5057, pp. 178-187](#)). International Society for Optics and Photonics
280. Song G, Mo YL. Increasing concrete structural survivability using smart materials. A proposal submitted to Grants to Enhance and Advance Research (GEAR), University of Houston. 2003 Jan.
281. Song G, Ma N, Li HN. Applications of shape memory alloys in civil structures. *Engineering structures*. 2006 Jul 31; [28\(9\):1266-74](#)
282. Jefferson A, Joseph C, Lark R, Isaacs B, Dunn S, Weager B. A new system for crack closure of cementitious materials using shrinkable polymers. *Cement and Concrete Research*. 2010 May 31; [40\(5\):795-801](#)
283. Qian S, Zhou J, De Rooij MR, Schlangen E, Ye G, Van Breugel K. Self-healing behavior of strain hardening cementitious composites incorporating local waste materials. *Cement and Concrete Composites*. 2009 Oct 31; [31\(9\):613-21](#)
284. Yang Y, Lepech MD, Yang EH, Li VC. Autogenous healing of engineered cementitious composites under wet-dry cycles. *Cement and Concrete Research*. 2009 May 31; [39\(5\):382-90](#)
285. Kan LL, Shi HS, Sakulich AR, Li VC. Self-Healing Characterization of Engineered Cementitious Composite Materials. *ACI Materials journal*. 2010 Nov 1; 107(6)
286. Herbert EN, Li VC. Self-healing of microcracks in engineered cementitious composites (ECC) under a natural environment. *Materials*. 2013 Jul 15; [6\(7\):2831-45](#)
287. Özbay E, Şahmaran M, Lachemi M, Yücel HE. Self-Healing of Microcracks in High-Volume Fly-Ash-Incorporated Engineered Cementitious Composites. *ACI Materials Journal*. 2013 Jan 1; 110(1)
288. Sahmaran M, Yildirim G, Ozbay E, Ahmed K, Lachemi M. Self-healing ability of cementitious composites: effect of addition of pre-soaked expanded perlite. *Magazine of Concrete Research*. 2014 Jan 1; 66(8):409-19
289. Yildirim G, Sahmaran M, Ahmed HU. Influence of hydrated lime addition on the self-healing capability of high-volume fly ash incorporated cementitious composites. *Journal of Materials in Civil Engineering*. 2014 Aug 14; [27\(6\):04014187](#)
290. Yang Y, Lepech MD, Yang EH, Li VC. Autogenous healing of engineered cementitious composites under wet-dry cycles. *Cement and Concrete Research*. 2009 May 31; [39\(5\):382-90](#)

- 291.Li VC, Herbert E. Robust self-healing concrete for sustainable infrastructure. *Journal of Advanced Concrete Technology*. 2012 Jun 28; [10\(6\):207-18](#)
- 292.Li VC, Yang EH. Self healing in concrete materials. In *Self healing materials 2007* (pp. [161-193](#)). Springer, Dordrecht.
- 293.Jacobsen S, Marchand J, Hornain H. SEM observations of the microstructure of frost deteriorated and self-healed concretes. *Cement and Concrete Research*. 1995 Dec 31; [25\(8\):1781-90](#)
- 294.Ismail M, Toumi A, François R, Gagné R. Effect of crack opening on the local diffusion of chloride in cracked mortar samples. *Cement and concrete research*. 2008 Aug 31; [38\(8\):1106-11](#)
- 295.Reinhardt HW, Jooss M. Permeability and self-healing of cracked concrete as a function of temperature and crack width. *Cement and Concrete Research*. 2003 Jul 31; [33\(7\):981-5](#)
- 296.Aldea CM, Song WJ, Popovics JS, Shah SP. Extent of healing of cracked normal strength concrete. *Journal of materials in civil engineering*. 2000 Feb; [12\(1\):92-6](#)
- 297.Clear CA. The effects of autogenous healing upon the leakage of water through cracks in concrete. 1985
- 298.Neville AM. *Properties of concrete*. London: Longman; 1995 Jan.
- 299.Neville A. Autogenous healing—A concrete miracle? *Concrete international*. 2002 Nov 1; [24\(11\):76-82](#)
- 300.Edvardsen C. Water permeability and autogenous healing of cracks in concrete. *Materials Journal*. 1999 Jul 1; [96\(4\):448-54](#)
- 301.Alyousif A, Lachemi M, Yildirim G, Şahmaran M. Effect of self-healing on the different transport properties of cementitious composites. *Journal of Advanced Concrete Technology*. 2015 Mar 4; [13\(3\):112-23](#)
- 302.Siad H, Alyousif A, Keskin OK, Keskin SB, Lachemi M, Sahmaran M, Hossain KM. Influence of limestone powder on mechanical, physical and self-healing behavior of engineered cementitious composites. *Construction and Building Materials*. 2015 Nov 30; [99:1-0](#)
- 303.Yildirim G, Sahmaran M, Balcikanli M, Ozbay E, Lachemi M. Influence of cracking and healing on the gas permeability of cementitious composites. *Construction and Building Materials*. 2015 Jun 15; [85:217-26](#)
- 304.Lawler JS, Zampini D, Shah SP. Microfiber and macrofiber hybrid fiber-reinforced concrete. *Journal of Materials in Civil Engineering*. 2005 Oct; [17\(5\):595-604](#)
- 305.Zhang L. Impact resistance of high strength fiber reinforced concrete (Doctoral dissertation, University of British Columbia)
- 306.Shajil N, Srinivasan SM, Santhanam M. Self-centering of shape memory alloy fiber reinforced cement mortar members subjected to strong cyclic loading. *Materials and structures*. 2013 Apr 1; [46\(4\):651-61](#)
- 307.Maji AK, Negret I. Smart prestressing with shape-memory alloy. *Journal of engineering mechanics*. 1998 Oct; [124\(10\):1121-8](#)
- 308.Kim DJ, Kim HA, Chung YS, Choi E. Pullout resistance of straight NiTi shape memory alloy fibers in cement mortar after cold drawing and heat treatment. *Composites Part B: Engineering*. 2014 Dec 1; [67:588-94](#)
- 309.Choi E, Kim D, Chung YS, Nam TH. Bond–slip characteristics of SMA reinforcing fibers obtained by pull-out tests. *Materials Research Bulletin*. 2014 Oct 1; [58:28-31](#)
- 310.Moser K, Bergamini A, Christen R, Czaderski C. Feasibility of concrete prestressed by shape memory alloy short fibers. *Materials and Structures*. 2005 Jun 1; [38\(5\):593-600](#)
- 311.Choi E, Kim DJ, Chung YS, Kim HS, Jung C. Crack-closing of cement mortar beams using NiTi cold-drawn SMA short fibers. *Smart Materials and Structures*. 2014 Dec 8; [24\(1\):015018](#)
- 312.Choi E, Kim DJ, Youn H, Nam TH. Repairing cracks developed in mortar beams reinforced by cold-drawn NiTi or NiTiNb SMA fibers. *Smart Materials and Structures*. 2015 Oct 27; [24\(12\):125010](#)
- 313.Kim MK, Kim DJ, Chung YS, Choi E. Direct tensile behavior of shape-memory-alloy fiber-reinforced cement composites. *Construction and Building Materials*. 2016 Jan 15; [102:462-70](#)
- 314.Ali MA, Soliman AM, Nehdi ML. Hybrid-fiber reinforced engineered cementitious composite under tensile and impact loading. *Materials & Design*. 2017 Mar 5; [117:139-49](#)
- 315.Ali MA, Nehdi ML. Innovative crack-healing hybrid fiber reinforced engineered cementitious composite. *Construction and Building Materials*. 2017 Sep 30; [150:689-702](#)
- 316.Naaman AE. *Prestressed concrete analysis and design: fundamentals*. New York: McGraw-Hill; 1982.
- 317.Roberts MH. Effect of calcium chloride on the durability of pre-tensioned wire in prestressed concrete. *Magazine of Concrete Research*. 1962 Nov; [14\(42\):143-54](#)
- 318.Salas Pereira RM. *Accelerated corrosion testing, evaluation and durability design of bonded post-tensioned concrete tendons 2005*
- 319.Muller JF, Dux PF. Fatigue of prestressed concrete beams with inclined strands. *Journal of Structural Engineering*. 1994 Apr; [120\(4\):1122-39](#)

320. Hurlbaeus S, Hueste MB, Karthik MM, Terzioglu T. Inspection Guidelines for Bridge Post-tensioning and Stay Cable Systems Using NDE Methods. 2017.
321. El-Tawil S, Ortega-Rosales J. Prestressing concrete using shape memory alloy tendons. *Structural Journal*. 2004 Nov 1; 101(6):846-51
322. Li L, Li Q, Zhang F. Behavior of smart concrete beams with embedded shape memory alloy bundles. *Journal of Intelligent Material Systems and Structures*. 2007 Oct; [18\(10\):1003-14](#)
323. Choi E, Park SH, Chung YS, Kim HS. Seismic fragility analysis of lap-spliced reinforced concrete columns retrofitted by SMA wire jackets. *Smart Materials and Structures*. 2013 Jul 16; [22\(8\):085028](#)
324. Ozbulut OE, Daghash S, Sherif MM. Shape memory alloy cables for structural applications. *Journal of Materials in Civil Engineering*. 2015 Oct 26; [28\(4\):04015176](#)
325. Daghash S, Ozbulut OE, Sherif MM. Shape memory alloy cables for civil infrastructure systems. In *ASME 2014 Conference on Smart Materials, Adaptive Structures and Intelligent Systems* 2014 Sep 8 (pp. [V001T01A017-V001T01A017](#)). American Society of Mechanical Engineers
326. Sherif MM, Ozbulut OE. Tensile and superelastic fatigue characterization of NiTi shape memory cables. *Smart Materials and Structures*. 2017 Nov 27; [27\(1\):015007](#)
327. Reedlunn B, Daly S, Shaw J. Superelastic shape memory alloy cables: Part I—iso-thermal tension experiments. *International Journal of Solids and Structures*. 2013 Oct 1; [50\(20-21\):3009-26](#)
328. Laplanche G, Birk T, Schneider S, Frenzel J, Eggeler G. Effect of temperature and texture on the reorientation of martensite variants in NiTi shape memory alloys. *Acta Materialia*. 2017 Apr 1; [127:143-52](#)
329. Zhang Y, Zhu J, Moumni Z, Van Herpen A, Zhang W. Energy-based fatigue model for shape memory alloys including thermomechanical coupling. *Smart Materials and Structures*. 2016 Feb 23; [25\(3\):035042](#)
330. Sherif MM, Tanks J, Ozbulut OE. Acoustic emission analysis of cyclically loaded superelastic shape memory alloy fiber reinforced mortar beams. *Cement and Concrete Research*. 2017 May 1; [95:178-87](#)
331. Sherif MM, Khakimova EM, Ozbulut OE, Harris DK, Ozyildirim HC. Behavior of mortar beams with randomly distributed superelastic shape memory alloy fibers. *Journal of Intelligent Material Systems and Structures*. 2017 Jul 21; [1045389X17721029](#)
332. Sherif MM, Ozbulut OE, Tanks J. Investigations on Cyclic Flexural Behavior of Fiber Reinforced Cementitious Composites Using Digital Image Correlation and Acoustic Emissions. In *International Digital Imaging Correlation Society 2017* (pp. [173-175](#)). Springer, Cham.
333. Khakimova EM, Sherif MM, Tanks JD, Ozbulut OE, Harris DK, Ozyildirim C. Feasibility of Using Shape Memory Alloys as Fiber Reinforcement in Concrete. 2016
334. Aggelis DG, Soulioti DV, Sapouridis N, Barkoula NM, Paipetis AS, Matikas TE. Acoustic emission characterization of the fracture process in fibre reinforced concrete. *Construction and Building Materials*. 2011 Nov 1; [25\(11\):4126-31](#)
335. Sagar RV, Prasad BR, Kumar SS. An experimental study on cracking evolution in concrete and cement mortar by the b-value analysis of acoustic emission technique. *Cement and Concrete Research*. 2012 Aug 1; [42\(8\):1094-104](#)
336. Paul SC, Pirkawetz S, Van Zijl GP, Schmidt W. Acoustic emission for characterising the crack propagation in strain-hardening cement-based composites (SHCC). *Cement and Concrete Research*. 2015 Mar 1; [69:19-24](#)
337. Aggelis DG, Mpalaskas AC, Matikas TE. Investigation of different fracture modes in cement-based materials by acoustic emission. *Cement and Concrete Research*. 2013 Jun 1; [48:1-8](#)
338. Aggelis DG, Soulioti DV, Barkoula NM, Paipetis AS, Matikas TE. Influence of fiber chemical coating on the acoustic emission behavior of steel fiber reinforced concrete. *Cement and Concrete Composites*. 2012 Jan 1; [34\(1\):62-7](#)
339. Granger S, Loukili A, Pijaudier-Cabot G, Chanvillard G. Experimental characterization of the self-healing of cracks in an ultra high performance cementitious material: Mechanical tests and acoustic emission analysis. *Cement and Concrete Research*. 2007 Apr 1; [37\(4\):519-27](#)
340. Soulioti D, Barkoula NM, Paipetis A, Matikas TE, Shiotani T, Aggelis DG. Acoustic emission behavior of steel fibre reinforced concrete under bending. *Construction and Building Materials*. 2009 Dec 1; [23\(12\):3532-6](#)
341. RILEM Technical Committee. Recommendation of RILEM TC 212-ACD: acoustic emission and related NDE techniques for crack detection and damage evaluation in concrete. *Materials and Structures*. 2010 Nov 1; [43\(9\):1183-6](#)
342. Ohno K, Ohtsu M. Crack classification in concrete based on acoustic emission. *Construction and Building Materials*. 2010 Dec 1; [24\(12\):2339-46](#)
343. Omondi B, Aggelis DG, Sol H, Sitters C. Improved crack monitoring in structural concrete by combined acoustic emission and digital image correlation techniques. *Structural Health Monitoring*. 2016 May; [15\(3\):359-78](#)

344. ASTM C1609/C1609M-12 Standard Test Method for Flexural Performance of Fiber-Reinforced Concrete (Using Beam With Third-Point Loading), ASTM International, West Conshohocken, PA, 2012, https://doi.org/10.1520/C1609_C1609M-12
345. Ozbulut OE, Hamilton RF, Sherif MM, Lanba A. Feasibility of self-pre-stressing concrete members using shape memory alloys. *Journal of Intelligent Material Systems and Structures*. 2015 Dec; [26\(18\):2500-14](#)
346. Sherif M, Ozbulut O, Landa A, Hamilton RF. Self-post-tensioning for concrete beams using shape memory alloys. In ASME 2014 Conference on Smart Materials, Adaptive Structures and Intelligent Systems 2014 Sep 8 (pp. [V002T04A014-V002T04A014](#)). American Society of Mechanical Engineers
347. Ozbulut OE, Sherif M, Hamilton RH. Self-post-tensioned concrete elements using shape memory alloys. 2015
348. Dwairi HM, Wagner MC, Kowalsky MJ, Zia P. Behavior of instrumented prestressed high performance concrete bridge girders. *Construction and Building Materials*. 2010 Nov 1; [24\(11\):2294-311](#)
349. Zhang CS, Zhao LC, Duerig TW, Wayman CM. Effects of deformation on the transformation hysteresis and shape memory effect in a Ni₄₇Ti₄₄Nb₉ alloy. *Scripta Metallurgica et Materialia*. 1990 Sep 1; [24\(9\):1807-12](#)
350. Zhao LC. Study of Ti-Ni-Nb shape memory alloys with a wide hysteresis. In *Materials science forum 2000* (Vol. 327, pp. 23-30). Trans Tech Publications
351. Piao M, Miyazaki S, Otsuka K, Nishida N. Effects of Nb addition on the microstructure of Ti-Ni alloys. *Materials Transactions, JIM*. 1992; [33\(4\):337-45](#)
352. Siegert W, Neuking K, Mertmann M, Eggeler G. Influence of Nb content and processing conditions on microstructure and functional properties of NiTiNb shape-memory alloys. In *Materials Science Forum 2001* (Vol. 394, pp. 361-364). Trans Tech Publications Ltd., Zurich-Uetikon, Switzerland
353. Otsuka K, Wayman CM, editors. *Shape memory materials*. Cambridge university press; 1999 Oct 7
354. ASTM E328-13 Standard Test Methods for Stress Relaxation Tests for Materials and Structures, ASTM International, West Conshohocken, PA, 2013, <https://doi.org/10.1520/E0328>
355. Yan Y, Jin W, Li XW. Texture development in the Ni₄₇Ti₄₄Nb₉ shape memory alloy during successive thermomechanical processing and its effect on shape memory and mechanical properties. *Metallurgical and Materials Transactions A*. 2013 Feb 1; [44\(2\):978-89](#)
356. Wang EM, Hong QH, Ni ZM, Han J. Influence of processing state on recovery stress in NiTiNb shape memory alloy. In *Advanced Materials Research 2014* (Vol. 875, pp. 1525-1528). Trans Tech Publications
357. Zhao LC. Study of Ti-Ni-Nb shape memory alloys with a wide hysteresis. In *Materials science forum 2000* (Vol. 327, pp. 23-30). Trans Tech Publications.
358. Cai W, Zhang CS, Zhao LC. Recovery stress of Ni-Ti-Nb wide-hysteresis shape memory alloy under constant strain and thermomechanical cycling. *Journal of materials science letters*. 1994 Jan 12; [13\(1\):8-9](#)
359. Kusagawa M, Nakamura T, Asada Y. Fundamental deformation and recovery behaviors of Ni-Ti-Nb shape memory alloy. *JSME International Journal Series A Solid Mechanics and Material Engineering*. 2001; [44\(1\):57-63](#)
360. Melton KN, Proft JL, Duerig TW. Wide Hysteresis Shape Memory Alloys Based on the NiTiNb System. In *Proceedings of the MRS International Meeting on Advanced Materials*. 1988 May (Vol. 9, pp. 165-170)
361. Pal NR, Pal SK. A review on image segmentation techniques. *Pattern recognition*. 1993 Sep 1; [26\(9\):1277-94](#)
362. Sahoo PK, Soltani SA, Wong AK. A survey of thresholding techniques. *Computer vision, graphics, and image processing*. 1988 Feb 1; [41\(2\):233-60](#)
363. Kim HY, Jinguu T, Nam TH, Miyazaki S. Cold workability and shape memory properties of novel TiNiHfNb high-temperature shape memory alloys. *Scripta Materialia*. 2011 Nov 1; [65\(9\):846-9](#)
364. Duerig TW, Melton KN. Wide hysteresis NiTiNb alloys. In *European Symposium on Martensitic Transformations 1989* (pp. 191-198). EDP Sciences
365. Zinn S, Semiatin SL. Coil design and fabrication: basic design and modifications. *Heat treating*. 1988 Jun; [12\(3\):32-6](#)
366. Liu HT, Sun GA, Wang YD, Chen B, Wang XL, Tian Q. In situ study of stress-induced martensitic transformation in Ni₄₇Ti₄₄Nb₉ shape-memory alloys. In *Advanced Materials Research 2013* (Vol. 652, pp. 1096-1101). Trans Tech Publications
367. Zheng YF, Cai W, Zhang JX, Zhao LC, Ye HQ. Microstructural development inside the stress induced martensite variant in a Ti-Ni-Nb shape memory alloy. *Acta materialia*. 2000 Apr 2; [48\(6\):1409-25](#)
368. Dong ZZ, Kajiwara S, Kikuchi T, Sawaguchi T. Effect of pre-deformation at room temperature on shape memory properties of stainless type FeMnSiCrNiNbC alloys. *Acta Materialia*. 2005 Sep 1; [53\(15\):4009-18](#)
369. Abeles PW, Bardhan-Roy MB, Bardhan-Roy BK. *Prestressed concrete designer's handbook*. CRC Press; 1981
370. Abdelatif AO, Owen JS, Hussein MF. Modeling the re-anchoring of a ruptured tendon in bonded post-tensioned concrete

Dissertation: Design and Characterization of Innovative Materials and Structural Systems for Resilient Concrete Structures

371. Piao M, Otsuka K, Miyazaki S, Horikawa H. Mechanism of the A_s temperature increase by pre-deformation in thermoelastic alloys. *Materials Transactions, JIM*. 1993; [34\(10\):919-29](#)
372. Shi H, Pourbabak S, Van Humbeeck J, Schryvers D. Electron microscopy study of Nb-rich nanoprecipitates in NiTiNb and their influence on the martensitic transformation. *Scripta Materialia*. 2012 Dec 1; [67\(12\):939-42](#)
373. Liu Y, Favier D. Stabilisation of martensite due to shear deformation via variant reorientation in polycrystalline NiTi. *Acta materialia*. 2000 Aug 1; [48\(13\):3489-99](#)